CP Violation at LHCb and a Novel Measurement of Hadronic Charm Inputs at BESIII

Innes Mackay

Lincoln College

University of Oxford

A thesis submitted for the degree of

Doctor of Philosophy

July 12, 2025

Acknowledgements

My first thanks goes to my supervisor, Sneha Malde, for her guidance and encouragement throughout my PhD. I am greatly appreciative that she always made time to provide useful feedback on my work, despite her busy schedule, and for her high standards which significantly improved the quality of my research.

I would like to express my gratitude to Alex Gilman for his collaboration. Our regular discussions were invaluable in performing the strong-phase measurement. Alex was very patient as I got to grips with the nuances of physics at BESIII and was always keen to share his wealth of knowledge.

Those who were members of the Oxford group during my time also deserve acknowledgment. In particular, Guy Wilkinson, for his insightful comments on the BESIII analysis, and Martin Tat and Seophine Stanislaus, who bore the brunt of my questions and helped me to understand many concepts.

I also want to take this opportunity to thank my parents for their unwavering encouragement, and my brother, Kieran, who often provided a much-needed distraction through laughs shared on the golf course.

Finally, my biggest thank you goes to my girlfriend, Katie, who has been my closest companion throughout this journey. I am eternally grateful that she has been so understanding through many late nights of working, and, more importantly, for her love and support.

Abstract

The angle γ of the Unitarity Triangle is measured by studying *CP* violation in $B^0 \to DK^*(892)^0$ decays, where D denotes a superposition of the D^0 and $\overline{D}^0$ mesons. The value $\gamma = \left(49^{+22}_{-19}\right)^\circ$ is determined, where the uncertainty combines the statistical and systematic sources. The measurement is made using a dataset with an integrated luminosity of $9\,\text{fb}^{-1}$, and is collected by the LHCb experiment in proton-proton collisions at centre-of-mass energies of 7, 8 and 13 TeV. The procedure examines *CP* violation across the kinematic phase space of the $D \to K^0_S\pi^+\pi^-$ and $D \to K^0_S K^+ K^-$ decays. The angle γ is interpreted from the data using hadronic inputs describing the D decays. The values of these inputs are provided by the BESIII experiment using quantum-correlated $D\overline{D}$ meson pairs, rather than relying on those provided by an amplitude model.

The second half of this thesis presents the determination of a hadronic charm parameter, specifically the strong-phase difference between D^0 and $\overline{D}^0$ decays to the $K^-\pi^+$ final state, $\delta_D^{K\pi}$. A dataset, which is collected by the BESIII experiment in e^+e^- collisions at centre-of-mass energies between 4.13 and 4.23 GeV, and has an integrated luminosity of $7.13\,\text{fb}^{-1}$, is used for the analysis. The parameter $\delta_D^{K\pi}$ is measured by exploiting interference in $D\overline{D} \to K^-\pi^+$ vs. X decays, where X is a *CP* eigenstate or $K^0_S\pi^+\pi^-$. It is determined to be $\delta_D^{K\pi} = \left(192.8^{+11.0+1.9}_{-12.4-2.4}\right)^\circ$, where the first uncertainty is statistical and the second is systematic. The study presented is the first to observe and use the quantum correlations in $D\overline{D}$ pairs produced above the $\psi(3770)$ resonance. At these higher energies, the $D\overline{D}$ pairs are produced in even and odd eigenstates of the charge-conjugation operator, C, compared to only the latter at $\psi(3770)$. Simultaneously using the C-even and C-odd $D\overline{D}$ pairs allows access to novel experimental observables that significantly reduce systematic uncertainties.

Preface

This thesis details two measurements I performed during my time as a PhD student. The first, covered in Chapter 4, is a determination of the CKM angle γ using $B^0 \to DK^*(892)^0$ decays collected at LHCb. The analysis was published in European Physics Journal C in February 2024 (*Eur. Phys. J. C* **84** (2024) 2, 206). The second measurement is of the strong-phase difference between $D^0 \to K^-\pi^+$ and $\overline{D}^0 \to K^-\pi^+$ decays, $\delta_D^{K\pi}$, at BESIII and is outlined in Chapter 7. For this study, two papers, targeting Physical Review D and Physical Review Letters, are currently in internal collaboration review with the aim of publishing before summer this year.

All work presented in this thesis is my own, except for the selection requirements used in Sec. 7.2, which are standard criteria used by the BESIII collaboration, the selection requirements outlined in Sec.7.3, which were developed by Dr. Alex Gilman, and the demonstration of quantum correlations discussed in Sec. 7.4, which is also Alex's work.

I was involved in numerous projects beyond the two measurements described in this thesis. First, I was solely responsible for the calibration of proton particle identification (PID) at LHCb. For this task, I developed the data samples, improved the fit models, and regularly provided the collaboration with efficiencies which are important to understand the detector after the recent upgrade. Furthermore, I progressed the selection of a secondary proton calibration sample, which required employing a boosted decision tree to improve the purity. Alongside this work, I developed, tested and maintained a software package used by the collaboration to obtain PID efficiencies from the calibration samples, and I served as a *data productions liaison* where my task was to check and submit data-processing jobs for my colleagues. Finally, I spent a small proportion of time working on a future detector, named TORCH, which can provide low momentum PID at LHCb in Upgrade II. My role was to investigate cost-saving options by experimenting with the geometry and specifications of the detector.

Contents

1 Introduction

The Standard Model (SM) of Particle Physics is one of the most successful theories, and it can describe almost everything in the Universe today. However, a few mysteries remain. One of the most famous puzzles is Dark Matter. Stars on the periphery of galaxies are travelling at much faster speeds than expected, which can be explained by additional mass, called *Dark Matter*, within the galaxy that we cannot observe. One hypothesis is that Dark Matter is caused by particles which interact very weakly with normal matter, however, despite many dedicated searches and experiments, there is no evidence yet that such particles exist.

Another big question is: where did all the anti-matter go? Looking out to the Universe, the astrophysical objects are observed to be made from normal matter. Suggestions that there exist gas clouds, stars and galaxies created from anti-matter are rejected because radiation from boundaries, where such objects meet normal matter and annihilate, are not seen. A small asymmetry that favours matter over anti-matter would explain the conundrum, which requires breaking of a symmetry, called *CP violation*.

CP violation was discovered in the neutral kaon system in 1964 by James Cronin and Val Fitch [1], who shared the Nobel Prize for their work in 1980. Since then, *CP* violation has been one of the most actively studied areas of Particle Physics, which

has lead to a significant improvement in our understanding. In 2001, *CP* violation was observed in beauty mesons by the Belle [2] and BaBar [3] experiments, and, more recently, in 2019 it was also seen in charmed mesons by the LHCb collaboration [4]. Finally, in 2025, *CP* violation was observed in baryon decays for the first time [5].

CP violation has only been observed in the weak-force interactions of quarks, where mixing occurs between the three generations via a charged current. The coupling strength of the quark mixing is governed by the Cabibbo–Kobayashi–Maskawa (CKM) matrix [6, 7]. An important parameter that describes the CKM matrix is the *CP*-violating phase, γ. It can be directly measured using *CP* violation in decays with a $B \to DK$-like topology, which are tree-level processes, and compared to the indirect determinations, which are sensitive to New Physics. This procedure is known as *over-constraining* the CKM angle γ, and it could reveal non-SM phenomena.

At present, the two determinations of γ are in agreement [8]. Therefore, a more precise estimation is needed to further probe the CKM matrix and weak interaction. To achieve the next precision milestone requires exhausting current and future datasets by measuring γ in many different decay channels. This strategy has decreased the uncertainty on γ from 30 to 3 degrees over the last 18 years, which has been driven by the LHCb experiment. In Chapter 4 of this thesis, the angle γ is determined by studying the *CP* violation in $B^0 \to DK^*(892)^0$ decays in phase-space regions of the $D \to K^0_S\pi^+\pi^-$ and $D \to K^0_S K^+K^-$ final states.

To extract γ from the data requires knowledge of the hadronic parameters associated with the D decays. These parameters are measured at charm factories by exploiting the unique properties of $D\overline{D}$ pairs that are produced in an entangled state. In the study described in Chapter 4, the inputs for the $D \to K^0_S\pi^+\pi^-$ and $D \to K^0_S K^+K^-$ decays are those determined by the BESIII experiment [9, 10, 11].

Many possible final states of the D meson can be used to determine γ. One channel which provides particularly good sensitivity is the $D \to K^-\pi^+$ decay [12]. The hadronic parameter for this mode is the strong-phase difference between the $D^0 \to K^-\pi^+$ and $\overline{D}^0 \to K^-\pi^+$ decays, denoted $\delta_D^{K\pi}$. The parameter $\delta_D^{K\pi}$ is important for measuring γ, but it is also a crucial input in studies of charm mixing.

At present, $\delta_D^{K\pi}$ is only known with a precision of around ten degrees from BESIII and CLEO measurements [13, 14], although, a combination of charm mixing and γ measurements at LHCb determines $\delta_D^{K\pi}$ with a precision of 2.5° [15]. However, if $\delta_D^{K\pi}$ was independently known to a precision of a few degrees, the uncertainties on γ and the charm-mixing parameters from the LHCb data could reach their full potential, rather than being used to improve the precision on the hadronic parameter. This strongly motivates the measurement of $\delta_D^{K\pi}$ using quantum-correlated $D\overline{D}$ pairs that is described in Chapter 7.

The knowledge of γ is currently limited by signal yields, but the recent upgrade of the LHCb detector [16] will provide significantly larger datasets in the coming years. Naturally, the systematic uncertainties will become more important, and they are often dominated by the hadronic charm inputs, as is the case for the measurement of γ using $B^{\pm} \to DK^{\pm}$ decays with the $D \to K^-\pi^+$ final state [12]. All current determinations of these hadronic parameters are performed using data collected at the charm threshold. They can also be carried out at higher energies, although, until now, it has never been done. Chapter 7 employs a novel technique to measure $\delta_D^{K\pi}$ using data collected at a range of energies above the charm threshold by the BESIII experiment. The analysis paves the way for other, similar measurements, which will maximise the utility of current and future data samples.

The rest of the thesis is structured as follows. It begins with Chapter 2 which will provide the background necessary to understand the direct determinations of γ. An overview of the LHCb detector is provided in Chap. 3, before Chap. 4 details the measurement of γ using $B^0 \to DK^*(892)^0$ decays. The second half of the thesis follows, with some background covering measurements of hadronic charm inputs using quantum-correlated $D\overline{D}$ pairs in Chap. 5 and the BESIII detector is discussed in Chap. 6. The measurement of $\delta_D^{K\pi}$ is described in Chap. 7. Finally, a summary and a look to the future is found in Chap. 8.

2

Theoretical background for γ measurements

Contents

2.1 The Standard Model

The Standard Model (SM) is a Quantum Field Theory describing the fundamental particles and their interactions. The SM is highly successful and, at present, it predicts almost all experimental measurements, culminating in the renowned discovery of the Higgs boson in 2012 [17, 18].

The particles in the SM, depicted in Fig. 2.1, interact via three forces through the exchange of spin-1 gauge bosons. The electromagnetic force is the most familiar, and it is mediated by the transfer of massless photons. The gluons are the gauge

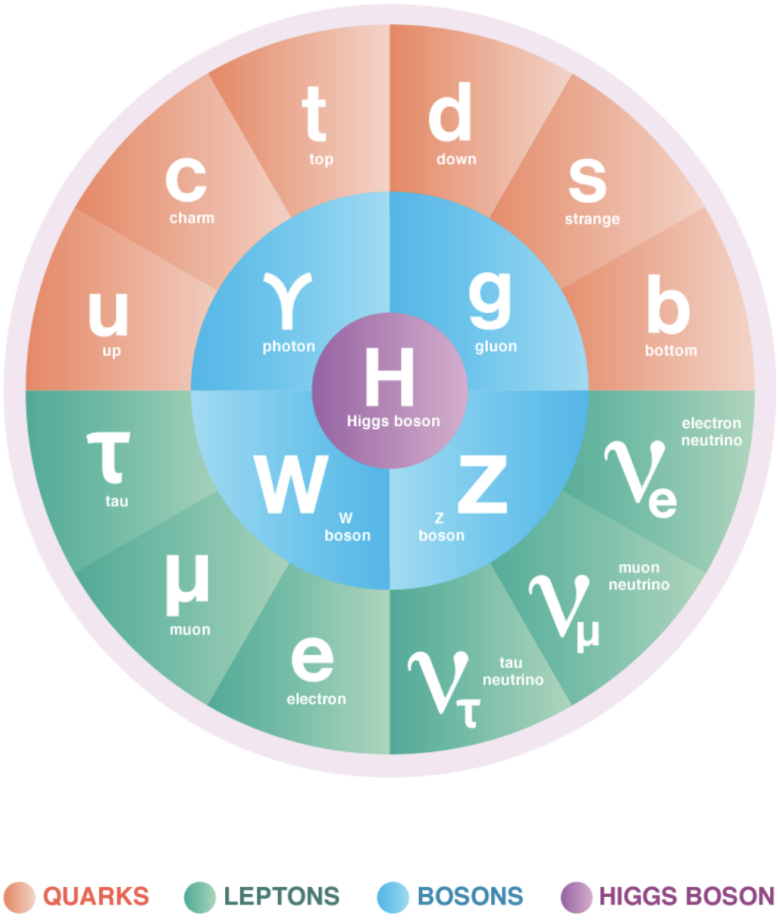

Figure 2.1: The fundamental particles of the Standard Model [19].

bosons exchanged in strong-force interactions, which are responsible for binding quarks together in composite particles such as protons and neutrons, whilst the $W^{\pm}$ and Z bosons participate in weak-force interactions, which are commonly associated with radioactive decays. Figure 2.2 displays Feynman diagrams that illustrate the interactions through the exchange of each gauge boson.

There are 12 elementary spin-half particles in the SM, named fermions, which are divided into two families of three generations. In the *lepton* family, the electron, muon and tau particles interact via the electromagnetic and weak forces, while the corresponding electrically-neutral *neutrinos*, ν_l where $l \in (e, \mu, \tau)$, only couple to the latter. The second family of fermions are the *quarks*, which interact with all three forces. In each generation, there is a quark with an electrical charge of

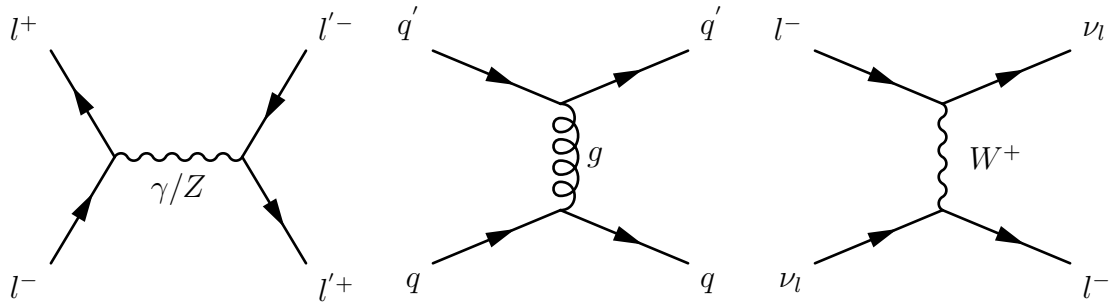

Figure 2.2: Feynman diagrams displaying the interactions of the gauge bosons in the Standard Model.

$+\frac{2}{3}e$, and another with $-\frac{1}{3}e$. For each fermion there is a corresponding anti-fermion which has the opposite additive quantum numbers.

The gauge bosons arise in the SM from requiring invariance under local symmetry transformations [20]. In the simplest case, a massless field A_μ is required to satisfy invariance under a local $U(1)$ transformation. At low energies, A_μ corresponds to a photon coupling to electric charge. In a similar manner, eight gluons, which carry *colour* charge, arise from the $SU(3)$ symmetry. The quarks interact via the strong force because they posses colour, unlike the leptons.

The satisfying idea of an all-encompassing theory lead to physicists attempting to unite the various forces. In the middle of the 20^{th} century, the electromagnetic and weak interactions were combined at high energies in the *electroweak* theory [21, 22, 23], where invariance under a combined $SU(2) \times U(1)$ symmetry naturally gives rise to the photon, $W^\pm$ and Z bosons. At the time, many already suspected the existence of the $W^\pm$ bosons, but the Z was entirely new. Both were later experimentally discovered at the European Organization for Nuclear Research (CERN) facility in the 1980s [24, 25].

A prediction of the electroweak theory is that the $W^\pm$ and Z attain mass by interacting with a scalar field which spontaneously breaks the $SU(2) \times U(1)$ symmetry [26, 27]. The same symmetry breaking is responsible for the mass of the fermions. A consequence of the so-called *Higgs mechanism* is the prediction of a new spin-0 particle, the Higgs boson. It's remarkable discovery in 2012 [17, 18] set the scene for modern Particle Physics, in which physicists spend their days searching for inconsistencies in the SM.

2.2 Discrete symmetries

In the 1950s, two particles, named τ^+ and θ^+, were observed to decay via the weak interaction into the $\pi^+\pi^-\pi^+$ and $\pi^+\pi^0$ final states, respectively. The pions are known to have an odd intrinsic parity, P, which is a quantum-mechanical property of a particle that describes how the wavefunction behaves under spatial inversion of $\vec{x} \to -\vec{x}$. Therefore, assuming parity conservation, which was a widely-held belief at the time, the τ and θ must be distinct. However, they were observed to possess identical physical properties, such as mass and lifetime, which was puzzling.

A suggestion to resolve the mystery is violation of parity in the weak interaction [28]. To test this hypothesis, an experiment was carried out by Wu et. al. in which they examined the angular distribution of electrons produced in the radioactive decay of polarised $^{60}\text{Co} \to\ ^{60}\text{Ni} + e^- + \overline{\nu}$ [29]. The momentum of the electron reverses under a parity transformation, and hence, if parity were conserved, the same number of electrons would be seen in opposite directions. However, an asymmetry was observed providing the first unequivocal evidence of parity violation. The theoretical description of the weak interaction was later revised, such that the $W^\pm$ bosons only couple to particles with a left-handed chirality and anti-particles with a right-handed chirality.

The new framework raised questions about other discrete symmetries. Of particular interest was charge conjugation, denoted by C, which swaps particles with anti-particles. This transformation converts left-handed particles to left-handed anti-particles, which do not couple to the $W^\pm$ bosons, and thus C must also be a violated symmetry in the weak interaction.

The combined action of C and P, however, converts left-handed particles to right-handed anti-particles, and thus CP was initially thought to be conserved. This idea remained until 1964 when Cronin and Fitch performed their famous experiment to examine the decays of the long and short-lived neutral kaons, where they found clear evidence of CP violation [1]. The theory was later reconciled through an altogether different mechanism discussed in the next section. Violation of CP

symmetry is an important area of research because it is one of the conditions, proposed by Sakharov [30], for the observed asymmetry between matter and anti-matter in the Universe.

2.3 *CP* violation in the Standard Model

In the SM, the $W^{\pm}$ bosons couple to the weak eigenstates of the up-type (u, c, t) quarks to those of the down-type (d, s, b) quarks, with a coupling strength governed by the Cabibbo-Kobayashi–Maskawa (CKM) matrix [6, 7],

$$V_{CKM} = \begin{pmatrix} V_{ud} & V_{us} & V_{ub} \\ V_{cd} & V_{cs} & V_{cb} \\ V_{td} & V_{ts} & V_{tb} \end{pmatrix}. \tag{2.1}$$

The 9 complex elements are described by 18 free parameters. This number is halved by imposing the SM requirement that V_{CKM} is unitary through the nine equations that arise from $V_{CKM}^{\dagger} V_{CKM} = \mathbb{1}$,

$$\begin{aligned} \sum_k V_{ik} V_{jk}^* &= 0 \text{ for } i \neq j, \\ \sum_i |V_{ik}|^2 &= 1 \text{ for } k = 1, 2, 3. \end{aligned} \tag{2.2}$$

The number of degrees of freedom is further reduced from 9 to 4 by reabsorbing phases into the definitions of the quark states, which leaves the physics unaffected. The remaining four parameters, which fully describe the matrix, are the three mixing angles, θ_{12}, θ_{13} , θ_{23}, and a complex phase, δ_{CP}, such that [31]

$$V_{CKM} = \begin{pmatrix} 1 & 0 & 0 \\ 0 & c_{23} & s_{23} \\ 0 & -s_{23} & c_{23} \end{pmatrix} \times \begin{pmatrix} c_{13} & 0 & s_{13} e^{-i\delta_{CP}} \\ 0 & 1 & 0 \\ -s_{13} e^{i\delta_{CP}} & 0 & c_{13} \end{pmatrix} \times \begin{pmatrix} c_{12} & s_{12} & 0 \\ -s_{12} & c_{12} & 0 \\ 0 & 0 & 1 \end{pmatrix}, \tag{2.3}$$

where $s_{ij} \equiv \sin\theta_{ij}$ and $c_{ij} \equiv \cos\theta_{ij}$. Under a *CP* transformation the quarks become anti-quarks, and thus the phase flips sign, $\delta_{CP} \to -\delta_{CP}$. This is the origin of *CP* violation in the quark sector of the SM.

The amplitude of a weak decay that proceeds via a single Feynman diagram is $Ae^{i(\delta+\delta_W)}$, where δ_W is the phase associated with the weak interaction, and δ is a phase from strong-interaction processes and conserves the *CP* symmetry. The

latter typically arises from QCD interactions between the final-state quarks and thus is known as the *strong phase*. The amplitude of the *CP*-conjugated decay is $Ae^{i(\delta-\delta_W)}$. The decay rate is proportional to the square of the amplitude, so clearly *CP* violation would not be seen by examining a decay that proceeds through a single Feynman diagram. However, if a final state could also be reached via another diagram, quantum-mechanical interference would occur which is sensitive to the weak phase and *CP* violation, as discussed in detail in the next section.

Early measurements found V_{CKM} to possess a hierarchical nature. The cross-generational couplings were observed to be smaller than those of the same generation, and therefore the CKM matrix is approximately diagonal. This led Lincoln Wolfenstein to devise a convenient parametrisation of V_{CKM} which reflected the structure, in which

$$s_{12} = \lambda, \tag{2.4}$$

$$s_{23} = A\lambda^2, \tag{2.5}$$

$$s_{13}e^{-i\delta_{CP}} = A\lambda^3(\rho - i\eta), \tag{2.6}$$

such that the CKM matrix becomes [32]

$$V_{CKM} = \begin{pmatrix} 1-\frac{\lambda^2}{2} & \lambda & A\lambda^3(\rho - i\eta) \\ -\lambda & 1-\frac{\lambda^2}{2} & A\lambda^2 \\ A\lambda^3(1-\rho-i\eta) & -A\lambda^2 & 1 \end{pmatrix} + \mathcal{O}(\lambda^4). \tag{2.7}$$

The Wolfenstein parametrisation is an expansion in powers of $\lambda \simeq 0.22$.

2.4 The Unitarity Triangle and the angle γ

At present, all observations of *CP* violation in the SM are consistent with originating from δ_{CP}, but the asymmetries are not large enough to explain our matter dominated Universe. Therefore, it is important to probe the SM and it's description of *CP* violation through the CKM matrix.

Six of the unitarity requirements in Eq. 2.2 produce triangles in the complex plane defined by $\bar{\rho} \equiv \rho(1-\frac{\lambda^2}{2})$ and $\bar{\eta} \equiv \eta(1-\frac{\lambda^2}{2})$. This concept is best understood

by considering the terms in the sum as two-component vectors with real and imaginary parts. The triangle that satisfies,

$$1 + \frac{V_{ud}V_{ub}^*}{V_{cd}V_{cb}^*} + \frac{V_{td}V_{tb}^*}{V_{cd}V_{cb}^*} = 0, \tag{2.8}$$

has three sides with lengths that are of a similar order in A and λ, which leads to large angles and *CP* asymmetries. It is commonly referred to as *the* Unitarity Triangle (UT), and it is plotted in Fig. 2.3.

The decays of B mesons involve the CKM elements in Eq. 2.8, and hence they are ideal for testing *CP* violation in the SM. The other triangles typically have at least one side which varies by $\mathcal{O}(\lambda)$ and thus are more difficult experimentally. For example, the triangle which is best studied in kaons is found by replacing $b \to s$ in Eq. 2.8. One side is $\mathcal{O}(\lambda^4)$ smaller than the others which leads to reduced *CP*-violating effects.

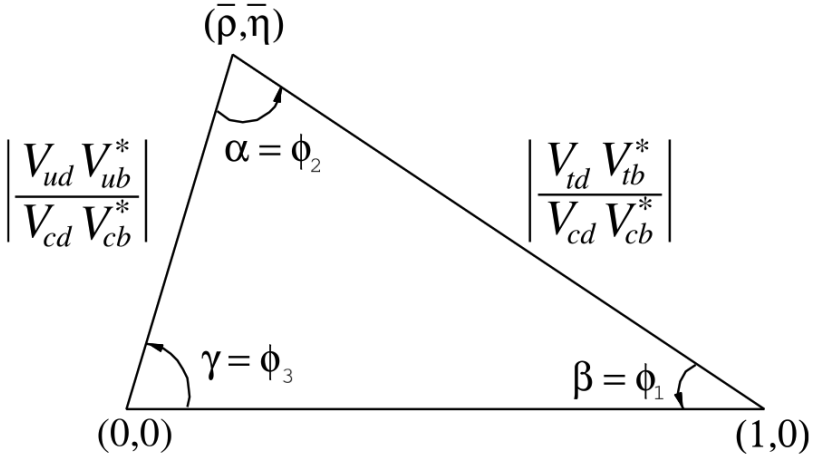

Figure 2.3: The Unitarity Triangle [33].

The angles in the UT are formally defined as

$$\beta = \arg\left(-\frac{V_{cd}V_{cb}^*}{V_{td}V_{tb}^*}\right), \tag{2.9}$$

$$\alpha = \arg\left(-\frac{V_{td}V_{tb}^*}{V_{ud}V_{ub}^*}\right), \tag{2.10}$$

$$\gamma = \arg\left(-\frac{V_{ud}V_{ub}^*}{V_{cd}V_{cb}^*}\right). \tag{2.11}$$

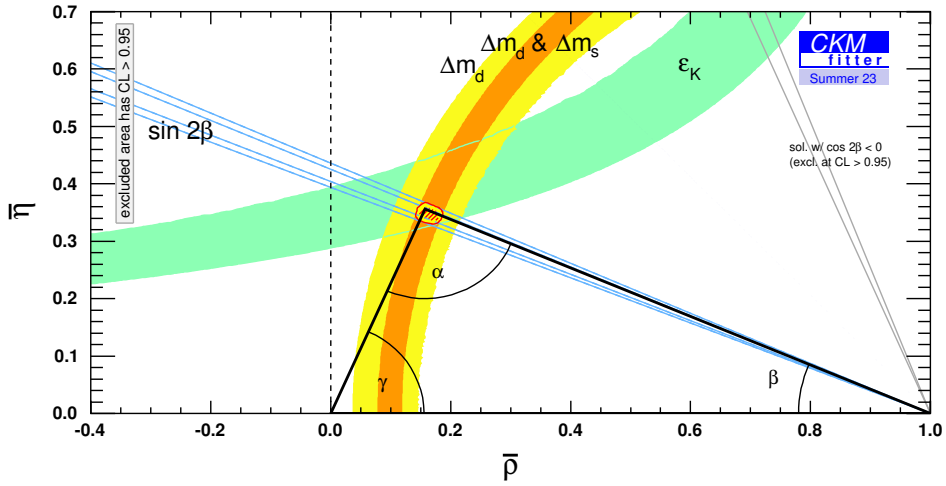

Figure 2.4: Current status of the loop-level constraints placed on the Unitarity Triangle [8].

It can be shown that γ, sometimes referred to as ϕ_3, is equivalent in magnitude to the *CP*-violating phase δ_{CP} to $\mathcal{O}(\lambda^4)$. The angle γ is of significant interest. It can be extracted cleanly because QCD effects are absorbed into nuisance parameters that are simultaneously determined alongside γ. Furthermore, γ is directly measured using only tree-level processes. The loop-level diagrams contribute at second order resulting in a theoretical uncertainty of $\delta\gamma/\gamma < 10^{-7}$ [34]. Therefore, γ is a high-precision *standard candle* of the SM.

Although there is no SM prediction for γ, because it is a function of the CKM elements which are free parameters, the value from direct measurements can be compared to the indirect determinations inferred from studying the UT [8, 35]. Some parameters that constrain the latter are measured using decays where loop-level diagrams, which can be enhanced by new particles, contribute at first order. Thus, by *over-constraining* the UT in this way, the consistency of the SM can be tested.

Figure 2.4 shows the constraints on the indirect value of γ placed by measurements sensitive to loop-level diagrams. The strongest limits are obtained through studies of time-dependent *CP* asymmetries in $B^0 \to \psi K^0_S$ decays to measure $\sin 2\beta$, and determinations of the mass differences between the flavour eigenstates in B^0-$\overline{B}^0$ (Δm_d) and B^0_s-$\overline{B}^0_s$ mixing (Δm_s), which proceed through box diagrams. The world

average for the direct measurements is $\gamma = \left(65.9^{+3.3}_{-3.5}\right)^\circ$ [36], whilst it is indirectly determined to be $\gamma = \left(66.29^{+0.72}_{-1.86}\right)^\circ$ [8] through global fits to the CKM parameters under the assumption of unitarity, and ignoring the direct γ measurements. The two determinations are currently in agreement, and thus a higher precision is required for a more scrupulous examination of the SM.

2.5 Direct measurements of γ

The *CP*-violating angle γ is the weak-phase difference between $b \to c\overline{u}s$ and $b \to u\overline{c}s$ quark transitions, and therefore it can be determined in decays with a $B \to DK$-like topology. The golden channel for such measurements is $B^\pm \to DK^\pm$, where D is a superposition of the D^0 and $\overline{D}^0$ mesons. As discussed in more detail below, for this decay mode the two interfering amplitudes are of a similar magnitude, each with a relatively high branching fraction, which leads to large *CP* asymmetries that can be precisely measured. Furthermore, the experimental procedure is relatively simple. The charged $B^\pm$ mesons do not mix, so time dependence does not need to be considered, and the *CP* asymmetries can be easily examined because the charge of the kaon unambiguously indicates the flavour of the $B^\pm$ meson.

The amplitudes for the $B^+ \to D^0K^+$ and $B^+ \to \overline{D}^0K^+$ decays are

$$A(B^+ \to \overline{D}^0K^+) = A_B e^{i\bar{\phi}_B}, \tag{2.12}$$

$$A(B^+ \to D^0K^+) = A_B r_{B^\pm} e^{i(\phi_B+\gamma)}, \tag{2.13}$$

where A_B is the magnitude of the $B^+ \to \overline{D}^0K^+$ decay, $\overset{(-)}{\phi}_B$ are the *CP*-conserving strong phases and $r_{B^\pm}$ is the magnitude of the ratio of amplitudes. A more condensed equation, which retains only the useful parameters, is

$$r_{B^\pm} e^{i(\delta_{B^\pm}+\gamma)} = \frac{A(B^+ \to \overline{D}^0K^+)}{A(B^+ \to D^0K^+)}, \tag{2.14}$$

where $\delta_{B^\pm} = \phi_B - \bar{\phi}_B$ is the strong-phase difference between the two decays.

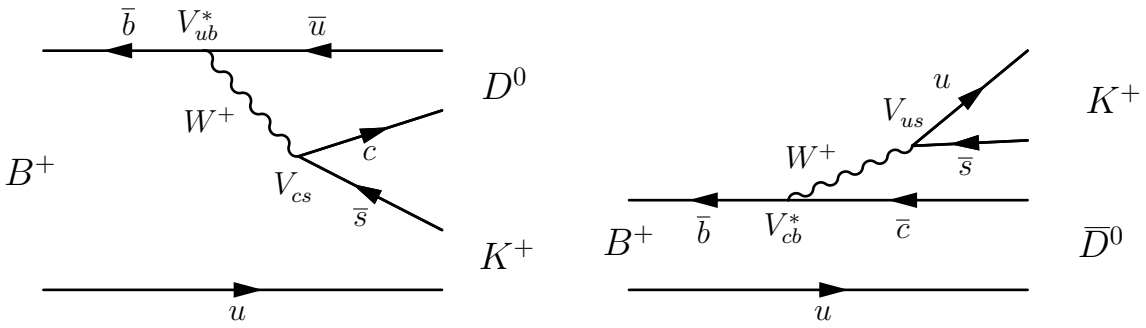

Figure 2.5: Feynman diagrams for the (left) $B^+ \to D^0 K^+$ and (right) $B^+ \to \bar{D}^0 K^+$ decays.

From the Feynman diagrams in Fig. 2.5, the weak-phase difference between the two decays is arg $\left(\frac{V_{cb}V_{us}^*}{V_{ub}V_{cs}^*}\right)$, which is not the definition of γ in Eq. 2.11. However, it can be easily shown using the Wolfenstein parametrisation that arg $\left(\frac{V_{cb}V_{us}^*}{V_{ub}V_{cs}^*}\right) = \gamma + \mathcal{O}(\lambda^4)$, and thus, at the current precision, they are effectively equivalent.

The amplitudes for the *CP*-conjugate $B^- \to DK^-$ decays are found by exchanging $\gamma \to -\gamma$, and it is this sign flip that is responsible for the *CP* violation between B^+ and B^- decays. As was already discussed, the *CP* violation can only be examined through quantum-mechanical interference, which is sensitive to the weak phase. Therefore, a final state of the D decay, denoted f, is used that is common to both the D^0 and $\bar{D}^0$ mesons, such that the two interfering paths to the common $B^+ \to [f]_D K^+$ final state are indistinguishable as depicted in Fig. 2.6.

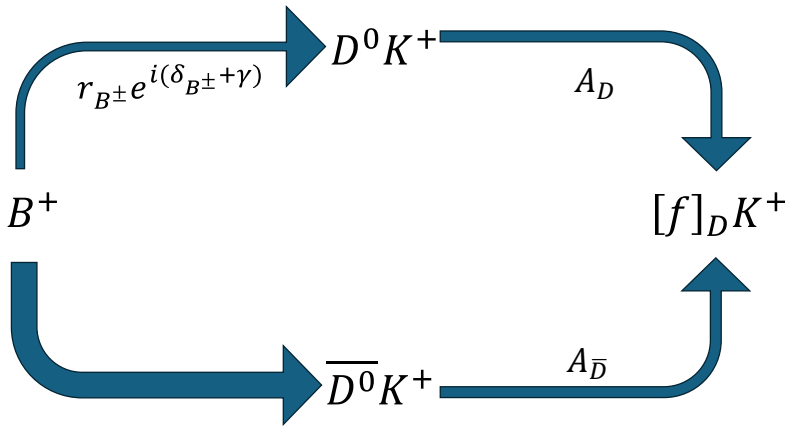

Figure 2.6: Diagram depicting the interference between $B^+ \to [f]_{D^0} K^+$ and $B^+ \to [f]_{\bar{D}^0} K^+$ decays where both D^0 and $\bar{D}^0$ decay to the final state, f.

The partial width for the $B^+ \to [f]_D K^+$ decay is given by

$$\begin{aligned}\Gamma(B^+ \to [f]_D K^+) &\propto |A_B e^{i\bar{\phi}_B} A_{\overline{D}} + A_B r_{B^\pm} e^{i(\phi_B+\gamma)} A_D|^2, \\ &\propto |A_{\overline{D}}|^2 + {r_{B^\pm}}^2 |A_D|^2 + r_{B^\pm}\left[A^*_{\overline{D}} A_D e^{i(\delta_{B^\pm}+\gamma)} + A_{\overline{D}} A^*_D e^{-i(\delta_{B^\pm}+\gamma)}\right],\end{aligned} \tag{2.15}$$

where A_D and $A_{\overline{D}}$ are the amplitudes of the $D^0 \to f$ and $\overline{D}^0 \to f$ decays, respectively. The equivalent formula for the *CP* conjugate is

$$\Gamma(B^- \to [\bar{f}]_D K^-) \propto |A_{\overline{D}}|^2 + {r_{B^\pm}}^2 |A_D|^2 + r_{B^\pm}\left[A^*_{\overline{D}} A_D e^{i(\delta_{B^\pm}-\gamma)} + A_{\overline{D}} A^*_D e^{-i(\delta_{B^\pm}-\gamma)}\right], \tag{2.16}$$

where it is assumed that direct *CP* violation in the charm sector is negligible, such that $A_D = A(D^0 \to f) = A(\overline{D}^0 \to \bar{f})$ and $A_{\overline{D}} = A(D^0 \to \bar{f}) = A(\overline{D}^0 \to f)$ [37]. Now, the effects of *CP* violation become clear. The interference terms in Eqs. 2.15 and 2.16 are different, and thus the asymmetry between the rates, which is an experimental observable with sensitivity to γ, will be non-zero.

Although the best limits on γ are made using $B^\pm$ decays, additional precision can be achieved using the B^0 and B^0_s meson channels, which is necessary for the best possible comparison with the indirect determinations from CKM matrix fits. This is motivation for the measurement of γ using $B^0 \to DK^*(892)^0$ decays[1] discussed in Chap. 4. At a glance, it appears that examining *CP* asymmetries as a function of decay time is necessary when using neutral B mesons due to mixing. However, the $B^0 \to DK^*(892)^0$ decay, which is shortened to $B^0 \to DK^{*0}$ in the remainder of this thesis, is *self tagging* - the charge on the kaon from the $K^{*0} \to K^+\pi^-$ decay unambiguously determines the flavour of the B meson at decay [38].

Both the $B^0 \to D^0 K^{*0}$ and $B^0 \to \overline{D}^0 K^{*0}$ decays are colour suppressed, as can be seen in the Feynman diagrams shown in Fig. 2.7, whereas only the $B^\pm \to D^0 K^\pm$ decay path is colour suppressed in $B^\pm$ decays. This property leads to an amplitude ratio in B^0 decays that is around three times larger than in $B^\pm$ decays, $r_{B^0} \sim 3 r_{B^\pm}$. It is evident from Eqs. 2.15 and 2.16 that the amplitude ratio modulates the

[1]The inclusion of charge-conjugate processes is implied through this thesis, unless explicitly stated otherwise.

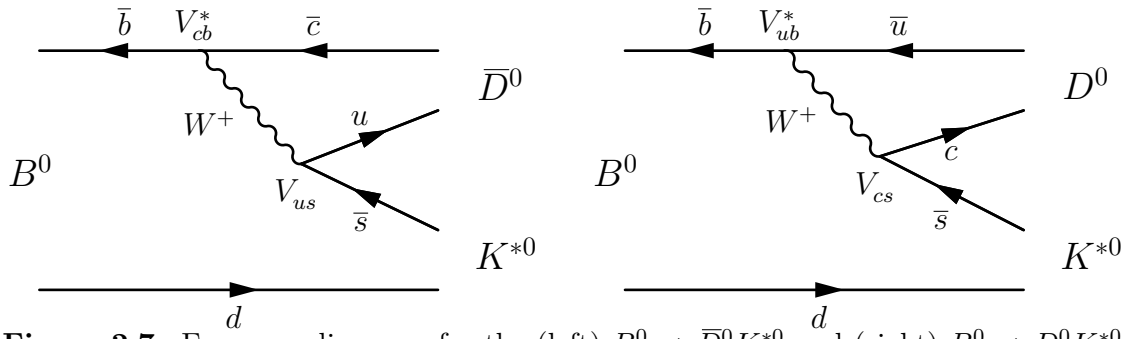

Figure 2.7: Feynman diagrams for the (left) $B^0 \to \overline{D}^0 K^{*0}$ and (right) $B^0 \to D^0 K^{*0}$ decays.

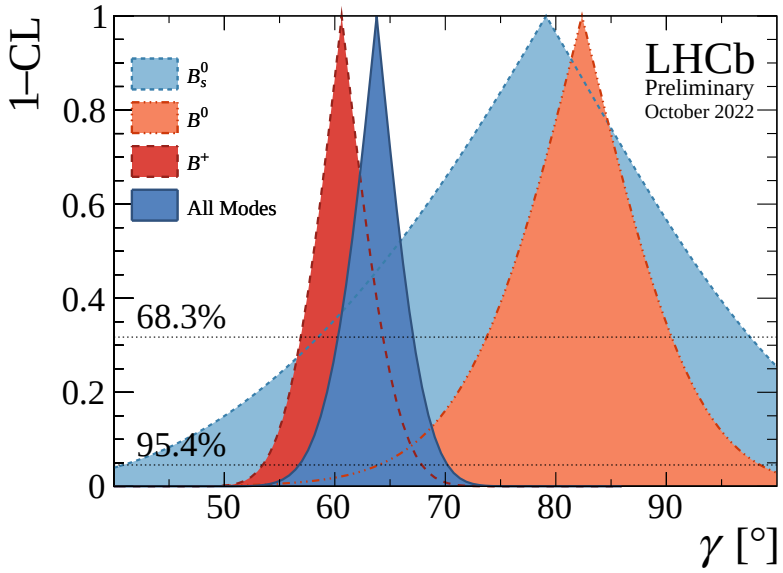

Figure 2.8: Measured γ values by B meson as determined by the LHCb collaboration [39].

interference term, and hence the size of the *CP* asymmetries and sensitivity to γ. Therefore, a competitive precision can be achieved using the B^0 decays despite having lower branching fractions than the $B^\pm$ decays.

In 2022, the LHCb collaboration combined the results of their direct γ measurements, which determined $\gamma = \left(63.8^{+3.5}_{-3.7}\right)^\circ$ [39]. The contributions from studies of the various B mesons are displayed in Figure 2.8, where there is a tension of around 2σ between the value using $B^\pm$ decays, $\gamma = \left(60.6^{+4.0}_{-3.8}\right)^\circ$, and B^0 decays, $\gamma = \left(82.0^{+8.1}_{-8.8}\right)^\circ$. Resolving the tension serves as further motivation to measure γ in the $B^0 \to DK^{*0}$ channel.

Due to the self-tagging property of the $B^0 \to DK^{*0}$ decay, the formalism is similar to that of the $B^\pm \to DK^\pm$ decays. However, since the K^{*0} is an intermediate resonance of the $K^+\pi^-$ final state, the amplitude is a mixture of all decays to the $K^+\pi^-$ final state,

$$A(B^0 \to \overline{D}^0 K^+\pi^-; \mathbf{p}) = A_c(\mathbf{p})e^{i\delta_c(\mathbf{p})}, \tag{2.17}$$

$$A(B^0 \to D^0 K^+\pi^-; \mathbf{p}) = A_u(\mathbf{p})e^{i(\delta_u(\mathbf{p})+\gamma)}, \tag{2.18}$$

where $A_{c(u)}$ denotes the magnitude of the decay with a $b \to c(u)$ transition and $\delta_{c(u)}$ is the corresponding strong phase, both of which vary over the phase space, $\mathbf{p}$. The amplitude ratio, r_s, and strong-phase difference, δ_s, are defined as integrals over the K^{*0} region of phase space,

$$r_s^2 = \frac{\int_{K^{*0}} A_u(\mathbf{p})^2 \mathrm{d}\mathbf{p}}{\int_{K^{*0}} A_c(\mathbf{p})^2 \mathrm{d}\mathbf{p}}, \tag{2.19}$$

$$\kappa e^{i\delta_s} = \frac{\int_{K^{*0}} A_c(\mathbf{p}) A_u(\mathbf{p}) e^{i[\delta_u(\mathbf{p})-\delta_c(\mathbf{p})]} \mathrm{d}\mathbf{p}}{\sqrt{\int_{K^{*0}} A_u(\mathbf{p})^2 \mathrm{d}\mathbf{p} \int_{K^{*0}} A_c(\mathbf{p})^2 \mathrm{d}\mathbf{p}}}, \tag{2.20}$$

where the *coherence factor*, κ, which satisfies $0 \leq \kappa \leq 1$, is introduced to account for interference between the various contributions to the total amplitude. In the case where the only contribution in the chosen region is from $B^0 \to DK^{*0}$ decays, the effective parameters become $r_s \to r_{B^0}$, $\delta_s \to \delta_{B^0}$ and $\kappa \to 1$. However, in reality, interference between the competing amplitudes reduces κ. The region of phase space is selected such that the dominant contribution is from $B^0 \to DK^{*0}$ decays, and the coherence factor is measured to be $\kappa = 0.958^{+0.005}_{-0.046}$ [40]. With these definitions the partial widths for the $B^0 \to [f]_D K^{*0}$ and $\overline{B}^0 \to [\bar{f}]_D \overline{K}^{*0}$ decays are

$$\Gamma(B^0 \to [f]_D K^{*0}) \propto |A_{\overline{D}}|^2 + r_s^2|A_D|^2 + \kappa r_s \left[A_{\overline{D}}^* A_D e^{i(\delta_s+\gamma)} + A_{\overline{D}} A_D^* e^{-i(\delta_s+\gamma)}\right], \tag{2.21}$$

$$\Gamma(\overline{B}^0 \to [\bar{f}]_D \overline{K}^{*0}) \propto |A_{\overline{D}}|^2 + r_s^2|A_D|^2 + \kappa r_s \left[A_{\overline{D}}^* A_D e^{i(\delta_s-\gamma)} + A_{\overline{D}} A_D^* e^{-i(\delta_s-\gamma)}\right]. \tag{2.22}$$

It is apparent from Eqs. 2.21 and 2.22 that knowledge of the D-decay amplitudes are necessary to extract the angle γ. These amplitudes are defined similarly to

those of the $B^{\pm}$ decays, such that

$$r_D^f e^{-i\delta_D^f} = \frac{A(\overline{D}^0 \to f)}{A(D^0 \to f)}. \tag{2.23}$$

In order to achieve the best possible precision on the direct measurements of γ many different D-decay final states are used.

The D-decay channels of interest, discussed in the remainder of this chapter, decay via the weak interaction. A valid question would then be: why is the above equation characterised by a single phase? The CKM elements involved in the processes are real numbers, so the weak phase is *CP* conserving, and therefore, it is absorbed by strong-phase difference which has the same quality. By convention, in charm decays δ_D^f is termed the strong-phase difference even though it contains weak-force contributions.

2.5.1 GLW method

The earliest proposals for direct γ measurements suggested using D decays to *CP* eigenstates due to their relative simplicity. This procedure is known as the GLW method after the authors of Refs. [41, 42]. As mentioned above, *CP* violation in charm is neglected, so $A(D^0 \to f) = A(\overline{D}^0 \to \bar{f}) = \pm A(\overline{D}^0 \to f)$, where the last equality holds because f is a *CP* eigenstate. Comparing to Eq. 2.23 it is clear that $r_D^f = 1$, and by convention, it is chosen that $\delta_D^f = 0$ for *CP*-even eigenstates and $\delta_D^f = \pi$ for *CP*-odd eigenstates.

At the LHCb experiment, the *CP*-even $D \to h^+h^-$ decay modes, where $h \in (\pi, K)$, are most commonly used [12] because they boast relatively high branching fractions and reconstruction efficiencies, so in the following equations $\delta_D^f = 0$ is assumed. Armed with this information, the partial decay widths from Eqs. 2.15 and 2.16 become

$$\Gamma(B^- \to D_{CP}K^-) \propto 1 + r_{B^{\pm}}^2 + 2r_{B^{\pm}} \cos(\delta_{B^{\pm}} - \gamma), \tag{2.24}$$

$$\Gamma(B^+ \to D_{CP}K^+) \propto 1 + r_{B^{\pm}}^2 + 2r_{B^{\pm}} \cos(\delta_{B^{\pm}} + \gamma), \tag{2.25}$$

from which it is evident that the main benefit of reconstructing the D decay in a *CP* eigenstate is that no amplitude information is needed to extract γ. The relevant *CP* asymmetry is

$$A_{CP}^{GLW} = \frac{\Gamma(B^- \to DK^-) - \Gamma(B^+ \to DK^+)}{\Gamma(B^- \to DK^-) + \Gamma(B^+ \to DK^+)} = \frac{2r_{B^\pm} \sin\delta_{B^\pm} \sin\gamma}{1 + r_{B^\pm}^2 + 2r_{B^\pm} \cos\delta_{B^\pm} \cos\gamma}. \tag{2.26}$$

Although the GLW method is relatively simple, it does not provide the best sensitivity to γ. From the CKM elements in Fig. 2.5 and colour suppression arguments the parameter $r_{B^\pm}$ is estimated to be $r_{B^\pm} \sim 0.1$. Therefore, the GLW asymmetry in Eq. 2.26 has a maximum of around 20% in $B^\pm$ decays, but it can be larger in B^0 decays. Furthermore, the GLW method does not unambiguously determine γ, because the asymmetry in Eq. 2.26 is invariant under the transformations $(\gamma \to \delta_{B^\pm}, \delta_{B^\pm} \to \gamma)$, $(\gamma \to \pi - \gamma, \delta_{B^\pm} \to \pi - \delta_{B^\pm})$ and $(\gamma \to \pi - \delta_{B^\pm}, \delta_{B^\pm} \to \pi - \gamma)$.

2.5.2 ADS method

Both of the drawbacks mentioned in the previous paragraph can, in principle, be resolved using the ADS method, again named after the authors of Ref. [43]. This procedure uses D-meson decays to final states which are not *CP* eigenstates, where the asymmetry is

$$\begin{aligned} A_{CP}^{ADS} &= \frac{\Gamma(B^- \to [\bar{f}]_D K^-) - \Gamma(B^+ \to [f]_D K^+)}{\Gamma(B^- \to [\bar{f}]_D K^-) + \Gamma(B^+ \to [f]_D K^+)} \\ &= \frac{2r_{B^\pm} r_D^f \sin(\delta_{B^\pm} + \delta_D^f) \sin\gamma}{r_{B^\pm}^2 + (r_D^f)^2 + 2r_{B^\pm} r_D^f \cos(\delta_{B^\pm} + \delta_D^f) \cos\gamma}. \end{aligned} \tag{2.27}$$

A large *CP* asymmetry will occur when $r_{B^\pm} \sim r_D^f$, and therefore particularly sensitive channels for use in conjunction with $B^\pm$ decays are those where the $D^0 \to f$ decay is favoured by the CKM mechanism, whilst the $\overline{D}^0 \to f$ decay is doubly suppressed. An example of such a decay is $f = K^-\pi^+$ where $r_D^{K\pi} \sim 0.06$, as can be determined from the CKM elements involved in the Feynman diagrams in Fig. 2.10. Large interference effects occur because the two paths shown in Figure 2.9 have a similar magnitude.

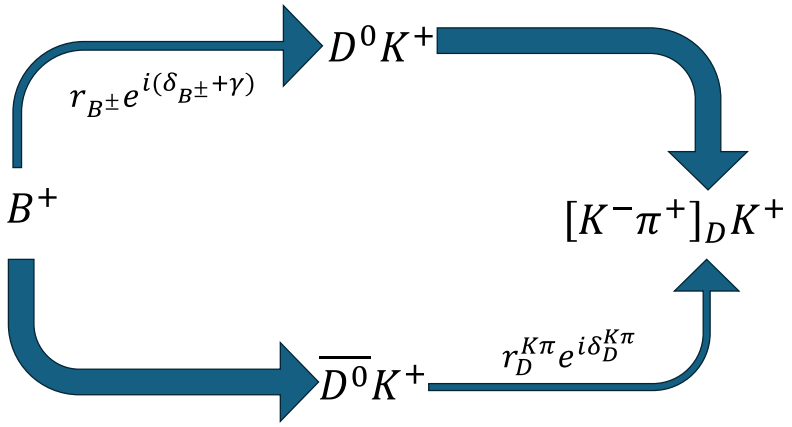

Figure 2.9: Diagram depicting the interference between $B^+ \to D^0K^+$ and $B^+ \to \overline{D}^0K^+$ where both D^0 and $\overline{D}^0$ decay to the $K^-\pi^+$ final state. The thickness of the arrow indicates the relative magnitude of the amplitudes for each decay.

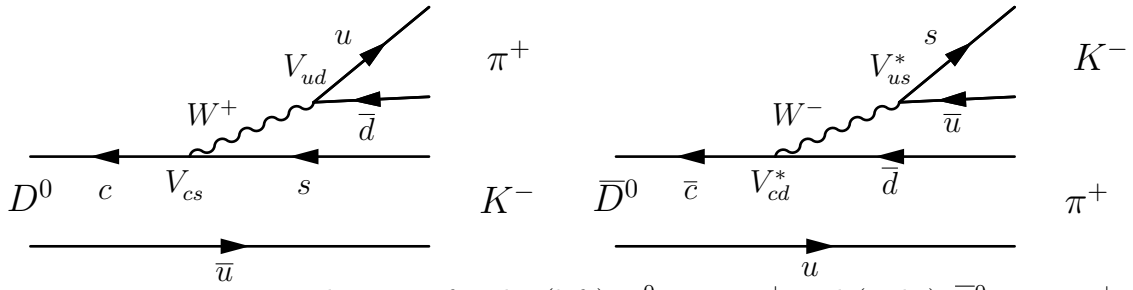

Figure 2.10: Feynman diagrams for the (left) $D^0 \to K^-\pi^+$ and (right) $\overline{D}^0 \to K^-\pi^+$ decays.

CP-asymmetry measurements with D decays to many non-*CP* eigenstates can resolve the ambiguity in γ because they all have unique strong-phase differences. However, many such decays are experimentally difficult, either due to low branching fractions and reconstruction efficiencies, or because they are intermediate resonances in multibody-decay modes. Therefore, in practice, only the $K^-\pi^+$ final state provides good sensitivity through the asymmetry,

$$A_{CP}^{K\pi} = \frac{2r_{B^\pm}r_D^{K\pi}\sin(\delta_{B^\pm}+\delta_D^{K\pi})\sin\gamma}{r_{B^\pm}^2+(r_D^{K\pi})^2+2r_{B^\pm}r_D^{K\pi}\cos(\delta_{B^\pm}+\delta_D^{K\pi})\cos\gamma}. \tag{2.28}$$

However, the achievable precision using the $K^-\pi^+$ final state is currently being limited by the knowledge of the strong-phase difference $\delta_D^{K\pi}$. The parameter $\delta_D^{K\pi}$ is measured using quantum-correlated $D\overline{D}$ pairs produced at charm factories, such as the BESIII experiment at the Institute of High Energy Physics (IHEP) in Beijing,

with a precision of around 10° [13]. However, γ is known significantly more precisely than 10° from other measurements. Therefore, in combinations such as Ref. [39], $\delta_D^{K\pi}$ is simply determined with a precision that mirrors that of γ. The analysis of the $K^-\pi^+$ channel [12] does not impact the precision on γ as much as it could with a more precise determination of $\delta_D^{K\pi}$, which provides strong motivation for the measurement of the parameter in Chap. 7.

2.5.3 BPGGSZ method

Currently, the best precision on γ is achieved using multibody D-decay modes with a strong resonant structure. In these measurements, localised *CP*-violation effects are studied by dividing the phase space of the D decay into regions which isolate the resonances. Depending on the resonances the *CP* asymmetries can be large.

For example, in $D \to K^0_S\pi^+\pi^-$ decays, the dominant resonance is the $D^0 \to K^*(892)^-\pi^+$ decay, where the $K^*(892)^-$ subsequently decays into the $K^0_S\pi^-$ final state. The branching fraction of the *CP*-conjugate $D^0 \to K^*(892)^+\pi^-$ decay is suppressed by an order of magnitude, and thus this would be an ideal final state to use in the ADS method. However, the $D \to K^0_S\pi^+\pi^-$ decay also contains many other resonances, for example the $D \to K^0_S\rho^0$ decay with $\rho^0 \to \pi^+\pi^-$, which is a *CP* eigenstate and thus is a suitable candidate for the GLW method. The BPGGSZ procedure, named after the authors of Refs. [44, 45, 46, 47], is particularly powerful because it simultaneously exploits the resonances across the full phase space of the D decays. The BPGGSZ method is outlined in this section for the $D \to K^0_S\pi^+\pi^-$ decays which are used in the measurement of γ discussed in Chap. 4.

2.5.3.1 Dalitz plots

Before discussing the formalism of the BPGGSZ method, it is first necessary to introduce *Dalitz plots*, which describe the phase space of three-body decays, $P \to p_1p_2p_3$. Such decays are specified by 12 degrees of freedom given by the four-momentum components of the three final-state particles. Seven of these are removed through constraints placed by conservation of four momentum and the known masses

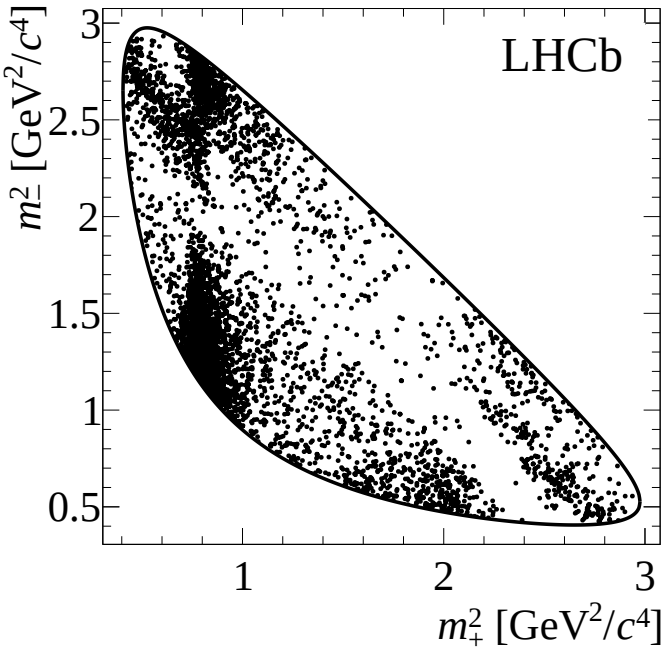

Figure 2.11: Dalitz plot of $\overline{D}^0 \to K^0_S\pi^+\pi^-$ decay candidates [48].

of the final-state particles. Furthermore, if all particles involved are scalars then the products are isotropically produced, and thus a further three degrees of freedom, corresponding to the angles between the momenta of the particles, are removed. Therefore, the three-body decay of a scalar particle is described by two parameters.

A parametrisation which is convenient to visualise intermediate resonances uses the invariant-mass squared of two two-particle combinations,

$$m^2_{12} = (q_1 + q_2)^2 \text{ and } m^2_{13} = (q_1 + q_3)^2, \tag{2.29}$$

where q_i is the four momentum of final-state particle i. An example of a Dalitz plot using this parametrisation is displayed in Fig. 2.11 for flavour-tagged $\overline{D}^0 \to K^0_S\pi^+\pi^-$ decays, where the coordinates are $m(K^0_S\pi^+)^2 \equiv m^2_+$ and $m(K^0_S\pi^-)^2 \equiv m^2_-$. The intermediate resonances correspond to bands in the Dalitz plot, for example the $K^*(892)^+$ resonance is centred at $m^2_+ = (0.892\,\text{GeV}/c^2)^2 \simeq 0.8\,\text{GeV}^2/c^4$.

2.5.3.2 Formalism

The amplitudes of multibody D decays have a kinematic dependence described by the coordinates of the Dalitz plot,

$$A(D^0 \to K^0_S\pi^+\pi^-) = \mathcal{A}_D(m^2_+, m^2_-) = A_D(m^2_+, m^2_-)e^{i\phi_D(m^2_+,m^2_-)}, \tag{2.30}$$

$$A(\overline{D}^0 \to K^0_S\pi^+\pi^-) = \mathcal{A}_{\overline{D}}(m^2_+, m^2_-) = A_{\overline{D}}(m^2_+, m^2_-)e^{i\bar{\phi}_D(m^2_+,m^2_-)}. \tag{2.31}$$

and thus Eq. 2.21 becomes

$$\begin{aligned}\Gamma(B^0 \to [K^0_S\pi^+\pi^-]_D K^{*0}) \propto A^2_{\overline{D}} + r^2_s A^2_D \\ + 2\kappa r_s A_D A_{\overline{D}} \left[\cos\delta_D \cos(\delta_s + \gamma) - \sin\delta_D \sin(\delta_s + \gamma)\right],\end{aligned} \tag{2.32}$$

where $\delta_D(m^2_+, m^2_-) = \phi_D(m^2_+, m^2_-) - \bar{\phi}_D(m^2_+, m^2_-)$ and the phase-space coordinates have been dropped for brevity.

As mentioned above, the measurement of γ proceeds by dividing the Dalitz plot into regions for analysis, and similarly to the ADS method, knowledge of the D-decay amplitudes are necessary inputs. More specifically, integrals over the partial width in Eq. 2.32 are performed in each region with index i, and the D-decay amplitudes are replaced with

$$K_i = \int_i \mathrm{d}m^2_- \mathrm{d}m^2_+ A^2_D(m^2_+, m^2_-), \tag{2.33}$$

$$c_i = \frac{1}{\sqrt{K_i K_{-i}}} \int_i \mathrm{d}m^2_- \mathrm{d}m^2_+ A_D(m^2_+, m^2_-) A_{\overline{D}}(m^2_+, m^2_-) \cos\delta_D(m^2_+, m^2_-), \tag{2.34}$$

$$s_i = \frac{1}{\sqrt{K_i K_{-i}}} \int_i \mathrm{d}m^2_- \mathrm{d}m^2_+ A_D(m^2_+, m^2_-) A_{\overline{D}}(m^2_+, m^2_-) \sin\delta_D(m^2_+, m^2_-). \tag{2.35}$$

The K_i can be identified as the probability for a $D^0 \to K^0_S\pi^+\pi^-$ decay to fall in a region, i. Whereas, the c_i and s_i parameters are defined similarly to Eq. 2.20, and so, more intuitively, they are the sizes of the real and imaginary parts of $\kappa_i e^{-i\delta^i_D}$, respectively, where κ_i is the coherence of the D decay in each region. The K_i, c_i and s_i parameters are all measured at charm factories using the procedure discussed in Sec. 5.5.

The $K^0_S\pi^+\pi^-$ final state is self conjugating, and thus the amplitudes of the $D^0 \to K^0_S\pi^+\pi^-$ and $\overline{D}^0 \to K^0_S\pi^+\pi^-$ decays are the same after swapping the momenta of the two pions,

$$\mathcal{A}_D(m^2_+, m^2_-) = \mathcal{A}_{\overline{D}}(m^2_-, m^2_+). \tag{2.36}$$

This relationship is exploited to conveniently divide the Dalitz plot. A scheme is chosen such that there are $2\mathcal{N}$ regions which are symmetric around the line $m^2_+ = m^2_-$. They are labelled from $i = -\mathcal{N}$ to $i = \mathcal{N}$ (excluding $\mathcal{N} = 0$) and regions where $m^2_- > m^2_+$ are assigned positive indices. Transforming between regions $i \leftrightarrow -i$ is equivalent to exchanging $m^2_+ \leftrightarrow m^2_-$, and therefore

$$K_{-i} = \int_i \mathrm{d}m^2_- \mathrm{d}m^2_+ A^2_D(m^2_-, m^2_+) = \int_i \mathrm{d}m^2_- \mathrm{d}m^2_+ A^2_{\overline{D}}(m^2_+, m^2_-), \tag{2.37}$$

$$s_{-i} = -s_i, \tag{2.38}$$

$$c_{-i} = c_i, \tag{2.39}$$

from which it is apparent that the K_{-i} parameters are the probabilities for a $\overline{D}^0 \to K^0_S\pi^+\pi^-$ decay to fall in each region. Using these definitions, the partial widths of the $B^0 \to DK^{*0}$ decays with $D \to K^0_S\pi^+\pi^-$ in each region are given by

$$\begin{aligned}\Gamma_i(B^0 \to [K^0_S\pi^+\pi^-]_D K^{*0}) \propto K_{-i} + r_s^2 K_i \\ + \kappa r_s \sqrt{K_i K_{-i}} \left[c_i \cos(\delta_s + \gamma) - s_i \sin(\delta_s + \gamma)\right].\end{aligned} \tag{2.40}$$

The expression for the rate of $\overline{B}^0 \to D\overline{K}^{*0}$ decays with $D \to K^0_S\pi^+\pi^-$ decays in the same region is determined by transforming $\gamma \to -\gamma$ and $m^2_+ \leftrightarrow m^2_-$,

$$\begin{aligned}\Gamma_i(\overline{B}^0 \to [K^0_S\pi^+\pi^-]_D \overline{K}^{*0}) \propto K_i + r_s^2 K_{-i} \\ + \kappa r_s \sqrt{K_i K_{-i}} \left[c_i \cos(\delta_s - \gamma) + s_i \sin(\delta_s - \gamma)\right].\end{aligned} \tag{2.41}$$

If there were no *CP* violation ($\gamma = 0$) then $\Gamma_i(B^0 \to [K^0_S\pi^+\pi^-]_D K^{*0}) = \Gamma_{-i}(\overline{B}^0 \to [K^0_S\pi^+\pi^-]_D \overline{K}^{*0})$. Conversely, the *CP* violation results in asymmetries in the rates of B^0 and $\overline{B}^0$ decays across the $D \to K^0_S\pi^+\pi^-$ decay phase space which are exploited to measure γ.

The combination of measurements performed by the LHCb collaboration using the GLW and ADS methods does not provide a single value for γ due to the aforementioned ambiguities. However, with the BPGGSZ method, assuming the K_i, c_i and s_i inputs are known there are $4\mathcal{N}$ equations, or measurable quantities, and 3 unknowns. Therefore, the multibody D decays provide unambiguous solutions for $\gamma \in [0, 180]^\circ$, r_s and δ_s provided the Dalitz plot is divided into at least 2 regions ($\mathcal{N} \geq 1$). As such, the BPGGSZ procedure plays a vital role in combinations of measurements, and facilitates the extraction of a single value of γ from the ADS and GLW results.

2.5.3.3 Division of $D \to K^0_S\pi^+\pi^-$ phase space

Recall the useful comparison that the c_i and s_i parameters are the sizes of the real and imaginary parts of $\kappa_i e^{-i\delta^i_D}$, such that $c_i \equiv \kappa_i \cos(\delta^i_D)$ and $s_i \equiv \kappa_i \sin(\delta^i_D)$. Using these alternative definitions, it is evident from Eqs. 2.41 and 2.40 that the interference is largest, and hence the sensitivity to γ will be optimal, when coherent regions of phase space are chosen such that κ_i is close to one. Therefore, a naive best-guess for a good division would contain regions with similar strong-phase differences. In fact, one of most commonly used schemes, named the *equal-*$\Delta\delta_D$ scheme [49], has $\mathcal{N} = 8$ regions, and each region covers the same range in the strong-phase difference, such that if the strong-phase difference at the point (m^2_+, m^2_-) satisfies

$$2\pi(i - 1/2)/\mathcal{N} < \delta_D(m^2_+, m^2_-) < 2\pi(i + 1/2)/\mathcal{N}, \tag{2.42}$$

it falls in region, i.

Clearly, in order to develop such a binning scheme, the strong-phase difference at each point in phase space must be known. These values are determined from a model developed by the BaBar collaboration [50], which is constructed from parameters describing the intermediate resonances that are measured in data. Practically, the model provides the amplitude and phase at each point in the Dalitz plot divided into 500×500 pixels. Then, each pixel is assigned to a region of phase space defined by the indices, i, above.

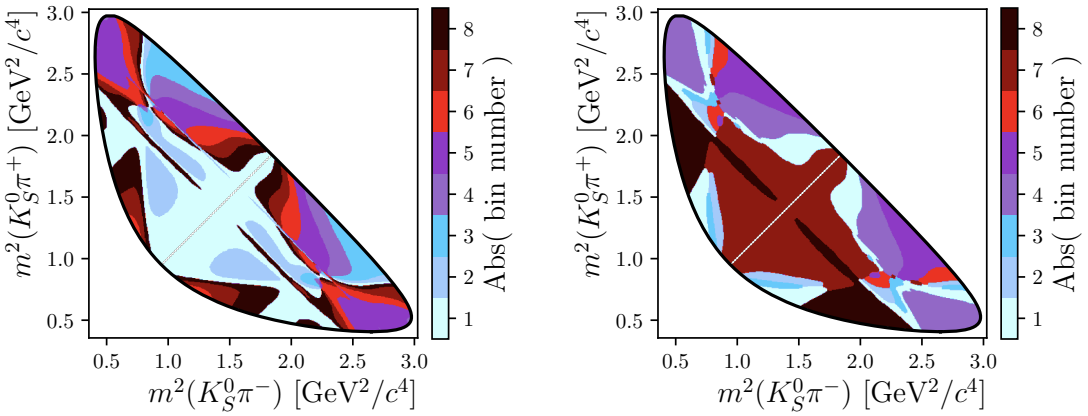

Figure 2.12: The (left) equal-$\Delta\delta_D$ and (right) optimal division of the Dalitz plot describing $D \to K^0_S\pi^+\pi^-$ decays. The black outline corresponds to the kinematic boundaries imposed by the D^0 mass constraint.

Although the equal-$\Delta\delta_D$ binning provides reasonably good sensitivity to γ, it is not optimal because the coherence also depends on the magnitudes A_D and $A_{\overline{D}}$. A precision improvement of around 13% is seen when using an alternative scheme, named the *optimal* binning [49], which is found through an iterative procedure which begins with the equal-$\Delta\delta_D$ binning and varies the pixels which border each region individually until the coherence factor $c_i^2 + s_i^2$, and hence the sensitivity to γ, is optimised. The optimal and equal-$\Delta\delta_D$ binning schemes are displayed in Fig. 2.12.

2.5.3.4 $D \to K^0_S K^+ K^-$ decays

In the measurement of γ described in Chap. 4, both the $D \to K^0_S K^+ K^-$ and $D \to K^0_S\pi^+\pi^-$ decays are used, and together they are referred to as $D \to K^0_S h^+ h^-$ where $h \in (\pi, K)$. The formalism described in Sec. 2.5.3.2 for the $D \to K^0_S\pi^+\pi^-$ decays identically applies to the $D \to K^0_S K^+ K^-$ decays. The phase space of the $D \to K^0_S K^+ K^-$ decay is divided such that $\mathcal{N} = 2$ as shown in Fig. 2.13 [49]. It is found that little is gained by increasing $\mathcal{N}$ because the amplitude is dominated by two resonances, $D^0 \to K^0_S\phi(1020)$ and $D^0 \to K^0_S a(980)^0$, even though measurements with $\mathcal{N} = 3, 4$ are available [49].

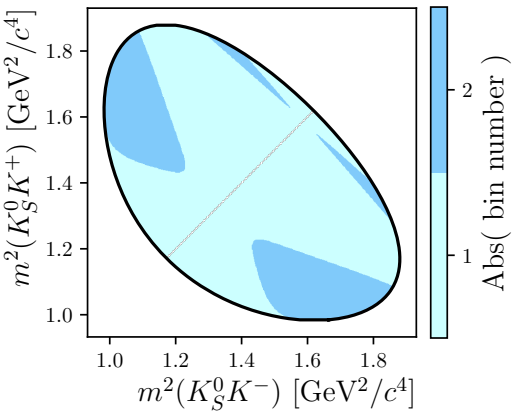

Figure 2.13: The $D \to K^0_S K^+ K^-$ decay Dalitz plot divided into $\mathcal{N} = 2$ regions. The black outline corresponds to the kinematic boundaries imposed by the D^0 mass constraint.

3

The LHCb experiment

Contents

3.1 Overview

The Large Hadron Collider (LHC) [51] is the biggest particle accelerator in the world, situated in a 27 km underground tunnel at the CERN facility on the outskirts of Geneva, Switzerland. At the LHC, two beams consisting of around 10^{14} protons are collided forty million times a second at centre-of-mass energies between 7 and 14 TeV. These enormous energies are gradually reached using a chain of smaller

accelerators depicted in Fig. 3.1. At the end of the chain, the protons are injected into the LHC with an energy of around 450 GeV and are further accelerated using sixteen superconducting radio frequency (RF) cavities. Put simply, the RF cavities are strong electric fields which oscillate at a frequency of 400 MHz and are finely tuned to accelerate the protons at the correct moment. The oscillatory behaviour ensures the protons remain sorted into around 3000 *bunches*, rather than being continuously spread throughout the accelerator. Moreover, the two beams are maintained in opposing circular trajectories using 1232 superconducting dipole magnets, and are focused by 474 quadrupole magnets.

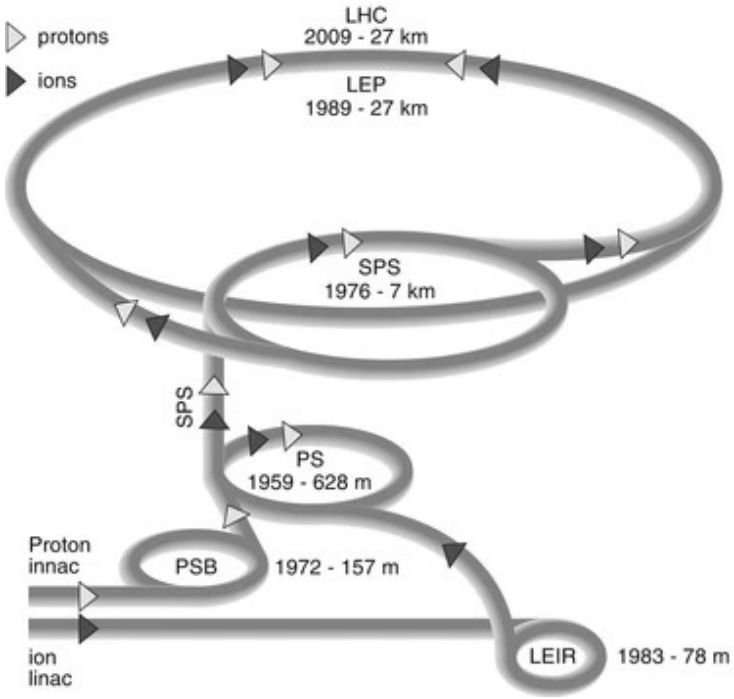

Figure 3.1: LHC accelerator chain [52].

The LHC beams cross four times, and an experiment is situated at each *crossing point* to study the particles produced in the collisions. One such experiment is LHCb, which was designed to improve our understanding of *CP* violation and the CKM matrix, primarily by measuring the properties of b-hadrons [53]. The LHCb detector [54] is designed with these goals in mind. At the LHC, the $b\bar{b}$ pairs are predominantly produced through gluon-gluon fusion. It is likely that there will be a large asymmetry in the momentum of the interacting gluons due to their

parton PDFs, and thus both the b and $\bar{b}$ quarks will be produced in the forward or backward directions [53]. Therefore, the LHCb detector, depicted in Fig. 3.2, covers only around 4% of the solid angle in the forward direction with access to around 12% of the $b\bar{b}$ pairs. More specifically, the angular acceptance in the $x-z$ plane is 10-300 mrad and in the $y-z$ plane it is 10-250 mrad, where z is the direction of the beam pipe, and x and y are the horizontal and vertical axes, respectively.

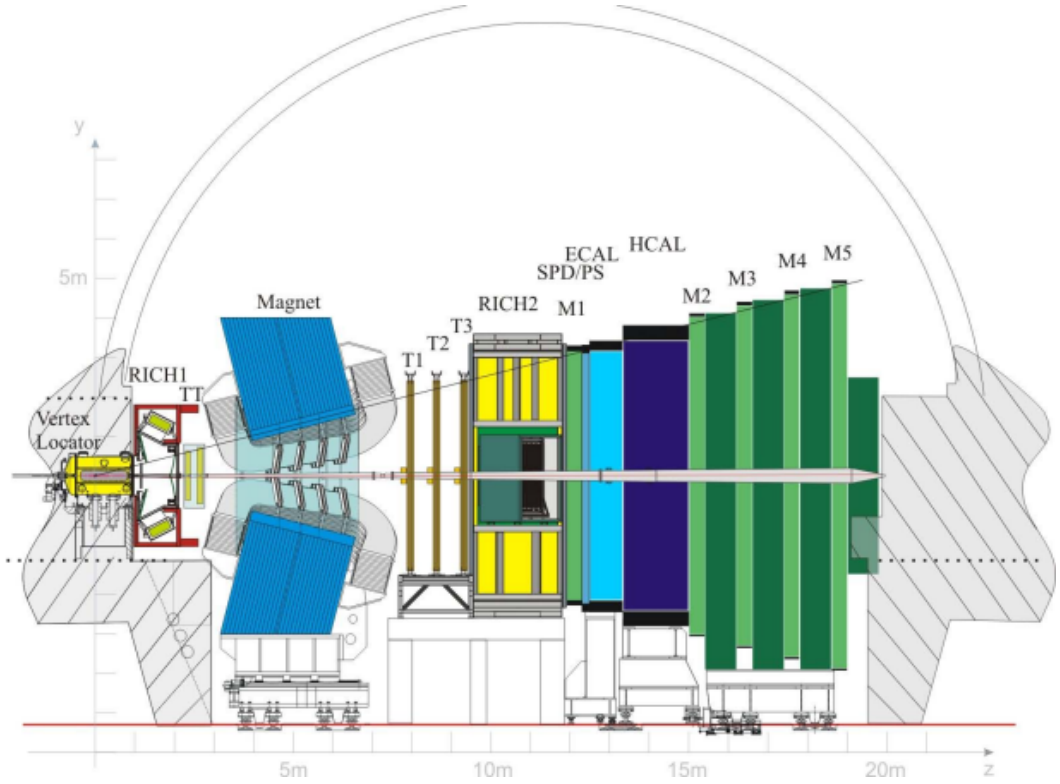

Figure 3.2: The LHCb detector [54].

The LHCb detector is composed of multiple elements each with an important purpose. For example, one distinguishing feature of B mesons is that they are relatively long-lived with a decay length of $c\tau \sim 0.46\,\text{mm}$, which is further increased by a forward boost that results in the decay which is displaced from the interaction point. The decay vertices are precisely reconstructed at LHCb using a silicon-strip detector, called the VErtex LOcator (VELO) [55], which is positioned near the beam pipe. Furthermore, precise determination of a particles momentum is achieved using tracking stations (TT and T1-T3) [56, 57] either side of a dipole magnet [58]. Many

decays of interest require accurate identification of the particles in the final state. At LHCb, the charged hadrons (π, K and p) are distinguished using two Ring Imaging Cerenkov (RICH) counters [59], whilst the muons and electrons are identified using wire chambers [60] and a calorimeter system [61], respectively. Finally, a tiered trigger system [62] is used to efficiently select the events with interesting interactions.

The performance of the sub-detectors at LHCb are highly dependent on the occupancy. For example, if there were many hits from tracks in the VELO it would be more difficult to accurately identify displaced decay vertices. Therefore, to ensure high performance, the instantaneous luminosity at LHCb is lowered by offsetting the beams at the crossing point, such that there are typically only one or two interactions per bunch crossing. Over time, the offset is reduced to balance the decrease in the number of protons per bunch, allowing for an approximately constant instantaneous luminosity. This procedure is called *luminosity levelling* [63].

The LHCb experiment collected a dataset corresponding to an integrated luminosity of $3\,\text{fb}^{-1}$ in 2011-12 during run 1 of the LHC, where the beam energy was either 3.5 or 4 TeV. A further $6\,\text{fb}^{-1}$ was collected between 2015-2018 in run 2 with a beam energy of 6.5 TeV.

3.2 Tracking detectors

3.2.1 VELO

At the LHCb experiment the displaced decay vertices of B mesons are resolved using the VErtex LOcator (VELO) [55]. A diagram of the VELO can be found in Fig. 3.3, which shows the 42 layers of silicon-strip sensors which alternate between layouts that determine the radial (R) and azimuthal (ϕ) coordinates of a charged track. The R and ϕ are found by arranging the strips in concentric circles and a radiant pattern, respectively, as displayed in Fig. 3.3. In both layouts, the pitch increases radially, from around 40 µm to 100 µm, to obtain the necessary precision closest to the beams where the occupancy is largest.

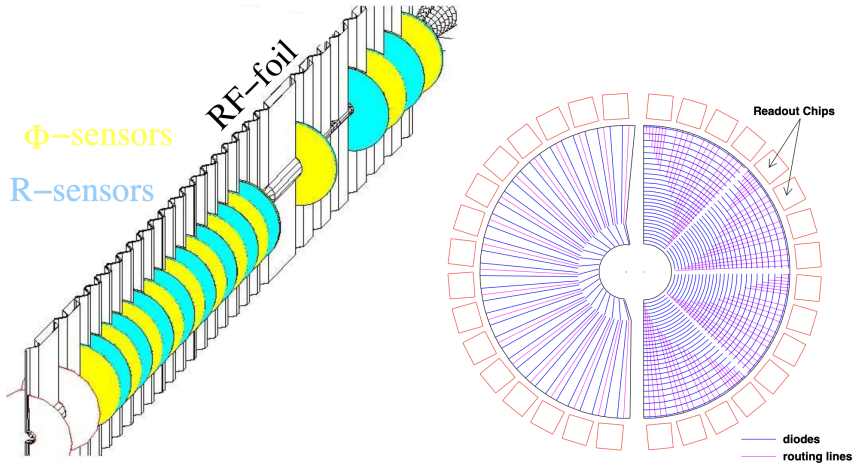

Figure 3.3: Diagram depicting the alternating layers of sensors in the VELO which determine the ϕ and R coordinates through the strip layout shown on the right [64].

A B meson produced at the primary vertex (PV) with a momentum of 100 GeV/c travels around 8 mm before decaying. Therefore, the VELO is positioned around 7 mm from the beam pipe. This distance is less than the aperture of the proton beams upon injection, so the VELO is split into two halves which retract to around 6 cm from the beams until they are focused. For stability, and to ensure the surrounding environment can be closely controlled, the silicon sensors are placed in a 250 µm thick aluminium container called the *RF box*.

To suppress prompt backgrounds it is necessary to identify tracks which originate from displaced decay vertices, rather than the PV. This is achieved using the impact parameter (IP), which is the distance of closest approach between the track and the PV, and can be measured using hits in the VELO. The IP resolution is studied in data by examining the measured IP of good quality tracks that originate from the PV. These tracks should have an IP of zero, and therefore any deviations are attributed to the finite resolution, which is given by the width of the IP distribution. Figure 3.4 shows that the resolution of the impact parameters in the x and y axes are less than 35 µm over a range of momenta [65].

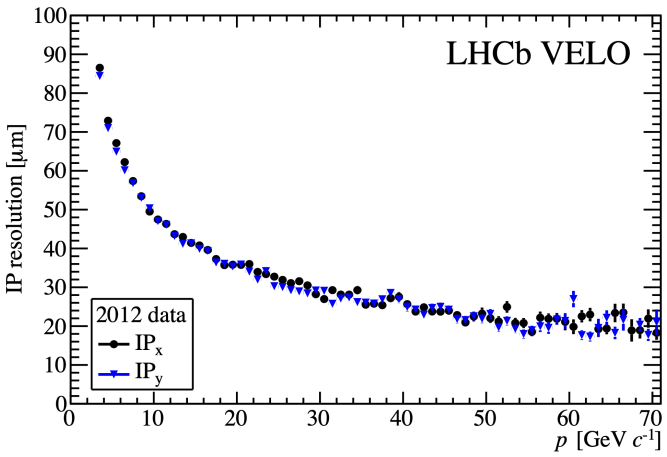

Figure 3.4: Impact parameter resolution in the x and y axes as a function of track momentum in 2012 data [65].

3.2.2 Tracking stations

The LHCb detector obtains a precise estimate of a charged particle's momentum using four tracking stations and a dipole magnet. A schematic of the first station, the trigger tracker (TT) [54], is shown in Fig. 3.5. It is located upstream of the magnet and consists of four layers of silicon detectors with vertical strips and a 200 μm pitch. The two central layers are rotated by +5° and -5° with respect to the outer layers. This *stereo* geometry allows the two-dimensional coordinates of each track to be determined.

An identical silicon-strip approach is used in the inner regions of the other three tracking stations (T1-T3), which are placed downstream of the magnet [56]. The outer regions in each of the T1-T3 stations consists of four double-layers of straw tubes arranged in the stereo layout, as shown in Fig. 3.6 [57]. Each straw is around 4.9 mm in diameter and is filled with a gas mixture which has a drift time less than 50 ns, corresponding to a spatial resolution of 200 μm. The total area covered by the tracking stations is around 5×6 m^2.

3.2.3 Magnet

A dipole magnet with a bending power of 4 Tm is placed around 5 m from the LHCb crossing point, which allows the determination of a particles momentum and

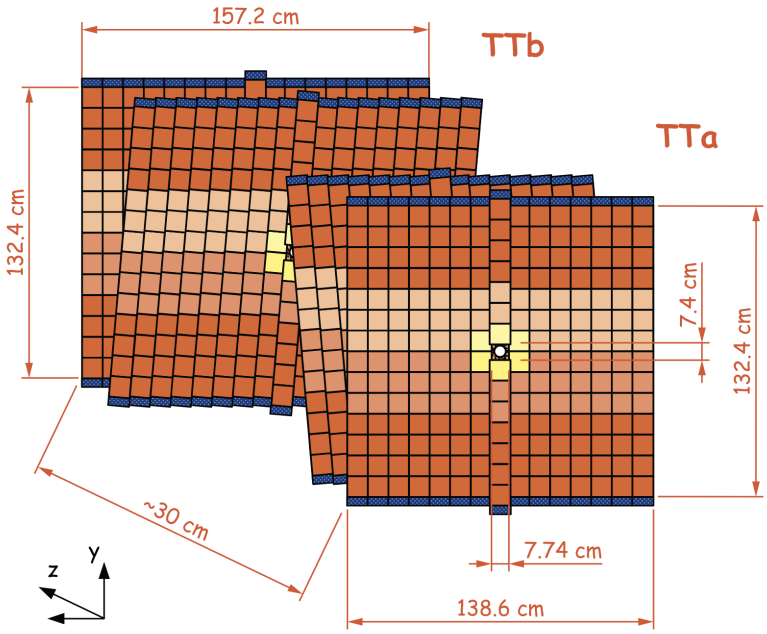

Figure 3.5: The four layers of the Trigger Tracker arranged in a stereo geometry [66].

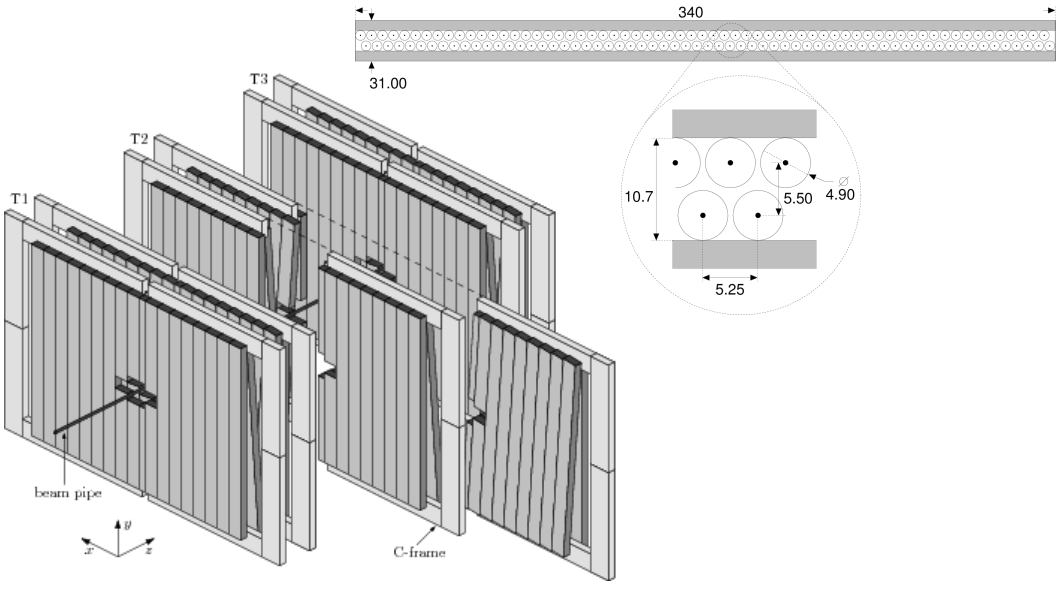

Figure 3.6: The layout of the three tracking stations T1-3 with dimensions in units of mm. Each station is divided into halves for easy beam pipe access as shown for T2. The right plot displays the top-view of the double-layers of straw tubes [67].

charge [58]. The magnetic field is applied in the y-direction and thus the trajectories are bent in the $x - z$ plane. To reduce systematic effects the polarity of the magnet is regularly flipped between the *up* and *down* configurations.

3.2.4 Reconstruction and performance

At LHCb, different types of tracks are reconstructed depending on the distribution of hits in the sub-detectors [68]. For reference, a diagram is provided in Fig. 3.7. Of interest in this thesis are the *long* and *downstream* tracks. The former are reconstructed by combining hits in the VELO with those in the tracking stations, whilst the latter do not use VELO information. The downstream tracks are particularly useful for reconstructing long-lived particles which may not decay inside the VELO, for example K^0_S mesons. They are reconstructed by matching hits in the TT with those estimated by backward-extrapolating tracks created using hits in T1-3 (T-tracks).

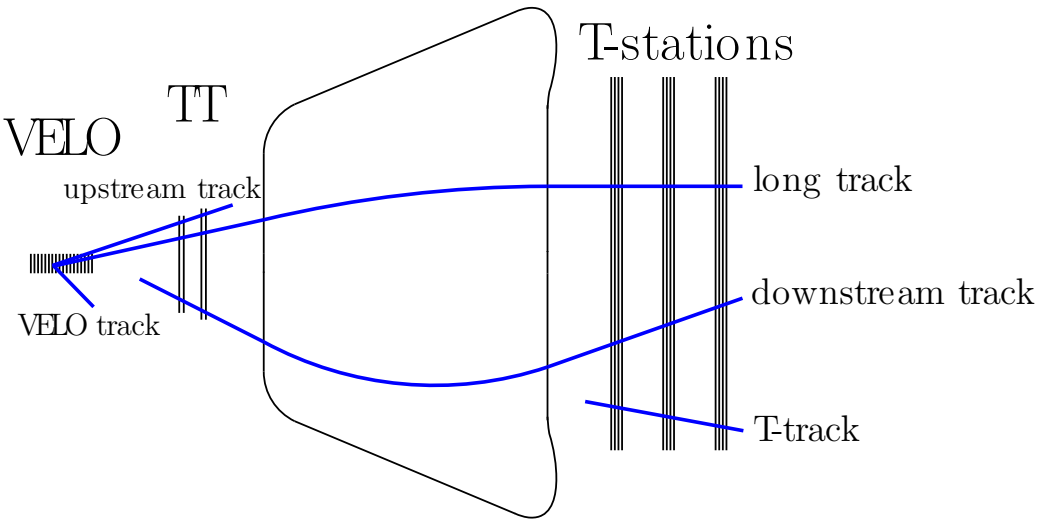

Figure 3.7: Types of tracks at LHCb [69].

Two algorithms are used to reconstruct long tracks. The first, known as *forward tracking* [70], begins by exploiting the absence of magnetic field in the VELO to search for hits in straight trajectories, which are called the *seeds* of long tracks. Each seed is combined with each individual hit in T1-3 to estimate of the momentum

of the potential track. With this information, each seed-hit combination can be extrapolated to a particular point in the detector. The extrapolated position will be roughly consistent for seed-hit combinations which originate from the same track, and therefore those that are clustered together can be used to build a trajectory.

The second algorithm extrapolates the VELO seeds and T-tracks to the same position in the detector to calculate the probability that they match [71]. In both algorithms, the accepted tracks are subsequently combined with information from the TT, and a fit is performed which accurately determines the momentum of each track and it's full trajectory.

The momentum resolution is found by examining the width of the invariant-mass distribution of $J/\psi \to \mu^+\mu^-$ decay candidates. It increases from 0.5% at low momentum to around 1% at 200 GeV/c, as shown in Fig. 3.8 [68].

The tracking efficiency is determined in data using $J/\psi \to \mu^+\mu^-$ decay candidates which are reconstructed using the *tag and probe* method [72]. In this procedure, the track of the tag muon is fully reconstructed, whilst that of the probe muon is partially reconstructed. The total number of signal candidates is determined through a fit to the $\mu^+\mu^-$ invariant mass. The fit is repeated using only the probe tracks which are successfully matched with a long track in the detector, and the efficiency is given by the ratio of signal yields in the two scenarios. Figure 3.8 shows the efficiency, which is around 96%, as a function of the number of tracks in the event [68].

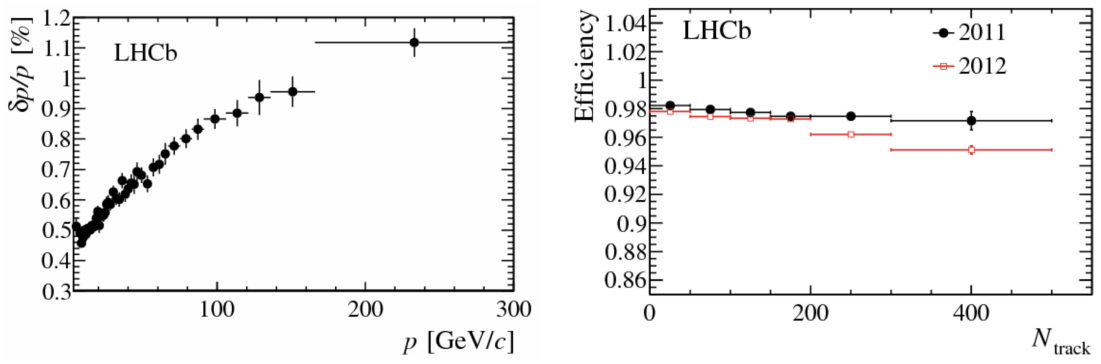

Figure 3.8: Left: the momentum resolution in run 1 data. Right: the tracking efficiency in 2011 and 2012 data as a function of the event track occupancy [68].

3.3 Particle identification

3.3.1 Ring Imaging Cerenkov detectors

A crucial capability of LHCb is to accurately recognize the various species of particles over a wide momentum range. This is particularly important in *CP*-violation measurements, where asymmetries are typically examined, and in studies of rare decays, where contamination from misidentified backgrounds could overwhelm the signal.

Discrimination between the charged protons, kaons and pions is achieved using two Ring Imaging Cerenkov (RICH) systems [59]. These detectors use mirrors to reflect the Cerenkov radiation emitted by charged particles travelling through a medium at faster-than-light speeds onto photon hybrid photon detectors (HPDs). The cone of light around the particle is produced with a Cerenkov angle, θ_c, given by,

$$\cos\theta_c = \frac{1}{n\beta}, \tag{3.1}$$

where n is the refractive index of the radiator material and β is the relativistic beta factor. The RICH detectors exploit the variation in Cerenkov angle with particle mass that is highlighted in Fig. 3.9.

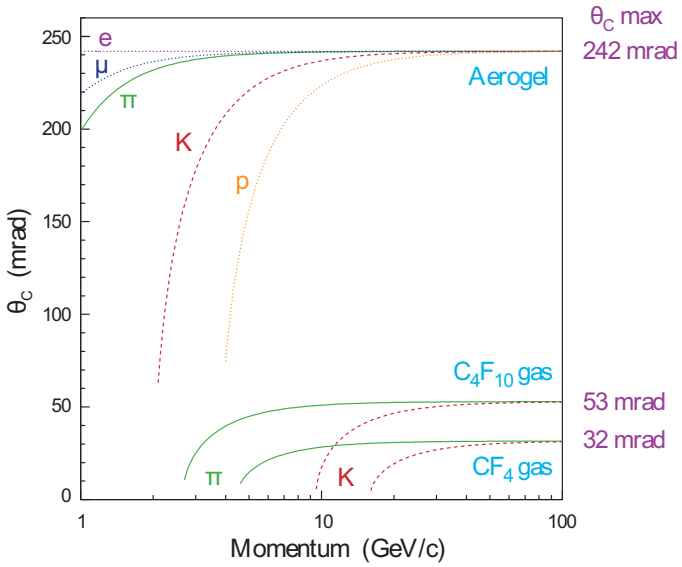

Figure 3.9: Cerenkov angle as a function of momentum and refractive index for pions, kaons and protons [54].

At LHCb the momentum distribution of the tracks at low pseudorapidities is softer than in the high-pseduorapidity regions [59]. Therefore, to effectively identify the particles across a range of momenta two RICH detectors are used. The first system, RICH1, is located upstream of the magnet and is optimised for tracks with momenta between 2-50 GeV/c. The RICH1 detector is filled with C_4F_{10} gas, which has a refractive index of $n = 1.0014$, and covers the full angular acceptance. A 5 cm thick layer of silica aerogel with $n = 1.03$ is placed in front of RICH1 to provide complimentary information for the tracks with a momentum less than around 20 GeV/c. Between run 1 and run 2 of the LHC, the aerogel layer was removed from the RICH1 detector because it did not work effectively. This improved PID performance in run 2 due to a reduced occupancy in the photon detectors. A diagram of RICH1 can be found in Fig. 3.10.

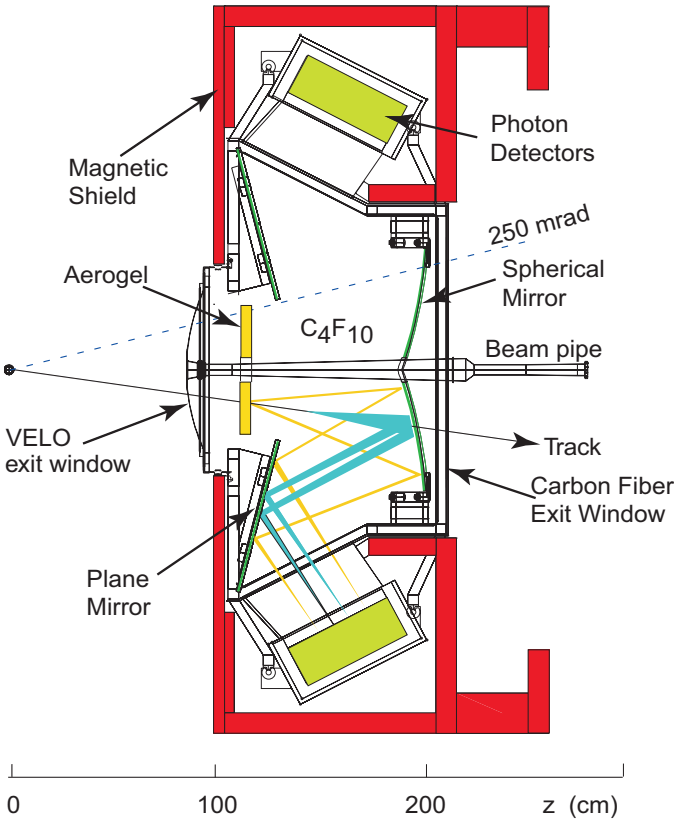

Figure 3.10: The RICH1 detector during run 2 of the LHC [73].

The second Cerenkov detector, RICH2, is situated downstream of the magnet. RICH2 is filled with CF_4 gas with a lower refractive index, $n = 1.00048$, which is

more optimal for high momentum tracks, and can distinguish between the species of particles in the region $15 < p < 150\,\text{GeV}/c$.

3.3.1.1 Charged hadron PID performance

The information from the RICH counters is used to determine a mass hypothesis for each track. The algorithm [74] constructs a global likelihood by comparing the observed pattern of hits on the HPDs to the prediction given the momentum, direction of travel and mass hypothesis of each track. The probability is initially computed assuming that all tracks are pions, since they are the most copiously produced charged particle at LHCb. Then, the mass hypothesis of each track is varied individually to find which species (π, K, e, p or μ) maximises the likelihood. Multiple iterations of this procedure are performed until the best-fit mass hypotheses are found. At this stage, the mass hypothesis of each individual track is once again separately varied, and the difference in log-likelihood (DLL) from the pion hypothesis is calculated for analysts to use as discriminating variables.

The efficiencies of requirements on the DLL variables are determined in data using decays which can be reconstructed without using RICH information [75]. For kaons and pions, the $D^{*+} \to [K^-\pi^+]_{D^0}\pi^+$ decays are used, where the kaon and pion tracks can be tagged from the charge on the pion from the D^{*+} decay. This channel is particularly advantageous because the large charm production cross-section at LHCb combined with the high branching fraction, purity and selection efficiency of $D^0 \to K^-\pi^+$ decays allows for a precise estimate of the PID efficiency. Figure 3.11 shows the efficiency of correctly identifying a kaon and misidentifying a pion with requirements on $\text{DLL}_{K\pi}$ as a function of momentum. A good separation is seen up to 100 GeV/c.

3.3.2 Calorimeters

A calorimeter system, which consists of four sub-detectors as shown in Fig. 3.12, is located downstream of the magnet and is used to identify and measure the energy of electrons, photons and hadrons [61]. The first two components are the Scintillating

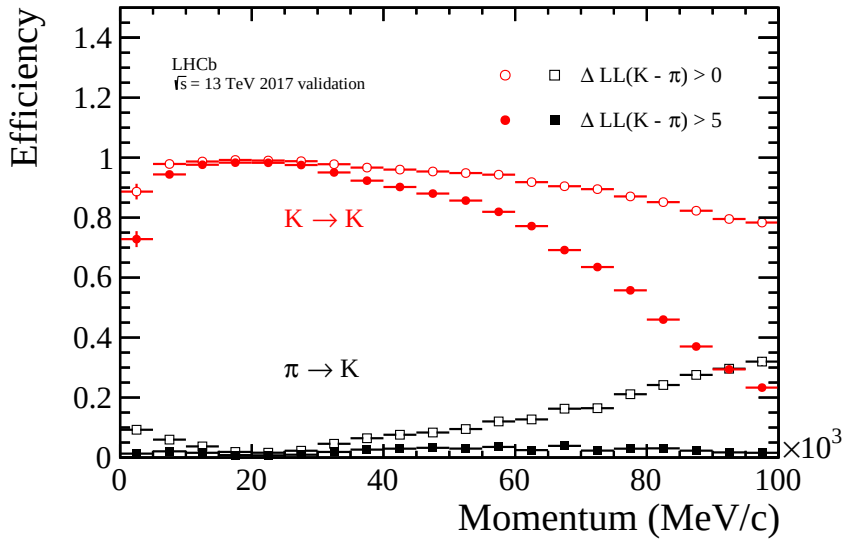

Figure 3.11: Efficiency in 2017 data of (red) correctly identifying kaons and (black) misidentifying pions as a function of momentum [73]. The requirements are placed on the difference in log likelihood between the track having a kaon and pion mass hypotheses.

Pad (SPD) and Preshower (PS), which are layers of scintillator separated by around 15 mm of lead. The electrons produce a signal in both scintillator layers, whilst light is detected in only the PS (SPD) for a photon (charged hadron). The primary use of the SPD and PS is to reject backgrounds in dedicated electron triggers.

The same principle of using alternating layers of absorber and scintillator are used in the remaining two components, the hadronic (HCAL) and electromagnetic (ECAL) calorimeters, which detect hadrons, and photons and electrons, respectively. The ECAL uses a lead absorber, whilst iron is used for the latter. Both components are divided into cells which use wavelength shifters to direct the scintillation light towards photomultiplier tubes. The size of the cells increases with distance from the beam pipe to achieve good resolution in the regions of high particle density.

3.3.3 Muon chambers

At LHCb muons are identified through five stations (M1-5), each of which contains a grid of multi-wire proportional chambers that provide a binary hit response [60]. The dimensions of these chambers dictate the spatial resolution. Similarly to the calorimeter, the resolution decreases with radial distance from the beam pipe

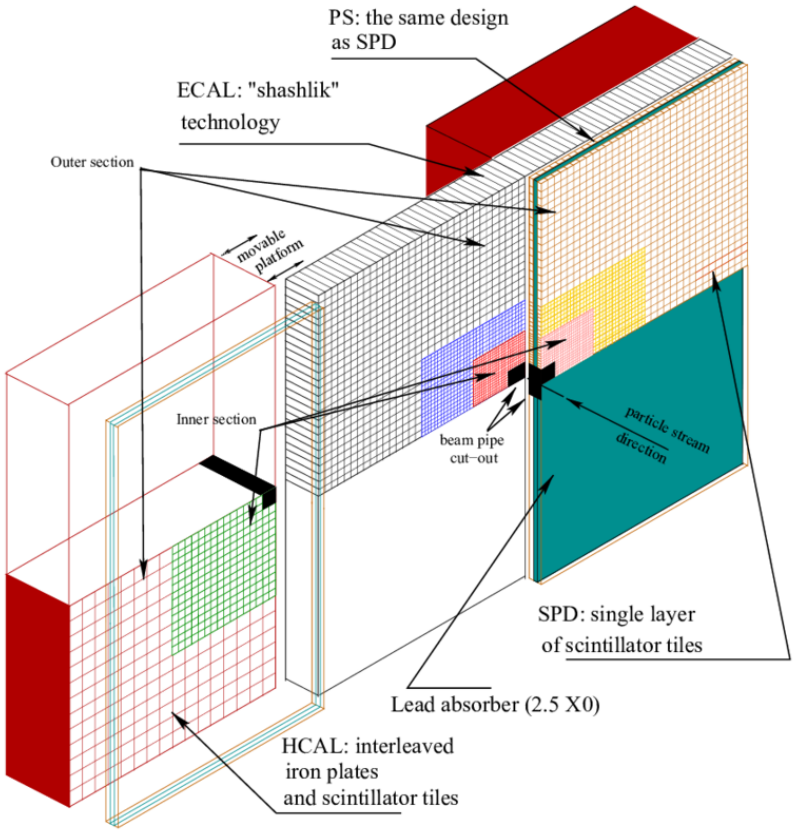

Figure 3.12: The four calorimeter components, the SPD, PS, ECAL and HCAL [76].

to account for the increased occupancy in the centre, as displayed in Fig. 3.13. The first station, M1, is located upstream of the calorimeters to enable more accurate p_{T} measurements for the trigger, which is discussed in more detail in the next section. The other stations, M2-5, are the components which are furthest downstream in the LHCb detector, and they are separated by 80 cm of iron to suppress hadronic backgrounds. A binary variable, called `isMuon`, is typically used for the identification of muons, and it is one for a track which has positive hits in the muon chambers and zero otherwise. The `isMuon` requirement is around 97% efficient on signal across a wide momentum range [77].

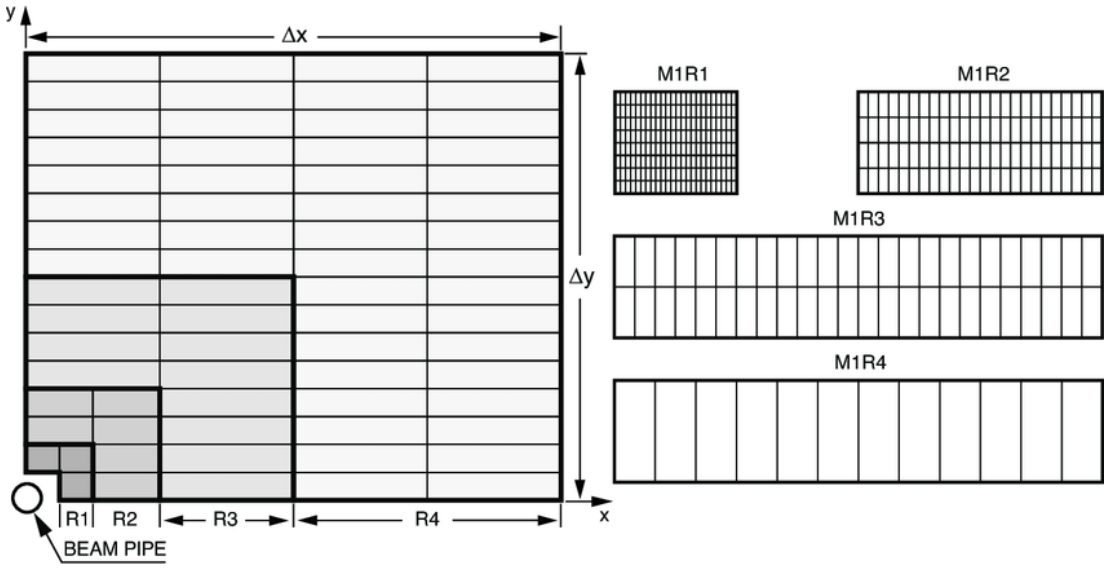

Figure 3.13: A single quadrant of the muon chambers [78].

3.4 The LHCb trigger system

Events with interesting interactions are efficiently selected at LHCb using a three-tiered trigger system [62, 69]. Staggering the triggers provides the later stages with more time to make a better informed decision. The first stage, which is called Level 0 (L0), accepts events with a photon, electron, hadron or muon with a high transverse energy. It is a hardware trigger which reads out information directly from the calorimeters and the muon chambers at 40 MHz and reduces the event rate to around 1 MHz.

Events accepted by the L0 trigger are accessed by the High Level Trigger (HLT), which is software based and has two stages. In the first stage, HLT1, a partial event reconstruction is performed. Information provided by the VELO is used to locate the PV and thus tracks with a high IP. The trajectories of the corresponding tracks are extrapolated to the tracking stations in search of matching hits. The search region is narrowed by specifying that the track must have a minimum p_{T}. A fit is performed using all the available hits which is required to be of good quality. Dedicated muon triggers at the HLT1 level use additional hits from the muon stations.

At the final stage, HLT2, a full event reconstruction is carried out. In the

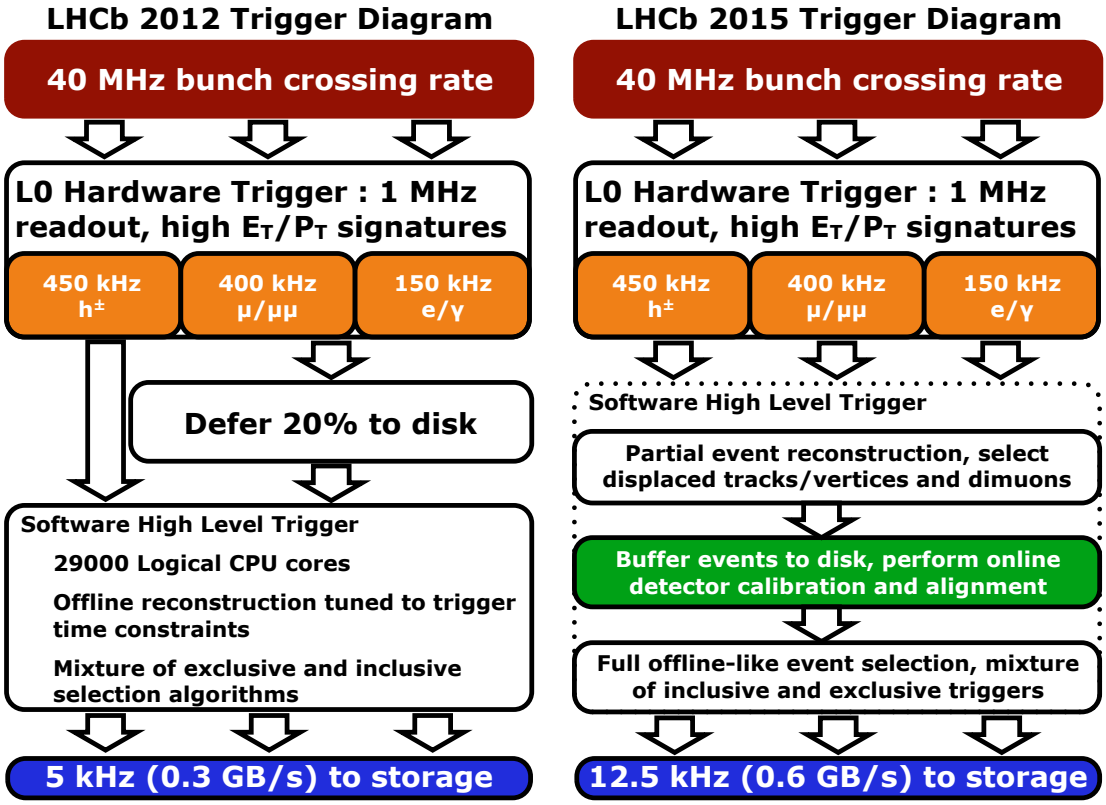

Figure 3.14: Flowcharts of the LHCb triggers in (left) 2012 and (right) 2015 [79].

measurement described in Chap. 4, events are required to meet the criteria for an inclusive-b HLT2 trigger. These use a multivariate technique to select events consistent with the topology of b-hadrons which possess displaced vertices decaying into 2, 3 or 4 high-p_{T} tracks. In other cases, exclusive triggers are used which can apply PID requirements using information from the RICH detectors. In run 1, the HLT reduced the rate of events being saved to disk to around 5 kHz, whilst it was 12.5 kHz in run 2.

In 2012, an improved trigger was employed where around 20% of the events that passed HLT1 were buffered onto a disk to be processed during the time when the detector was not collecting data. A further evolution took place during run 2, and the events retained in the buffer were used to perform a real-time detector alignment [69]. For example, the VELO physically moves between fills, since it retracts from the beam pipe, and therefore it must be calibrated. Another example

is the temperature and pressure dependence of the RICH gas refractive indices. The benefit of performing this real-time alignment is two-fold. First, the signal efficiency and purity of the trigger is improved through increased momentum resolution and better PID. And secondly, it reduces differences between reconstruction performed in the trigger and offline, which makes offline data processing redundant and saves significant computing resources. Figure 3.14 displays flowcharts summarising the triggers in 2012 and 2015.

3.5 Simulation at LHCb

In the measurement described in Chap. 4, which uses LHCb data, simulation is used to study background contributions and their efficiencies. The simulation is created as follows. First, the interactions between the protons are modelled using a version of the Pythia [80, 81] package tuned to LHCb [82]. Next, EvtGen [83] handles particle decays accounting for final-state radiation with Photos [84]. Finally, the response of the detector to the particles is simulated using the Geant4 toolkit [85, 86] as outlined in Ref. [87]

4

Measurement of the CKM angle γ using $B^0 \to DK^{*0}$ decays at LHCb

Contents

4.1 Measurement strategy

Chapter 2 provides an overview of the principles behind a measurement of γ using $B^0 \to DK^{*0}$ decays with $D \to K^0_S h^+ h^-$. This section naturally follows and outlines the strategy for applying those principles in an experimental setting.

As previously discussed, the measurement proceeds by examining the distributions of B^0 and $\overline{B}^0$ decays across the $D \to K^0_S h^+ h^-$ decay phase space, which are described by Eq. 2.40 and 2.41. However, the derivation of these equations does not consider the varying reconstruction efficiency across the Dalitz plot.

At the LHCb experiment the flight distance of K^0_S mesons is typically $\mathcal{O}(1m)$ due to their relatively long lifetime. However, higher momentum K^0_S mesons possess a larger Lorentz boost, and therefore travel further before decaying, often outside of the LHCb acceptance. This causes a decreasing selection efficiency across the diagonal of the Dalitz plot, as displayed in Fig. 4.1, because the invariant mass of the h^+h^- pair is correlated with the momentum of the K^0_S. This is clear to see in the rest frame of the D meson where $\vec{p}_{K^0_S} = -\vec{p}_{h^+h^-}$. To account for this effect, the K_i are replaced with efficiency-modulated probabilities, denoted F_i, and defined as

$$F_i = \frac{\int_i \mathrm{d}m^2_- \mathrm{d}m^2_+ \mathcal{A}^2_D(m^2_+, m^2_-)\eta(m^2_+, m^2_-)}{\sum_j \int_j \mathrm{d}m^2_- \mathrm{d}m^2_+ \mathcal{A}^2_D(m^2_+, m^2_-)\eta(m^2_+, m^2_-)}, \tag{4.1}$$

where $\eta(m^2_+, m^2_-)$ is the efficiency profile. In theory, the same corrections should apply to the c_i and s_i parameters, but previous measurements [88] find they have little impact on the final result. Therefore, it is sufficient to directly use the c_i

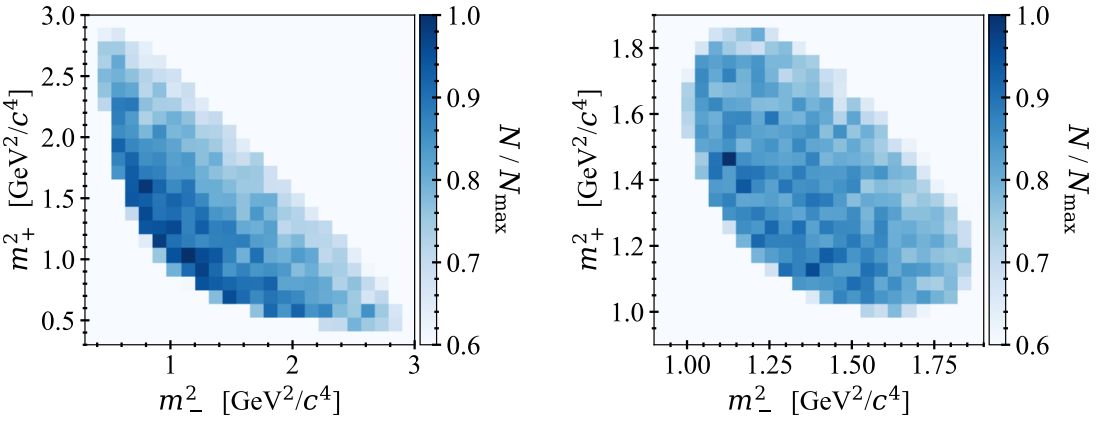

Figure 4.1: Relative efficiency profile of (left) $D \to K^0_S\pi^+\pi^-$ and (right) $D \to K^0_S K^+K^-$ decays in simulation.

Table 4.1: Values of the F_i [88], c_i and s_i inputs [10, 11] used in this measurement.

Region index	F_i (LL)	F_i (DD)	F_{-i} (LL)	F_{-i} (DD)	c_i	s_i
			$D \to K^0_S\pi^+\pi^-$			
1	0.022 ± 0.0006	0.020 ± 0.0004	0.095 ± 0.0012	0.097 ± 0.0008	-0.04 ± 0.05	0.83 ± 0.10
2	0.005 ± 0.0003	0.005 ± 0.0002	0.153 ± 0.0014	0.153 ± 0.0009	0.84 ± 0.07	0.29 ± 0.15
3	0.004 ± 0.0003	0.004 ± 0.0002	0.160 ± 0.0014	0.160 ± 0.0010	0.15 ± 0.07	0.79 ± 0.15
4	0.055 ± 0.0009	0.056 ± 0.0006	0.095 ± 0.0012	0.095 ± 0.0008	-0.91 ± 0.02	0.08 ± 0.06
5	0.027 ± 0.0006	0.022 ± 0.0004	0.046 ± 0.0008	0.042 ± 0.0005	-0.29 ± 0.04	-1.02 ± 0.06
6	0.004 ± 0.0003	0.003 ± 0.0002	0.062 ± 0.0001	0.056 ± 0.0006	0.27 ± 0.08	-0.98 ± 0.18
7	0.055 ± 0.0009	0.057 ± 0.0006	0.127 ± 0.0013	0.133 ± 0.0009	0.92 ± 0.02	-0.18 ± 0.07
8	0.067 ± 0.0001	0.072 ± 0.0007	0.024 ± 0.0006	0.024 ± 0.0004	0.77 ± 0.03	0.28 ± 0.12
			$D \to K^0_S K^+K^-$			
1	0.289 ± 0.005	0.296 ± 0.003	0.221 ± 0.004	0.230 ± 0.003	0.71 ± 0.03	0.11 ± 0.13
2	0.282 ± 0.005	0.271 ± 0.003	0.207 ± 0.004	0.203 ± 0.003	-0.76 ± 0.04	-0.39 ± 0.17

and s_i from Refs. [10, 11], which are displayed in Tab. 4.1, and account for the efficiency profile as a systematic uncertainty.

The obvious method of determining the efficiency profile is to use simulation. However, differences from data caused by imperfect descriptions of the detector, reconstruction effects, experimental conditions and decay kinematics can result in large systematic uncertainties. To minimise reliance on the simulation a data-driven control channel is typically used which has large yields and high purity. Then, one could precisely measure the F_i parameters through the fraction of candidates that fall

in a particular region of the Dalitz plot, and knowledge of $\eta(m_+^2, m_-^2)$ is unnecessary.

In the run 1 measurement of γ using $B^0 \to DK^{*0}$ decays [89] a semileptonic $B^0 \to D^{*-}\mu^+\nu_\mu X$ decay channel was used, where X denotes particles that are not reconstructed. The charge of the muon from the B^0 decay and the pion from the $D^{*-} \to [K^0_S h^+ h^-]_{\overline{D}^0}\pi^-$ decay unambiguously indicate the flavour of the $\overline{D}^0$ meson, and thus allow the F_i to be extracted.

Although most of the efficiency effects cancel between the signal and control channels, there are still obvious differences. For example, the semileptonic decays are triggered by hits in the muon stations, whilst the signatures of hadronic decays are more relevant for the signal sample. The differences between the two final states and their selection criteria sculpt the kinematic distributions and thus the efficiency profile. These differences were studied using simulation and the corresponding systematic uncertainty was still relatively large.

The strategy for the measurement described in this chapter aims to reduce the systematic uncertainty by using the F_i values determined in $B^+ \to D\pi^+$ decays, which have a hadronic final state and a similar topology to signal. However, in principle, this choice of control channel introduces another problem - $B^+ \to D\pi^+$ decays are *CP* violating. Therefore, the yield of $B^+ \to D\pi^+$ decays in a particular region of the Dalitz plot is not exactly equal to F_i due to interference between $B^+ \to D^0\pi^+$ and $B^+ \to \overline{D}^0\pi^-$ decays, and it also depends on γ, $r_B^{D\pi}$ and $\delta_B^{D\pi}$.

At the time of the run 1 measurement of γ using $B^0 \to DK^{*0}$ decays the hadronic parameters describing $B^+ \to D\pi^+$ decays had not been precisely measured. From suppression arguments, the amplitude ratio, which dictates the amount of interference, was known to be small, $r_B^{D\pi} \sim 0.005$, but $\delta_B^{D\pi}$ was unknown. So, although the F_i values could be estimated assuming little or no interference they came with a large systematic uncertainty. However, in 2020 the LHCb collaboration published a measurement of γ using a novel strategy by simultaneously fitting the distributions of $B^+ \to DK^+$ and $B^+ \to D\pi^+$ decays in regions of the Dalitz plot [88]. This allowed simultaneous determination of γ, where the precision was dominated by the $B^+ \to DK^+$ decays since $r_B^{DK} \sim 0.1$, and the F_i parameters,

which were predominantly constrained by the $B^+ \to D\pi^+$ decays. Those F_i parameters measured in Ref. [88] are used directly in the measurement described in this chapter, and are displayed in Tab. 4.1.

To minimise differences in the Dalitz plot efficiency profiles of $B^0 \to DK^{*0}$ and $B^+ \to D\pi^+$ decays, the reconstruction of the former, described in Sec. 4.2, closely follows that of the $B^+ \to D\pi^+$ decays, listed in Ref. [88]. Again, simulation is used to assign a systematic uncertainty associated with the efficiency differences, but it is significantly reduced compared to the run 1 measurement which validates the change in strategy.

The uncertainty on γ is inversely proportional to the value of r_s, which leads to a biased determination. Therefore, in the fits described in Sec. 4.5, the parameters r_s, δ_s and γ are replaced with the *CP-violation observables*, defined as

$$x_\pm = r_s \cos(\delta_s \pm \gamma), \tag{4.2}$$

$$y_\pm = r_s \sin(\delta_s \pm \gamma), \tag{4.3}$$

which exhibit a better statistical behaviour.

With these experimental considerations the yields for B^0 and $\overline{B}^0$ decays in a region, i, are written as

$$N(B^0)_i = h\left(F_{-i} + (x_+^2 + y_+^2)F_i + 2\kappa\sqrt{F_i F_{-i}}\,[x_+ c_i - y_+ s_i]\right), \tag{4.4}$$

$$N(\overline{B}^0)_i = \bar{h}\left(F_i + (x_-^2 + y_-^2)F_{-i} + 2\kappa\sqrt{F_i F_{-i}}\,[x_- c_i + y_- s_i]\right). \tag{4.5}$$

where the h and $\bar{h}$ parameters are normalisation factors. Allowing these to float in the fit absorbs global asymmetries between B^0 and $\overline{B}^0$ decays, such as production rates and reconstruction effects, and leaves the *CP*-violation observables insensitive to such effects.

In the derivation of the yields in Eq. 4.4 and 4.5 mixing between D^0 and $\overline{D}^0$ mesons is neglected. The F_i parameters are determined from $B^\pm \to D\pi^\pm$ decays in data, and therefore they inherently account for mixing to first order. However, the c_i and s_i parameters do not, which can bias the measured *CP*-violation observables

and γ. The bias is discussed in detail in Refs. [90, 91], where it is shown to be less than 0.1°, and therefore the effect of not correcting for charm mixing is negligible in this analysis given the expected precision.

4.2 Reconstruction and selection of candidates

The selection of signal candidates proceeds in stages. It begins at the trigger, where loose requirements are placed on the typical signatures of heavy-flavour decays, such as the transverse momenta of tracks in the event and the displacement of the reconstructed decay vertices. Additional criteria are placed on the quality of the reconstructed tracks and vertices, which are effective at rejecting background.

The output of the trigger is processed by a dedicated *stripping line*, which effectively builds $B^0 \to DK^{*0}$ candidates from the raw event information given the topology. It assigns mass hypotheses to the charged tracks which allows the composite K^{*0}, K^0_S, D and B^0 candidates to be created and assigned properties. Separate stripping lines are used for candidates with K^0_S mesons reconstructed using two long (LL) or downstream (DD) tracks, which are treated separately throughout the measurement because the former typically have a better resolution and higher reconstruction efficiency.

The specific requirements placed in the trigger and stripping are not listed, because they are relatively loose requirements which are designed to reduce background whilst retaining a large portion of signal. Furthermore, they are superseded by tighter criteria more specific to the signal decay which significantly improves the purity in the sample. These tighter criteria include a series of rectangular requirements and application of a boosted decision tree, both of which are detailed in the following sections.

In the reconstruction, the momentum of each final-state track is recalculated in a kinematic fit which simultaneously constrains the masses of the D and K^0_S mesons to the PDG values[1], and the momentum of the B meson to be parallel

[1]The 2022 edition of the PDG [92] is used throughout this chapter.

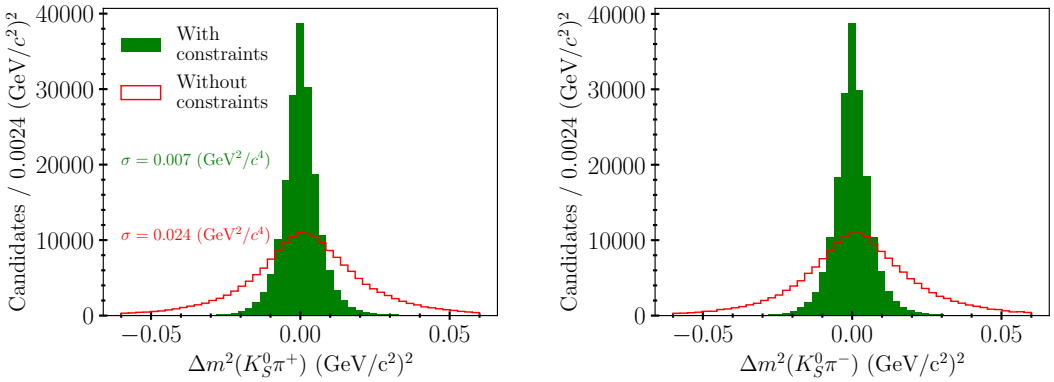

Figure 4.2: Difference between the true and reconstructed Dalitz plot coordinates in $D \to K^0_S\pi^+\pi^-$ decays (green) with and (red) without the constraints described in the text. The left and right plots show $m^2(K^0_S\pi^+)$ and $m^2(K^0_S\pi^-)$, respectively.

with the vector connecting the PV and the B-meson decay vertex. This is achieved using the `DecayTreeFitter` package [93]. The fit improves the resolution of the B-meson invariant mass and the phase-space coordinates, which is important to correctly identify the Dalitz plot region. Figure 4.2 displays the difference between the true and reconstructed Dalitz plot coordinates, where the resolution improves by around a factor of 3 when the constraints are applied. The momenta from the fit are used throughout this chapter unless stated otherwise.

4.2.1 Core selection requirements

The majority of the selection requirements, which are discussed in this section and summarised in Tab. 4.2, are taken from Ref. [88] to reduce differences between the Dalitz plot efficiency profiles of $B^0 \to DK^{*0}$ and $B^\pm \to D\pi^\pm$ decays, with the obvious exception of the criteria imposed on the K^{*0} candidate. Throughout, each composite particle must have an invariant mass close to it's known value, and tracks with tight PID requirements must also have a momentum less than 100 GeV/c and hits in the RICH detector, such that the PID efficiency is high.

The charged kaons which make up the $D \to K^0_S K^+K^-$ decay candidates are required to satisfy tight PID requirements to reduce background from $D \to K^0_S K^+\pi^-$ decays. In the $D \to K^0_S\pi^+\pi^-$ channel, the $D \to K^0_S K^+\pi^-$ background is already suppressed by the branching fraction, so the children pions are only subject to

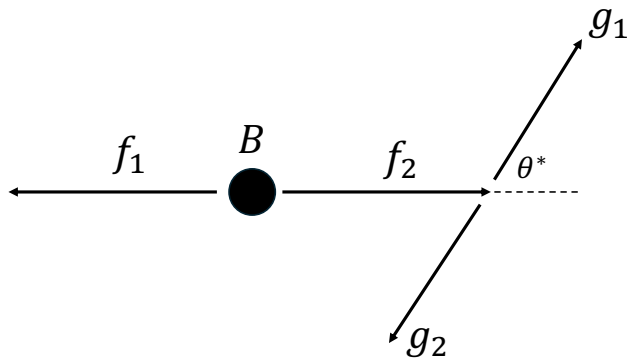

Figure 4.3: Diagram depicting the helicity angle in $B \to f_1[g_1 g_2]_{f_2}$ decays, denoted θ^*. It is defined as the angle between the momentum of g_1 in the rest frame of f_2, and the momentum of f_2 in the rest frame of the B meson.

loose PID requirements. The kaon and pion candidates that form the K^{*0} meson are also subject to tight PID requirements, which is necessary to ensure the flavour of the B^0 meson is correctly identified, and that the rate of misidentified $B^0 \to \overline{D}^0\pi^+\pi^-$ decays is low.

As discussed in Sec. 2.5, it is necessary to isolate a region of $B^0 \to DK^+\pi^-$ decay phase space where the $B^0 \to DK^{*0}$ resonance dominates. The same criteria are applied as in Ref. [40] where the coherence factor is determined. Specifically, the reconstructed mass of the K^{*0} candidate must be within 50 MeV/c^2 of the PDG value, $|m(K^+\pi^-) - m_{\rm PDG}(K^{*0})| < 50\,{\rm MeV}/c^2$, chosen to match the natural width of the K^{*0} meson, $(47.3 \pm 0.5)\,{\rm MeV}/c^2$ [33].

The angular distribution of the K^{*0}-decay products is exploited to further reduce backgrounds. The B^0 and D mesons are pseudoscalars with $J^P = 0^-$, whereas the K^{*0} is a vector meson such that $J^P = 1^-$. To ensure conservation of angular momentum, the K^{*0} particle must be longitudinally polarised such that it has a helicity of 0. Consequently, the momentum of the K^+ meson in the rest frame of the K^{*0} is preferentially produced parallel to the momentum of the K^{*0} in the rest frame of the B^0. The angle between these momenta is denoted θ^*, as depicted in Fig. 4.3, and the candidates are required to satisfy $|\cos\theta^*| > 0.4$.

A number of requirements are placed to reject specific backgrounds. In the *LL* sample, the K^0_S-decay vertex is required to be displaced from the D-decay vertex to reduce contamination from $D^0 \to h^+h^-\pi^+\pi^-$ decays. The same requirement is not necessary in the *DD* sample because, by definition, the K^0_S-decay vertex must already be displaced. Specifically, the flight-distance chi-squared, defined as $\chi^2_{\rm FD} = \frac{L}{\sigma(L)}$, where L is the fitted flight distance of the K^0_S, must be greater than 49.

A similar requirement is placed on the displacement of the D-decay vertex to reduce backgrounds from *charmless* B^0 decays which proceed without the intermediate D meson. The significance of the distance between the z-coordinates of the B and D-meson decay vertices,

$$\Delta z^{B-D} = \frac{z^B - z^D}{\sqrt{\sigma^2(z^B) + \sigma^2(z^D)}}, \tag{4.6}$$

is required to be greater than 0.5. This requirement does not remove all charmless decays but further tightening it begins to remove a significant fraction of signal. Residual charmless decays are studied in Sec. 4.3.2 and the findings are used to assign a systematic uncertainty.

To reduce background from semileptonic $D^0 \to [K^0_S h^-]_{K^{*-}} l^+ \nu_l$ decays, the D-decay child particle with the opposite charge from the kaon from the K^{*0} decay is required to satisfy $\mathrm{DLL}_{e\pi} < 0$ and `isMuon` $= 0$. The other charged D-decay product must also satisfy `isMuon` $= 0$ to reduce the impact of pions which decay in the detector. The resolution of the Dalitz plot coordinates for such particles is typically poor, which can lead to assigning the wrong region of D-decay phase space.

4.2.2 Boosted decision tree

The candidate selection continues with a gradient boosted decision tree (BDT) [94] which is used to reduce the combinatorial background. To minimise efficiency differences across the Dalitz plot between the $B^0 \to DK^{*0}$ and $B^\pm \to D\pi^\pm$ decays, a BDT is employed which is trained using similar variables to those described in Ref. [88], where significant optimisation studies were performed. However, due to the different decay topologies, the BDT is retrained with the inclusion of input

Table 4.2: Summary of requirements applied to select $B^0 \to DK^{*0}$ decays.

Requirement	Comment
$K^{*0} \to K^+\pi^-$	
$\lvert m(K^+\pi^-) - m_{\rm PDG}(K^{*0})\rvert < 50\,{\rm MeV}/c^2$	–
$\lvert\cos(\theta^*)\rvert > 0.4$	–
${\rm DLL}_{K\pi}(K^+) > 5$	–
${\rm DLL}_{K\pi}(\pi^-) < 3$	–
$p(K^+) < 100\,{\rm GeV}/c$	–
$D \to K^0_{\rm S}h^+h^-$	
$\lvert m(K^0_{\rm S}h^+h^-) - m_{\rm PDG}(D^0)\rvert < 25\,{\rm MeV}/c^2$	–
$\lvert m(\pi^+\pi^-) - m_{\rm PDG}(K^0_{\rm S})\rvert < 15\,{\rm MeV}/c^2$	–
${\rm DLL}_{K\pi}(\pi^\pm_D) < 20$	$D \to K^0_{\rm S}\pi^+\pi^-$ only
${\rm DLL}_{K\pi}(K^\pm_D) < -5$	$D \to K^0_{\rm S}K^+K^-$ only
$p(K^\pm_D) < 100\,{\rm GeV}/c$	$D \to K^0_{\rm S}K^+K^-$ only
Background-suppressing cuts	
$\Delta z^{B-D} > 0.5$	To reduce charmless B^0 decays
$\chi^2_{\rm FD} > 49$	To reduce $D \to \pi^+\pi^-h^+h^-$ decays (LL $K^0_{\rm S}$ mesons only)
$\texttt{isMuon}(h^\pm_D) = 0$	To reduce $D^0 \to [K^0_{\rm S}h^-]_{K^{*-}}l^+\nu_l$ decays
${\rm DLL}_{e\pi}(\pi_D) < 0$	Applied to π with opposite charge from bachelor kaon to reduce $D^0 \to [K^0_{\rm S}h^-]_{K^{*-}}l^+\nu_l$ decays in the $D \to K^0_{\rm S}\pi^+\pi^-$ channel.

variables to describe the additional final-state particle. Specifically, each variable used to describe the $\pi^\pm$ from the $B^\pm$ decay in Ref. [88] is applied to both K^{*0}-decay products. A full list of the training variables and brief descriptions can be found in Tab. 4.3. To understand the variables the following definitions are necessary:

- DIRA – angle between the vector joining a composite particles production and decay vertices, and the combined three-momentum vector of the particles produced at the decay vertex.

- $\chi^2_{\rm IP}$ – χ^2 agreement between the impact parameter of a track and the vertex

from which it originated.

- DOCA – distance of closest approach between two tracks.
- p_{T} asymmetry – asymmetry between the p_{T} of the B candidate and the combined p_{T} of all other tracks in a 1.5 radian cone around the B-meson vertex, $(p_{\mathrm{T}}(B) - \Sigma p_{\mathrm{T}})/(p_{\mathrm{T}}(B) - \Sigma p_{\mathrm{T}})$.

Table 4.3: Summary of the variables used in the BDT training.

Variable	Description	Rank in training	
		DD	*LL*
log10(1-Ks_DIRA_BPV)	DIRA of the K^0_S	16	1
log(Bu_RHO_BPV)	Radial distance between the B-meson vertex and the beam line	12	2
log(Bu_constDOKSPV_CHI2NDOF)	Reduced χ^2 from the DecayTreeFit	3	3
log(min_Ksh1h2_IPCHI2_OWNPV)	Minimum χ^2_{IP} of the two K^0_S decay products	23	4
log(Bu_P)	Momentum of the B meson	7	5
log(Bach_PT)	p_T of the kaon from the K^{*0} decay	5	6
log(Bu_VTXCHI2DOF)	Reduced χ^2 of the fit to the B meson vertex	14	7
Bu_PTASY_1.5	Asymmetry between the B meson and the surrounding tracks	8	8
log(D0_PT)	p_T of D meson	9	9
log(KstarPi_IPCHI2_OWNPV)	χ^2_{IP} of π from the K^{*0} decay	13	10
log(Bach_P)	Momentum of the kaon from the K^{*0} decay	4	11
log(Bu_IPCHI2_OWNPV)	χ^2_{IP} between the three momentum of the B meson and it's vertex	6	12
log(max_Ksh1h2_IPCHI2_OWNPV)	Maximum χ^2_{IP} of the two K^0_S decay products	19	13
log10(1-D0_DIRA_BPV)	DIRA of the D meson	1	14
log(max_h1h2_IPCHI2_OWNPV)	Maximum χ^2_{IP} of the h^+ and h^- from the D decay	20	15
log10(1-Bu_DIRA_BPV)	DIRA of the B meson	2	16
log(KstarPi_PT)	p_T of pion from the K^{*0} decay	10	17
D0_MAXDOCA	Maximum DOCA of all combinations of the D-meson decay products	25	18
log(min_h1h2_IPCHI2_OWNPV)	Minimum χ^2_{IP} of the h^+ and h^- from the D decay	15	19
log(KstarPi_P)	Momentum of the pion from the K^{*0} decay	11	20
log(D0_P)	Momentum of D meson	17	21
log(Bach_IPCHI2_OWNPV)	χ^2_{IP} of kaon from the K^{*0} decay	18	22
log(Bu_FDCHI2_OWNPV)	χ^2_{FD} of the B meson	22	23
log(Ks_VTXCHI2DOF)	Reduced χ^2 from the K^0_S-meson vertex fit	24	24
log(D0_RHO_BPV)	Radial distance between the D-meson vertex and the beam line	21	25
log(D0_VTXCHI2DOF)	Reduced χ^2 from the D-meson vertex fit	27	26
log(D0_IPCHI2_OWNPV)	χ^2_{IP} between the three momentum of the D meson and its vertex	26	27
log(Bu_PT)	p_T of B meson	28	28
Bu_MAXDOCA	Maximum DOCA of all combinations of the B meson decay products	29	29

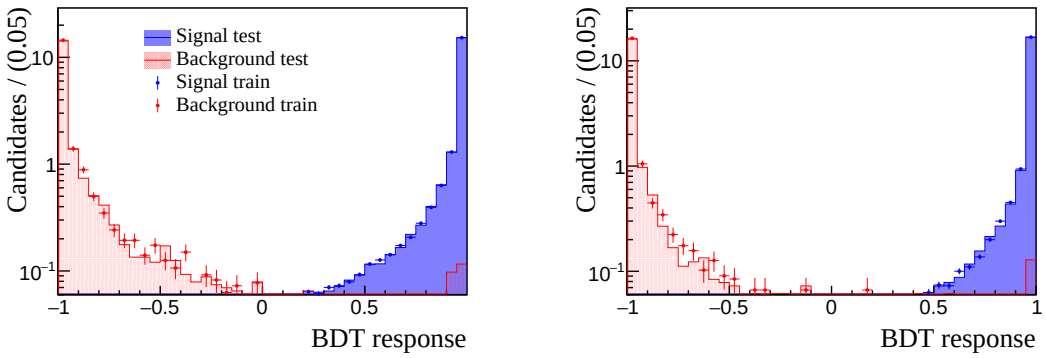

Figure 4.4: Comparison between the response of the BDT to the testing and training samples for signal (blue) and background (red). The response for K^0_S mesons reconstructed with (left) *DD* and (right) *LL* tracks are shown.

The BDT is trained and tested separately for the *LL* and *DD* samples. A simulation sample is used to represent signal, and the high-mass region from data, where $m(DK^+\pi^-) > 5.8\,\text{GeV}/c^2$, is chosen to represent the combinatorial background. The region below the B^0 mass is not used for training because it contains partially reconstructed $B^0 \to D^*K^{*0}$ decays where $D^* \to D\pi^0/\gamma$. Half of the candidates in each sample are used for training whilst the remainder are reserved for testing.

Figure 4.4 displays a comparison between the BDT response for the testing and training samples. Good agreement is seen between the two for signal and background candidates, which shows the BDT is not overtrained. There is a small peak at around 1 in the background response, which is caused by minor contamination from a background with a similar topology to signal in the high-mass region. However, the effect of this is negligible given the yield relative to the actual combinatorial background.

The BDT response is calculated for each candidate in data and those with a response below a chosen threshold are rejected. The optimal thresholds minimise the statistical uncertainties on the *CP*-violation observables, which are directly dependent on the total signal yield and sample purity. A global fit to all the candidates is performed, as described in Sec. 4.4, for a range of BDT requirements to estimate the signal and background yields. Then, using those yields, pseudo

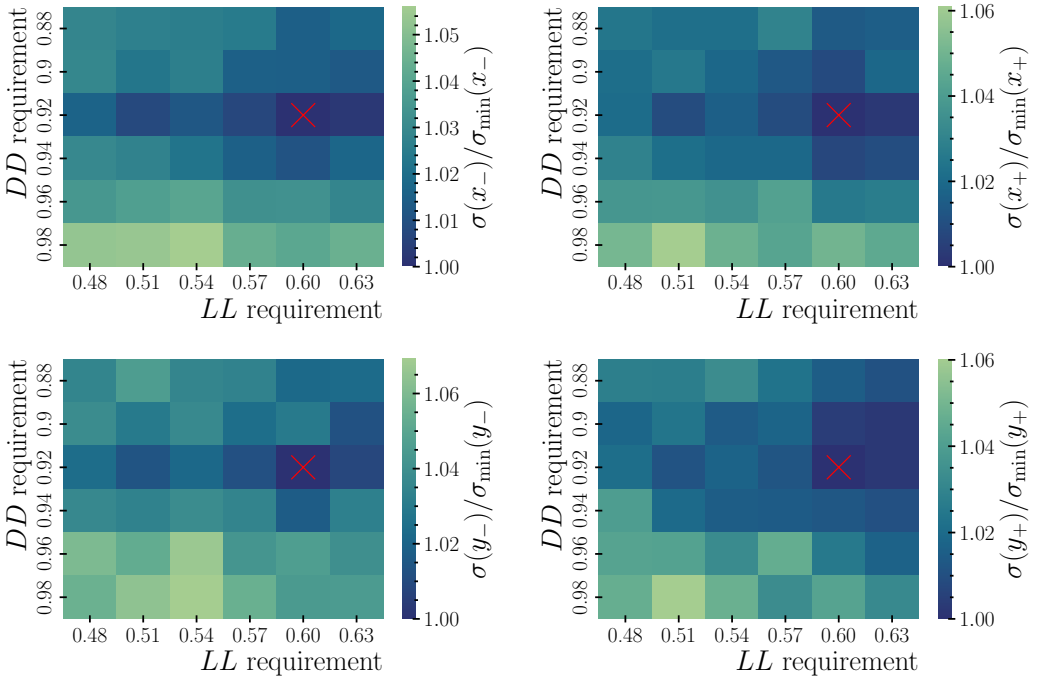

Figure 4.5: Relative uncertainty on the (top left) x_-, (top right) x_+, (bottom left) y_- and (bottom right) y_+ *CP*-violation observables, determined in pseudo data studies described in the text, as a function of the BDT requirements on candidates where the K^0_S meson is reconstructed with *DD* and *LL* tracks.

data samples are generated and fitted in regions of the Dalitz plot to estimate the uncertainties on the *CP*-violation observables. A more detailed explanation of this procedure is described in Sec. 4.5.2 as it requires knowledge of the fit model.

Figure 4.5 shows the mean statistical uncertainties on the *CP*-violation observables from 1000 pseudo experiments as a function of the BDT requirements, which show a shared minimum at 0.92 for *DD* tracks and 0.6 for *LL* tracks. In the testing sample these requirements retain 81% (95%) of the signal whilst removing around 99% (98%) of the background for the *DD* (*LL*) categories.

After application of the BDT, a single candidate is chosen at random from each event with multiple candidates, the fraction of which in data is $(1.08 \pm 0.13)\%$.

4.2.3 Dalitz plots of candidates

Figure 4.6 displays the Dalitz plots of candidates that pass the selection criteria and have an invariant mass within a 30 MeV/c^2 region either side of the PDG value

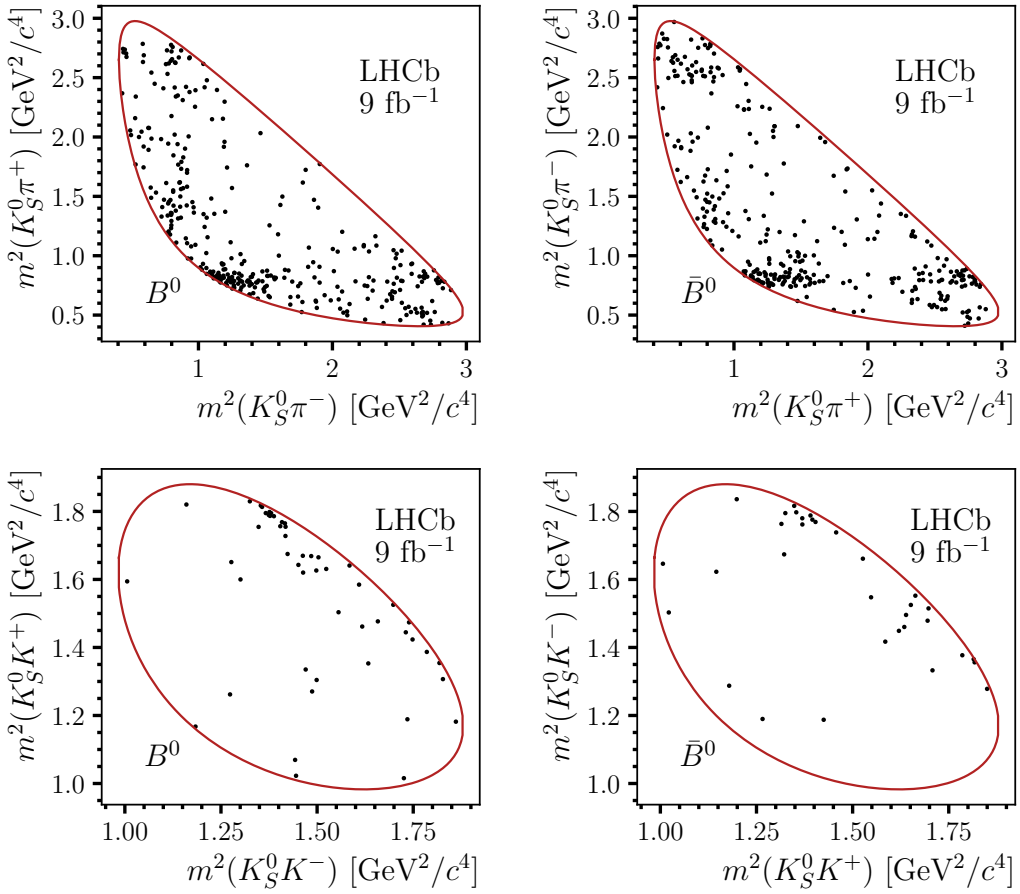

Figure 4.6: Dalitz plots of the candidates in data that pass all selections and have an invariant mass within 30 MeV/c^2 of the PDG value for the B^0 mass. The Dalitz plots for (left) $B^0 \to DK^{*0}$ and (right) $\overline{B}^0 \to D\overline{K}^{*0}$ decays with (top) $D \to K^0_S\pi^+\pi^-$ and (bottom) $D \to K^0_SK^+K^-$ are displayed. The axes for the plots showing $\overline{B}^0$ decays are rotated to compare with those of the B^0 decays. No distinction is made between K^0_S mesons reconstructed with *LL* and *DD* tracks.

for the B^0 mass, where the approximate purity is 60%. Dalitz plots are displayed for both D-decay modes and are split by the B^0-meson flavour. The axes are rotated for $\overline{B}^0$ decays such that a simple comparison can be made with B^0 decays to examine local *CP*-violation effects. Although differences between the plots are present, there are no definitive signs of *CP* violation.

4.2.4 Dalitz plot efficiency comparison with $B^+ \to D\pi^+$

A critical assumption in the analysis is that the Dalitz plot efficiency profile is similar in $B^0 \to DK^{*0}$ and $B^\pm \to D\pi^\pm$ decays after imposing selection criteria.

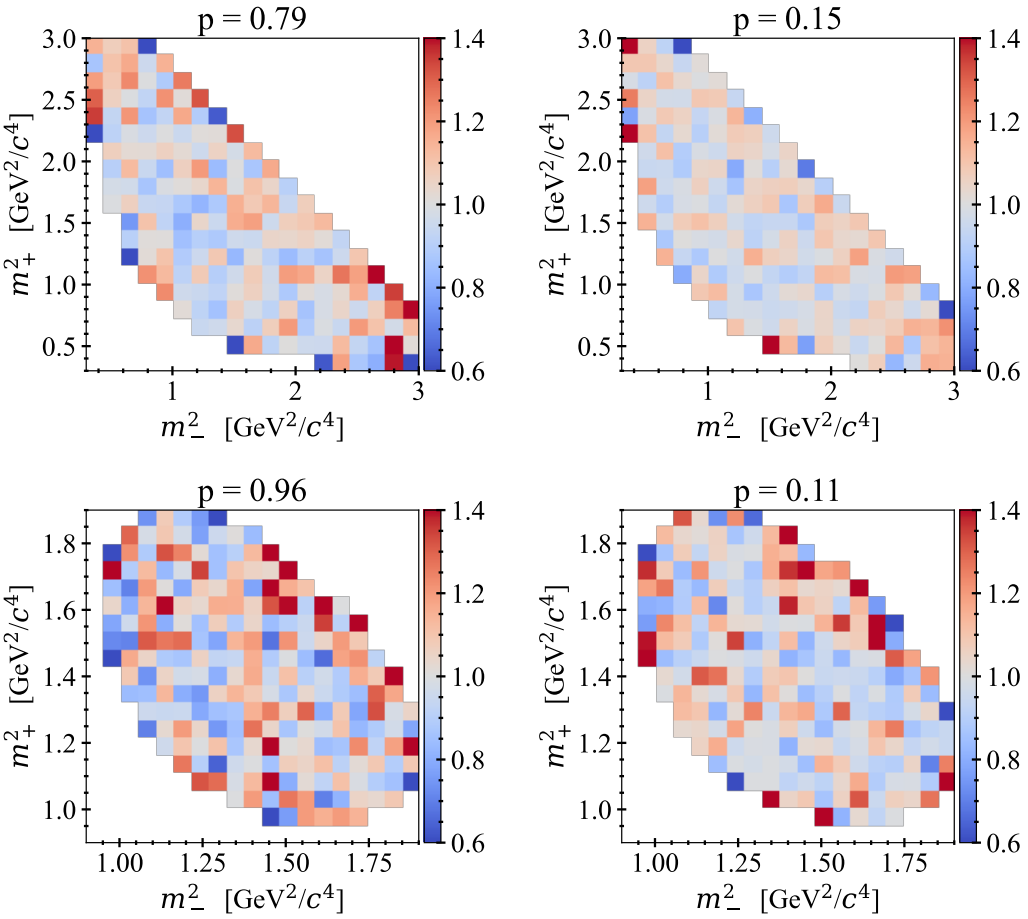

Figure 4.7: Ratio of the relative simulated yields of $B^0 \to DK^{*0}$ and $B^+ \to D\pi^+$ decays across the Dalitz plot for (top) $D \to K^0_S\pi^+\pi^-$ and (bottom) $D \to K^0_S K^+K^-$ decays where the K^0_S meson is reconstructed with (left) *LL* and (right) *DD* tracks. The probability displayed at the top of each plot is determined using a two-sample χ^2 test.

This is validated by comparing the relative distributions of simulated candidates in the two decays, which are generated uniformly across the Dalitz plot such that selection effects are responsible for any differences. Figure 4.7 displays the ratio between the distributions of the two channels for both D-decay final states and K^0_S reconstruction types, where no clear trends are visible. For each category, a two-sample χ^2 test [95] is performed to quantify the compatibility of the two distributions, and confirms the agreement with probabilities above 10%.

A further check is performed by comparing the one-dimensional distributions of $m^2(h^+h^-)$ in the two channels, as displayed in Fig. 4.8. This variable is chosen because the Dalitz plot coordinates are calculated with a K^0_S mass constraint and

thus have limited freedom. The ratio between the two distributions in each category is fit using a straight line with gradient, a, and intercept, b, and are all consistent with being flat ($a = 0$) as displayed in Tab. 4.4. The parameters a and b account for small differences and are used to estimate a systematic uncertainty as discussed in Sec. 4.6.

Table 4.4: Values of the gradient, a, and intercept, b, determined in a fit to the ratio of $m^2(h^+h^-)$ in simulated $B^\pm \to D\pi^\pm$ and $B^0 \to DK^{*0}$ decays.

D decay	Track type	a ($\times 10^{-2}$)	b
$K^0_S\pi^+\pi^-$	LL	-5 ± 2	1.03 ± 0.02
	DD	-4 ± 1	1.03 ± 0.01
$K^0_S K^+ K^-$	LL	-8 ± 6	1.10 ± 0.09
	DD	-1 ± 4	1.01 ± 0.06

4.3 Background studies

Despite the selection described in the previous section, a number of backgrounds remain in the sample because they are not easily vetoed without removing a large fraction of signal. These backgrounds, which are combinatorial background, $B^0_s \to D^0 K^{*0}$ decays, partially reconstructed $B^0_{(s)} \to D^* K^{*0}$ decays, $B^\pm \to DK^\pm$ decays and misidentified $B^0 \to \overline{D}{}^0\pi^+\pi^-$ decays are modelled in the invariant-mass fit as detailed in Sec. 4.4. The possibility of other backgrounds, such as signal with incorrectly assigned tracks, charmless B^0 decays and $B^0_{(s)} \to D^-_{(s)}h^+$ decays, are discussed in this section.

4.3.1 $B^0_{(s)} \to D^-_{(s)}h^+$ and track-swapped backgrounds

The possibility of $B^0_{(s)} \to D^-_{(s)}X$ decays, where X denotes a combination of particles, and signal decays with wrongly assigned tracks (such that one of the hadrons from the D decay actually originated from the K^{*0} meson) are investigated. This is achieved by reconstructing the invariant mass of all charge-allowed 2, 3 and 4-body combinations of the final-state tracks. If they originated from a D^-_s or D^- decay there would be a clear peak at the corresponding mass.

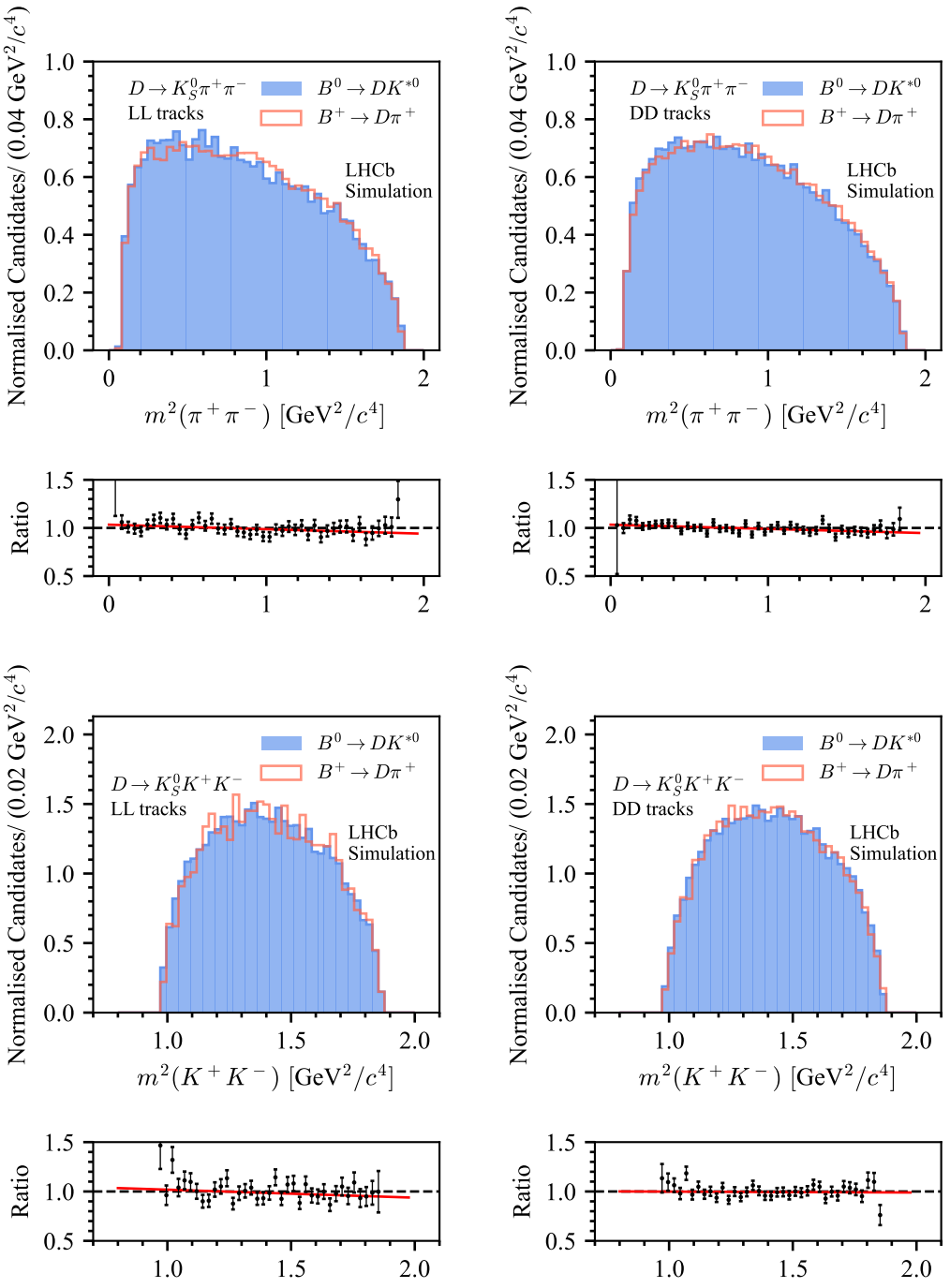

Figure 4.8: Ratio of the normalised simulated distribution of $m^2(h^+h^-)$ in $B^0 \to DK^{*0}$ and $B^+ \to D\pi^+$ decays with (top) $D \to K^0_S\pi^+\pi^-$ and (bottom) $D \to K^0_S K^+K^-$ decays where the K^0_S meson is reconstructed with (left) *LL* and (right) *DD* tracks. A fit to the ratio using a straight line with gradient, a, and intercept b, is shown below each plot and the corresponding values can be found in Tab. 4.4.

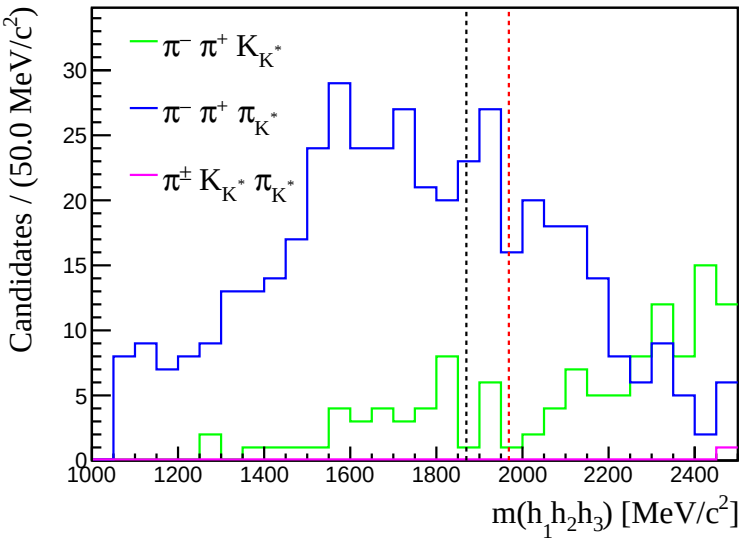

Figure 4.9: Invariant-mass distributions of three-body combinations of the final-state tracks, which are used to search for background from $B^0_{(s)} \to D^-_{(s)}h^+$ decays. The black and red dashed lines correspond to the masses of the D^- and D^-_s mesons, respectively.

For example, there are only three permutations of three body $D^\pm_{(s)}$ decays: $D^\pm_{(s)} \to h^\pm \pi_{K^{*0}} K_{K^{*0}}$, $D^\pm_{(s)} \to h^\pm h^\mp K^\pm_{K^{*0}}$ and $D^\pm_{(s)} \to h^\pm h^\mp \pi^\pm_{K^{*0}}$, where the K^{*0} subscript denotes that the particle is originally reconstructed as the child of the K^{*0} meson. Figure 4.9 displays the invariant-mass distribution in each case from which it is clear there are no peaks. No evidence for this type of background is found.

4.3.2 Charmless B decays

The background from charmless B^0 decays is significantly reduced by removing candidates with a D-meson flight-distance significance less than 0.5. However, as previously mentioned, residual amounts of charmless events can remain in the sample. These are particularly problematic because they cannot be distinguished from signal in the invariant-mass fit, and since they will be distributed differently across the Dalitz plot, can result in incorrect CP-violation observables.

The number of charmless decays in the sample is estimated through an unbinned likelihood fit to the B^0 invariant-mass distributions of candidates which lie in the sidebands of the reconstructed D mass, where $m(K^0_S\pi^+\pi^-) \in [1915, 2000]\,\text{MeV}/c^2$

and $m(K^0_S K^+ K^-) \in [1750, 1815]\,\text{MeV}/c^2$. The different regions for the two D-decay channels are chosen to remove residual contributions from misidentified $D \to K^0_S K^+ \pi^-$ decays. In the fits, all selection criteria are applied to the candidates, including a requirement on an alternative BDT which is trained without mass-constrained or `DecayTreeFitter` variables, which remove the sideband of the D-meson mass distribution.

Figure 4.10 displays the fits to the candidates for both D-decay modes and K^0_S reconstruction categories. The green peak in each plot corresponds to charmless B^0_s decays which are a background and do not impact the *CP*-violation observables. No significant charmless B^0 decay contribution is found in the $D \to K^0_S K^+ K^-$ channel, with fitted yields of 0 ± 2 and 2 ± 3 in the LL and DD categories respectively. In the $D \to K^0_S \pi^+ \pi^-$ decay channel the yields are determined to be 6 ± 5 and 11 ± 7. After correcting for the expected amount of signal candidates in the fit which leak into the D-mass sideband using the selection efficiency from simulation and the signal yield determined in Sec. 4.4, the estimated charmless yields are 5 ± 5 (LL) and 8 ± 7 (DD). The yields are consistent with zero, but to be conservative a systematic uncertainty is assigned as discussed in Sec. 4.6.

4.4 Global invariant-mass fit

A two-stage fitting strategy is employed to determine the *CP*-violation observables. Both stages involve an unbinned maximum likelihood fit to the invariant-mass distribution of candidates in the range $m(DK^{*0}) \in [5.2, 5.8]\,\text{GeV}/c^2$. The first stage is a *global* fit to the candidates integrated over the D-decay phase space to determine the values of various floating parameters so they can be fixed at the second stage, which distinguishes between candidates in different regions of the Dalitz plot. The former is the subject of this section, whilst the latter is discussed in Sec. 4.5.

The global fit is simultaneously performed to the data divided into four categories, given by the two D decays and the two K^0_S reconstruction types. This is because various parameters are common (different) between all categories, for example

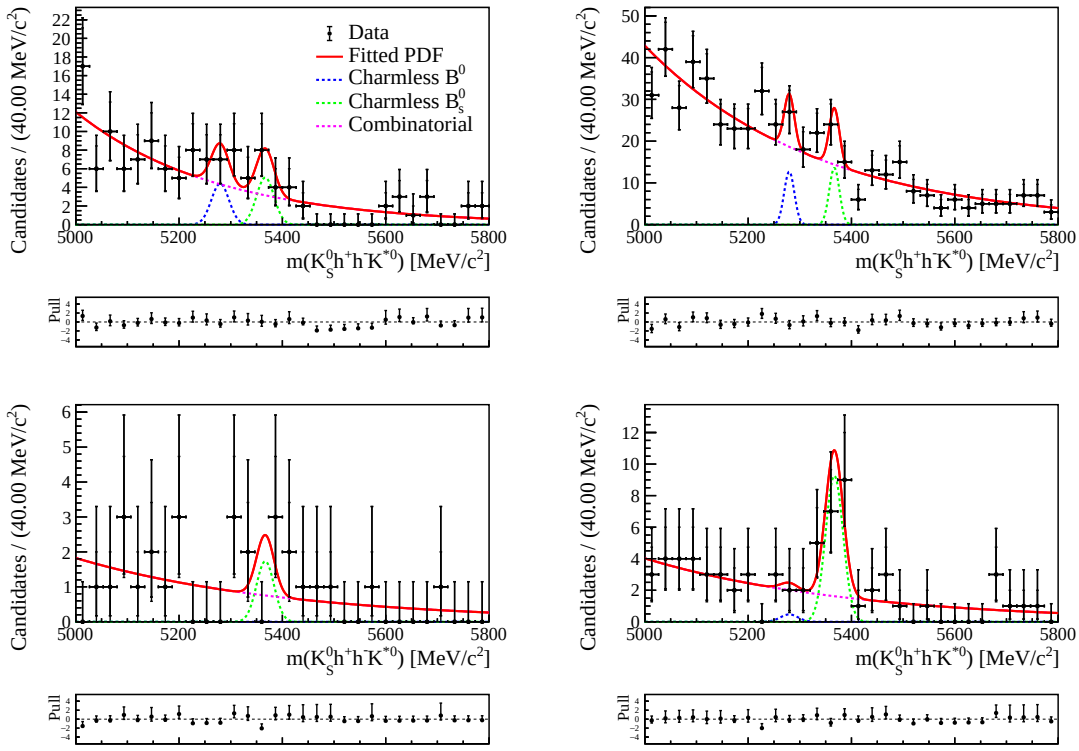

Figure 4.10: Fit to the invariant mass of charmless B-decay candidates which lie in the sideband of the $K^0_S h^+ h^-$ mass. The fits to (top) $K^0_S \pi^+ \pi^-$ and (bottom) $K^0_S K^+ K^-$ candidates are displayed, where the K^0_S is reconstructed using (left) *LL* and (right) *DD* tracks.

the mean (resolution) of the distribution which models the signal. The fit model contains six components which are discussed in the following sections.

4.4.1 Fit components

4.4.1.1 Signal and $\overline{B}^0_s \to D^0 K^{*0}$ decays

The largest physics background in the sample originates from $\overline{B}^0_s \to DK^{*0}$ decays, where the yield is particularly large because it has a branching fraction ∼10 times larger than signal, and has an identical topology which results in a high reconstruction efficiency. In principle, the $\overline{B}^0_s \to DK^{*0}$ decays can also be used to measure γ, however the amplitude ratio is $r_{B^0_s} \sim 0.02$, and thus the limited interference between the two final-state paths leads to a low sensitivity. In the remainder of this chapter, the interference in $\overline{B}^0_s \to DK^{*0}$ decays is neglected

and the background is referred to as $\overline{B}{}^0_s \to D^0 K^{*0}$, where the flavour of the D^0 meson is specified.

The $\overline{B}{}^0_s \to D^0 K^{*0}$ decays appears to meet the criteria for a control channel. However, the yield in certain regions of D-decay phase space is currently too low to precisely measure the F_i. In the future, a simultaneous fit of the $B^0 \to DK^{*0}$ and $\overline{B}{}^0_s \to D^0 K^{*0}$ decays could be explored.

Due to their identical topologies, the signal and $\overline{B}{}^0_s \to D^0 K^{*0}$ decays are represented by the same shape in the global fit, which is a Gaussian modified to have an asymmetric core and tails. The corresponding PDF is

$$f(m) = \begin{cases} \exp(-\delta m^2(\frac{1+\beta\delta m^2}{f_{\mathrm{L}}})), & \delta m < 0 \\ \exp(-\delta m^2(\frac{1+\beta\delta m^2}{f_{\mathrm{R}}})), & \delta m > 0 \end{cases} \quad \text{where} \quad \begin{array}{c} \delta m = m - \mu, \\ f_{\mathrm{L}} = 2\sigma_{\mathrm{L}}^2 + \alpha_{\mathrm{L}}(m-\mu)^2, \\ f_{\mathrm{R}} = 2(\frac{\sigma_{\mathrm{L}}}{r_\sigma})^2 + \alpha_{\mathrm{R}}(m-\mu)^2, \end{array} \tag{4.7}$$

where m is the invariant mass, μ is the mean, β is the overall asymmetry, $\alpha_{\mathrm{L,R}}$ parameterise the left- and right-sided tails, σ_{L} describes the left-sided width and r_σ is the ratio between the widths of the left and right sides.

The values of these parameters are determined by fitting Eq. 4.7 to a combined sample of simulated $B^0 \to [K^0_{\mathrm{S}}\pi^+\pi^-]_D K^{*0}$ and $B^0 \to [K^0_{\mathrm{S}} K^+ K^-)]_D K^{*0}$ decays, which have similar B^0 invariant-mass distributions due to the D-mass constraint. A simultaneous fit is performed to candidates in MC where the K^0_{S} meson is reconstructed with LL and DD tracks, and where the yields are weighted to those in data. The two K^0_{S}-meson track categories share all parameters except the resolution σ_{L}. The fit projections are displayed in Fig. 4.11 and the parameter values can be found in Tab. 4.5.

The pulls in Fig. 4.11 display a small beating pattern around the mean because the actual simulated signal yield in the fit is large, around three hundred thousand candidates, which the PDF cannot precisely model. A number of alternative shapes are tried but no improvement is found. To be conservative, a systematic uncertainty is assigned using the best alternative model as described in Sec. 4.6. As

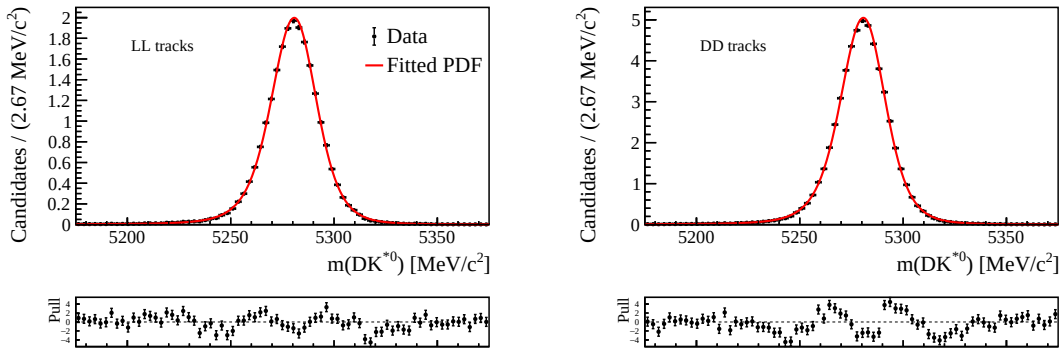

Figure 4.11: Fits to signal candidates in simulation using the modified Gaussian function described by Eq. 4.7, where the K^0_S mesons are reconstructed with (left) *LL* and (right) *DD* tracks.

Table 4.5: Values of the parameters describing the modified Gaussian function in Eq. 4.7 determined in a fit to simulated signal decays.

Parameter	Fitted value
μ	(5280.76 ± 0.05) MeV/c^2
σ_{L}^{DD}	(10.63 ± 0.04) MeV/c^2
σ_{L}^{LL}	(10.70 ± 0.05) MeV/c^2
r_σ	0.961 ± 0.006
α_{L}	0.1413 ± 0.0008
α_{R}	0.1174 ± 0.0007
β	$(-8.3 \pm 3.1) \times 10^{-7}$

a further cross-check, the pull plots produced by overlaying the signal shape with the invariant-mass distribution of randomly sampled candidates in MC with yields similar to those found in data are examined, and a good agreement is found.

To account for alignment and resolution differences between data and simulation, the mean and width parameters are afforded some freedom in the fit to data. Specifically, the mean of the PDF describing $\overline{B}{}^0_s \to D^0 K^{*0}$ decays is a free parameter, whilst that of signal is fixed using the known mass difference $\Delta m = m_{B^0_s} - m_{B^0} = (87.42 \pm 0.14)\,\mathrm{MeV}/c^2$ [92]. In addition, the signal and $\overline{B}{}^0_s \to D^0 K^{*0}$ decays share the floating width parameter σ_{L}, which is different for K^0_S mesons reconstructed with *LL* and *DD* tracks. All other parameters are fixed to the values in Tab. 4.5.

4.4.1.2 Combinatorial background

The combinatorial background is modelled with an exponential function whose slope and yield are free parameters in each category given by the D-meson decay and K^0_S-meson track type.

4.4.1.3 Partially reconstructed $B^0_{(s)} \to D^* K^{*0}$ decays

The dominant background in the low-mass region is from $B^0 \to D^* K^{*0}$ and $\overline{B}^0_s \to D^{*0} K^{*0}$ decays with $D^* \to DX$, where X is an unreconstructed π^0 or γ. The former are particularly problematic because they are *CP* violating and the hadronic parameters of the decay are unknown, so a potentially large systematic uncertainty would be associated with modelling their Dalitz plot distribution in the second fitting stage. To mitigate this potential uncertainty, the lower boundary in the fits is chosen to be 5.2 GeV/c^2, which removes almost all of the $B^0 \to D^* K^{*0}$ decays and a significant fraction of $\overline{B}^0_s \to D^{*0} K^{*0}$ decays.

Through conservation of four momentum, it can be shown that the invariant mass of the DK^{*0} combination is given by

$$m^2_{DK^{*0}} = m^2_D + m^2_{K^{*0}} + 2E_D E_{K^{*0}} + 2|p_D||p_{K^{*0}}| \cos\theta^*_{D^*}, \tag{4.8}$$

which is dependent on the angular distribution of the D meson produced in the D^* decay through the helicity angle, $\theta^*_{D^*}$. The angular distributions depend on the helicity of the D^* meson and the spin of the missing particle, which can be a π^0 meson with $J^P = 0^-$ or a γ with $J^P = 1^-$.

Recall the B^0 and B^0_s are pseudoscalar mesons, so the initial state has zero angular momentum. Therefore, the angular momentum of the D^* and K^{*0} vector mesons in the final state must cancel. So, there are two possibilities: they can both be longitudinally polarised, or they can have opposite transverse polarisations. In both cases, the D^* and K^{*0} have the same helicity values because they have equal and opposite momentum in the rest frame of the B meson. Specifically, the helicities are $\lambda = 0$ in the first scenario and $\lambda = \pm 1$ in the second.

Consider the case of a D^* meson with $\lambda = 0$ decaying into the $D\pi^0$ final state. The angular distribution of the D meson is $\propto \cos^2(\theta^*_{D^*})$ and therefore is preferentially produced with $\theta^*_{D^*} = 0$ or π. From Eq. 4.8, this results in a quadratic mass distribution with a minimum at $C \equiv m_D^2 + m_{K^{*0}}^2 + 2E_D E_{K^{*0}}$, and well defined end points, denoted $a \equiv m_D^2 + m_{K^{*0}}^2 + 2E_D E_{K^{*0}} - 2|p_D||p_{K^{*0}}|$ and $b \equiv m_D^2 + m_{K^{*0}}^2 + 2E_D E_{K^{*0}} + 2|p_D||p_{K^{*0}}|$. The quadratic function is combined with Gaussian and linear terms to account for the effects of detector resolution and selection efficiency, respectively, such that the PDF is given by

$$f(m) = \int_a^b dm(m - \frac{a+b}{2})^2 \mathrm{DG}(m|\mu, \sigma, f, r)\mathrm{L}(m|a, b, \xi), \tag{4.9}$$

where

$$\mathrm{DG}(m|\mu, \sigma, f, r) = f\mathrm{G}(m|\mu, \sigma) + (1-f)\mathrm{G}(m|\mu, r\sigma), \tag{4.10}$$

$$\mathrm{L}(m|a, b, \xi) = \frac{1}{b-a}\left[(1-\xi)m + (b\xi - a)\right]. \tag{4.11}$$

In the above equations $\mathrm{G(m}|\mu, \sigma)$ is a Gaussian with mean μ and width σ.

In the case of a D^* meson with $\lambda = \pm 1$ decaying into the $D\pi^0$ final state the angular distribution of the D meson is $\propto \sin^2\theta^*_{D^*}$. Using the same logic as above this results in a mass distributions which is a single peaked quadratic, with a maximum at C and minima at the end points a and b. The PDF is given by

$$f(m) = \int_a^b dm\left[-(m-a)(m-b)\right]\mathrm{DG}(m|\mu, \sigma, f, r)\mathrm{L}(m|a, b, \xi). \tag{4.12}$$

The D mesons produced in $D^* \to D\gamma$ decays, where the helicity of the D^* is 0, share the same angular distribution and therefore are also modelled by the above PDF.

Finally, in the case of a D^* with $\lambda = \pm 1$ decaying into the $D\gamma$ final state the angular distribution of the D meson is $\propto 1 + \cos^2\theta^*_{D^*}$. Therefore, the mass distribution will be the same quadratic in Eq. 4.9 summed with a constant term, such that the PDF is

$$f(m) = \int_a^b dm\left[(m - \frac{a+b}{2})^2 + (\frac{a-b}{2})^2\right]\mathrm{DG}(m|\mu, \sigma, f, r)\mathrm{L}(m|a, b, \xi). \tag{4.13}$$

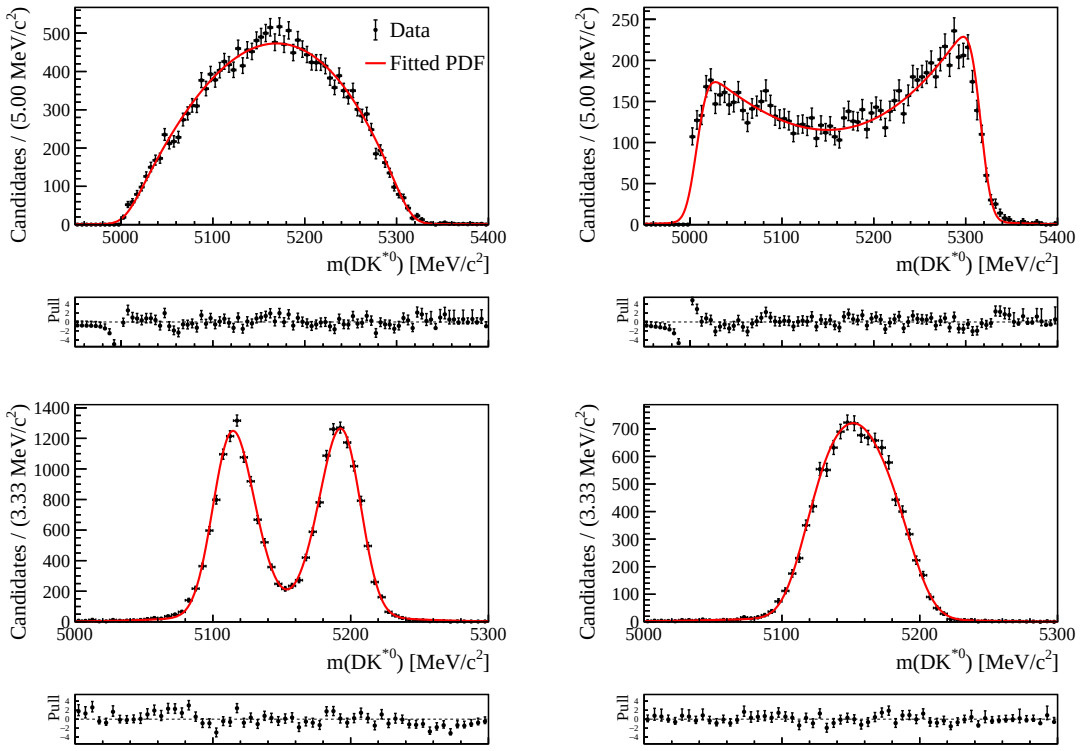

Figure 4.12: Fits to partially reconstructed $B^0 \to D^* K^{*0}$ decays in simulation using the PDFs described in the text where the helicity of the D^* is (left) 0 or (right) ± 1, and the particle missed in the reconstruction is a (top) γ or (bottom) π^0.

Due to their different mass shapes, the backgrounds from the partially reconstructed $B^0 \to D^* K^{*0}$ decays are divided into the four categories outlined above in the global mass fit. The values of the parameters describing the PDFs are fixed in the global fit, and are determined using simulated $B^0 \to D^* K^{*0}$ decays with $D \to K^0_S \pi^+ \pi^-$, where candidates reconstructed using the two K^0_S-meson track categories are combined. The fits to MC for each category are displayed in Fig. 4.12, and the corresponding values of the parameters are displayed in Tab. 4.6. In the global fit, the shapes of the $\overline{B}^0_s \to D^{*0} K^{*0}$ decay backgrounds are identical to those of the $B^0 \to D^* K^{*0}$ decays, but the end points, a and b, are shifted by Δm.

The fit is unable to accurately determine the yield of the 8 categories of $B^0 \to D^* K^{*0}$ and $\overline{B}^0_s \to D^{*0} K^{*0}$ decays because their mass distributions overlap. Instead, the total yield of the partially reconstructed decay is fixed relative to the fully reconstructed equivalent, and the relative contribution of each category given by

Table 4.6: Values of the parameters describing the PDFs outlined in the text for partially reconstructed $B^0 \to D^*K^{*0}$ decays, where the D^* has a helicity, λ, and decays to a D meson and an unreconstructed γ or π^0 meson. The parameter values are determined in a fit to simulated $B^0 \to D^*K^{*0}$ decay candidates. The parameters a, b and σ have units of MeV/c^2, whilst the others are dimensionless.

	$D^* \to D\gamma$		$D^* \to D\pi^0$	
	$\lambda = 0$	$\lambda = 1$	$\lambda = 0$	$\lambda = 1$
a	5002.7 ± 0.5	5001.4 ± 0.3	5104.62 ± 0.08	5107.8 ± 0.4
b	5311.9 ± 0.4	5314.0 ± 0.2	5202.91 ± 0.08	5206.3 ± 0.04
f	0.9717 ± 0.0012	0.869 ± 0.005	0.9364 ± 0.0010	0.9725 ± 0.0010
r	13.8 ± 1.3	17.0 ± 1.9	8.28 ± 0.15	9.6 ± 0.3
ξ	0.666 ± 0.015	0.690 ± 0.009	0.941 ± 0.007	1.55 ± 0.03
σ	15.1 ± 0.4	13.1 ± 0.2	12.52 ± 0.05	13.2 ± 0.3

the D^*-meson helicity and missed particle, are fixed in the global fit. Specifically, the following ratios are used:

- $r_L^{(s)}$ - the fraction of candidates originating from a D^* with $\lambda = 0$,
- $r_{\gamma,\lambda}^{(s)}$ - the fraction of $D^* \to D\gamma$ where the D^* has helicity, λ,
- $R^{(s)}$ - the total partially reconstructed yield with respect to its fully reconstructed counterpart,

such that the total PDF for partially reconstructed $B_{(s)} \to D^*K^{*0}$ decays is given by

$$N(B_{(s)} \to DK^{*0})R^{(s)} \left[r_L^{(s)} f_0(m) + (1 - r_L^{(s)}) f_{\pm 1}(m) \right], \tag{4.14}$$

where

$$f_\lambda(m) = r_{\gamma,\lambda}^{(s)} f_\lambda^\gamma(m) + (1 - r_{\gamma,\lambda}^{(s)}) f_\lambda^{\pi^0}(m), \tag{4.15}$$

and $f_\lambda^X(m)$ is the PDF for the final state where the D^* has helicity, λ, and the particle, X, is missed in the reconstruction.

The fraction of longitudinally polarised D^* mesons, r_L, is a priori unknown, so it is necessary to determine the value from data. This is achieved in Ref. [96], where

Table 4.7: Values of the ratios describing the relative yields of the different categories of partially reconstructed $B^0 \to D^* K^{*0}$ and $\overline{B}{}^0_s \to D^{*0} K^{*0}$ decays. Each ratio is defined in the text.

Parameter	$B^0 \to D^* K^{*0}$	$\overline{B}{}^0_s \to D^{*0} K^{*0}$
r_L	0.884 ± 0.015	0.736 ± 0.024
$r_{\gamma,0}$	0.824 ± 0.007	0.536 ± 0.009
$r_{\gamma,1}$	0.992 ± 0.002	0.851 ± 0.005
R	0.035 ± 0.002	0.219 ± 0.005

a fit is performed to the invariant-mass distribution of $B^0 \to DK^{*0}$ candidates with $D \to K\pi$, and the lower boundary is 5 GeV/c^2. Requiring that the D decay is reconstructed in the $K^+\pi^-$ final state significantly reduces the overlapping contributions from partially reconstructed $\overline{B}{}^0_s \to D^{*0} K^{*0}$ decays due to CKM suppression, and allows clean extraction of r_L and R. The inverse scenario is also true, where reconstructing the $D \to K^-\pi^+$ decay allows determination of r_L^s and R^s.

The fit in Ref. [96] still has 4 overlapping components, and therefore cannot accurately measure $r^{(s)}_{\gamma,\lambda}$. Instead, they are determined using the selection efficiencies from simulation and the $D^* \to DX$ decay branching fractions from the PDG. The value of each parameter used in this measurement, after correcting for the reduced fit range by integrating over the PDFs, is given in Tab. 4.7.

Each parameter taken from Ref. [96] is given by a ratio of yields, and therefore, to first order, differences in selection from this measurement will cancel, even if different D decays are used. However, it is possible that the differences can change the invariant-mass distributions of the four overlapping components, which would alter the ratios. A study is performed comparing the invariant-mass distributions of $B^0 \to D^*(\to D(\to K\pi)X)K^{*0}$ and $B^0 \to D^*(\to D(\to K^0_S\pi^+\pi^-)X)K^{*0}$ decays in MC. The two distributions are found to be in good agreement, and the ratio between them is determined to be flat with no trends for each partially reconstructed category.

4.4.1.4 Misidentified $B^0 \to D\pi^+\pi^-$ decays

The tight PID requirement of $\mathrm{DLL}_{K\pi} > 5$ on the kaon from the K^{*0} candidate reduces background from misidentified $B^0 \to \overline{D}{}^0\pi^+\pi^-$ decays, but a small amount remains in the sample. They are modelled by the sum of two Crystal Ball functions [97] with a common mean,

$$f\ \mathrm{CB}(m|\mu, \sigma_L, \alpha_L, n_L) + (1-f)\ \mathrm{CB}(m|\mu, r\sigma_L, \alpha_R, n_R), \tag{4.16}$$

where f is the fraction of the first function. The Crystal Ball has a Gaussian core with mean, μ, and width, σ, and power law tails with exponent, n, above a threshold dictated by the parameter α. These parameters are fixed in the global fit to the values determined in Ref. [96], where a fit to a simulated sample of $B^0 \to \overline{D}{}^0\pi^+\pi^-$ decays with $D \to K\pi$ is performed. The fit is reproduced in Fig. 4.13 and the corresponding parameters are provided in Tab. 4.8.

The $B^0 \to \overline{D}{}^0\pi^+\pi^-$ decay yield is fixed in the global fit relative to that of the $\overline{B}{}^0_s \to D^0K^{*0}$ decays. The ratio is a floating parameter in the invariant-mass fit described in Ref. [96] and the value, $R_{D\pi^+\pi^-} = 0.016 \pm 0.004$, is used directly in this analysis. Given the studies described in the previous section for partially reconstructed $B^0_{(s)} \to D^*K^{*0}$ decays, it is assumed that the PDF and ratio are not altered by the different D-decay selections.

4.4.1.5 $B^\pm \to DK^\pm$ decays

A background is present from $B^+ \to DK^+$ decays combined with a random charged pion. These could be effectively removed by vetoing the region around $m(B^+)$ in the reconstructed mass of the DK^+ system. However, studies performed in Ref. [89] determined that such a requirement removes most of the candidates from the high-mass region, which are necessary to accurately model the combinatorial background slope. Therefore, the $B^+ \to DK^+$ candidates are modelled in the global fit.

The $B^+ \to DK^+$ background candidates are represented by a Crystal Ball function where the values of the parameters are fixed to those determined in

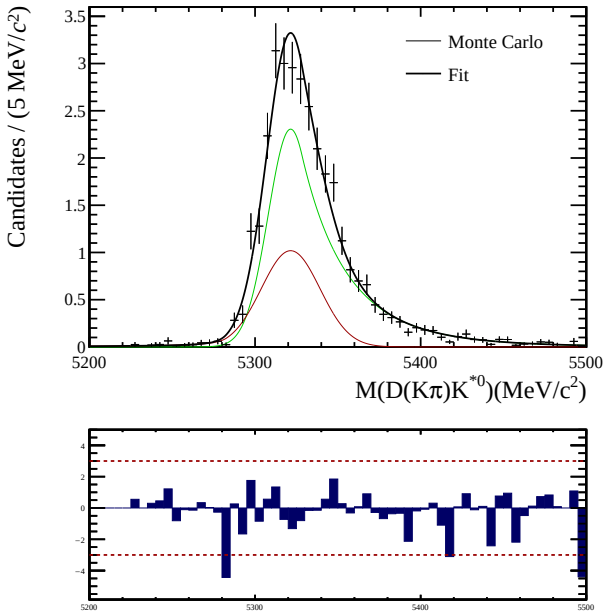

Figure 4.13: Fit to simulated $B^0 \to \overline{D}^0\pi^+\pi^-$ decays using the sum of two Crystal Ball functions.

Table 4.8: Values of the parameters describing the sum of two Crystal Ball functions determined in a fit to simulated $B^0 \to \overline{D}^0\pi^+\pi^-$ decays. Each parameter is defined in the text.

Parameter	Value
μ	(5321.5 ± 2.9) MeV/c^2
σ_L	(18 ± 4) MeV/c^2
r	0.76 ± 0.24
α_L	2.2 ± 0.6
α_R	-0.50 ± 0.3
n_L	1 (fixed)
n_R	9 ± 5
f	0.3 ± 0.3

simulation. The parameter values are displayed in Tab. 4.9 and the corresponding fit is shown in Fig. 4.14.

The $B^+ \to DK^+$ decay yield is constrained to that of the $\overline{B}{}^0_s \to D^0K^{*0}$ decay candidates using the ratio

$$R_{DK^+} = \frac{\varepsilon(B^+ \to DK^+)}{\varepsilon(\overline{B}{}^0_s \to D^0K^{*0})} \frac{\mathcal{B}(B^+ \to DK^+)}{\mathcal{B}(\overline{B}{}^0_s \to D^0K^{*0})} \frac{f_u}{f_s}, \tag{4.17}$$

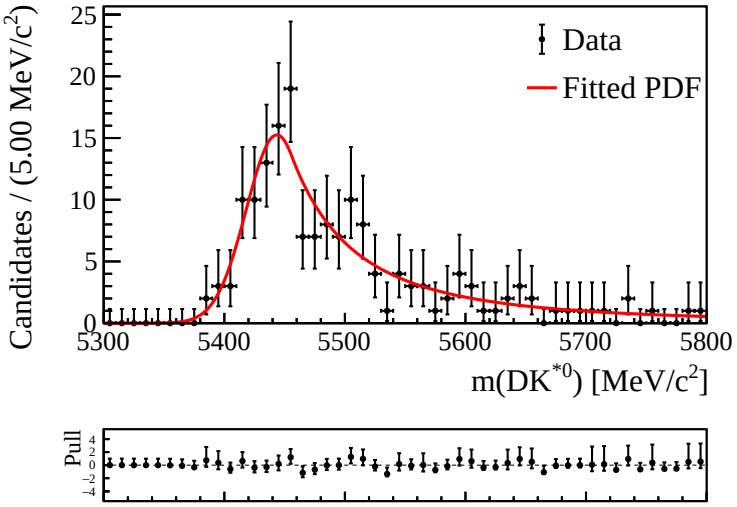

Figure 4.14: Fit to simulated $B^+ \to DK^+$ decays using a Crystal Ball function.

Table 4.9: Values of the parameters describing a Crystal Ball function determined in a fit to simulated $\overline{B} \to DK^+$ decays.

Parameter	Value
μ	5442.7 $\pm$ 4.2 MeV/c^2
σ	23.6 $\pm$ 2.8 MeV/c^2
α	-0.39 $\pm$ 0.13
n	2.5 $\pm$ 1.5

where ϵ is the selection efficiency, $\mathcal{B}$ is the PDG branching fraction and $f_s(f_u)$ is the probability for a b quark to hadronise into a B_s^0 (B^+) meson. Due to isospin symmetry, it is assumed that $f_u \simeq f_d$, and therefore the ratios $f_s/f_d = 0.256 \pm 0.020$ at $\sqrt{s} = 7\,\text{TeV}$ [98] and $\frac{f_s/f_d\ (13\,\text{TeV})}{f_s/f_d\ (7\,\text{TeV})} = 1.064 \pm 0.008$ [99] measured by the LHCb collaboration are used for data collected in runs 1 and 2, respectively.

The efficiencies of the selection criteria, excluding the tight PID requirements, are estimated in simulation for both $B^+ \to DK^+$ and $\overline{B}_s^0 \to D^0 K^{*0}$ decays. As discussed in Sec. 3.3.1.1, a calibration data sample is required to accurately estimate the efficiency of PID requirements because they are particularly sensitive to the experimental conditions, which are too computationally expensive to include in the simulation. For example, the gas inside the RICH detectors is not fixed at

a particular pressure and therefore it can vary between data taking runs. The general principle behind the procedure is as follows. The PID likelihood assigned to a particular track is highly dependent on its momentum, p, and pseudorapidity, η. Therefore, to estimate the efficiency of a PID requirement, the kinematic distributions in the calibration sample must be reweighted to match those of the tracks in $\overline{B}{}^0_s \to D^0 K^{*0}$ and $B^+ \to DK^+$ decays. Practically, this is achieved by dividing the two-dimensional phase space, given by p and η, into regions. The efficiency in a particular region is predetermined in the calibration sample, ε_i, and therefore the average PID efficiency in the sample of interest is given by

$$\overline{\epsilon} = \frac{\Sigma_i \epsilon_i w_i C_i}{\Sigma_i w_i C_i}, \tag{4.18}$$

where w_i and C_i are the kinematic weight and calibration sample signal yield in region, i, respectively.

Clearly, the PID efficiency is dependent upon the division in p and η. The default scheme has 5 uniform regions between $2 < \eta < 5.5$ and 19 regions in p, with boundaries at 2, 9.3, 15.6 and 19 GeV/c, then 16 uniform regions between 19 and 100 GeV/c. The first few boundaries correspond to the momentum thresholds of the kaons in the RICH detectors. A systematic uncertainty is estimated using three alternative divisions, which is determined to be 0.2% for $\overline{B}{}^0_s \to D^0 K^{*0}$ decays and 0.4% for $B^+ \to DK^+$ decays. An additional pre-estimated systematic uncertainty of 0.2% is included to account for the efficiencies, ε_i, determined in the calibration sample. The total systematic uncertainty is small in comparison to the statistical uncertainty associated with $\overline{B}{}^0_s \to D^0 K^{*0}$ and $B^+ \to DK^+$ simulation samples.

The total selection efficiency is determined separately in categories of data-taking period and magnet polarity, before being combined to determine a value for runs 1 and 2, as displayed in Tab. 4.10. Then, an average of the efficiencies, weighted by the number of $\overline{B}{}^0_s \to D^0 K^{*0}$ decays collected in runs 1 and 2, is performed to determine $R_{DK^+} = 0.031 \pm 0.006$.

Table 4.10: Rate of $B^+ \to DK^+$ and $\overline{B}{}^0_s \to D^0 K^{*0}$ decays passing various selection criteria. The efficiencies for the trigger, core (Sec. 4.2.1), BDT (Sec.4.2.2), PID and multiple event-selection requirements are displayed. Each efficiency is estimated using simulation, excluding that of the PID requirements which is determined in data as described in the text.

Decay	Run	ϵ_{trig} (%)	ϵ_{core} (%)	ϵ_{PID} (%)	ϵ_{BDT} (%)	Multiple candidates (%)	ϵ_{tot} (%)
$B^+ \to DK^+$	1	0.400 ± 0.003	1.84 ± 0.11	72.7 ± 1.9	47 ± 4	0	0.0025 ± 0.0003
$B^+ \to DK^+$	2	0.633 ± 0.003	1.54 ± 0.05	82.5 ± 2.1	50 ± 2	0.7 ± 0.5	0.004 ± 0.0002
$\overline{B}{}^0_s \to D^0 K^{*0}$	1	1.68	16.35 ± 0.09	79.8 ± 0.5	93.61 ± 0.17	0.71 ± 0.09	0.2036 ± 0.0017
$\overline{B}{}^0_s \to D^0 K^{*0}$	2	2.61	16.12 ± 0.09	84.8 ± 0.4	92.79 ± 0.18	0.76 ± 0.08	0.3285 ± 0.0026

4.4.2 Global fit results

To summarise, the global fit is performed simultaneously to the data divided into four categories given by the D-decay mode and the type of tracks used to reconstruct the K^0_{S} meson. In total, there are 7 fit components: signal and 6 backgrounds, each of which is described in the previous section. The fit projections for each of the categories are displayed in Fig. 4.15, and Tab. 4.11 details the fitted values of the floating parameters and their uncertainties.

The total signal yield is 469 ± 34, and the total $\overline{B}{}^0_s \to D^0 K^{*0}$ decay yield is 1176 ± 42. This corresponds to a ratio of $N(\overline{B}{}^0_s \to D^0 K^{*0})/N(B^0 \to DK^{*0}) = 2.5 \pm 0.2$. This ratio is in good agreement with the prediction given the fragmentation and branching fractions and assuming the two channels have the same selection efficiencies, 2.6 ± 0.5. Furthermore, the figures highlight the effectiveness of the BDT in reducing the combinatorial background, and the signal purity in a 30 MeV/c^2 window either side of the B^0 mean is $(57 \pm 5)\%$. Finally, it is clear that the choice of lower fit boundary removes a significant fraction of partially reconstructed $B^0 \to D^* K^{*0}$ decays such that only around 10 candidates remain in the sample.

4.5 Phase-space fit

To determine the *CP*-violation observables, a simultaneous fit is performed to the invariant-mass distribution of the candidates in 80 categories, given by the two types of track used to reconstruct the K^0_{S} mesons, the flavour of the B^0 meson

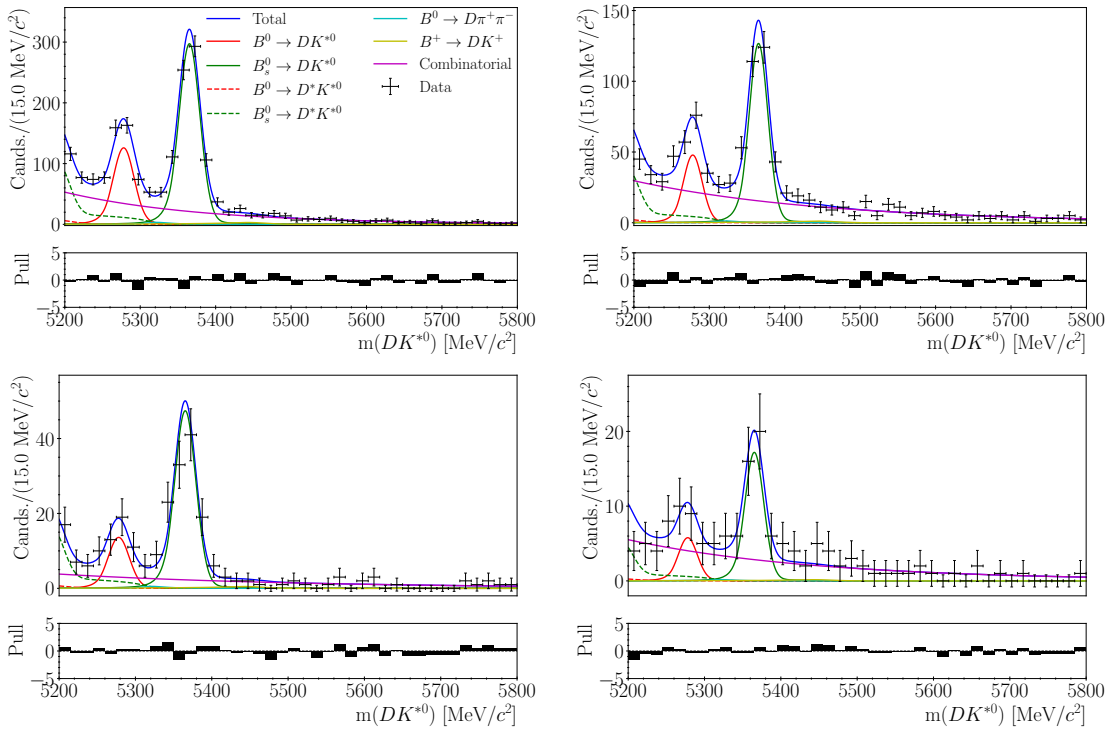

Figure 4.15: Invariant-mass distributions of $B^0 \to DK^{*0}$ candidates with (upper) $D \to K^0_S\pi^+\pi^-$ and (lower) $D \to K^0_S K^+K^-$ decays, separated by the (left) DD and (right) LL K^0_S mesons. The data are overlaid with the global fit projection.

given the charge of the kaon, and the 16 and 4 regions of $D \to K^0_S\pi^+\pi^-$ and $D \to K^0_S K^+K^-$ decay phase space, respectively.

4.5.1 Fit setup

The same model is used as in the global fit, so the shape of each component is fixed and is assumed not to vary across the Dalitz plot. This assumption is found to be valid by comparing the mass distribution in signal MC in each region of D-decay phase space.

The yield of each component, excluding the combinatorial background, in a region of D-decay phase space is given by the Dalitz plot integrated yield of that component multiplied by the expected fraction of candidates in a particular region. The integrated signal and $\overline{B}{}^0_s \to D^0K^{*0}$ decay yields are floating parameters in 8 categories given by the D-decay mode, the type of tracks used to reconstruct the K^0_S meson, and the flavour of the B^0 meson. The integrated yields of the background

Table 4.11: Fitted values of the floating parameters in the global fit.

Parameter	Value
$D \to K^0_S\pi^+\pi^-$ with LL tracks	
Signal yield	109 ± 18
$\overline{B}^0_s \to D^0K^{*0}$ yield	285 ± 22
Combinatorial yield	440 ± 37
Combinatorial slope	$(-0.0039 \pm 0.0004)\ (\mathrm{MeV}/c^2)^{-1}$
$D \to K^0_S\pi^+\pi^-$ with DD tracks	
Signal yield	312 ± 27
$\overline{B}^0_s \to D^0K^{*0}$ yield	733 ± 32
Combinatorial yield	598 ± 47
Combinatorial slope	$(-0.0055 \pm 0.0004)\ (\mathrm{MeV}/c^2)^{-1}$
$D \to K^0_SK^+K^-$ with LL tracks	
Signal yield	13 ± 6
$\overline{B}^0_s \to D^0K^{*0}$ yield	39 ± 8
Combinatorial yield	82 ± 13
Combinatorial slope	$(-0.004 \pm 0.008)\ (\mathrm{MeV}/c^2)^{-1}$
$D \to K^0_SK^+K^-$ with DD tracks	
Signal yield	35 ± 9
$\overline{B}^0_s \to D^0K^{*0}$ yield	119 ± 13
Combinatorial yield	63 ± 17
Combinatorial slope	$(-0.0028 \pm 0.0014)\ (\mathrm{MeV}/c^2)^{-1}$
Shared	
$\overline{B}^0_s \to D^0K^{*0}$ mean	$(5365.7 \pm 0.5)\,\mathrm{MeV}/c^2$
Signal and $\overline{B}^0_s \to D^0K^{*0}$ width (LL tracks)	$(11.6 \pm 0.9)\,\mathrm{MeV}/c^2$
Signal and $\overline{B}^0_s \to D^0K^{*0}$ width (DD tracks)	$(12.7 \pm 0.5)\,\mathrm{MeV}/c^2$

components are fixed relative to those of signal and $\overline{B}^0_s \to D^0K^{*0}$ decays using the ratios described in Sec. 4.4.1.3-4.4.1.5, similarly to the global fit.

The signal yields in each region of phase space are parametrised by Eqs. 4.4 and 4.5, where the *CP*-violation observables are shared between all categories, κ is fixed to $\kappa = 0.958^{+0.005}_{-0.046}$ [40], and the F_i, c_i and s_i parameters are fixed to the

values in Tab. 4.1. As a reminder, the normalisation constants h and $\bar{h}$ in Eqs. 4.4 and 4.5 correspond to the floating integrated yields.

Due to the limited interference in $\overline{B}{}^0_s \to D^0 K^{*0}$ decays the charge of the kaon from the K^{*0} decay effectively indicates the flavour of the D^0 meson in the final state. Therefore, the $\overline{B}{}^0_s \to D^0 K^{*0}$ ($B^0_s \to \overline{D}{}^0 \overline{K}{}^{*0}$) yield in a particular region of phase space is given by the integrated yield multiplied by F_i (F_{-i}). The same applies to $\overline{B}{}^0_s \to D^{*0} K^{*0}$ decays.

Given there are few $B^0 \to D^* K^{*0}$ decays in the sample, and that their corresponding hadronic parameters are unknown, it is assumed they all decay through the $B^0 \to \overline{D}{}^{*0} K^{*0}$ decay path. Therefore, the $B^0 \to D^* K^{*0}$ ($\overline{B}{}^0 \to D^* \overline{K}{}^{*0}$) decay yield in a region of D-decay phase space is given by the integrated yield multiplied by F_{-i} (F_i). This assumption is assigned a systematic uncertainty in Sec. 4.6.11.

The two pions in $B^0 \to \overline{D}{}^0 \pi^+ \pi^-$ decays are equally likely to be misidentified as a kaon, so the two decays, $B^0 \to \overline{D}{}^0 \pi^+ \pi^-$ and $\overline{B}{}^0 \to D^0 \pi^- \pi^+$, cannot be distinguished. Therefore, the fractional yield in a region of D-decay phase space is given by $0.5(F_i + F_{-i})$.

The phase-space distribution of CP-violating $B^\pm \to DK^\pm$ decay candidates is parametrised similarly to signal. Specifically, the yields in each region are given by

$$N(B^+)_i = h^{DK^+} \left(F_{-i} + ((x_+^{DK})^2 + (y_+^{DK})^2) F_i + 2\sqrt{F_i F_{-i}} \left[x_+^{DK} c_i - y_+^{DK} s_i \right] \right), \tag{4.19}$$

$$N(B^-)_i = h^{DK^-} \left(F_i + ((x_-^{DK})^2 + (y_-^{DK})^2) F_{-i} + 2\sqrt{F_i F_{-i}} \left[x_-^{DK} c_i + y_-^{DK} s_i \right] \right), \tag{4.20}$$

where the corresponding CP-violation observables are taken from Ref. [88] and the F_i, c_i and s_i parameters are fixed to those in Tab. 4.1.

Finally, the phase-space distribution of combinatorial background is unknown, and therefore the yield is a floating parameter in each category.

4.5.2 Closure check

A closure study of the procedure is performed by generating and fitting many pseudo data samples to ensure the *CP*-violation observables are unbiased and the uncertainties are correctly estimated. The pseudo data is generated from a PDF which requires inputs for the integrated yields of each fit component. They are chosen to be those determined from the fit to data. Then, the yield of component in a region of D-decay phase space is parametrised as discussed in the previous subsection. For signal decays, this requires input values for the *CP*-violation observables, which are calculated using γ and the hadronic parameters from Ref. [39]. Finally, the combinatorial background is assumed to be produced uniformly across the Dalitz plot, such that the probability is given by the area of the relevant region of D-decay phase space.

The above procedure is performed ten thousand times with a success rate of 99.3%. The $x_\pm$ observables are found to be unbiased with correctly estimated uncertainties. However, the y_+ and y_- observables are determined to have a bias corresponding to $+13\%$ and -12% of the statistical error, respectively, and each uncertainty is underestimated by around 3%. The biases are determined to be a consequence of the small signal yields in some regions of phase space, since they become negligible when the above procedure is repeated after scaling the yields by a factor of ten. The bias on each observable, δo, is accounted for by subtracting it from the fitted value, such that $o_{\text{corr.}} = o_{\text{fit}} - \delta o$, and the default statistical uncertainties are inflated to correct for the under coverage.

Table 4.12: Statistical correlation coefficients between the *CP*-violation observables in percent.

	x_+	x_-	y_+	y_-
x_+	100	0	18	0
x_-		100	0	8
y_+			100	0
y_-				100

4.5.3 Fit results

After correcting for the biases and statistical uncertainty under coverage, the *CP*-violation observables are

$$\begin{aligned} x_+ &= 0.074^{+0.085}_{-0.086}, \\ x_- &= -0.215^{+0.088}_{-0.084}, \\ y_+ &= -0.336^{+0.108}_{-0.102}, \\ y_- &= -0.012^{+0.126}_{-0.130}, \end{aligned} \tag{4.21}$$

with the statistical correlation coefficients displayed in Tab. 4.12. In the fit, all of the common parameters between the PDFs describing B^0 and $\overline{B}^0$ decays, which are those of the mass shape, the F_i, c_i and s_i are fixed. Therefore, the PDF describing the B^0 and $\overline{B}^0$ decays can be considered approximately independent, and hence the correlations between (x_-, y_-) and (x_+, y_+) are negligible.

A visual representation of the *CP*-violation observables is displayed in Fig. 4.16. It shows the 68.3% and 95.5% statistical confidence regions around the coordinates (x_-, y_-) and (x_+, y_+), which describe the $\overline{B}^0$ and B^0 decays, respectively. Evidence for *CP* violation would be clear in this type of plot because the coordinates would be well separated. However, with the current precision, no evidence of *CP* violation is seen. Using trigonometric relations and the definitions of the *CP*-violation observables it can be shown the angle between the vectors connecting the origin with the coordinates (x_-, y_-) and (x_+, y_+) is equal to 2γ. From the plot, it is already clear that the value of γ is expected to be around 50°.

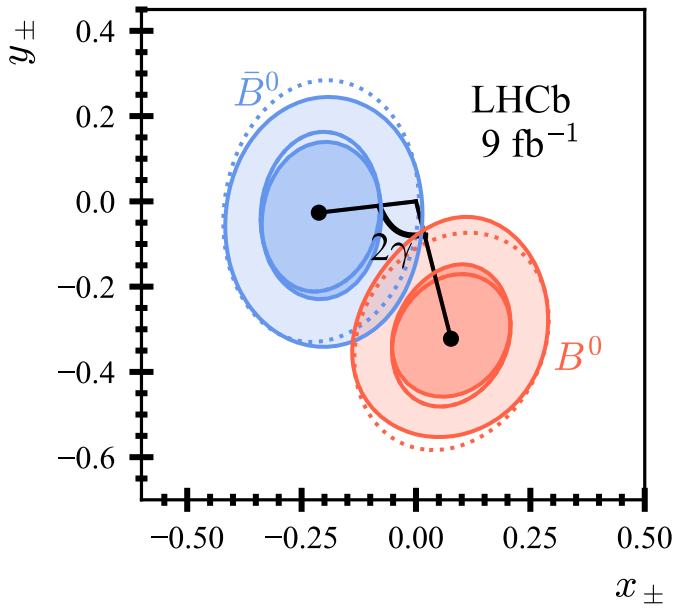

Figure 4.16: The 68.3% and 95.5% statistical confidence regions for the measured $(x_\pm, y_\pm)$ values. The orange (blue) contours correspond to the observables related to B^0 ($\overline{B}^0$) decays. A comparison is made between the confidence regions determined by scanning the likelihood function from the fit (shaded) and the assumption of Gaussian likelihoods (lines).

Confidence regions computed with two methods can be found in the plot. Firstly, the dashed lines show the regions computed assuming correlated Gaussian likelihoods for the *CP*-violation observables. They are in good agreement with the filled regions, which are determined directly from the fit by scanning over each *CP* observable with all other parameters fixed. Therefore, in Sec. 4.7, where a fit is performed to interpret γ and the hadronic parameters from the *CP*-violation observables, Gaussian likelihoods are safely assumed.

An example of the fit projections are displayed in Fig. 4.17. It compares $\overline{B}^0 \to D\overline{K}^{*0}$ decays in region with index -1 and the *CP* conjugate $B^0 \to DK^{*0}$ decays in region with index $+1$ to highlight the *CP* asymmetry, where the D meson is reconstructed in the $K^0_S\pi^+\pi^-$ final state with *LL* tracks. In contrast to the global fit, the $\overline{B}^0_s \to D^0K^{*0}$ decays appear to be suppressed relative to signal in Fig. 4.17. This is explained by noting that the probability of the $\overline{B}^0_s \to D^0K^{*0}$ decay falling in region $i = 1$ is $F_1 = 0.022 \pm 0.0006$, whereas the dominant contribution in

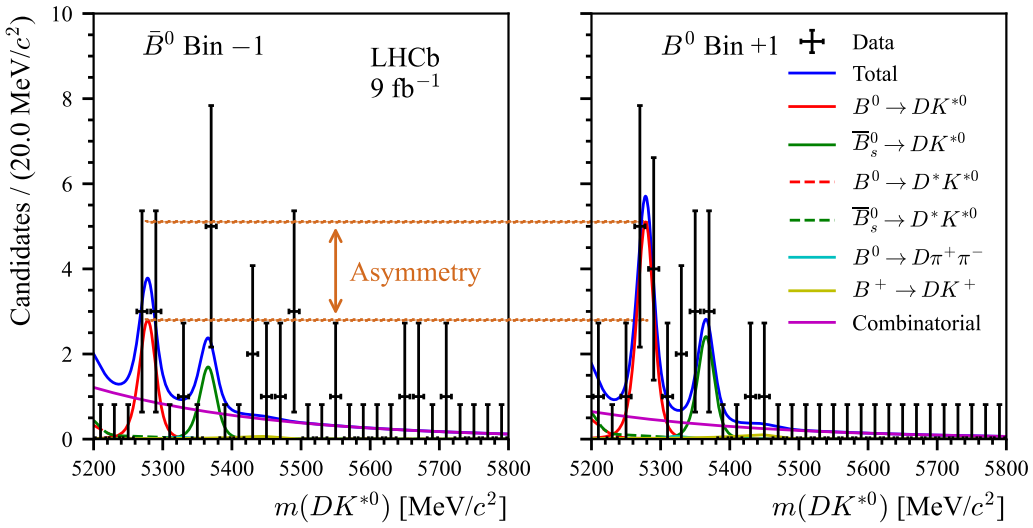

Figure 4.17: Invariant-mass distributions of (left) $\overline{B}^0 \to D\overline{K}^{*0}$ and (right) $B^0 \to DK^{*0}$ decay candidates in regions with indices -1 and +1, respectively. The data are overlaid with the fit result, and the asymmetry, given by the difference in signal yields between the two plots, is highlighted.

$B^0 \to DK^{*0}$ decays is $\sim F_{-1} = 0.095 \pm 0.0012$.

4.5.4 Consistency checks

To ensure the fit is robust and that various assumptions are appropriate, a number of fits with alternative parametrisations are performed as discussed below.

4.5.4.1 Signal and $\overline{B}^0_s \to D^0K^{*0}$ decay yields as floating parameters

The results of an alternative fit, where the signal yields are floating parameters in each category, are studied to ensure the parametrisations used in Eqs. 4.4 and 4.5 are a good fit the data. The fitted yields in the *LL* and *DD* categories are combined to determine an asymmetry in each effective bin, i, defined as $\left(N_i(B^0) - N_{-i}(\overline{B}^0)\right) / \left(N_i(B^0) + N_{-i}(\overline{B}^0)\right)$. A comparison between the asymmetries determined with floating signal yield parameters, and with signal yields parametrised by Eqs. 4.4 and 4.5, is displayed in Fig. 4.18. The agreement is quantified through $\chi^2 = 20.6$ from 20 independent regions.

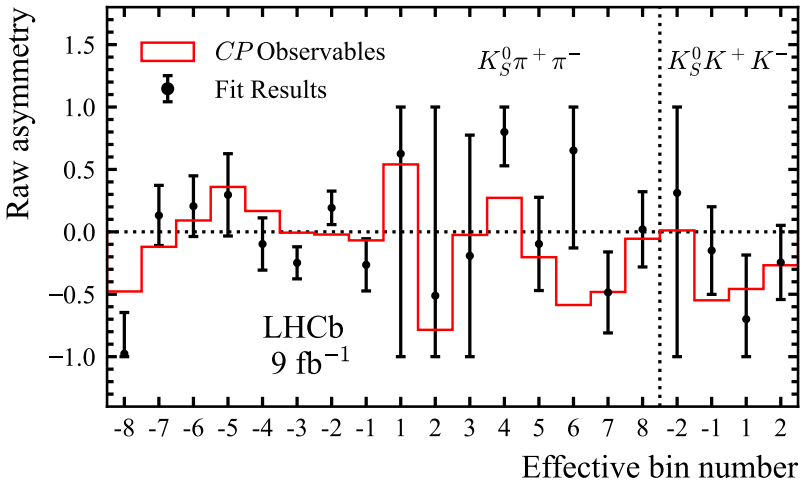

Figure 4.18: The raw asymmetry, defined as $\left(N_i(B^0) - N_{-i}(\overline{B}^0)\right) / \left(N_i(B^0) + N_{-i}(\overline{B}^0)\right)$, in each effective bin pair, where the yields from K^0_S mesons reconstructed with *LL* and *DD* tracks are combined. The red histogram displays the asymmetries from the default fit where the signal yields are parametrised by the *CP*-violation observables, and the black data points are calculated from signal yields which are floating parameters in the fit. The statistical uncertainties on the latter are capped to the physical limits.

Figure 4.18 also highlights the benefit of measuring the *CP* violation in regions of the Dalitz plot, because if an integrated study were performed the positive and negative asymmetries would cancel and thus the sensitivity to γ would be low.

A similar study is performed where the $\overline{B}^0_s \to D^0 K^{*0}$ decay yields are floating parameters in each category to check if the fraction in each phase-space region agrees with the F_i values used. The results are displayed in Fig. 4.19 where the good agreement between the two is clear.

4.5.4.2 *CP* violation in $\overline{B}^0_s \to D^0 K^{*0}$ decays

The interference between $\overline{B}^0_s \to D^0 K^{*0}$ and $B^0_s \to \overline{D}^0 K^{*0}$ decays is small, and therefore *CP* violation is ignored for this background. To test this assumption, an alternative fit is performed where the $\overline{B}^0_s \to DK^{*0}$ decay yield in each category is parametrised similarly to signal, but with different *CP*-violation observables

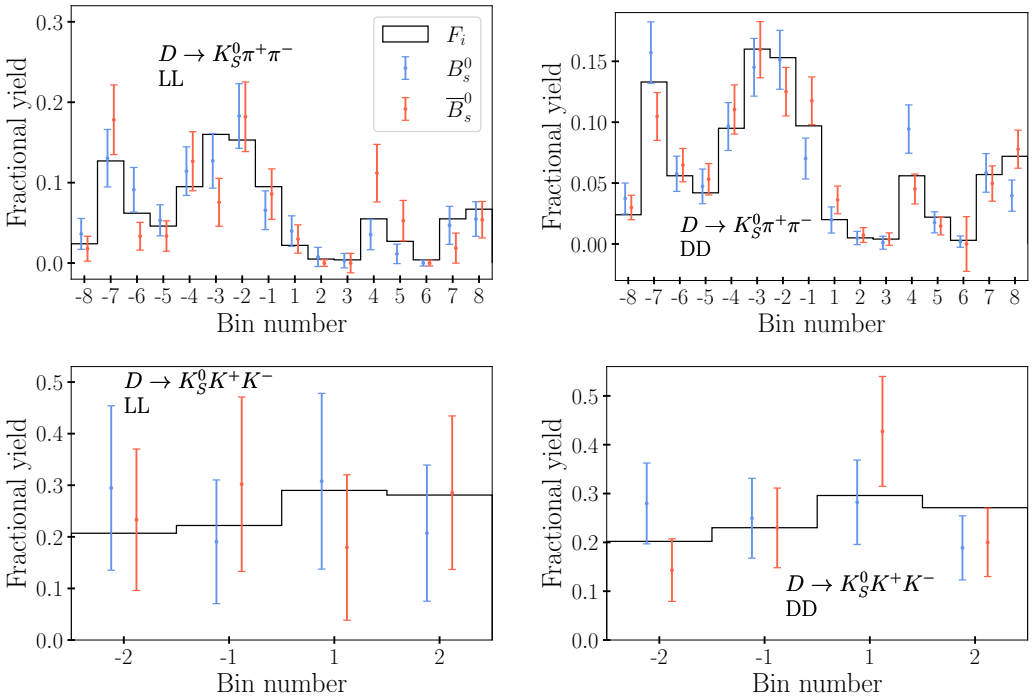

Figure 4.19: Comparison between the (black histogram) F_i values and the fractional yield in each region of phase space determined using (red points) $\overline{B}^0_s \to D^0 K^{*0}$ and (blue points) $B^0_s \to \overline{D}^0 \overline{K}^{*0}$ decays with (top) $D \to K^0_S\pi^+\pi^-$ and (bottom) $D \to K^0_S K^+K^-$, where the K^0_S meson is reconstructed using (left) *LL* and (right) *DD* tracks.

$(x^s_\pm, y^s_\pm)$. The fit determines

$$\begin{aligned} x^s_+ &= -0.024 \pm 0.037, \\ x^s_- &= -0.014 \pm 0.036, \\ y^s_+ &= 0.056 \pm 0.044, \\ y^s_- &= 0.089 \pm 0.048. \end{aligned} \tag{4.22}$$

The *CP*-violation observables are plotted in Fig. 4.20, where there is significant overlap between those that parameterise B^0_s and $\overline{B}^0_s$ decays, which confirms that the *CP* violation is negligible.

4.5.5 Dividing the dataset

A further check of the robustness of the results is performed by measuring the *CP*-violation observables in subsets of the data. The fit is repeated to the data for

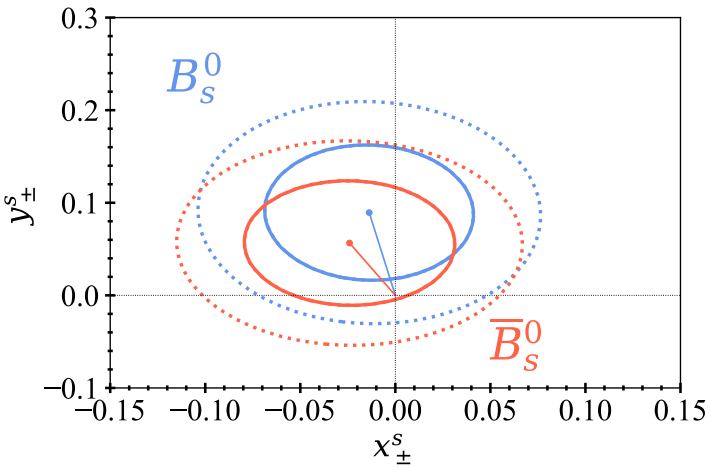

Figure 4.20: The 68.3% and 95.5% statistical confidence regions on the *CP*-violation observables $(x^s_\pm, y^s_\pm)$ parametrising $\overline{B}^0_s \to D^0 K^{*0}$ decays. The orange (blue) contours correspond to the observables related to $\overline{B}^0_s$ (B^0_s) decays, where Gaussian likelihoods are assumed.

Table 4.13: Values of the *CP*-violation observables determined in fits to subsets of the data. Specifically, the results are shown for the data collected with opposite LHCb magnet polarities, and for data collected in runs 1 and 2.

Data subset	x_+	x_-	y_+	y_-
Magnet up	0.13 ± 0.10	-0.09 ± 0.11	-0.22 ± 0.13	0.02 ± 0.12
Magnet down	0.03 ± 0.15	-0.31 ± 0.13	-0.43 ± 0.16	-0.07 ± 0.29
Run 1	0.51 ± 0.31	-0.20 ± 0.20	-0.73 ± 0.33	0.10 ± 0.21
Run 2	0.00 ± 0.09	-0.21 ± 0.10	-0.23 ± 0.11	-0.09 ± 0.16

each LHCb magnet polarity, and also for data collected during runs 1 and 2. The results are detailed in Tab. 4.13. In both cases the *CP*-violation observables are in good agreement.

A comparison can also be made to the results reported in Ref. [89], which is a measurement equivalent to that discussed in this chapter performed with

run 1 data, and determined

$$\begin{aligned} x_+ &= 0.05 \pm 0.35, \\ x_- &= -0.31 \pm 0.20, \\ y_+ &= -0.81 \pm 0.28, \\ y_- &= 0.31 \pm 0.21. \end{aligned}$$

Naively, one would expect these to be similar to those reported in Tab. 4.13, since, in principle, the same dataset is used. However, the many differences between the two analyses reduce the correlation between the results. The largest difference is in the selection requirements, which are improved in this analysis because a more effective BDT is applied. The processed data used in Ref. [89] is not preserved so the overlap between the samples could not be precisely calculated. However, the same study performed in the analysis of $B^\pm \to Dh^\pm$ decays with $D \to K^0_S h^+ h^-$ estimated a correlation of around 70%. The correlation is further reduced because the F_i, c_i and s_i values used in Ref. [89] are not the same as those used here. The former are determined using a semileptonic control channel, whilst the latter were Gaussian constrained to the values measured by the CLEO collaboration [49], which have since been updated by BESIII. Finally, an alternative division of $D \to K^0_S \pi^+ \pi^-$ decay phase space, which is optimised for lower purity samples, is used in Ref. [89]. Studies using only signal decays estimate the statistical correlation coefficient due to the different divisions to be around 85%. Therefore, in total the statistical correlation between the *CP*-violation observables reported in Ref. [89] and Tab. 4.13 is estimated to be around 50%, for which a good agreement is seen.

4.6 Systematic uncertainties

The *CP*-violation observables are assigned systematic uncertainties to account for assumptions in the fit, or to propagate the statistical uncertainties of fixed parameters. The latter are given by the standard deviations of the distributions of the *CP*-violation observables determined through many fits to the data with

smeared values of fixed parameters, and the former are given by the biases in the distributions of the *CP*-violation observables determined by generating pseudo data samples with alternate assumptions and then fitting with the default model.

4.6.1 Strong-phase difference inputs

A systematic uncertainty is assigned to account for the statistical errors on the c_i and s_i inputs from Refs. [10, 11], which are fixed in the fit. It is estimated by repeating the fit one thousand times using alternate c_i and s_i values generated according to their uncertainties and correlations. Specifically, the values which are used to estimate the same systematic uncertainty in the measurement of γ using $B^\pm \to Dh^\pm$ decays with $D \to K^0_S h^+ h^-$ are used here. This allows the correlations between the *CP*-violation observables in different measurements to be computed, such that this systematic uncertainty, which is often the largest in analyses similar to this, is not being double counted in future combinations to determine γ such as that reported in Ref. [100]. The correlations would be more challenging to estimate if the c_i and s_i parameters were Gaussian constrained in the invariant-mass fits, which forces the choice of strategy to fix them.

The systematic uncertainties are found to be 5×10^{-3}, 4×10^{-3}, 17×10^{-3} and 24×10^{-3} for x_+, x_-, y_+ and y_-, respectively. The larger errors on the $y_\pm$ observables reflect the more limited knowledge of the s_i inputs. Appendix A displays the correlations between the *CP*-violation observables presented in this analysis and in Ref. [88].

4.6.2 Charmless B decays

In the fit to determine the *CP*-violation observables, the contribution from charmless B decays is ignored because the contribution is found to be consistent with 0. It was estimated there are 5 ± 5 and 8 ± 7 charmless B decays, where the D decay is reconstructed in the $K^0_S\pi^+\pi^-$ final state, and the K^0_S is reconstructed using DD and LL tracks, respectively. No significant charmless contribution is found when candidates are reconstructed as $D \to K^0_S K^+ K^-$ decays. To be conservative,

a systematic uncertainty is assigned by generating pseudo data samples which include the charmless contribution. Since these decays do not proceed through an intermediate D meson it is assumed they are evenly distributed across the D decay phase space, such that the yield in a particular region is given by $N \times A_i$, where N is the total charmless yield and A_i is the fractional area of that region. The corresponding systematic uncertainties are determined to be 9×10^{-3}, 8×10^{-3}, and 5×10^{-3} for x_+, x_- and y_-, respectively, and negligible for y_+.

4.6.3 Efficiency effects on the F_i inputs

Differences in the selection criteria between this analysis and Ref. [88] can alter the values of the F_i parameters. The effect is quantified by comparing the distributions of $m^2(h^+h^-)$ in simulation, as displayed in Fig. 4.8. The ratios of the distributions in $B^0 \to DK^{*0}$ and $B^\pm \to D\pi^\pm$ decays in each category, given by the D decay and the type of tracks used to reconstruct the K^0_S meson, are fit with a straight line with gradient, a, and intercept, b. In the $D \to K^0_S K^+ K^-$ decay mode the lines are consistent with being flat, and therefore a systematic uncertainty is not considered. The same is not true for the $D \to K^0_S \pi^+ \pi^-$ decay channel.

It is not immediately apparent how to use a and b to compute altered F_i values. Broadly speaking, it is achieved by reweighting the original F_i values using factors which are determined by considering the effect of the different efficiency profiles on the $D \to K^0_S \pi^+ \pi^-$ amplitude model developed by the BaBar and Belle collaborations in 2018 [101]. Practically, the amplitude model provides the magnitude, $|A|$, and phase, ϕ, of the $D \to K^0_S \pi^+ \pi^-$ decay at each point in the Dalitz plot divided into 500×500 pixels. The efficiency profile in $B^\pm \to D\pi^\pm$ decays with $D \to K^0_S \pi^+ \pi^-$, denoted $\eta_{D\pi}$, is given by the fraction of simulated candidates at each point. Then, the efficiency profile of $B^0 \to DK^{*0}$ decays with $D \to K^0_S \pi^+ \pi^-$ decays is given by $\eta_{DK^{*0}} = (a + b m^2_{\pi^+\pi^-})\eta_{D\pi}$. The reweighting factors are given by

$$R_i = \frac{\sum_p |A(p)|^2 (a + b m^2_{\pi^+\pi^-}) \eta_{D\pi}(p)}{\sum_p |A(p)|^2 \eta_{D\pi}(p)}, \tag{4.23}$$

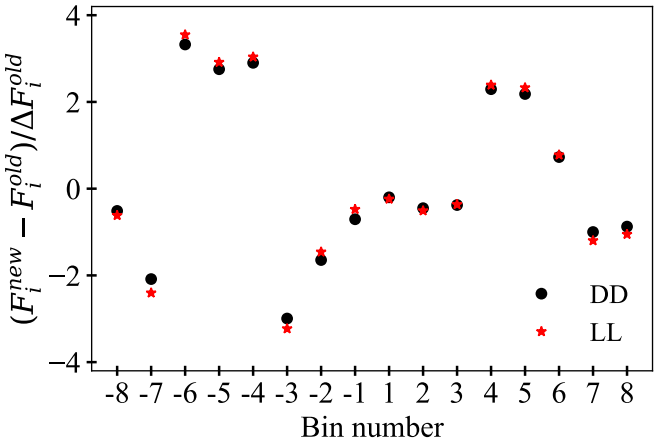

Figure 4.21: The shift in the F_i values relative to the statistical error caused by the efficiency differences between the selection requirements for $B^0 \to DK^{*0}$ decays in this measurement and $B^{\pm} \to Dh^{\pm}$ decays in Ref. [88].

where p denotes a pixel. The maximum reweighting factor is around 3%. Furthermore, the pull for each F_i, given by ratio of the shift and the statistical uncertainty, is displayed in Fig. 4.21. The pulls for the DD and LL K^0_S-meson track categories do not significantly differ because the values of a and b in each are similar.

The systematic error is determined using pseudo data samples which are generated using the altered F_i parameters and fitted with the default model. Uncertainties of 6×10^{-3}, 7×10^{-3} and 1×10^{-3} are found for x_+, x_- and y_+, respectively, whilst that of y_- is negligible. It is worth noting the altered F_i values are shifted by up to four times the statistical errors, and therefore the systematic uncertainty due to the limited knowledge of the F_i values is not estimated because it will be negligible.

4.6.4 Fixed ratios in the invariant-mass fit

The ratios parametrising the $B^0 \to D\pi^+\pi^-$, $B^+ \to DK^+$ and partially reconstructed $B^0 \to D^*K^{*0}$ and $\overline{B}^0_s \to D^{*0}K^{*0}$ decay backgrounds are all fixed in the invariant-mass fit. The systematic uncertainty associated with the limited knowledge of each ratio is estimated by refitting the data many times with alternative ratios generated according to their uncertainties. The results are summarised in Tab. 4.14.

Table 4.14: Summary of the systematic uncertainties, in units of $\times 10^{-3}$, associated with fixed ratios in the invariant-mass fit model. Uncertainties with values $< 1 \times 10^{-3}$ are denoted '–' and are considered negligible.

Fixed ratio	x_+	x_-	y_+	y_-
r_L	1	1	3	–
$r_{\gamma,0}$ and $r_{\gamma,1}$	–	–	1	–
R^s	–	1	1	–
R	–	–	–	–
$R_{D\pi^+\pi^-}$	–	–	–	–
R_{DK^+}	1	1	–	1

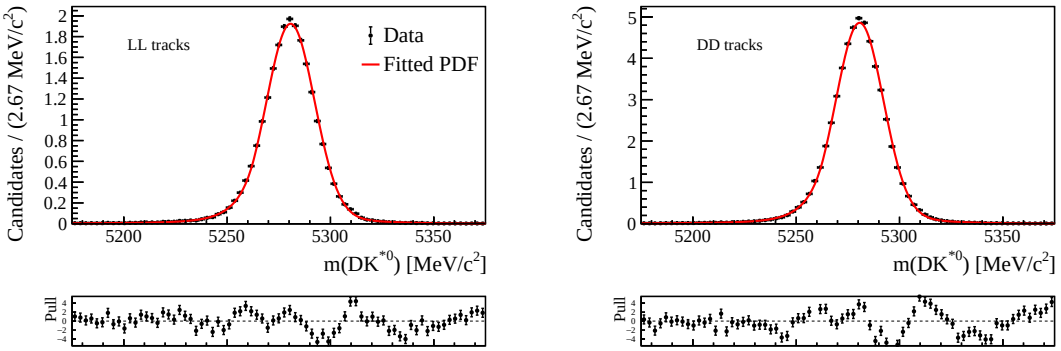

Figure 4.22: Fits to the invariant mass of signal candidates in simulation using the sum of two Crystal Ball functions, where the K^0_S mesons are reconstructed with (left) *LL* and (right) *DD* tracks.

4.6.5 Signal shape in the invariant-mass fit

The choice of PDF used to represent signal candidates provides a reasonably good fit to the MC sample in Fig. 4.11. However, as a large sample is used there is a beating pattern in the pull distributions. Therefore, a systematic uncertainty is conservatively assigned using an alternative shape, which is the sum of two Crystal Ball functions. A fit to the simulation sample using this PDF is displayed in Fig. 4.22. The systematic uncertainties are evaluated by fitting pseudo data samples generated from a PDF where signal candidates are represented by the double Crystal Ball shape with fixed tail parameters, and they are determined to be 1×10^{-3}, 3×10^{-4}, 3×10^{-3} and 3×10^{-3} for x_+, x_-, y_+ and y_-, respectively.

It is evident from Fig. 4.22 that the right tail is not well modelled by the alternative PDF. Therefore, a further cross-check is performed. First, the global fit to data is carried out with the tail parameters of the modified Gaussian shape allowed to float. They are determined to be $\alpha_{\rm L} = 0.15 \pm 0.04$ and $\alpha_{\rm R} = 0.14 \pm 0.04$, which are in good agreement with those found in simulation. Then, the above procedure is repeated, where pseudo data samples are generated from a PDF where the tail parameters are fixed to those determined in data, before being fitted with the default model where the tail parameters are fixed to those determined in MC. The corresponding systematic uncertainty is negligible for all *CP*-violation observables.

4.6.6 Fixed global parameters in the invariant-mass fit

In the fit to determine the *CP*-violation observables, seven parameters are fixed to the values determined in the global fit. They are the combinatorial background slopes in each global fit category, the mean of the function representing $\overline{B}{}^0_s \to D^0 K^{*0}$ decays, and the resolution shared by signal and $\overline{B}{}^0_s \to D^0 K^{*0}$ decays for the *LL* and *DD* track samples. A systematic uncertainty is assigned to propagate the statistical errors on these parameters to the *CP*-violation observables. Separately for each parameter, pseudo data samples are generated with the default model, and they are fitted using the same PDF allowing freedom in the parameter. The width of the distribution for each observable is assigned as the systematic uncertainty, and are found to be 1×10^{-3}, 5×10^{-4}, 2×10^{-3} and 3×10^{-3} for x_+, x_-, y_+ and y_-, respectively.

4.6.7 Bias correction

The correction to the *CP*-violation observables discussed in Sec. 4.5.2 is dependent on the input values of r_s, δ_s and γ. The bias study is repeated many times using values generated according to the uncertainties of r_s, δ_s and γ, and the width of the bias distribution for each *CP* observable is taken as the systematic uncertainty. It is found to be 3×10^{-3}, 3×10^{-3}, 6×10^{-3}, 4×10^{-3} for x_+, x_-, y_+ and y_-, respectively.

4.6.8 Value of the coherence factor

A systematic uncertainty is evaluated to account for fixing the coherence factor to $\kappa = 0.958^{+0.005}_{-0.046}$ [40] in the fit. It is estimated by fitting the default model to pseudo data samples generated separately for $\kappa+\sigma(\kappa)$ and $\kappa-\sigma(\kappa)$, and is determined to be 1×10^{-3}, 3×10^{-3} and 2×10^{-3} for x_-, y_+ and y_-, respectively, and negligible for x_+.

As previously mentioned, the same selection as Ref. [40] is applied to the $K^+\pi^-$ meson pair, which allows the value of the coherence factor to be used directly in the fit. This implicitly assumes the remaining selection requirements do not significantly affect the value of κ. To test this assumption, a study similar to that described in Sec. 4.6.3 is performed using an amplitude model for $B^0 \to DK^+\pi^-$ decays developed using the results outlined in Ref. [40]. The integration in Eq. 2.20 is performed using the amplitudes for each pixel in a 500×500 scheme, with and without weighting according to the simulated selection efficiency profile. The bias in the coherence factor is found to be -3×10^{-3}. Given the results described in the previous paragraph, this bias corresponds to a negligible systematic uncertainty, and therefore it is ignored.

4.6.9 Efficiency corrections to the strong-phase inputs

The c_i and s_i inputs are used directly from Refs. [10, 11] without any corrections. The effect of the selection efficiency profile on these inputs is evaluated by performing the integrations in Eqs. 2.34 and 2.35 using an amplitude model, with and without weighting by the efficiency in simulation. Fig. 4.23 displays the ratio of the difference between the strong-phase inputs calculated in the two scenarios and the statistical uncertainty for the $D \to K^0_S\pi^+\pi^-$ decay mode. All of the shifts in the c_i (s_i) are less than half (a fifth) of the relevant statistical uncertainty. Therefore, the corresponding systematic uncertainty is expected to be small. The effect on the *CP*-violation observables is measured by generating pseudo data samples using strong-phase inputs which are shifted from the default values by the differences

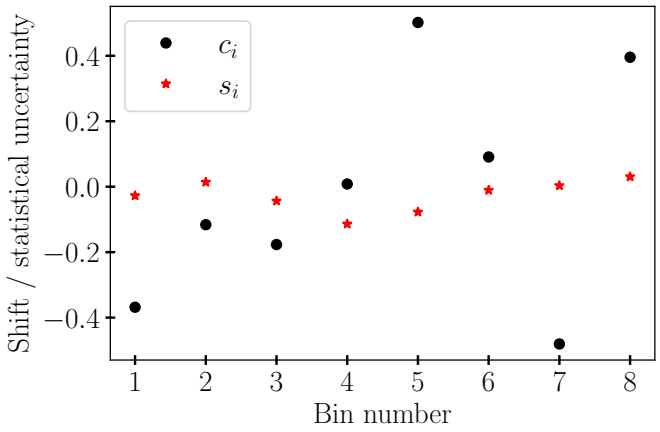

Figure 4.23: The efficiency-induced shift of the (black) c_i and (red) s_i values.

in Fig. 4.23, and fitting it with the default model. The corresponding biases are 1×10^{-3}, 1×10^{-3}, 2×10^{-3} and 1×10^{-3} for x_+, x_-, y_+ and y_-, respectively.

4.6.10 Dalitz plot migration

The finite momentum resolution results in decays which are assigned to the incorrect region of the Dalitz plot. To first order, the F_i values already account for this effect because they are determined in data through a fit to the $B^\pm \to D\pi^\pm$ decay yields. However, the migration smears the *CP* asymmetries across the Dalitz plot, and since these asymmetries are different between the $B^0 \to DK^{*0}$ and $B^\pm \to D\pi^\pm$ decays, not accounting for the migration can result in biased *CP* observables. It is a small effect, so no correction is applied by default, and instead a systematic uncertainty is assigned.

The systematic uncertainty is evaluated using pseudo data generated from alternative F_i values which are estimated as follows. Using the amplitude model for the $D \to K^0_S\pi^+\pi^-$ decay [101], the *CP*-violation observables describing the $B-$decay modes [39], and the efficiency profiles from simulation, 10 million events are generated across the Dalitz plot for each $B-$decay channel. The coordinates of each event are then smeared according to the resolution in simulation, which is found to be approximately $0.007(\,\mathrm{GeV}/c^2)^2$, as displayed in Fig. 4.2, to determine the true and smeared Dalitz plot region. The smeared yields deviate from the default

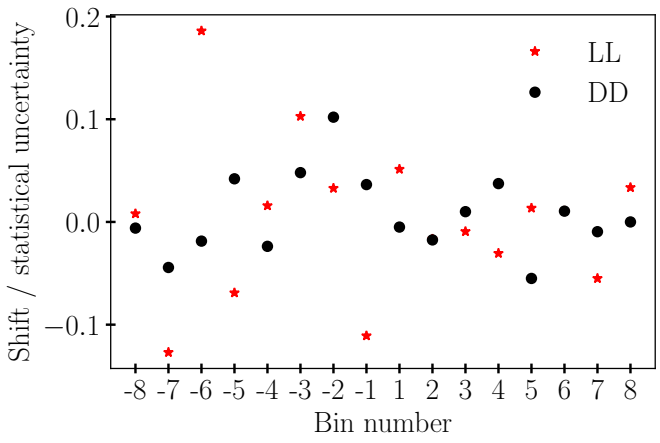

Figure 4.24: The shift in the F_i values relative to the statistical uncertainties due to migration of the Dalitz plot region.

by a maximum of around 3% for each $B-$decay mode. The alternative F_i are given by the default F_i multiplied by the ratio of deviations in the $B^0 \to DK^{*0}$ and $B^{\pm} \to D\pi^{\pm}$ decays that result from the smearing. The shift in the F_i values relative to their statistical errors are shown in Fig. 4.24. Using these alternative F_i results in systematic uncertainties which are $< 2 \times 10^{-3}$ for all *CP*-violation observables.

4.6.11 *CP* violation in $B^0 \to D^* K^{*0}$ decays

In the fit, it is assumed the partially reconstructed $B^0 \to D^* K^{*0}$ decays are not *CP* violating because there are only a small amount in the sample. The corresponding systematic uncertainty is evaluated using pseudo data samples which are generated assuming the $B^0 \to D^* K^{*0}$ decays are distributed across the Dalitz plot similarly to Eqs. 4.4 and 4.5. The hadronic parameters are unknown for this final state. However, from the CKM elements, it can be assumed that the amplitude ratio $r_B \sim 0.2$, and therefore the same *CP*-violation observables as signal are used. The systematic uncertainty is found to 1×10^{-3} for all *CP*-violation observables. Given this is small, different values of r_B are not pursued.

Table 4.15: Systematic uncertainties, in units of $\times 10^{-3}$, for the *CP*-violation observables. The statistical uncertainties are given for reference.

Source	x_+	x_-	y_+	y_-
Efficiency correction on (c_i, s_i)	1	1	2	1
Efficiency correction on F_i	6	7	1	–
Fixed background ratios	1	2	3	1
Signal shape	1	3	3	3
Fixing global fit parameters	1	5	2	3
$B^0 \to D^*K^{*0}$ *CP* violation	1	1	1	1
Value of κ	–	1	3	2
Charmless background	9	8	–	5
Dalitz plot migration	1	1	–	2
Bias correction	3	3	6	4
Total of above systematics	11	13	9	11
Strong-phase measurements	5	4	17	24
Statistical uncertainty	86	86	105	128

4.6.12 Summary of systematic uncertainties

A summary of the systematic uncertainties is presented in Tab . 4.15. The dominant systematic uncertainty on the $y_\pm$ observables is from the knowledge of the strong-phase inputs, whilst for $x_\pm$ the efficiency corrections on the F_i parameters and potential charmless backgrounds are large contributions. For each observable, the total systematic uncertainty is between $14 - 20\%$ of the symmetrised statistical uncertainty. The correlations between the systematic uncertainties on the *CP*-violation observables are displayed in Tab. 4.16.

4.7 Determination of γ

The values and uncertainties of the parameters γ, r_s and δ_s are extracted from the *CP*-violation observables through a maximum likelihood fit performed using the

Table 4.16: Systematic correlations between the *CP*-violation observables.

	x_+	x_-	y_+	y_-
x_+	100	-3	15	-4
x_-		100	2	6
y_+			100	-5
y_-				100

`GammaCombo` [100] package developed by analysts at LHCb. The likelihood is created by comparing the measured observables, $\vec{A}_{\text{obs}}$, to predictions, $\vec{A}(\vec{\alpha})_{\text{pred}}$, which are calculated using the floating parameters in the fit, $\vec{\alpha}$. In this measurement, the above vectors correspond to

$$\begin{aligned}
\vec{A}_{\text{obs}} &= \{x_+, x_-, y_+, y_-\}, \\
\vec{\alpha} &= \{r_s, \delta_s, \gamma\}, \\
\vec{A}(\vec{\alpha})_{\text{pred}} &= \{r_s\cos(\gamma+\delta_s), r_s\cos(\gamma-\delta_s), r_s\sin(\gamma+\delta_s), r_s\sin(\gamma-\delta_s)\}\,.
\end{aligned}$$

From the elliptical confidence regions displayed in Fig. 4.16, it is clear the *CP*-violation observables have Gaussian probability distributions, and therefore the likelihood function in the fit is given by

$$\mathcal{L}(\vec{\alpha}) \propto \exp\left(-\frac{1}{2}(\vec{A}_{\text{obs}} - \vec{A}(\vec{\alpha})_{\text{pred}})^T V^{-1} (\vec{A}_{\text{obs}} - \vec{A}(\vec{\alpha})_{\text{pred}})\right), \tag{4.24}$$

where V is the covariance matrix. Maximising this likelihood function, or equivalently minimising $\chi^2(\vec{\alpha}) = -2\ln\mathcal{L}(\vec{\alpha})$, returns the best estimates of the parameters, denoted $\hat{\vec{\alpha}}$.

The uncertainty on each parameter in $\vec{\alpha}$, denoted θ, is given by the range of possible values of θ which do not reject the hypothesis $\theta_{\text{true}} = \theta$ with some predefined confidence. Practically, this is achieved using Wilks' theorem, which when applied in this case states that the distribution,

$$\Delta\chi^2(\theta) = \chi^2_{\text{min}}(\vec{\alpha}') - \chi^2(\hat{\vec{\alpha}}), \tag{4.25}$$

is a χ^2 function in θ with one degree of freedom, such that, for example, the values θ_{low} and θ_{high} where $\Delta\chi^2 = 1$ define the 68.3% confidence interval. In the above

equation, $\chi^2_{\rm min}(\vec{\alpha}')$ is determined by minimising the χ^2 function with θ fixed to the appropriate value, whilst the other parameters in $\vec{\alpha}$ have freedom. By definition, $\chi^2_{\rm min}(\vec{\alpha}')$ must always be greater than $\chi^2(\hat{\vec{\alpha}})$. This technique to calculate confidence intervals is commonly referred to as the `PROB` method.

The scenario discussed in the above paragraph applies the `PROB` method to a single parameter, so for example it can be used to determine the confidence interval on γ. However, the idea extends to multiple parameters to determine *confidence regions*. In this case, $\Delta\chi^2 = \Delta\chi^2(\vec{\theta})$, where $\vec{\theta}$ is a subset of $\vec{\alpha}$, is a χ^2 distribution with n degrees of freedom, where n is the number of parameters in $\vec{\theta}$. So, for example, when applied to this measurement, confidence regions can be determined in a parameter space defined by γ and r_s.

As mentioned above, the `PROB` method relies on Wilks' theorem, which only applies to the asymptotic limit. So, if the sample size is not large $\Delta\chi^2(\vec{\theta})$ may not be χ^2 distributed. Therefore, a second method is used to estimate the confidence intervals as a cross-check, which determines $\Delta\chi^2(\vec{\theta})$ from pseudo experiments as opposed to the χ^2 assumption.

As before, a scan over the parameters is performed to determine $\Delta\chi^2(\vec{\theta})$. However, unlike the `PROB` method, there is not a one-to-one correspondence between the value of $\Delta\chi^2$ and the confidence interval at this stage, and a further step is required. At each scan point, pseudo values of the observables, denoted $\vec{A}_{\rm toy}$, are generated from the PDF $f(\vec{A}_{\rm toy}|\vec{\alpha}')$. The minimisation is performed using $A_{\rm toy}$ and the equivalent $\Delta\chi^2_{\rm toy}$ is calculated. The procedure is repeated $N_{\rm toy}$ times at each scan point, and the confidence level is given by ${\rm CL} = N(\Delta\chi^2_{\rm toy} \geq \Delta\chi^2)/N_{\rm toy}$. This procedure is commonly referred to as the `PLUGIN` method.

There are two degenerate solutions for γ, δ_s and r_s because the *CP*-violation observables are identical under the transformation $\gamma \to \gamma + 180°$, $\delta_s \to \delta_s + 180°$.

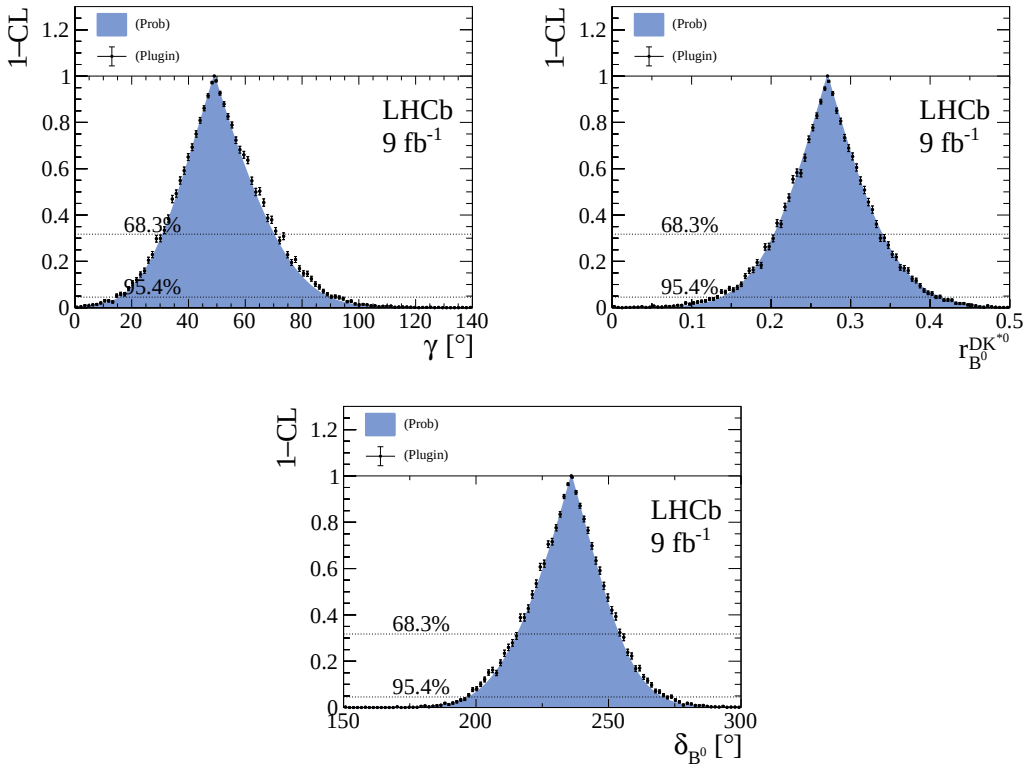

Figure 4.25: The confidence levels for (top left) γ, (top right) r_s and (bottom) δ_s determined in the maximum likelihood fit using the (shaded blue) `PROB` and (points) `PLUGIN` methods. The 68.3% and 95.4% confidence levels are displayed as horizontal black dashed lines.

In the region $0 < \gamma < 180°$, the best fit values are

$$\begin{aligned} \gamma &= \left(49^{+22}_{-19}\right)^{\circ}, \\ r_s &= 0.271^{+0.065}_{-0.066}, \\ \delta_s &= \left(236^{+19}_{-21}\right)^{\circ}, \end{aligned} \tag{4.26}$$

where the uncertainties correspond to the 68.3% confidence intervals calculated using the `PLUGIN` method. However, Fig. 4.25 shows that the confidence levels for γ, r_s and δ_s determined with the `PROB` and `PLUGIN` methods are consistent. The 68.3% and 95.5% confidence regions for each pairwise combination of variables from γ, r_s and δ_s can be found in Fig. 4.26.

The value of γ is consistent with the 2022 LHCb combination, which determined $\gamma = \left(63.8^{+3.5}_{-3.7}\right)^{\circ}$. Furthermore, each parameter is consistent with those measured

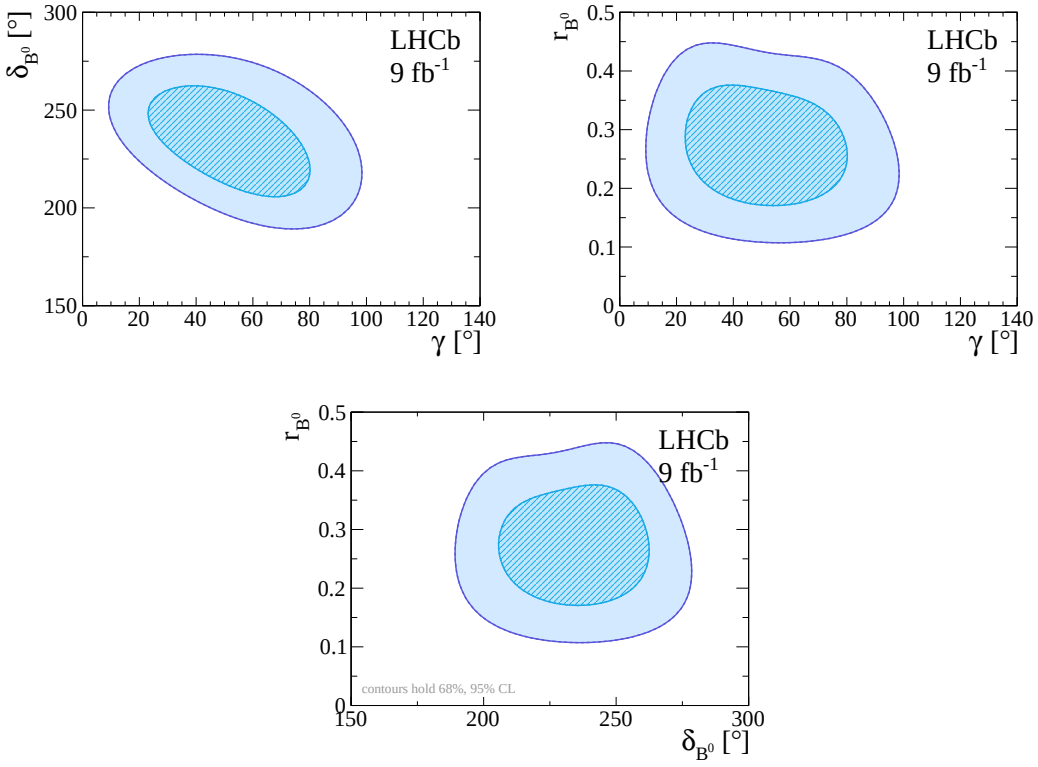

Figure 4.26: The 68.3% and 95.5% confidence regions determined in the maximum likelihood fit for (top left) γ versus δ_s, (top right) γ versus r_s and (bottom) δ_s versus r_s.

in the equivalent run 1 analysis [89],

$$\begin{aligned} \gamma &= (71 \pm 20)^\circ, \\ r_s &= 0.56 \pm 0.17, \\ \delta_s &= \left(204^{+21}_{-20}\right)^\circ. \end{aligned} \tag{4.27}$$

Despite the larger dataset used in the measurement presented in this chapter, the precision on γ is not significantly improved compared to Ref. [89]. The reason is that the uncertainty on γ is inversely proportional to the value of r_s, which is determined to be approximately double the expectation from CKM elements in Ref. [89]. However, to reiterate, the statistical impact of this measurement does not come from the precision on γ, r_s and δ_s, but rather the precision on the *CP*-violation observables, which are used as inputs in combinations of measurements such as that described in the next section. The precision improvement on the

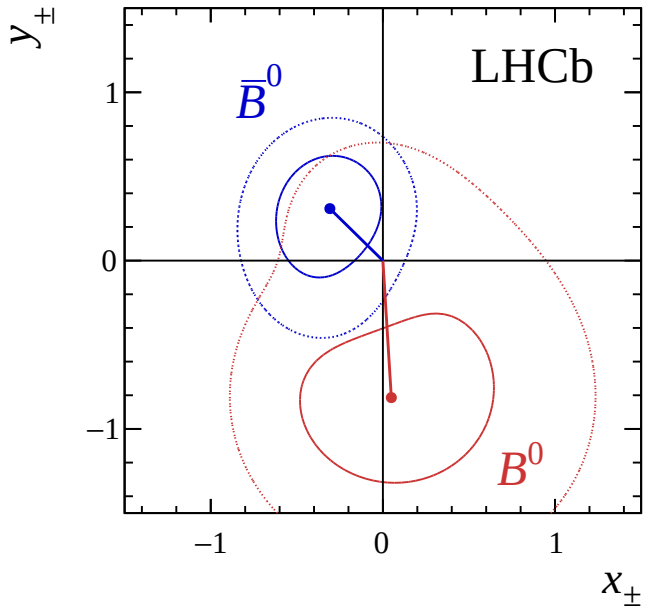

Figure 4.27: The (solid lines) 68.3% and (dashed lines) 95.5% statistical confidence regions for the measured $(x_\pm, y_\pm)$ values from Ref. [89]. The plot is reproduced from Ref. [89].

CP-violation observables can be clearly seen by comparing Fig. 4.16 with the equivalent plot from the run 1 analysis, which is reproduced in Fig. 4.27, and by comparing the uncertainties on r_s.

Finally, a comparison is made with the values of γ, r_s and δ_s found with B^0 decays in the 2022 combination of γ and charm analyses performed by the LHCb collaboration [39]. The combination simultaneously fit the *CP*-violation observables from Ref. [89] and Ref. [102], where $B^0 \to DK^{*0}$ decays are studied with the ADS and GLW methods using the data collected in run 1, 2015 and 2016. The results are

$$\begin{aligned} \gamma &= \left(82.0^{+8.1}_{-8.8}\right)^\circ, \\ r_s &= 0.249^{+0.022}_{-0.025}, \\ \delta_s &= \left(198^{+10}_{-9.6}\right)^\circ, \end{aligned} \tag{4.28}$$

which are again consistent with those determined in this chapter.

4.8 Combination of γ measurements using $B^0 \to DK^{*0}$ decays

The same 2022 LHCb combination also determined γ from studies of $B^\pm$ decays to be $\gamma = \left(60.6^{+4.0}_{-3.8}\right)^\circ$, which is a deviation of around 2.2 standard deviations from the value using B^0 decays presented in Eq. 4.28. In 2024, the global LHCb combination was repeated [15] using updated measurements of $B^0 \to DK^{*0}$ decays described in this chapter and in Ref. [96], both of which use the full LHCb dataset. The values of γ, r_s and δ_s determined with the B^0 decays are

$$\begin{aligned} \gamma &= \left(64.6^{+6.5}_{-7.5}\right)^\circ, \\ r_s &= 0.234^{+0.015}_{-0.016}, \\ \delta_s &= (192 \pm 6)^\circ, \end{aligned} \tag{4.29}$$

where a notable precision improvement on γ of around 1.3° is found. This is highlighted in Fig. 4.28, which shows a comparison between the 68.3% and 95.5% confidence regions in the γ versus r_s and δ_s parameter spaces in the 2021 [100], 2022 [39] and 2024 [15] LHCb combinations. Furthermore, the tension with the value of γ determined using $B^\pm$ decays, $\gamma = \left(63.4^{+3.2}_{-3.3}\right)^\circ$, is resolved as displayed in Fig. 4.29. The updated LHCb average using all B-decay modes is $\gamma = (64.6 \pm 2.8)^\circ$, compared to a value of $\gamma = \left(63.8^{+3.5}_{-3.7}\right)^\circ$ found in 2022 [39].

4.9 Summary

A dataset corresponding to an integrated luminosity of around $9\,\text{fb}^{-1}$ collected by the LHCb experiment is used to perform a model-independent study of *CP* violation in $B^0 \to DK^{*0}$ decays with $D \to K^0_S h^+ h^-$, where $h^\pm$ is a pion or kaon. The differences between the distributions of $B^0 \to DK^{*0}$ and $\overline{B}^0 \to D\overline{K}^{*0}$ decays across the $D \to K^0_S h^+ h^-$ decay phase space are parametrised by the *CP*-violation observables, $x_\pm = r_s \cos(\gamma \pm \delta_s)$ and $y_\pm = r_s \sin(\gamma \pm \delta_s)$, which are determined to be

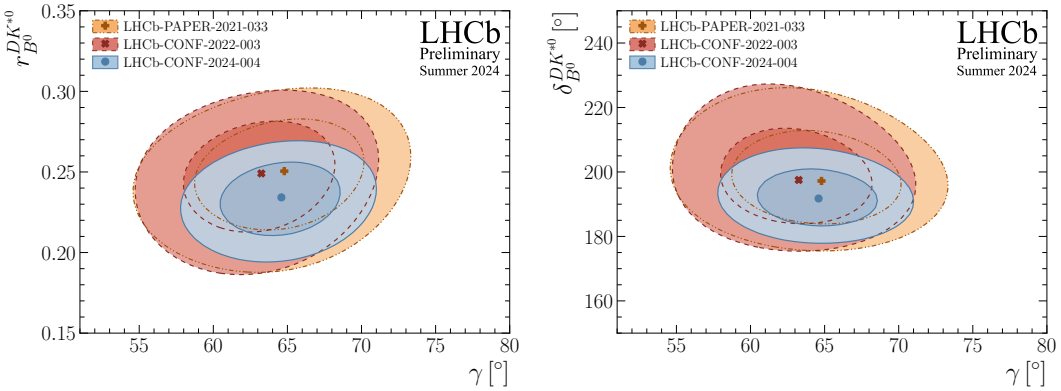

Figure 4.28: Comparison between the 68.3% and 95.5% confidence regions in the (left) γ versus δ_s and (right) γ versus r_s parameter spaces in the 2021 [100], 2022 [39] and 2024 [15] LHCb combinations. Plots reproduced from Ref. [15].

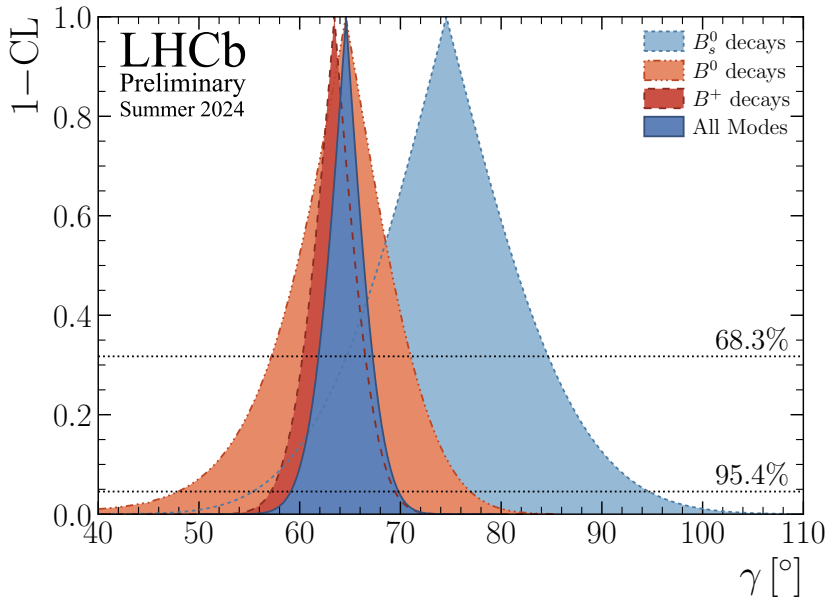

Figure 4.29: Measured γ values by B meson as determined by the LHCb collaboration [15]. Plot reproduced from Ref. [15].

$$
\begin{aligned}
x_+ &= 0.074 \pm 0.086 \pm 0.005 \pm 0.011, \\
x_- &= -0.215 \pm 0.086 \pm 0.004 \pm 0.013, \\
y_+ &= -0.336 \pm 0.105 \pm 0.017 \pm 0.009, \\
y_- &= -0.012 \pm 0.128 \pm 0.024 \pm 0.011,
\end{aligned}
$$

where the first uncertainty is statistical, the second is the systematic contribution from the D-decay strong-phase inputs measured by the CLEO and BESIII collaborations [10, 11], and the third is from the experimental systematic uncertainties.

A maximum likelihood fit to the observables is performed to determine

$$\gamma = \left(49^{+22}_{-19}\right)^\circ,$$
$$r_s = 0.271^{+0.065}_{-0.066},$$
$$\delta_s = \left(236^{+19}_{-21}\right)^\circ.$$

The CKM angle γ is in good agreement with the current LHCb average [15], and the values of r_s and δ_s are consistent with other measurements [96, 89]. In combination with the results of $B^0 \to DK^{*0}$ decays with D decays to the ADS and GLW modes discussed in Ref. [96], the value of γ from B^0 decays is determined to be $\gamma = \left(64.6^{+6.5}_{-7.5}\right)^\circ$. The new average has resolved tensions with γ measured using $B^\pm$ decays and the precision is improved by around 1.3° compared to the previous combination [39].

5

Strong-phase measurements using quantum-correlated $D\overline{D}$ pairs

Contents

5.1 Quantum-correlated $D\overline{D}$ pairs

Charm factories, such as BESIII and CLEO, exploit the $e^+e^- \to \gamma^* \to c\bar{c}$ process to produce many pairs of charmed mesons. Typically, these experiments operate at the $\psi(3770)$ resonance, where the cross-sections of the $e^+e^- \to D^0\overline{D}^0$ and $e^+e^- \to D^+D^-$ processes are large. The self-conjugating intermediate virtual photon is in an eigenstate of the charge-conjugation operator, C, with eigenvalue $C_\gamma = -1$, which is conserved in the hadronisation to the D-meson pair. At the

$\psi(3770)$ resonance, the amplitude of the $D\overline{D}$ pair is

$$|\mathcal{A}_{D\overline{D}}\rangle = \frac{1}{\sqrt{2}}\left(|D\overline{D}\rangle - |\overline{D}D\rangle\right), \tag{5.1}$$

such that the condition $C|\mathcal{A}_{D\overline{D}}\rangle = C_\gamma|\mathcal{A}_{D\overline{D}}\rangle$ is satisfied.

Consider two final states which are accessible to both the D and $\overline{D}$ mesons, denoted f_1 and f_2, which, due to charge conservation is only possible when a pair of neutral charm mesons are produced in the hadronisation. In the remainder of this thesis, such a decay is denoted $D\overline{D} \to f_1$ vs. f_2, which avoids associating a D meson of a particular flavour, which cannot be uniquely determined, with a specific final state. The amplitude becomes

$$\langle f_1 f_2|\mathcal{A}_{D\overline{D}}\rangle = \frac{1}{\sqrt{2}}\left(A_1\bar{A}_2 - \bar{A}_1 A_2\right), \tag{5.2}$$

where $A_i = \langle f_i|D^0\rangle$ and $\bar{A}_i = \langle f_i|\overline{D}^0\rangle$. Therefore, the decay rate[1] is given by,

$$\begin{aligned}\Gamma(D\overline{D} \to f_1 \text{ vs. } f_2) = \int\int (&|A_1|^2|\bar{A}_2|^2 + |\bar{A}_1|^2|A_2|^2 - \\ &A_1^*\bar{A}_1\bar{A}_2^* A_2 - A_1\bar{A}_1^*\bar{A}_2 A_2^*)\mathrm{d}\mathbf{\Phi}_D \mathrm{d}\mathbf{\Phi}_{\overline{D}},\end{aligned} \tag{5.3}$$

where the integrals are performed over the phase space, Φ, of each D decay. The amplitude ratio, r_i, strong-phase difference, δ_i, and coherence factor, κ_i, are defined as,

$$\mathcal{A}_i^2 = \int |A_i|^2 \mathrm{d}\mathbf{\Phi}, \tag{5.4}$$

$$\bar{\mathcal{A}}_i^2 = \int |\bar{A}_i|^2 \mathrm{d}\mathbf{\Phi}, \tag{5.5}$$

$$r_i^2 = \frac{\bar{\mathcal{A}}_i^2}{\mathcal{A}_i^2}, \tag{5.6}$$

$$\kappa_i e^{i\delta_i} = \frac{\int A_i \bar{A}_i^* \mathrm{d}\mathbf{\Phi}}{\sqrt{\mathcal{A}_i^2 \bar{\mathcal{A}}_i^2}}, \tag{5.7}$$

[1]Equation 5.3 should inherit a factor of $\frac{1}{2}$ from the normalisation of the amplitude. However, throughout this thesis, ratio observables are used where the normalisation trivially cancels, or yields are compared to predictions assuming the decays of the D and $\overline{D}$ mesons are *independent*. There is a slight subtlety in the definition of the decay rate in the case of the latter. For a direct comparison with the correlated scenario, the uncorrelated decay rates must be defined *per pair* of $D\overline{D}$ mesons, and therefore they are also multiplied by a factor of $\frac{1}{2}$ to account for the two possible indistinguishable time orderings, depending on which D decayed first. As such, the convention is to typically omit this normalisation in both cases.

which simplifies the expression to,

$$\Gamma(D\overline{D} \to f_1 \text{ vs. } f_2) = \mathcal{A}_1^2\mathcal{A}_2^2\left[r_1^2 + r_2^2 - 2\kappa_1\kappa_2 r_1 r_2 \cos(\delta_1 - \delta_2)\right]. \tag{5.8}$$

The interference between the two indistinguishable paths to the final state provides sensitivity to the amplitudes of the $D^0 \to f$ and $\overline{D}^0 \to f$ decays at first order, which is exploited to determine the strong-phase differences. As was discussed in Sec. 2.5, and displayed through the measurement of γ in Chap. 4, such inputs are crucial for *CP*-violation measurements.

To date, all strong-phase measurements performed by the BESIII and CLEO collaborations have used C-odd $D\overline{D}$ pairs produced at the $\psi(3770)$ resonance. However, in principle, it is possible to use quantum-correlated $D\overline{D}$ pairs produced at higher centre-of-mass energies through $e^+e^- \to D\overline{D}$, $D^*\overline{D}$ and $D^*\overline{D}^*$ production. The D^* mesons decay into a D meson and a γ or π^0, which results in the six possible decay chains shown in Tab. 5.1. The γ and π^0 particles are C eigenstates with eigenvalues of $C_\gamma = -1$ and $C_{\pi^0} = +1$, respectively, and thus in the process $e^+e^- \to D\overline{D} + n\gamma + m\pi^0$, the C eigenvalue of the $D\overline{D}$ pair is

$$C = (C_\gamma)^{n+1} \times (C_{\pi^0})^m = (-1)^{n+1}, \tag{5.9}$$

which can be $+1$ or -1.

As discussed in Sec. 2.5.2, improving the precision on the strong-phase difference between $D^0 \to K^-\pi^+$ and $\overline{D}^0 \to K^-\pi^+$ decays, $\delta_D^{K\pi}$, is crucial to obtain the best limits on the CKM angle γ. To reach this goal requires using all available datasets, including those collected above the open charm threshold at BESIII, as is achieved for the first time in Chapter 7 by exploiting the quantum-correlated $D\overline{D}$ pairs produced in the decay chains shown in Tab. 5.1. The novel technique paves the way for future determinations of key hadronic charm inputs, both at BESIII and future colliders [103]. Finally, the C-even $D\overline{D}$ pairs, which are observed for the first time, have interesting prospects for time-integrated studies of the charm-mixing parameters. Such measurements are beyond the scope of this thesis but more detail can be found in Ref. [104].

Table 5.1: Decay chains resulting in quantum-correlated $D\overline{D}$ pairs with eigenvalue C produced through the $e^+e^- \to D\overline{D}$, $D^*\overline{D}$ and $D^*\overline{D}^*$ processes.

Production mechanism	C
$e^-e^- \to DD$	-1
$e^-e^- \to D^*\overline{D} \to DD\gamma$	$+1$
$e^-e^- \to D^*\overline{D} \to DD\pi^0$	-1
$e^-e^- \to D^*\overline{D}^* \to DD\gamma\gamma$	-1
$e^-e^- \to D^*\overline{D}^* \to DD\pi^0\gamma$	$+1$
$e^-e^- \to D^*\overline{D}^* \to DD\pi^0\pi^0$	-1

The above derivation for the decay rate of quantum-correlated $D\overline{D}$ pairs at the $\psi(3770)$ resonance is generalised using the amplitude,

$$|\mathcal{A}_{D\overline{D}}\rangle = \frac{1}{\sqrt{2}}\left(|D\overline{D}\rangle + C|\overline{D}D\rangle\right), \tag{5.10}$$

$$= \frac{1}{\sqrt{2}}\left(A_1\bar{A}_2 + C\bar{A}_1A_2\right), \tag{5.11}$$

which applies to $D\overline{D}$ pairs which are C-even or odd. The decay rate becomes

$$\Gamma(D\overline{D} \to f_1 \text{ vs. } f_2) = \mathcal{A}_1^2\mathcal{A}_2^2\left[r_1^2 + r_2^2 + 2C\kappa_1\kappa_2 r_1 r_2\cos(\delta_1 - \delta_2)\right]. \tag{5.12}$$

5.2 Charm-mixing effects

In deriving Eq. 5.12 charm mixing has been ignored, which is a good approximation for C-odd $D\overline{D}$ pairs, however, as will be seen, it is not a good assumption for the C-even $D\overline{D}$ pairs [90]. In the SM, the neutral mesons can mix into the anti-mesons and vice versa through the box diagrams displayed in Fig. 5.1. The physical states, defined as

$$|D_1\rangle = \frac{1}{\sqrt{2}}\left(|D^0\rangle + |\overline{D}^0\rangle\right), \tag{5.13}$$

$$|D_2\rangle = \frac{1}{\sqrt{2}}\left(|D^0\rangle - |\overline{D}^0\rangle\right), \tag{5.14}$$

are a superposition of the flavour states, and have a mass, m_i, and decay rate Γ_i. In these expressions, it is assumed that CP violation in charm mixing is

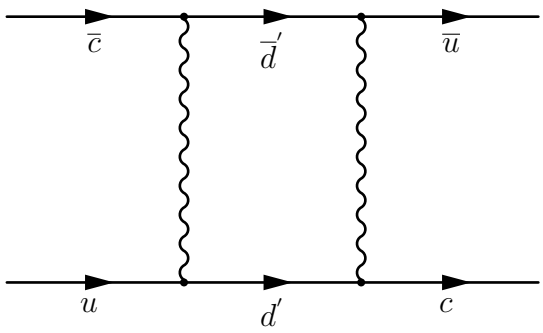

Figure 5.1: Box diagram for $D^0 - \overline{D}^0$ mixing.

small, which is expected in the SM because the CKM elements involved in the box diagrams are $V_{cq}V_{uq}^*$, where $q \in (d, s, b)$, which have an imaginary component which is $\mathcal{O}(10^{-5})$ [37]. Therefore, to a good approximation, the physical states are also *CP* eigenstates. The convention is set by the action of the *CP* operator on the D^0 flavour state, $CP|D^0\rangle = |\overline{D}^0\rangle$, and hence D_1 is *CP* even and D_2 is *CP* odd.

Due to the mixing, a D meson which is initially produced in the D^0 flavour state develops a $\overline{D}^0$ component, such that the rate of the $D \to f$ decay is found by integrating the square of the amplitude over time and phase space,

$$\begin{aligned}\Gamma(D \to f) &= \int |\langle f|D(t)\rangle|^2 dt\ d\mathbf{\Phi} \\ &= \int |g_+(t)\langle f|D^0\rangle + g_-(t)\langle f|\overline{D}^0\rangle|^2 dt\ d\mathbf{\Phi}, \\ &= \mathcal{A}^2\left[1 - \kappa r(y_D\cos\delta + x_D\sin\delta)\right], \end{aligned} \tag{5.15}$$

where terms $\mathcal{O}(x_D^2, y_D^2) \sim 10^{-5}$ are neglected. The decay rate for the inverse scenario, where a an initially-produced $\overline{D}^0$ meson develops a D^0 component, is

$$\Gamma(\overline{D} \to f) = \mathcal{A}^2\left[r^2 - \kappa r(y_D\cos\delta_D^{K\pi} - x_D\sin\delta_D^{K\pi})\right]. \tag{5.16}$$

In Eq. 5.15, the $g_\pm$ terms arise from time-evolving the physical states using the eigenvalues of the Schrödinger equation which describes the mixing, and are given by

$$g_+(t) = e^{-imt}e^{-\Gamma t/2}\cos\left[\frac{x_D t}{2} - \frac{iy_D\Gamma t}{2}\right] \tag{5.17}$$

$$g_-(t) = -e^{-imt}e^{-\Gamma t/2}i\sin\left[\frac{x_D t}{2} - \frac{iy_D\Gamma t}{2}\right], \tag{5.18}$$

where the following definitions are used,

$$\Gamma = (\Gamma_1 + \Gamma_2)/2 \tag{5.19}$$

$$M = (m_1 + m_2)/2 \tag{5.20}$$

$$2y_D\Gamma = \Gamma_1 - \Gamma_2 \tag{5.21}$$

$$x_D\Gamma = m_1 - m_2. \tag{5.22}$$

The x_D and y_D parameters are experimental observables which quantify charm mixing. Due to the GIM mechanism [105], x_D and y_D are expected to be small in the SM, but they can be enhanced in New Physics scenarios. Therefore, precisely measuring x_D and y_D is an important active area of research, and the current world averages are $x_D = (0.407 \pm 0.044)\%$ and $y_D = (0.645^{+0.024}_{-0.023})\%$ [36].

Having developed the mixing formalism for the decay of a single D meson, it is relatively trivial to include it in the description of the quantum-correlated $D\overline{D}$ pairs. The mixing-corrected amplitude is found by substituting $A_i \to g_+(t)A_i + g_-(t)\bar{A}_i$ and $\bar{A}_i \to g_-(t)A_i + g_+(t)\bar{A}_i$ into Eq. 5.2, such that it becomes

$$\begin{aligned}\langle f_1 f_2|\mathcal{A}_D\overline{D}\rangle(t) =& \frac{1}{\sqrt{2}}\Big[\Big(g_+(t_1)A_1 + g_-(t_1)\bar{A}_1\Big)\Big(g_-(t_2)A_2 + g_+(t_2)\bar{A}_2\Big) \\ &+C\Big(g_-(t_1)A_1 + g_+(t_1)\bar{A}_1\Big)\Big(g_+(t_2)A_2 + g_-(t_2)\bar{A}_2\Big)\Big].\end{aligned} \tag{5.23}$$

Then, the mixing-corrected decay rate is found by integrating over phase space and time,

$$\begin{aligned}\frac{\Gamma(D\overline{D} \to f_1 \text{ vs. } f_2)}{\mathcal{A}_1^2\mathcal{A}_2^2} =& \Big[r_1^2 + r_2^2 + 2C\kappa_1\kappa_2 r_1 r_2\cos(\delta_1 - \delta_2)\Big] \\ &- (1+C)y_D\Big[\kappa_1 r_1\cos\delta_1(1+r_2^2) + \kappa_2 r_2\cos\delta_2(1+r_1^2)\Big] \\ &- (1+C)x_D\Big[\kappa_1 r_1\sin\delta_1(1-r_2^2) + \kappa_2 r_2\sin\delta_2(1-r_1^2)\Big],\end{aligned} \tag{5.24}$$

where, again, terms $\mathcal{O}(x_D^2, y_D^2)$ are neglected.

5.3 Forbidden and enhanced final states

The $D\overline{D}$ pairs produced at higher energies have not previously been used, so it is necessary to show that they are quantum correlated with the expected C quantum

number. This is achieved using decays which are expected to be forbidden or enhanced relative to the scenario where the $D\overline{D}$ pair is not quantum correlated.

The first type of final state used are decays into two *CP* eigenstates. Ignoring mixing for now, the amplitude in Eq. 5.11 is transformed to the *CP* basis using Eqs. 5.13 and 5.14, which gives

$$|\mathcal{A}_{D\overline{D}}\rangle \propto (1+C)(|D_1D_1\rangle + |D_2D_2\rangle) + (1-C)(|D_2D_1\rangle - |D_1D_2\rangle). \tag{5.25}$$

Clearly, the decay of a $D\overline{D}$ pair with $C = -1$ into two *CP* even or two *CP* odd final states is forbidden, whilst the same final state would be enhanced by a factor of 2 when $C = +1$. The opposite is true for decays into final states with different *CP* eigenvalues. As an interesting aside, these final states have prospects for measurements of direct *CP* violation in charm mesons [106].

The hadronic parameters in decays to *CP* eigenstates are $r = 1$, $\kappa = 1$ and $\delta = 0$ or π for two-body *CP* even and odd final states, respectively. Using Eq. 5.25, which does now consider the mixing correction, it can be shown that the rate of quantum-correlated $D\overline{D}$ pairs decaying into two *CP* eigenstates is

$$\frac{\Gamma(D\overline{D} \to f_1 \text{ vs. } f_2)}{\mathcal{A}_1\mathcal{A}_2^2} = 2\left[1 + C\lambda_1\lambda_2 - (1+C)y_D(\lambda_1+\lambda_2)\right], \tag{5.26}$$

where $\lambda = \cos\delta = 1$ (-1) for *CP*-even (odd) final states. The charm-mixing correction is $\sim 2y_D \sim 1\%$, much smaller than the expected sensitivity.

The three-body $D \to \pi^+\pi^-\pi^0$ decay is also used for this study. It is a mixed state of *CP*-even and odd contributions due to the intermediate resonances. The *CP*-even fraction has been precisely measured to be $F_+^{\pi\pi\pi^0} = 0.9406 \pm 0.0042$ [107], and therefore the above equation can be used identically by replacing λ with the average *CP* content, given by $\lambda_{\pi\pi\pi^0} = (+1 \times F_+^{\pi\pi\pi^0}) + (-1 \times (1 - F_+^{\pi\pi\pi^0})) = 2F_+^{\pi\pi\pi^0} - 1$.

The $D\overline{D} \to K^-\pi^+$ vs. $K^-\pi^+$ decays are also used to demonstrate the quantum correlations. Again, initially ignoring mixing, it is evident from Eq. 5.11 that this channel is forbidden when $C = -1$ and enhanced when $C = +1$ through the

substitutions $A_2 = A_1$ and $\bar{A}_2 = \bar{A}_1$. The mixing-corrected decay rate is

$$\frac{\Gamma(D\overline{D} \to K^-\pi^+ \text{ vs. } K^-\pi^+)}{\mathcal{A}^4_{K^-\pi^+}} = 2(1+C)(r_D^{K\pi})^2 \left[1 - \frac{(y_D \cos\delta_D^{K\pi} + x_D \sin\delta_D^{K\pi})}{r_D^{K\pi}}\right]. \tag{5.27}$$

From the world-average values of x_D, y_D, $r_D^{K\pi}$ and $\delta_D^{K\pi}$, the contribution from the mixing term in Eq. 5.27 enhances the decay rate by an additional 10%.

5.4 Measuring $\delta_D^{K\pi}$ using quantum-correlated $D\overline{D}$ pairs

In Chap. 7, the strong-phase difference between $D^0 \to K^-\pi^+$ and $\overline{D}^0 \to K^-\pi^+$ decays, denoted $\delta_D^{K\pi}$, is measured using quantum-correlated $D\overline{D} \to K^-\pi^+$ vs. f decays. The final state, f, is referred to as the *tag mode* throughout. Two types of tag are used in the analysis: *CP*-even and odd eigenstates, and $D \to K^0_S\pi^+\pi^-$ decays.

The decay rate for the *CP* tags is

$$\frac{\Gamma(D\overline{D} \to K^-\pi^+ \text{ vs. } CP)}{\mathcal{A}_{K^-\pi^+}\mathcal{A}^2_{CP}} = 1 + (r_D^{K\pi})^2 + 2C\lambda r_D^{K\pi}\cos\delta_D^{K\pi} - (1+C)\lambda y_D, \tag{5.28}$$

where only terms larger than $\mathcal{O}(r_D^{K\pi}y_D, r_D^{K\pi}x_D)$ are included. The *CP* tags only constrain the parameter $r_D^{K\pi}\cos\delta_D^{K\pi}$, so used in isolation they find multiple solutions for $\delta_D^{K\pi}$. Once again, the ambiguity is resolved using the $D \to K^0_S\pi^+\pi^-$ decay as a tag mode, where the independent constraints from different regions of phase space produce a single solution for $\delta_D^{K\pi}$.

By comparing Eqs. 5.4-5.7 with Eqs. 2.33-2.35, it is evident that the quantum-correlated $D\overline{D} \to f_1$ vs. $K^0_S\pi^+\pi^-$ decay rate in a region of phase-space with index, i, is found by substituting $\mathcal{A}_2^2 \to K_i$, $r_2^2\mathcal{A}_2^2 \to K_{-i}$, $\kappa_2\cos\delta_2 \to c_i$ and $\kappa_2\sin\delta_2 \to s_i$ into Eq. 5.25, which becomes

$$\begin{aligned}\frac{\Gamma(D\overline{D} \to f_1 \text{ vs. } K^0_S\pi^+\pi^-)}{\mathcal{A}_1^2} &= \left[r_1^2K_i + K_{-i} + 2C\kappa_1 r_1\sqrt{K_iK_{-i}}(c_i\cos\delta_1 + s_i\sin\delta_1)\right] \\ &- (1+C)y_D\left[\kappa_1 r_1\cos\delta_1(K_i + K_{-i}) + c_i\sqrt{K_iK_{-i}}(1+r_1^2)\right] \\ &- (1+C)x_D\left[\kappa_1 r_1\sin\delta_1(K_i - K_{-i}) + s_i\sqrt{K_iK_{-i}}(1-r_1^2)\right].\end{aligned} \tag{5.29}$$

The amplitude of the $D^0 \to f_1$ decay is clearly independent of the $D \to K^0_S\pi^+\pi^-$ decay phase-space coordinates, and thus the right-hand-side of the above expression can be interpreted as the fraction of $D\overline{D} \to f_1$ vs. $K^0_S\pi^+\pi^-$ decays in a particular region, denoted Y_i. For $D\overline{D} \to K^-\pi^+$ vs. $K^0_S\pi^+\pi^-$ decays the Y_i becomes

$$\begin{aligned} Y_i = &\left[(r_D^{K\pi})^2 K_i + K_{-i} + 2C r_D^{K\pi}\sqrt{K_i K_{-i}}(c_i \cos\delta_D^{K\pi} + s_i \sin\delta_D^{K\pi})\right] \\ &- (1+C)\sqrt{K_i K_{-i}}(y_D c_i + x_D s_i), \end{aligned} \tag{5.30}$$

where only terms larger than $\mathcal{O}(r_D^{K\pi} y_D, r_D^{K\pi} x_D)$ are included.

As discussed in detail in Sec. 2.5.2, the primary motivation to measure $\delta_D^{K\pi}$ is to improve the precision, which will aid studies of the CKM angle γ. However, there are additional incentives. In recent years, a proposed Super τ-Charm Factory (STCF) [103] has been a hot topic in particle physics. The e^+e^- collider aims to operate in the energy range $\sqrt{s} = 2 - 7\,\text{GeV}$ and is expected to achieve enormous datasets of around one ab^{-1} each year[2]. For the most part, the STCF will operate above the $\psi(3770)$ resonance, around $\sqrt{s} \sim 4\,\text{GeV}$, where a wide range of physics is possible through the $\tau^+\tau^-$, $D_s^+ D_s^-$, $D^{*0}\overline{D}^0$ and $D^0\overline{D}^0$ pairs that are produced. The determination of $\delta_D^{K\pi}$ in Chap. 7 serves as a proof-of-principle for measurements in this regime, and enables the full leverage of the high-energy datasets in future colliders.

5.5 Measuring the hadronic parameters in $D \to K^0_S\pi^+\pi^-$ decays

The hadronic parameters in the $D \to K^0_S\pi^+\pi^-$ decays are determined using quantum-correlated $D\overline{D}$ pairs produced at $\psi(3770)$ [9, 10]. The c_i and s_i are most precisely measured using $D\overline{D} \to K^0_S\pi^+\pi^-$ vs. $K^0_S\pi^+\pi^-$ decays. The number of decays in a category labelled ij, where i and j are the indices corresponding to the regions of phase space where the two D decays fall, is given by

$$N_{ij} \propto K_i K_{-j} + K_{-i} K_j - 2\sqrt{K_i K_{-j} K_{-i} K_j}(c_i c_j + s_i s_j). \tag{5.31}$$

[2]For reference, in 2023 the BESIII experiment collected a sample corresponding to an integrated luminosity of 8.16 fb^{-1} at $\psi(3770)$.

Additional precision is achieved on the c_i parameters using *CP*-eigenstate tags, where, using Eq. 5.29, the fractional yield is

$$Y_i = K_i + K_{-i} - 2\lambda\sqrt{K_i K_{-i}}c_i. \tag{5.32}$$

Since $\sin\delta_{CP} = 0$ the *CP* tags cannot be used to measure the s_i parameters.

From the above equation it is evident that extracting the c_i and s_i parameters requires prior knowledge of the K_i, which are determined using tags which specify the flavour of each D meson. The best example is $D^0 \to K^-e^+\nu_e$ decays, where the charge on the kaon unambiguously indicates the flavour of the parent D meson, and thus that of the D meson that decayed to the $K^0_S\pi^+\pi^-$ final state. Therefore, the fraction of $D\overline{D} \to K^+e\overline{\nu}_e$ vs. $K^0_S\pi^+\pi^-$ decays in each region of phase-space is K_i, whilst that of the $D\overline{D} \to K^-e^+\nu_e$ vs. $K^0_S\pi^+\pi^-$ decays is K_{-i}. Hence, by reconstructing $D\overline{D}$ decays to $K^0_S\pi^+\pi^-$ and many types of tag, measurements of the K_i, c_i and s_i values are accomplished at BESIII [9, 10].

6 The BESIII experiment

Contents

6.1 Overview

The third Beijing Spectrometer (BESIII) [108], along with its predecessors, BES [109] and BESII [110], have studied the τ-charm energy region for over 30 years. A variety of physics is performed at BESIII, including precise measurements of the τ mass [111], world-leading contributions to the CKM elements [112, 113] and discoveries of new exotic particles [114]. Finally, quantum-correlated $D\overline{D}$ pairs are uniquely accessible at BESIII, and are of vital importance to studies of *CP* violation and charm mixing [10, 13].

BESIII is located in the Beijing Electron Positron Collider (BEPCII) [115] at the Institute of High Energy Physics. A 202 m linear accelerator is used to

boost the electron and positron beams before they are injected into a storage ring with a circumference of 238 m. The beams collide with a crossing angle of ± 11 mrad at centre-of-mass energies between $\sqrt{s} = 2 - 4.95$ GeV, and with a maximum luminosity of $1 \times 10^{-33}\,\mathrm{cm}^{-2}\,\mathrm{s}^{-1}$ at the charm threshold where $\sqrt{s} = 3.77$ GeV [116]. These high luminosities are achieved using 93 bunches per beam, with a spacing of 8 ns, and quadrupole magnets at the interaction point, which squeeze the beams. The beams are topped up during operation to ensure the particle densities remain consistently high.

Table 6.1: Integrated luminosity of the datasets used in the measurement described in Chap. 7 at each centre-of-mass energy.

Centre-of-mass energy (GeV)	Integrated luminosity (fb^{-1})	Year
4.13	0.402	2019
4.16	0.409	2019
4.18	3.189	2016-17
4.19	0.527	2017
4.20	0.526	2017
4.21	0.517	2017
4.22	0.515	2017
4.23	1.056	2013

The majority of the BESIII data is collected at the $\psi(3770)$ resonance, where many $D\overline{D}$ pairs are produced and a clean analysis can be performed by reconstructing both D decays. In fact, the collaboration boasts the world's largest dataset at the charm threshold, which corresponds to an integrated luminosity of around $20\,\mathrm{fb}^{-1}$ [117]. The first $3\,\mathrm{fb}^{-1}$ of this dataset were collected in 2010 and 2011. The instantaneous luminosity of the BEPCII collider was gradually improved over time, and increased by a factor of 5 between 2010 and 2016, when it reached the design goal [118]. In 2021, the BEPCII collider once again operated at the charm threshold for around 2 years, and this time a dataset with an integrated luminosity of around

$17\,\text{fb}^{-1}$ was collected. Despite the large intermediate-time period the reconstruction efficiency differences in the two datasets are small.

Over the years, the BESIII experiment has also operated at higher centre-of-mass energies, as detailed in Tab. 6.1. For example, in 2016, a sample of around $3.2\,\text{fb}^{-1}$ for dedicated studies of D^* mesons was collected at $\sqrt{s} = 4.18$ GeV. In addition, between 2013 and 2019, a further $\sim 4\,\text{fb}^{-1}$ was collected at various centre-of-mass energies between $\sqrt{s} = 4.13 - 4.23$ GeV in search of new exotic particles. In these energy regions the cross-sections of the $e^+e^- \to D\overline{D}$, $D^*\overline{D}$ and $D^*\overline{D}^*$ processes are large [119]. Therefore, the accumulated dataset, which has an integrated luminosity of around $7.1\,\text{fb}^{-1}$, is ideal for the measurement of the strong-phase difference, $\delta_D^{K\pi}$, discussed in the next chapter.

A schematic of the BESIII spectrometer [108], which has an angular acceptance that is 93% of the 4π solid angle, can be found in Fig. 6.1. The shape of the detector leads to a natural description in a cylindrical coordinate system with radial position, r, azimuthal angle, ϕ, and z-axis position, z. The innermost component is a Multilayer Drift Chamber (MDC) used for reconstructing charged tracks. The next layer measures a particles time-of-flight (TOF) using scintillators, which is used to identify it's species. A superconducting magnet surrounds the TOF, and along with information provided by the MDC, allows the momentum of charged tracks to be determined. The outer two layers are the Electromagnetic Calorimeter (EMC), which measures the energies of electrons and photons, and the Muon Chamber (MUC). The remainder of this chapter discusses each detector sub-component.

6.2 Multilayer drift chamber

The MDC is divided into inner and outer regions and extends from a radius of 59 mm to around 810 mm. The separated design allows the former, which lies just 2 mm from the beam pipe, to be replaced in case of performance degradation due to radiation damage. Furthermore, the inner region also has stepped conical shaped end caps, as can be seen in Fig. 6.1, to accommodate exterior quadrupole magnets

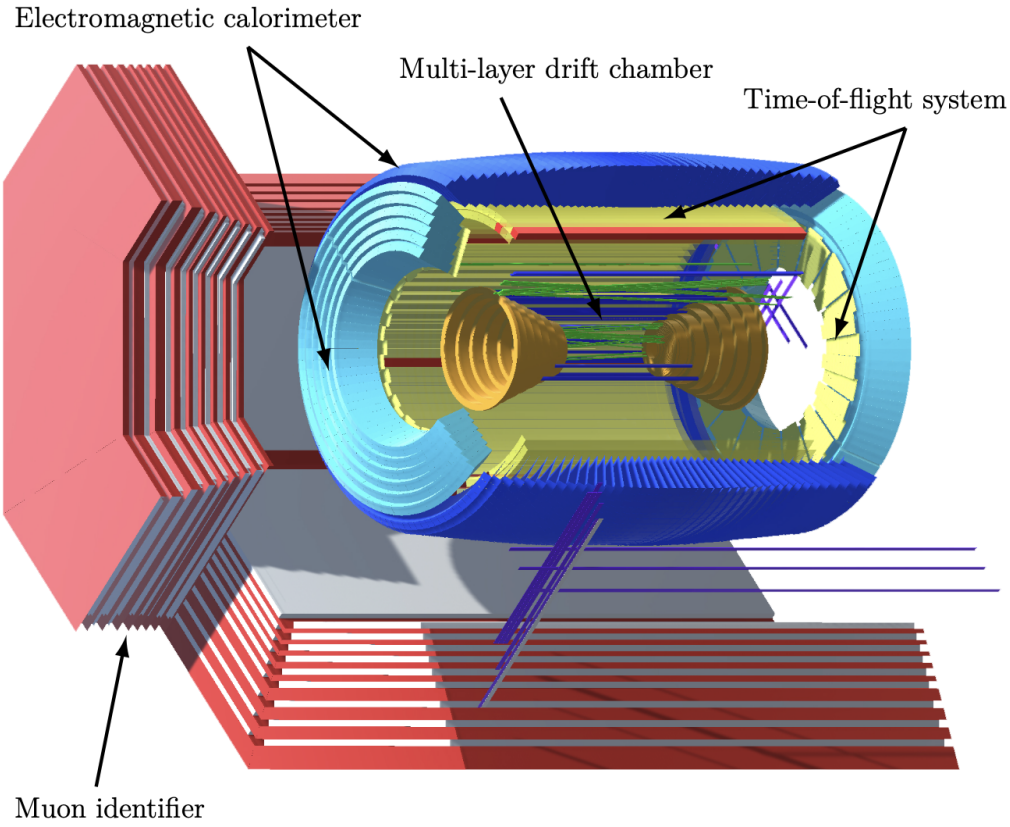

Figure 6.1: The BESIII detector [120].

which focus the beams at the interaction point. As a consequence, the angular acceptance of the innermost point is $|\cos\theta| < 0.93$, where θ is the angle with respect to the beam axis, whereas it is $|\cos\theta| < 0.83$ in the outer region of the MDC.

When a charged particle enters the MDC volume it ionises the gas inside, which is a mixture of 60% helium and 40% propane that is chosen to provide good performance whilst minimising multiple scattering. The resulting electrons drift towards grounded sense wires due to the electric field that is produced by field wires with a potential of 2.2kV. The drift time gives the radial distance of the track from the sense wire. Eight field wires surround each sense wire, forming a 12 mm (16 mm) square cell in the inner (outer) region. There are 43 layers of these cells, as shown in Fig. 6.2. Hits in multiple layers allows the two-dimensional (radial and azimuthal) trajectory of a track to be reconstructed. The position in the third dimension, along the beam axis, is determined using a stereo geometry where layers

of wires are angled at around ±3° with respect to the axial layers.

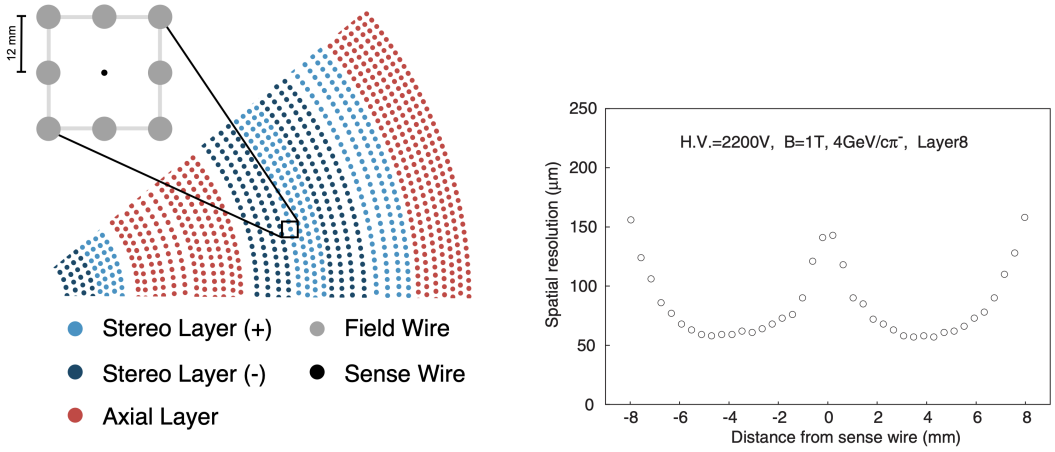

Figure 6.2: The left plot displays the projection of the MDC wires onto the $r - \phi$ plane [121]. The right plot shows the spatial resolution as a function of radial distance from the sense wire [122].

The momentum is estimated from the curvature of each track in the 1T field from the magnet. The momentum resolution is determined to be 0.5% for a 1 GeV track, and is dominated by two effects which roughly contribute equally, multiple scattering and the spatial resolution. The former is determined to be 0.35% using an empirical formula which depends on the magnetic field strength, the length of the track and the radiation length of the gas. Whereas the latter is measured in a test beam study using a prototype of the drift chamber with only 12 layers [122]. Figure 6.2 shows the spatial resolution as a function of the drift distance from a sense wire. The finite resolution arises because the drift electrons arrive at different times, and is worst at the cell edges where the electric field is distorted. On average the spatial resolution is around 110 μm.

The second purpose of the MDC is to measure the energy loss per unit distance due to the ionisation, $\mathrm{d}E/\mathrm{d}x$, which can be used to identify particles. Two distinct particles with the same momentum will have different velocities, and therefore, through the Bethe-Bloch formula they can be discriminated using $\mathrm{d}E/\mathrm{d}x$. The energy loss at each point in the MDC is proportional to the number of ionisation electrons, and hence the height of the corresponding electrical signal (pulse).

Measuring the pulse height as the track traverses the material gives $\mathrm{d}E/\mathrm{d}x$, which is measured with a resolution of around 6%. Figure 6.3 shows the discrimination between the various species of particle. Kaons and pions can be separated using $\mathrm{d}E/\mathrm{d}x$ with a 3σ significance below a momentum of 0.6 GeV/c.

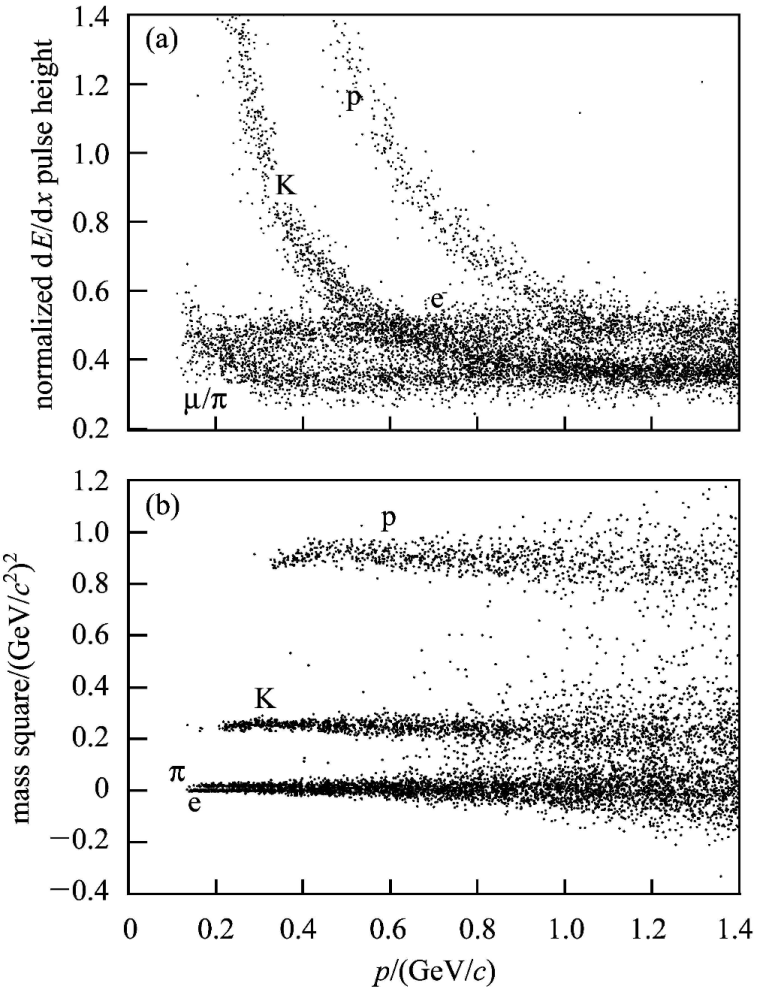

Figure 6.3: Discrimination between the particle species using (top) $\mathrm{d}E/\mathrm{d}x$ and (bottom) time-of-flight measurements [123].

6.3 Time-of-flight detector

The mass of a particle, m, can be measured using knowledge of its momentum, p, and distance travelled, L, in time, t, through the relations

$$m^2 = p^2 \left(\frac{1 - \beta^2}{\beta^2} \right),$$
$$\beta = \frac{L}{ct}. \tag{6.1}$$

At BESIII, the distance and momentum are provided by the MDC, and the time is measured by the TOF detector. Figure 6.3 shows the squared mass of different species as a function of momentum.

The TOF detector is composed of a barrel and two end caps. The former consists of two layers of 88 axially-arranged plastic scintillator bars with photomultiplier tubes at both ends. The timing resolution in the barrel is around 80 ps and is dominated by intrinsic effects, such as the spread in the times that the photons arrive at the PMT. The end caps contain a single layer of 48 scintillators arranged in a fan-like pattern. In 2015, the scintillators in the end cap were replaced with Multigap Resistive Plate Chambers (MPRCs), which improved the timing resolution from 110 ps to 65 ps, and allowed discrimination between pions and kaons at higher momentum [124].

6.4 Electromagnetic calorimeter

The primary purpose of the EMC is to measure the energies of photons and electrons. Good spatial resolution is another important feature, which is essential for reconstructing the decays of neutral pions. Finally, the EMC provides discrimination between electrons and charged pions.

Similarly to the TOF detector, the EMC consists of a barrel and two end caps. The barrel is composed of 44 rings along the beam axis, each with 120 caesium-iodide crystals that are doped with tellurium and are individually read out. The end caps contain six concentric rings each with 80 crystals. The choice of crystal

permits a high light yield, which is vital for detecting low momentum photons that originate from radiative processes and π^0 decays.

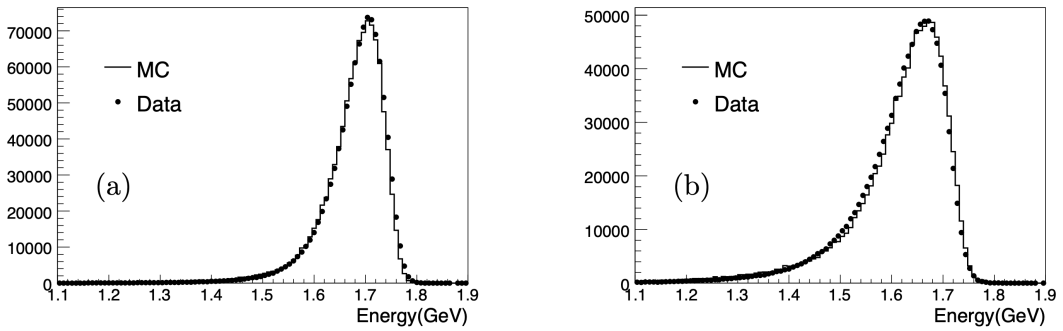

Figure 6.4: Energy of $e^{\pm}$ from Bhabha scattering in the (left) barrel and (right) end caps of the EMC [125].

The energy resolution of electrons is studied using Bhabha scattering events [125]. Figure 6.4 shows the energy distribution in data and simulation of the $e^{\pm}$ in the barrel and end cap. The resolution in the former is $\sim 2.5\%$, whilst it is slightly larger in the latter, $\sim 5\%$, because there is more intervening dead material. The low-energy tail is primarily caused by the shower leaking outside of the cluster of crystals associated with the particle. The energy resolution of photons is determined to be similar by studying $e^+e^- \to \gamma\gamma$ diphoton production [125].

6.5 Muon chamber

The outermost sub-component is the MUC, which has the purpose of identifying muons. Due to the material in the inner regions, primarily the EMC, the MUC is only effective above a momentum of around 0.4 GeV. The barrel part of the MUC is divided into octants, each containing nine layers of Resistive Plate Chambers (RPCs) interspersed with the steel from the flux return yoke of the magnet, which acts as a natural absorber. The end caps are also arranged as octants, but in the $r - \phi$ plane and with only eight layers of RPCs. Limited spatial resolution is achieved by alternating the position of the readout strips to allow determination of the z and ϕ coordinates.

6.6 Trigger

The rate of interesting physics events at BESIII is at most around 2 kHz, whereas the beam-related backgrounds, such as lost particles or Coulomb scattering, occur around one thousand times more frequently [126]. The role of the trigger is to reduce these backgrounds to a lower rate than the physics events, whilst maintaining a high signal efficiency. A two-stage trigger is adopted. Events that pass the first stage (L1), which is hardware based, are passed to the second stage (L3), which uses software.

The L1 trigger applies raw information from the MDC, TOF and EMC detectors to create up to sixteen dedicated channels, which have a combined rate of 4 kHz and apply requirements that are driven by studies of simulation. An event which passes any of these channels is saved. For example, a typical hadronic trigger requires at least one track in the MDC, hits in the TOF detector and a shower in the EMC [127].

The second stage uses information from the full event to categorise different processes, again based on requirements from simulation [128]. The L3 trigger reduces the background by a further factor of 2, such that the corresponding rate is around 1 kHz. The signal efficiency of the BESIII trigger is close to 100% for hadronic final states [127, 128].

6.7 Simulation at BESIII

The production of all processes through electron-positron annihilation is simulated using KKMC [129, 130], which accounts for initial state radiation (ISR) and the energy spread of the beams. The decays of the final-state particles are handled by EVTGEN [83, 131] using branching fractions from the Particle Data Group [33] or LUNDCHARM [132, 133], and final-state radiation (FSR) is accounted for by PHOTOS [84]. The response of the detector is simulated by a GEANT4-based [86] software package.

At BESIII, inclusive simulation samples that account for all production processes and particle decays are centrally produced. In the measurement of $\delta_D^{K\pi}$ described in

the next chapter, the simulation is used to determine signal efficiencies, invariant-mass shapes and to estimate background contributions. The inclusive sample ignores quantum correlations, which does not effect the signal efficiencies or mass shapes, but it can impact the expected background yields, and therefore manual corrections are applied where appropriate using known hadronic inputs.

7

Measurement of the strong-phase difference between $D^0 \to K^-\pi^+$ and $\overline{D}^0 \to K^-\pi^+$ decays at BESIII

Contents

7.1 Overview

The measurement described in this chapter is the first to exploit quantum-correlated $D\overline{D}$ pairs produced at centre-of-mass energies above the $\psi(3770)$ resonance. A dataset is used which corresponds to an integrated luminosity of around $7.13\,\text{fb}^{-1}$, collected between $\sqrt{s} = 4.13 - 4.23\,\text{GeV}$ (see Tab. 6.1 for a detailed breakdown). At these centre-of-mass energies, the $D\overline{D}$ pairs can be produced through the $e^+e^- \to D\overline{D}$, $e^+e^- \to D^*\overline{D}$ and $e^+e^- \to D^*\overline{D}^*$ processes, which have large cross-sections as shown in Fig. 7.1. The D^* mesons decay into a D meson and γ or a π^0, resulting in six possible decay chains shown in Tab. 5.1 with quantum-correlated $D\overline{D}$ pairs in C-even or odd eigenstates. To exploit the quantum correlations for a measurement of $\delta_D^{K\pi}$, pure samples of the $D\overline{D}$ pairs from each decay chain must be isolated, which is achieved through the selection criteria outlined in Sec. 7.3.

Given the novelty of the measurement, it is necessary to show that the $D\overline{D}$ pairs produced in each decay chain exhibit the expected behaviour, or in other words, that they are coherently correlated with the predicted C eigenvalue. This is achieved by examining the rates of $D\overline{D}$ decays to final states which are forbidden or enhanced depending on the value of C, as discussed in Sec. 7.4. Then, having demonstrated

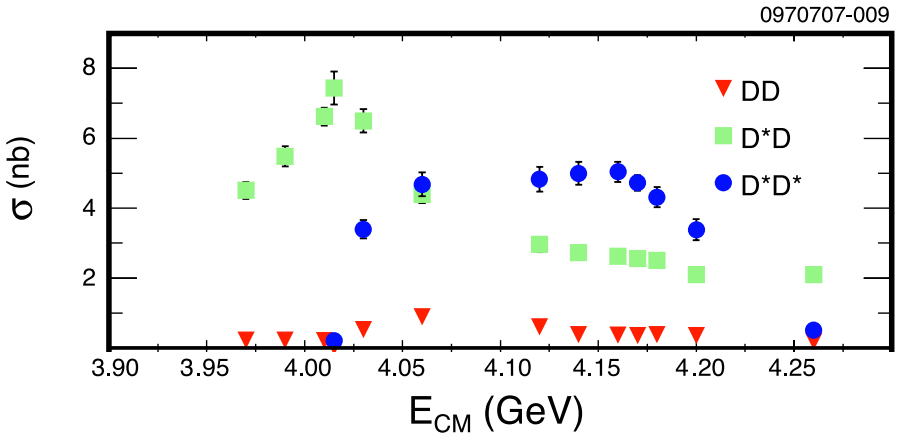

Figure 7.1: Cross-sections of the $e^+e^- \to D\overline{D}$, $D^*\overline{D}$ and $D^*\overline{D}^*$ processes measured by the CLEO experiment [119].

the quantum correlations, the $D\overline{D}$ pairs are used to measure the strong-phase difference $\delta_D^{K\pi}$. The observables, $r_D^{K\pi}\cos\delta_D^{K\pi}$ and $r_D^{K\pi}\sin\delta_D^{K\pi}$, are determined using $D\overline{D} \to K^-\pi^+$ vs. f decays, where f is a CP eigenstate or $K^0_S\pi^+\pi^-$, and are combined to find $\delta_D^{K\pi}$ as detailed in Secs. 7.5–7.10.

Throughout this chapter, $D\overline{D} \to K^-\pi^+$ vs. $K^+\pi^-$ decays are used as a control channel because the sample displays large yields and a high purity. Furthermore, the decay rate is approximately unaffected by the quantum correlations. In one path to the final state both decays are Cabibbo favoured, whilst in the other, both are doubly Cabibbo suppressed, so the interference effects are small. From Eq. 5.25, the decay rate of $D\overline{D} \to K^-\pi^+$ vs. $K^+\pi^-$ decays is

$$\frac{\Gamma(D\overline{D} \to K^-\pi^+ \text{ vs. } K^+\pi^-)}{\mathcal{A}^4_{K^-\pi^+}} = 1 + 2C(r_D^{K\pi})^2\cos(2\delta_D^{K\pi}) - 2r_D^{K\pi}(1+C)(y_D\cos\delta_D^{K\pi} - x_D\sin\delta_D^{K\pi}). \quad (7.1)$$

In the uncorrelated scenario, the decay rate is given by

$$\left[\Gamma(D^0 \to K^-\pi^+)\Gamma(\overline{D}^0 \to K^+\pi^-) + \Gamma(\overline{D}^0 \to K^-\pi^+)\Gamma(D^0 \to K^+\pi^-)\right]/\mathcal{A}^4_{K^-\pi^+} = 1 - 2r_D^{K\pi}(y_D\cos\delta_D^{K\pi} + x_D\sin\delta_D^{K\pi}), \quad (7.2)$$

using Eqs. 5.15 and 5.16. By substituting the values of $r_D^{K\pi}$, $\delta_D^{K\pi}$, x_D and y_D from Ref. [15] into the ratio of Eqs. 7.1 and 7.2, it can be shown that the quantum-

correlated $D\overline{D} \to K^-\pi^+$ vs. $K^+\pi^-$ decay rate is only enhanced by around $\pm 0.7\%$, where the sign depends on C.

7.2 Selection of D-decay candidates

The selection of candidates is a two-step process. In the first stage, which is outlined in this section, the D decays are reconstructed in six final states: $K^\mp\pi^\pm$, K^+K^-, $\pi^+\pi^-$, $\pi^+\pi^-\pi^0$, $K^0_S\pi^0$ and $K^0_S\pi^+\pi^-$, by applying standard BESIII requirements that are used by the whole collaboration. If there are multiple candidates, the best $D\overline{D}$ pair is chosen to be that which has an average invariant mass closest to the PDG value[1] for the D^0 meson. In the second stage, which is the subject of the next section, the kinematics of the reconstructed $D\overline{D}$ pair are used to distinguish between the various production mechanisms.

7.2.1 Charged tracks from D decays

All charged tracks which are reconstructed as the children of the D decays are required to be in the acceptance of the MDC, $|\cos\theta| < 0.93$, so the momentum can be determined. To reduce backgrounds originating from the beam and cosmic rays the tracks are also required to have an impact parameter less than 1 cm and 10 cm in the transverse and beam directions, respectively. Finally, PID criteria are imposed. A likelihood, $\mathcal{L}$, is constructed under the hypothesis of each particle species using TOF and $\mathrm{d}E/\mathrm{d}x$ information. Tracks reconstructed as kaons are required to satisfy $\mathcal{L}(K) > \mathcal{L}(\pi)$, and the opposite is necessary for pions.

7.2.2 Photon requirements

To reduce backgrounds from electrical noise and synchrotron radiation, the photon candidates must shower within 700 ns of the event time and produce a minimum energy deposit of 25 (50) MeV in the barrel (end cap). Finally, photons produced in radiative decays are suppressed by requiring the angle of the shower and closest track to be more than 10°.

[1]The 2024 edition of the PDG [33] is used throughout this chapter.

7.2.3 Selection of π^0 decays

The π^0 mesons are reconstructed through their decay into the $\gamma\gamma$ final state using two photons which satisfy the criteria in the previous section. To ensure a good energy resolution at least one of the photons must produce a shower in the barrel. The invariant mass of the two photons must be $m_{\gamma\gamma} \in [115, 150]\,\mathrm{MeV}/c^2$, where an asymmetric region is chosen due to shower leakage. The resolution on the invariant mass of the D-decay candidates is improved by using the momentum of the π^0 meson determined in a kinematic fit where the mass of the π^0 is constrained to the PDG value. The kinematic fit must converge with $\chi^2 < 50$.

7.2.4 Selection of K^0_S mesons

The K^0_S mesons are reconstructed through the $K^0_S \to \pi^+\pi^-$ decay. Both charged tracks are required to be in the acceptance of the MDC with a transverse impact parameter $< 20\,\mathrm{cm}$, to allow for the relatively long lifetime of the K^0_S meson, and have a combined invariant mass which satisfies $m_{\pi^+\pi^-} \in [0.487, 0.511]\,\mathrm{GeV}/c^2$. A kinematic fit is performed in which the mass of the K^0_S meson is constrained to the PDG value, and the tracks are required to originate from a common vertex. The kinematic fit, which must converge with $\chi^2 < 100$, finds the decay length, L, and it's uncertainty, σ_L. The ratio of these two quantities, L/σ_L, is the *flight-distance significance*, which is required to be greater than 2. In the analysis described in this chapter, it is important to distinguish $D \to K^0_S\pi^0$ decays from $D \to \pi^+\pi^-\pi^0$ decays because they have opposite *CP* eigenvalues, which is achieved by requiring $L/\sigma_L < 2$ on the latter.

7.3 Isolating the production mechanisms

Requirements are devised to distinguish between the $D\overline{D}$ pairs from each production mechanism in Tab. 5.1. The decay chains are minimally reconstructed to maximise the selection efficiencies, which are poor for the low momentum photons produced in $D^* \to \gamma D$ and $D^* \to [\gamma\gamma]_{\pi^0} D$ decays. Therefore, the γ and π^0 particles produced

in the D^* decays are inferred through the missing energy and missing mass of the remaining particles in the event after reconstruction, given that the collision energy is known. The selection begins by separating the three processes $e^+e^- \to D\overline{D}$, $D^*\overline{D}$ and $D^*\overline{D}^*$, before discriminating between the possible D^* decays.

7.3.1 Isolating $e^+e^- \to D\overline{D}$ production

The $e^+e^- \to D\overline{D}$ process is isolated from the others using the missing energy in the event after reconstructing the $D\overline{D}$ pair. The missing energy is given by,

$$E_{\text{miss}} \equiv E - \sqrt{|\vec{p}_{D_1}|^2 + m^2_{D^0}} - \sqrt{|\vec{p}_{D_2}|^2 + m^2_{D^0}}, \tag{7.3}$$

where E is the collision energy and $\vec{p}_D$ is the momentum of the D meson. The latter is found in a kinematic fit which constrains the masses of all intermediate particles in the event to their PDG values. In $e^+e^- \to XD\overline{D}$ production, where X is a collection of photons and neutral pions, the missing energy will be that of X. So, for the $e^+e^- \to D\overline{D}$ process, $E_{\text{miss}} \sim 0\,\text{GeV}$, whilst it is larger for those with D^* mesons. This is shown in Fig. 7.2 for $D\overline{D} \to K^-\pi^+$ vs. $K^+\pi^-$ decays in simulation.

Each process displays a long tail at higher missing energies. This is caused by events with initial state radiation (ISR), where the e^- or e^+ radiates a photon and effectively reduces the energy of the $D\overline{D}$ pair. The shape of the tails are dictated by the energy of the ISR photon. The best example of this can be seen in the E_{miss} distribution of candidates which originate from the $e^+e^- \to D^*\overline{D}^*$ process, where the ISR tail is significantly shorter than it is for the others. For production of a $D^*\overline{D}^*$ pair to be kinematically allowed the ISR photon must have an energy less than $E - 2m_{D^{*0}}$, which in this dataset corresponds to a maximum of $\sim 220\,\text{MeV}$. The same threshold is $\sim 360\,\text{MeV}$ for $e^+e^- \to D^*\overline{D}$ production. A consequence of the ISR is that the selection requirements discussed throughout this section do not isolate pure samples of each decay chain. The *cross-feed* is accounted for in the measurement through the procedure outlined in Sec. 7.4.

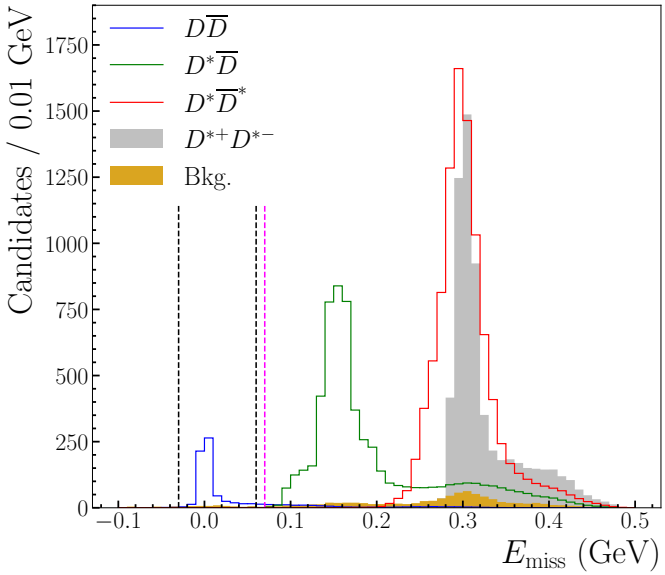

Figure 7.2: The missing energy in the event after reconstructing the $D\overline{D}$ decay for simulated $D\overline{D} \to K^-\pi^+$ vs. $K^+\pi^-$ candidates. The black dashed lines display the requirements placed to isolate the $D\overline{D}$ pairs produced through the $e^+e^- \to D\overline{D}$ process. The magenta lines show the inverse requirement placed to isolate $D\overline{D}$ pairs from $e^+e^- \to D^*\overline{D}$ and $D^*\overline{D}^*$ production.

7.3.2 Distinguishing $e^+e^- \to D^*\overline{D}$ from $e^+e^- \to D^*\overline{D}^*$

In principle, the E_{miss} can also be used to separate the $e^+e^- \to D^*\overline{D}$ and $e^+e^- \to D^*\overline{D}^*$ processes. However, the *recoil mass* of the D mesons is used instead as it displays a higher selection efficiency due to improved resolution. The recoil mass is defined as the invariant mass of the remaining particles in an event after reconstructing the decay of a single D meson, and is given by,

$$M_{\text{rec},D} = \sqrt{(p - p_D)^2}, \tag{7.4}$$

where $p = (E, \vec{0})$ and $p_D = (E_D, \vec{p}_D)$ are the four momentum of the beams and the D meson, respectively. For the $D\overline{D}$ pairs that originate from $e^+e^- \to D^*\overline{D}$ production the recoil mass of each D meson will be close to that of the D^* meson, and it will be larger for those from the $e^+e^- \to D^*\overline{D}^*$ process.

The recoil mass is computed for both D-decay candidates in the event, and a requirement is placed on the one which is closest to the mass of the D^{*0} meson to distinguish between the $D\overline{D}$ pairs which arise from $e^+e^- \to D^*\overline{D}$ and $e^+e^- \to$

$D^*\overline{D}^*$ production. Figure 7.3 shows the simulated distribution of the variable, $\Delta M_{\mathrm{rec},D}$, which is defined as

$$\Delta M_{\mathrm{rec},D} \equiv \min\left(\left|M_{\mathrm{rec},D_1} - m_{D^{*0}}\right|, \left|M_{\mathrm{rec},D_2} - m_{D^{*0}}\right|\right), \tag{7.5}$$

after applying the E_{miss} requirement to isolate $e^+e^- \to D^*\overline{D}$ and $D^*\overline{D}^*$ production.

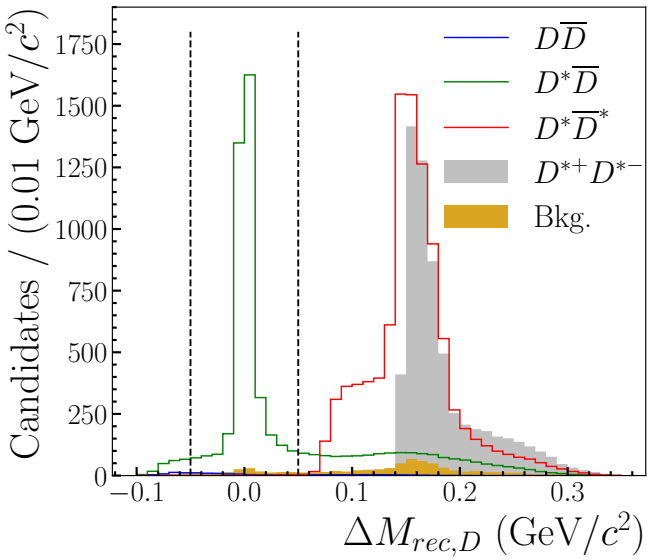

Figure 7.3: The minimum D-meson recoil mass in simulated $D\overline{D} \to K^-\pi^+$ vs. $K^+\pi^-$ candidates. The black dashed lines display the requirements placed to separate $e^+e^- \to D^*\overline{D}$ and $e^+e^- \to D^*\overline{D}^*$ production.

Two backgrounds remain in the $e^+e^- \to D\overline{D}$, $D^*\overline{D}$ and $D^*\overline{D}^*$ samples, as can be seen in Figs 7.2 and 7.3. They are $D\overline{D}$ decays to the incorrect final state (labelled 'Bkg.' in the plots) and $D^0\overline{D}^0$ decays to the correct final state, where the $D^0\overline{D}^0$ pair comes from $e^+e^- \to D^{*+}D^{*-}$ production with $D^{*+} \to \pi^+D^0$. The latter largely contributes to the $D^*\overline{D}^*$ sample where the topology is similar, and are significantly reduced by the requirements to distinguish between the three possible decay chains discussed below. The background from $D\overline{D}$ decays to the incorrect final state peaks underneath signal due to the D-meson mass constraints in the kinematic fit, and are accounted for later in the analysis (see Sec. 7.6.1 for more details).

7.3.3 Discriminating between $D^*\overline{D} \to \gamma D\overline{D}$ and $D^*\overline{D} \to \pi^0 D\overline{D}$

The squared missing mass of the remaining particles in the event after reconstructing the $D\overline{D}$ pair,

$$M^2_{\text{miss},D\overline{D}} \equiv (p - p_{D_1} - p_{D_2})^2, \tag{7.6}$$

is used to isolate between the $D^*\overline{D} \to \gamma D\overline{D}$ and $D^*\overline{D} \to \pi^0 D\overline{D}$ production mechanisms. Figure 7.4 shows the $M^2_{\text{miss},D\overline{D}}$ distribution in simulation after applying the selection criteria to isolate $e^+e^- \to D^*\overline{D}$ production. The $D^*\overline{D} \to \gamma D\overline{D}$ decays peak at 0, whilst the $D^*\overline{D} \to \pi^0 D\overline{D}$ decays peak around $m^2_{\pi^0}$.

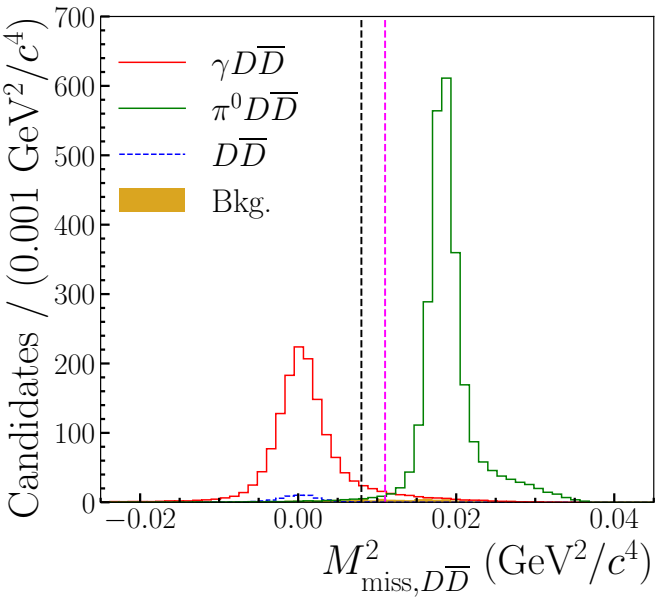

Figure 7.4: The squared missing mass in simulation of the remaining particles in the event after reconstructing $D\overline{D} \to K^-\pi^+$ vs. $K^+\pi^-$ decays. The black (magenta) dashed line displays the requirement placed to isolate $D\overline{D}$ pairs produced in the $D^*\overline{D} \to \gamma D\overline{D}$ ($D^*\overline{D} \to \pi^0 D\overline{D}$) decay chain.

7.3.4 Separating $\gamma\gamma D\overline{D}$ and $\gamma\pi^0 D\overline{D}$ from $\pi^0\pi^0 D\overline{D}$

At this stage, criteria have been presented which use only the kinematics of the $D\overline{D}$ pair to distinguish between the $D\overline{D}$, $D^*\overline{D} \to \gamma D\overline{D}$ and $D^*\overline{D} \to \pi^0 D\overline{D}$ production mechanisms, and to isolate the $D^*\overline{D}^*$ processes. However, the same strategy

is not effective in discriminating between the decay chains that originate from the $D^*\overline{D}^*$ process. For example, one might naively consider using the $M^2_{\text{miss},D\overline{D}}$ variable. However, when *two* particles X and Y are missed in the reconstruction, the $M^2_{\text{miss},D\overline{D}}$ is given by

$$M^2_{\text{miss},D\overline{D}} = (p - p_{D_1} - p_{D_2})^2 = (p_X + p_Y)^2, \tag{7.7}$$

which does not peak at the mass of the missing particles due to the additional momentum contributions. Subsequently, the $M^2_{\text{miss},D\overline{D}}$ distributions for the three possible decay chains significantly overlap. To overcome this issue, a single $D^* \to \gamma D$ candidate is reconstructed in each event, chosen to be that which has an invariant mass closest to the D^{*0} from all combinations of the two selected D mesons and all photon candidates.

The D^* candidate is employed to separate the $D^*\overline{D}^* \to \gamma\gamma D\overline{D}$ and $D^*\overline{D}^* \to \pi^0\gamma D\overline{D}$ production mechanisms from $D^*\overline{D}^* \to \pi^0\pi^0 D\overline{D}$. Two variables are used: the difference between the reconstructed invariant mass of the D^* candidate and the PDG value, denoted ΔM_{D^*}, and the recoil mass of the D^* candidate, M_{rec,D^*}, which is defined similarly to Eq. 7.4.

Figure 7.5 shows the distributions of ΔM_{D^*} and M_{rec,D^*} in simulation after applying the requirements to isolate the $e^+e^- \to D^*\overline{D}^*$ process. For the decay chains with a photon the peaks are at $\Delta M_{D^*} \sim 0\,\text{GeV}/c^2$ and $M_{\text{rec},D^*} \sim m_{D^{*0}}$. However, for the $\pi^0\pi^0 D\overline{D}$ process, the D^* candidate is reconstructed using a random photon, which leads to displaced peaks in ΔM_{D^*} and M_{rec,D^*}. The same applies to $D^0\overline{D}^0$ pairs produced in the $D^{*+}D^{*-}$ process. To isolate the decay chains with a photon a region is selected by the following requirements,

- $|\Delta M_{D^*}| < 0.02\,\text{GeV}/c^2$,
- $|M_{\text{rec},D^*} - 2.015| < 0.025\,\text{GeV}/c^2$,
- $M_{\text{rec},D^*} < 0.455\Delta M_{D^*} + 2.04$,

as highlighted in Fig. 7.5.

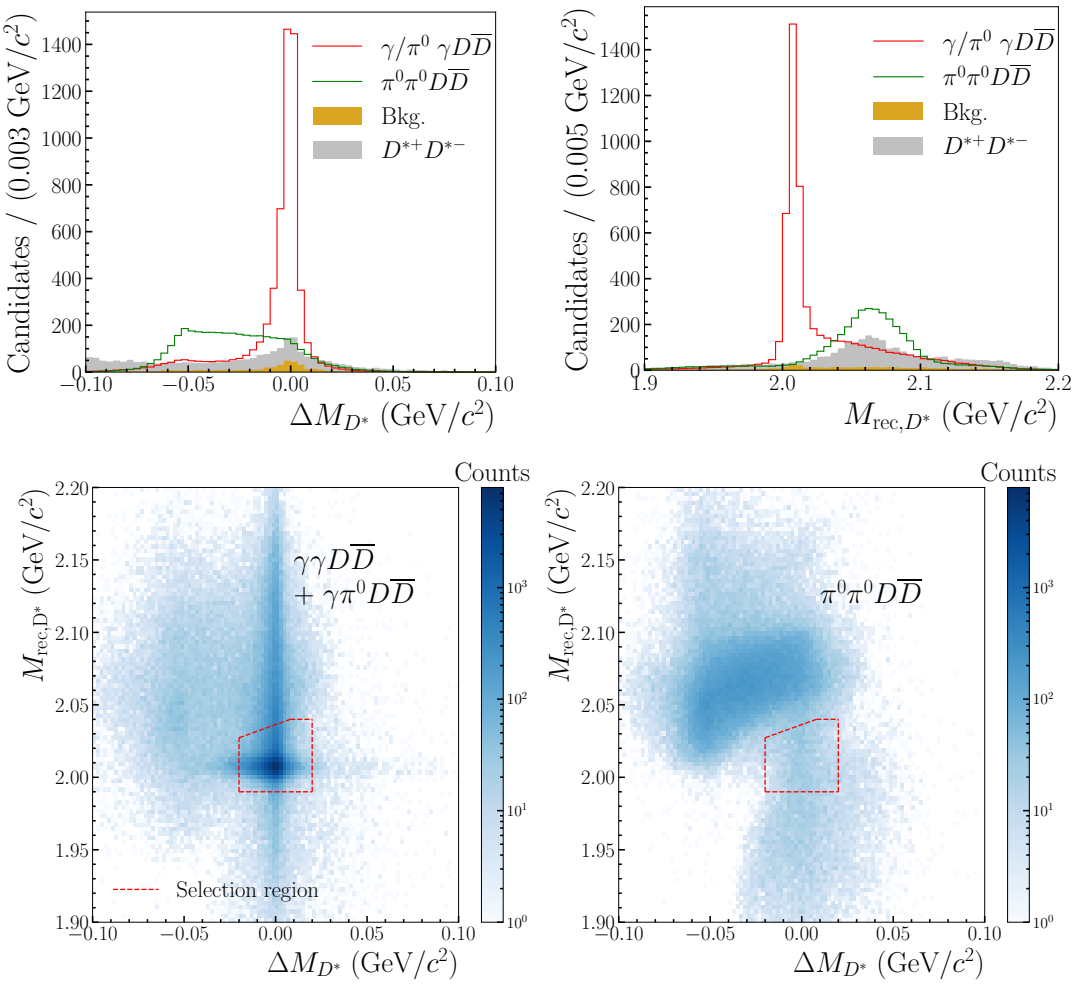

Figure 7.5: The top left plot displays the difference between the invariant mass of the reconstructed $D^* \to \gamma D$ candidate and that of the D^* meson (ΔM_{D^*}), and the top right plot shows the invariant mass of all other particles in the event after reconstructing the $D^* \to \gamma D$ candidate (M_{rec,D^*}). The bottom plots display the two-dimensional distributions of ΔM_{D^*} and M_{rec,D^*} which are used to separate the $\gamma\gamma D\overline{D}$ and $\gamma\pi^0 D\overline{D}$ decay chains from $\pi^0\pi^0 D\overline{D}$ by selecting candidates which lie in the red dashed region shown. All plots shown the distributions of simulated $D\overline{D} \to K^-\pi^+$ vs. $K^+\pi^-$ decays.

7.3.5 Discriminating between $\gamma\gamma D\overline{D}$ and $\gamma\pi^0 D\overline{D}$

The missing mass after reconstructing the D and $\overline{D}^*$ mesons, defined as

$$M^2_{\mathrm{miss},\gamma D\overline{D}} \equiv (p - p_D - p_{\overline{D}^*})^2, \tag{7.8}$$

is used to separate the $D^*\overline{D}^* \to \gamma\gamma D\overline{D}$ production mechanism from $D^*\overline{D}^* \to \pi^0\gamma D\overline{D}$. Figure 7.6 displays the $M^2_{\mathrm{miss},\gamma D\overline{D}}$ distribution in simulation after applying the selection requirements to isolation $e^+e^- \to D^*\overline{D}^*$ production where at least

one $D^* \to \gamma D$ decay occurs. Residual background from $D^{*+}D^{*-}$ production is further reduced by requiring the slowest charged pion in the event to have a momentum above 100 MeV/c.

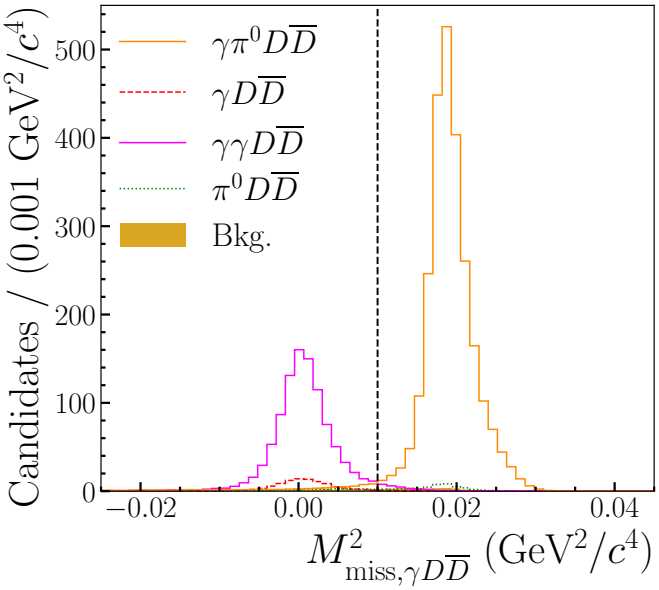

Figure 7.6: The squared missing mass in simulation of the remaining particles in the event after reconstructing $D\overline{D} \to K^-\pi^+$ vs. $K^+\pi^-$ decays and a $D^* \to \gamma D$ candidate. The black dashed line displays the requirement placed to distinguish between $D\overline{D}$ pairs produced in the $\gamma\pi^0 D\overline{D}$ and $\gamma\gamma D\overline{D}$ decay chains.

7.3.6 Attempts at isolating $\pi^0\pi^0 D\overline{D}$

Two techniques can be applied to reconstruct $D\overline{D}$ pairs from the $D^*\overline{D}^* \to \pi^0\pi^0 D\overline{D}$ decay chain. The first proceeds by reconstructing a single $D^* \to [\gamma\gamma]_{\pi^0} D$ candidate in each event. However, the selection efficiency is deemed too low to be useful due to the low momentum of the two photons.

The second attempt examines the candidates that do not pass the requirements placed to reconstruct the decay chains from the $D^*\overline{D}^*$ process with a photon. However, the irreducible background from $D^{*+}D^{*-}$ production is found to be too large. Therefore, in this analysis, the $e^+e^- \to \pi^0\pi^0 D\overline{D}$ production mechanism is not explicitly isolated. The small amount that remain in the sample are incorporated as signal alongside the $e^+e^- \to \gamma\gamma D\overline{D}$ decay chain, where the $D\overline{D}$ pair has the same C eigenvalue. Together they are referred to as $D^*\overline{D}^* \to \gamma\gamma/\pi^0\pi^0 D\overline{D}$.

7.3.7 Summary

Table 7.1 summarizes the selection requirements applied to isolate the $D\overline{D}$ pairs produced through each decay chain. A flowchart is also supplied in Fig. 7.7.

Table 7.1: The $D\overline{D}$ pair production mechanisms of interest and the criteria applied to isolate each sample. A '✓' in the ΔM_{D^*} vs. M_{rec,D^*} column means that candidates are required to be in the red dashed region displayed in the bottom left plot of Fig. 7.5.

Production mechanism	E_{miss} (MeV)	$\Delta M_{\mathrm{rec},D}$ (MeV/c^2)	$M^2_{\mathrm{miss},D\overline{D}}$ (GeV^2/c^4)	ΔM_{D^*} vs. M_{rec,D^*} region	$M^2_{\mathrm{miss},\gamma D\overline{D}}$ (GeV^2/c^4)	$p_{\pi,\mathrm{slow}}$ (MeV)
$D\overline{D}$	> -30 & < 60	–	–	×	–	–
$D^*\overline{D} \to \gamma D\overline{D}$	> 70	> -50 & < 50	< 0.008	×	–	–
$D^*\overline{D} \to \pi^0 D\overline{D}$	> 70	> -50 & < 50	> 0.011	×	–	–
$D^*\overline{D}^* \to \gamma\pi^0 D\overline{D}$	> 70	> 70	–	✓	< 0.01	> 100
$D^*\overline{D}^* \to \gamma\gamma/\pi^0\pi^0 D\overline{D}$	> 70	> 70	–	✓	> 0.01	> 100

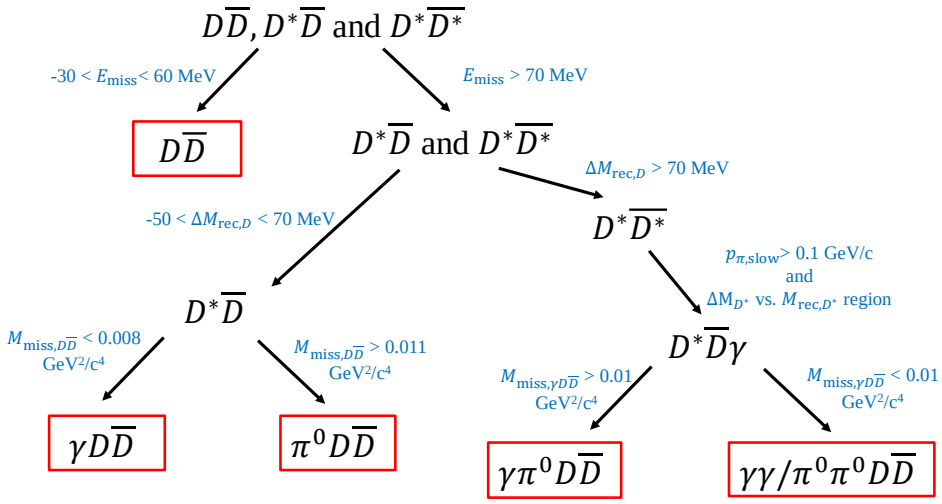

Figure 7.7: Flowchart displaying the requirements placed to isolate $D\overline{D}$ pairs from each production mechanism.

7.4 Demonstration of quantum coherence

The quantum correlations are demonstrated by studying $D\overline{D}$ decays to channels which are expected to be suppressed and enhanced. As discussed in Sec. 5.3, decays

to two *CP* eigenstates and $D\overline{D} \to K^-\pi^+$ vs. $K^-\pi^+$ decays are used. The specific final states examined in the case of the former are shown in Tab. 7.4, which combine the four D decays in Tab. 7.3. The $D \to \pi^+\pi^-\pi^0$ decay is not a pure *CP* eigenstate, however it can be treated as such after accounting for the precisely measured *CP*-even fraction, $F_+^{\pi\pi\pi^0} = 0.9406 \pm 0.0042$ [107]. Table 7.2 summarises the branching fractions from the PDG of decays used throughout the chapter.

Table 7.2: Summary of branching fractions used throughout the measurement [33].

Decay			$\mathcal{B}$		
D^0	$\to$	$K^-\pi^+$	$(3.947$	$\pm$	$0.030)\%$
D^0	$\to$	K^+K^-	$(4.08$	$\pm$	$0.06) \times 10^{-3}$
D^0	$\to$	$\pi^+\pi^-$	$(1.454$	$\pm$	$0.024) \times 10^{-3}$
D^0	$\to$	$\pi^+\pi^-\pi^0$	$(1.49$	$\pm$	$0.07)\%$
D^0	$\to$	$K^0_S\pi^0$	$(1.240$	$\pm$	$0.022)\%$
D^0	$\to$	$K^-\pi^+\pi^0$	$(14.4$	$\pm$	$0.6)\%$
D^-	$\to$	$K^0_S\pi^-\pi^0$	$(7.36$	$\pm$	$0.20)\%$
D^{*0}	$\to$	$\pi^0 D^0$	$(64.7$	$\pm$	$0.9)\%$
D^{*0}	$\to$	γD^0	$(35.3$	$\pm$	$0.9)\%$
D^{*+}	$\to$	$\pi^+ D^0$	$(67.7$	$\pm$	$0.5)\%$

A qualitative display of the effects of the quantum correlations is shown in Fig. 7.8, which compares the $M^2_{\text{miss},D\overline{D}}$ distributions in data and MC for each final state. The $D\overline{D}$ pairs produced in the $D^*\overline{D} \to \gamma D\overline{D}$ decay chain have $C = 1$ and are found in the region $M^2_{\text{miss},D\overline{D}} < 0.008\,\text{GeV}^2/c^4$, whilst those from $D^*\overline{D} \to \pi^0 D\overline{D}$ production have $C = -1$ and are seen at $M^2_{\text{miss},D\overline{D}} > 0.011\,\text{GeV}^2/c^4$. In the final states which are expected to be enhanced when $C = -1$, for example $D\overline{D} \to K^0_S\pi^0$ vs. K^+K^-, the data are enhanced relative to the MC (which does not account for quantum correlations) in the $D^*\overline{D} \to \pi^0 D\overline{D}$ region, and are suppressed in the $D^*\overline{D} \to \gamma D\overline{D}$ region. The opposite is true for decays that are enhanced when $C = 1$, for example $D\overline{D} \to K^0_S\pi^0$ vs. $K^0_S\pi^0$.

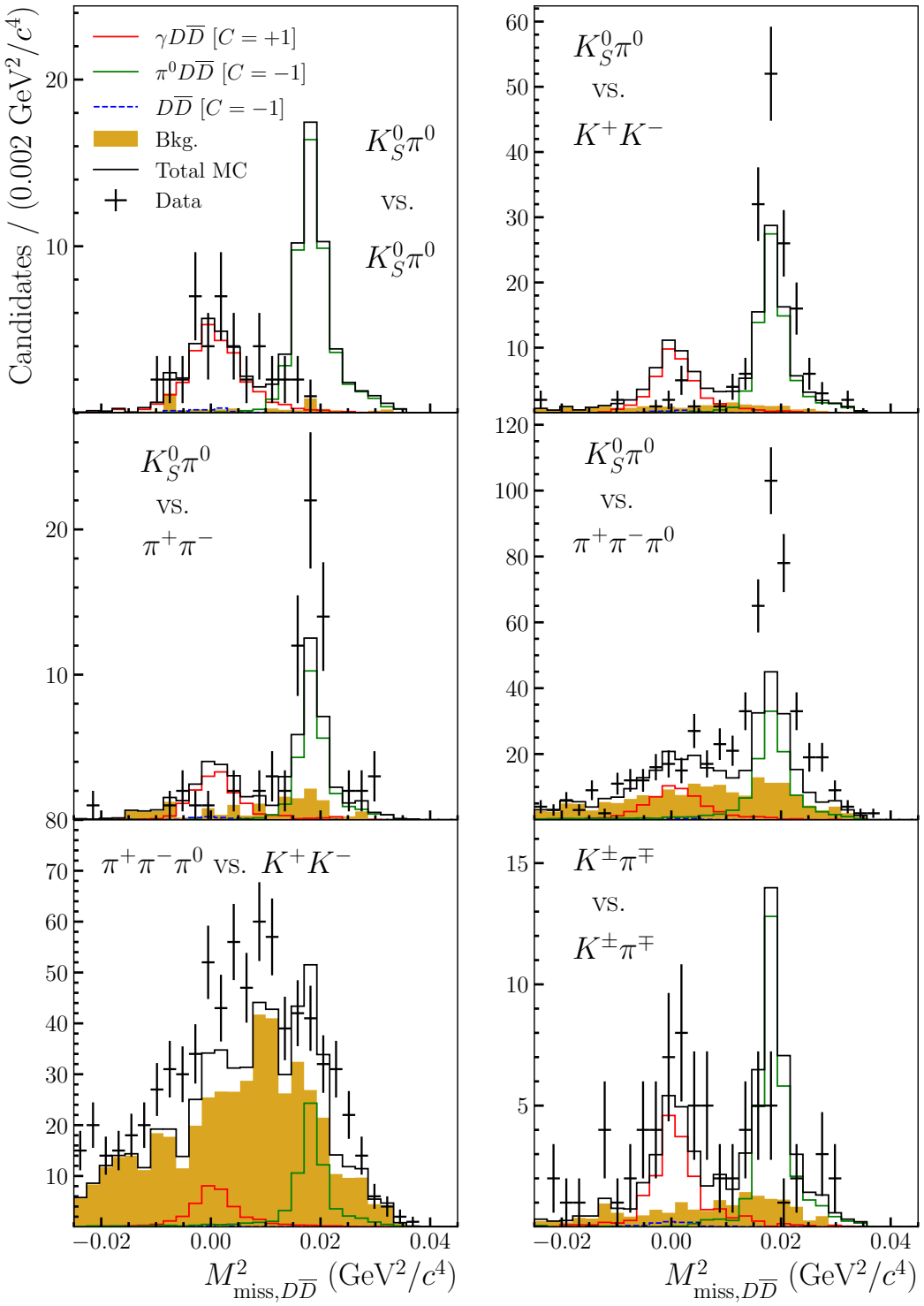

Figure 7.8: Comparison between the $M^2_{\mathrm{miss},D\overline{D}}$ distributions in data and MC for each of the final states used to demonstrate the C-coherence of the $D\overline{D}$ pairs. The data are enhanced or suppressed relative to the MC, which does not account for quantum correlations, depending on the final state and the expected C-eigenvalue of the $D\overline{D}$ pairs that can be found in a particular region.

Table 7.3: The D decays to CP eigenstates used throughout the measurement.

$D \to$	CP eigenvalue
$\pi^+\pi^-\pi^0$	$+1$
K^+K^-	$+1$
$\pi^+\pi^-$	$+1$
$K^0_S\pi^0$	-1

Table 7.4: The double CP-eigenstate decays used to demonstrate the quantum correlations.

$D\overline{D} \to$			CP eigenvalue
$\pi^+\pi^-\pi^0$	vs.	$K^0_S\pi^0$	-1
$\pi^+\pi^-\pi^0$	vs.	K^+K^-	$+1$
$K^0_S\pi^0$	vs.	$K^0_S\pi^0$	$+1$
$K^0_S\pi^0$	vs.	K^+K^-	-1
$K^0_S\pi^0$	vs.	$\pi^+\pi^-$	-1

After applying the requirements to select $D\overline{D}$ pairs from each production mechanism, the signal yields for each final state are determined through two-dimensional fits to the invariant mass of both D decay candidates, similar to those described later in Sec. 7.6. The results are shown in Tab. 7.5. However, as mentioned, the criteria imposed do not isolate perfectly pure samples due to ISR, so corrections are applied to account for the cross-feed. This is achieved through the matrix calculation,

$$\vec{n} = \mathbf{A}^{-1}\vec{N}, \tag{7.9}$$

which simultaneously accounts for the impurities and selection efficiencies. In the equation, $\vec{N}$ is a vector containing the yields determined in the fits, $\vec{n}$ is a vector containing the efficiency-corrected yields for the $D\overline{D}$ pairs produced through each production mechanism, and $\mathbf{A}_{ij}$ corresponds to the rate of $D\overline{D}$ pairs which originate from production mechanism i passing the selection criteria to isolate production

mechanism j. The efficiency matrices for each final state are determined in simulation, and an example is shown in Tab. 7.6 for $D\overline{D} \to K^-\pi^+$ vs. $K^+\pi^-$ decays.

Table 7.5: Measured signal yields for all final states used to demonstrate the quantum correlations in each production mechanism.

Final state			$D\overline{D}$	$D^*\overline{D} \to \gamma D\overline{D}$	$D^*\overline{D} \to \pi^0 D\overline{D}$	$D^*\overline{D}^* \to \gamma\pi^0 D\overline{D}$	$D^*\overline{D}^* \to \gamma\gamma/\pi^0\pi^0 D\overline{D}$
$K^-\pi^+$	vs.	$K^+\pi^-$	681.5 ± 28.8	1198.0 ± 38.8	2477.0 ± 50.6	2316.7 ± 51.5	1146.6 ± 37.4
$\pi^+\pi^-\pi^0$	vs.	$K^0_S\pi^0$	$80.2^{+11.0}_{-10.3}$	$23.0^{+8.0}_{-7.2}$	$272.6^{+19.2}_{-18.6}$	$29.6^{+8.2}_{-7.3}$	$92.9^{+11.4}_{-10.8}$
$\pi^+\pi^-\pi^0$	vs.	K^+K^-	$15.4^{+9.5}_{-7.7}$	$85.1^{+14.0}_{-12.9}$	$21.9^{+7.7}_{-6.3}$	$177.5^{+16.8}_{-16.0}$	$8.9^{+6.5}_{-5.7}$
$K^0_S\pi^0$	vs.	$K^0_S\pi^0$	$1.0^{+2.0}_{-1.0}$	$30.0^{+6.2}_{-6.2}$	$4.8^{+2.6}_{-2.6}$	$57.7^{+8.4}_{-7.8}$	$6.2^{+4.0}_{-3.4}$
$K^0_S\pi^0$	vs.	K^+K^-	$28.7^{+6.0}_{-5.4}$	$2.9^{+3.1}_{-2.7}$	$100.9^{+11.3}_{-10.3}$	$1.7^{+2.0}_{-1.3}$	$32.5^{+6.5}_{-5.8}$
$K^0_S\pi^0$	vs.	$\pi^+\pi^-$	$10.0^{+3.8}_{-3.2}$	$-1.6^{+2.5}_{-2.7}$	$54.0^{+7.8}_{-7.1}$	$-0.3^{+1.4}_{-1.4}$	$17.6^{+4.7}_{-4.1}$
$K^-\pi^+$	vs.	$K^-\pi^+$	$-0.2^{+2.1}_{-1.4}$	18 ± 6	2 ± 3	35^{+7}_{-6}	5 ± 3

It is not immediately apparent from the equation above that the procedure to determine the efficiency-corrected yields is valid when the $D\overline{D}$ pairs are quantum correlated. A validation study is performed as follows. For each final state, a vector, $\vec{N}_{\rm MC}$, is found which contains the predicted signal yields from simulation. Due to the cross-feed, each element in $\vec{N}_{\rm MC}$ contains contributions from the target production mechanism as well as the others. Each contribution is manually corrected for the effects of the quantum correlations, and the new vector is denoted $\vec{N}'_{\rm MC}$. Then, the matrix calculation in Eq. 7.9 is performed to determine the vector $\vec{n}'_{\rm MC}$, the

Table 7.6: Efficiency, in percent, of reconstructing the $D\overline{D} \to K^-\pi^+$ vs. $K^+\pi^-$ final state in simulation. An element with row, i, and column, j, gives the efficiency of reconstructing the production mechanism, i, after applying the selection requirements devised to isolate $D\overline{D}$ pairs produced by process, j.

		Identified as				
		$D\overline{D}$	$D^*\overline{D} \to \gamma D\overline{D}$	$D^*\overline{D} \to \pi^0 D\overline{D}$	$D^*\overline{D}^* \to \gamma\pi^0 D\overline{D}$	$D^*\overline{D}^* \to \gamma\gamma/\pi^0\pi^0 D\overline{D}$
True	$D\overline{D}$	32.45	2.98	0	0	0.07
	$D^*\overline{D} \to \gamma D\overline{D}$	0	25.44	1.57	0	1.94
	$D^*\overline{D} \to \pi^0 D\overline{D}$	0	0.4	30.06	0.55	0.5
	$D^*\overline{D}^* \to \gamma\pi^0 D\overline{D}$	0	0	0	25.23	1.04
	$D^*\overline{D}^* \to \gamma\gamma/\pi^0\pi^0 D\overline{D}$	0	0	0	0.25	8.83

elements of which are found to be in perfect agreement with the generated yields in simulation for each production mechanism after applying manual corrections to account for the quantum correlations.

The effects of the quantum correlations are shown in data by examining the ratio of the efficiency-corrected yields to the predictions assuming the $D\overline{D}$ pairs are not quantum correlated. The latter are calculated using those measured in the $D\overline{D} \to K^-\pi^+$ vs. $K^+\pi^-$ decay channel, which are shown in Tab. 7.5. The expected uncorrelated yields are given by

$$\vec{n}_{f_1,f_2} = \left(2 - \delta^{f_2}_{f_1}\right) \frac{\mathcal{B}_{D^0\to f_1}\mathcal{B}_{D^0\to f_2}}{\mathcal{B}^2_{D^0\to K^-\pi^+}} \mathbf{A}^{-1}_{K\pi,K\pi} \vec{N}_{K\pi,K\pi}, \tag{7.10}$$

where $\left(2 - \delta^{f_2}_{f_1}\right)$ is a combinatoric correction that accounts for charge conjugation.

The predictions for the ratios are found by dividing the quantum-correlated decay rates in Eqs. 5.26 and 5.27 by the uncorrelated decay rates, which are determined similarly to Eq. 7.2. For the decays to double *CP*-eigenstates, the ratio is

$$\begin{aligned} &\frac{\Gamma(D\overline{D} \to f_1 \text{ vs. } f_2)}{\Gamma(D^0 \to f_1)\Gamma(\overline{D}^0 \to f_2) + \Gamma(D^0 \to f_2)\Gamma(\overline{D}^0 \to f_1)} \\ &\qquad = 1 + C\lambda_1\lambda_2 - Cy_D(\lambda_1 + \lambda_2), \end{aligned} \tag{7.11}$$

where $\lambda = 1$ (-1) for *CP*-even (*CP*-odd) decays and $\lambda = 2F_+^{\pi\pi\pi^0} - 1$ for the $D \to \pi^+\pi^-\pi^0$ decay. For the $D\overline{D} \to K^-\pi^+$ vs. $K^-\pi^+$ decays it is

$$\begin{aligned} &\frac{\Gamma(D\overline{D} \to K^-\pi^+ \text{ vs. } K^-\pi^+)}{\Gamma(D^0 \to K^-\pi^+)\Gamma(\overline{D}^0 \to K^-\pi^+) + \Gamma(D^0 \to K^-\pi^+)\Gamma(\overline{D}^0 \to K^-\pi^+)} \\ &\qquad = (1 + C)\left(1 - \frac{(y_D \cos\delta_D^{K\pi} + x_D \sin\delta_D^{K\pi})}{r_D^{K\pi}}\right). \end{aligned} \tag{7.12}$$

Figure 7.9 shows the measured ratios for each final state and production mechanism, which are all in agreement with the predictions assuming the $D\overline{D}$ pairs are produced coherently with the expected C eigenvalue.

A further study is carried out to quantify the quantum coherence of each production mechanism. A χ^2 fit is performed which compares the measured yields of the double *CP*-eigenstate decays to the predictions which are parametrised

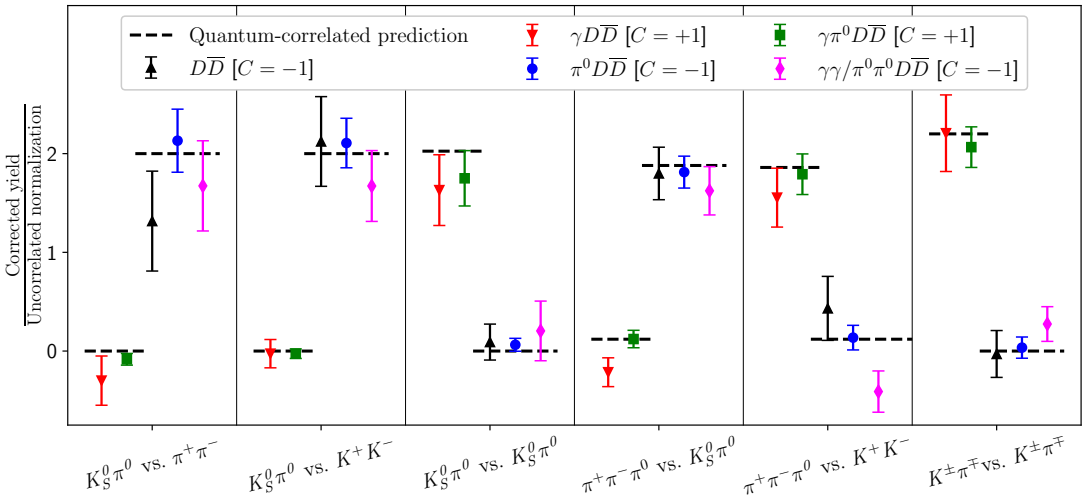

Figure 7.9: The ratio of efficiency-corrected yields observed in data to the predictions assuming the decays of the D and $\overline{D}$ mesons are uncorrelated for each $D\overline{D}$ final state and production mechanism.

according to the coherence of the $D\overline{D}$ pairs. Again, the predictions are calculated using those found in the $D\overline{D} \to K^-\pi^+$ vs. $K^+\pi^-$ decay channel,

$$\vec{N}_{f_1,f_2} = \left(2 - \delta^{f_2}_{f_1}\right) \frac{\mathcal{B}_{D^0\to f_1}\mathcal{B}_{D^0\to f_2}}{\mathcal{B}^2_{D^0\to K^-\pi^+}} \mathbf{A}_{f_1,f_2}\mathbf{R}\mathbf{A}^{-1}_{K\pi,K\pi}\vec{N}_{K\pi,K\pi}. \tag{7.13}$$

In this equation, the matrix, $\mathbf{R}$, contains the parameters of interest, and the elements are given by

$$R_{ij} = \begin{cases} R_i & \text{when } i = j \text{ and } i \text{ is } C\text{-enhanced}, \\ 1 - R_i & \text{when } i = j \text{ and } i \text{ is } C\text{-forbidden}, \\ 0 & \text{when } i \neq j, \end{cases} \tag{7.14}$$

such that $R_i = 1$ for a decay chain where the $D\overline{D}$ pairs all possess the expected C eigenvalue, and $R_i = 0.5$ if the $D\overline{D}$ pairs are uncorrelated. For the final states which include the $D \to \pi^+\pi^-\pi^0$ decay, the coherence factors contain a small correction to account for the CP-odd content.

The $D\overline{D} \to K^-\pi^+$ vs. $K^-\pi^+$ decays are included in the fit by comparing the ratio of efficiency-corrected yields to those in the $D\overline{D} \to K^-\pi^+$ vs. $K^+\pi^-$ decay channel. The predicted ratio is

$$\frac{n(D\overline{D} \to K^-\pi^+ \text{ vs. } K^-\pi^+)}{n(D\overline{D} \to K^-\pi^+ \text{ vs. } K^+\pi^-)} = 4(r_D^{K\pi})^2 f_R \left(1 - \frac{(x_D \sin\delta_D^{K\pi} + y_D \cos\delta_D^{K\pi})}{r_D^{K\pi}}\right), \tag{7.15}$$

where $f_R = R_i$ for processes that result in C-even $D\overline{D}$ pairs, and $(1 - R_i)$ in the C-odd scenario.

In the fit, the external parameters x_D, y_D, $r_D^{K\pi}$ and $\delta_D^{K\pi}$ are fixed to the values found in Ref. [39]. Table 7.7 shows the measured values of the coherence parameters for each production mechanism, which are all in good agreement with one.

Table 7.7: Measured coherence parameters for each production mechanism.

Production mechanism $[C]$	R
$D\overline{D}$ $[-1]$	1.015 ± 0.066
$D^*\overline{D} \to \gamma D\overline{D}$ $[+1]$	1.044 ± 0.044
$D^*\overline{D} \to \pi^0 D\overline{D}$ $[-1]$	1.028 ± 0.024
$D^*\overline{D}^* \to \gamma\pi^0 D\overline{D}$ $[+1]$	1.027 ± 0.017
$D^*\overline{D}^* \to \gamma\gamma/\pi^0\pi^0 D\overline{D}$ $[-1]$	0.963 ± 0.060

7.5 Strategy to measure $r_D^{K\pi}\cos\delta_D^{K\pi}$ with CP tags

The parameter $r_D^{K\pi}\cos\delta_D^{K\pi}$ is measured using $D\overline{D} \to K^-\pi^+$ vs. f_{CP} decays, where f_{CP} is one of the four CP eigenstate tag modes in Tab. 7.3. The quantum correlations result in interference between the $D^0 \to K^-\pi^+$, $\overline{D}^0 \to f_{CP}$ and $D^0 \to f_{CP}$, $\overline{D}^0 \to K^-\pi^+$ paths to the final state, which enhances or suppresses the decay rate relative to the scenario where the D and $\overline{D}$ mesons decay independently by the factor

$$\frac{\Gamma(D\overline{D} \to K^-\pi^+ \text{ vs. } f_{CP})}{\Gamma(D^0 \to K^-\pi^+)\Gamma(\overline{D}^0 \to f_{CP}) + \Gamma(D^0 \to f_{CP})\Gamma(\overline{D}^0 \to K^-\pi^+)} = 1 + \frac{2C\lambda r_D^{K\pi}\cos\delta_D^{K\pi} - (1+C)y_D}{1 + (r_D^{K\pi})^2}, \tag{7.16}$$

where $\lambda = +1$ (-1) $[2F_+^{\pi\pi\pi^0} - 1]$ for the CP-even (CP-odd) $[\pi^+\pi^-\pi^0]$ tags. Using the values of $r_D^{K\pi}$, $\delta_D^{K\pi}$ and y_D from Ref. [15], the relative enhancement is expected to be around $\pm 12\%$, where the sign depends on the values of C and λ. A technique similar to that presented in the previous section is used, where the relative enhancement is exploited to extract $r_D^{K\pi}\cos\delta_D^{K\pi}$ by comparing the measured yields to the predictions given those found in the $D\overline{D} \to K^-\pi^+$ vs. $K^+\pi^-$ decay control channel.

7.6 *CP*-tag signal yield determination

After applying the selection requirements to isolate $D\overline{D}$ pairs from each production mechanism, the signal yields for each final state are determined through two-dimensional unbinned maximum likelihood fits to the reconstructed invariant mass of both D-decay candidates. A total of twenty fits (5 production mechanisms $\times$ 4 channels) are performed.

7.6.1 Invariant-mass fit configurations

7.6.1.1 Signal component

In each fit, the signal candidates are modelled by a kernel density estimate (KDE) of the invariant-mass distributions in simulation for each D decay, convolved with Gaussians which have freedom in the mean and width parameters to account for resolution differences between data and MC. The yield is a floating parameter in each fit.

7.6.1.2 Background components

The data sample for each *CP*-tag final state contains multiple backgrounds. In contrast, the fits to the $D\overline{D} \to K^-\pi^+$ vs. $K^+\pi^-$ decays have minimal contributions due to the large branching fractions and the relatively simple final state which has a high reconstruction efficiency. Typically, the backgrounds originate from the decays of $D\overline{D}$ pairs produced through the signal processes, where at least one of the D mesons is incorrectly reconstructed. The contributions from the background processes, excluding $e^+e^- \to D^{*+}D^{*-}$ production, which is discussed later, are found to be negligible in simulation because they are suppressed by the selection criteria or because they have low cross-sections.

Simulated $D\overline{D}$ decays are used to examine and model the backgrounds in each fit. Figure 7.10 displays the invariant-mass distributions of these backgrounds in truth-matched simulation for each final state, after applying the selection criteria to isolate the $D^*\overline{D} \to \gamma D\overline{D}$ production mechanism where they are typically largest

(with the exception of the $\pi^+\pi^-\pi^0$ tag where the $D^*\overline{D}^* \to \gamma\pi^0 D\overline{D}$ requirements are applied to display a specific background discussed below).

Throughout, backgrounds with a correctly reconstructed D decay are represented in the fits by the corresponding signal shape. Those of the incorrectly reconstructed D decays are given by a KDE of the distributions in simulation (unless stated otherwise). The yield parametrisations are different for each background and are discussed below. A summary of the backgrounds which do not contain a combinatorial component can be found in Tab. 7.8.

$D\overline{D} \to K^-\pi^+$ **vs.** K^+K^-

The top plot in Fig. 7.10 shows the backgrounds reconstructed as $D\overline{D} \to K^-\pi^+$ vs. K^+K^- decays. There are two contributions to the $D \to K^-\pi^+$ invariant-mass spectrum:

- correctly reconstructed $D \to K^-\pi^+$ decays,
- and combinatorial background.

Meanwhile, there are four contributions to the $D \to K^+K^-$ invariant-mass distribution:

- correctly reconstructed $D \to K^+K^-$ decays,
- $D \to K^+\pi^-$ decays where the π^- is reconstructed as a K^-,
- $D \to K^+\pi^-\pi^0$ decays where the π^- is reconstructed as a K^- and the π^0 is missed,
- and combinatorial background.

In total there are 7 possible background components given by the various combinations. The scenario where both D decays are correctly reconstructed is signal.

The distribution of $D \to K^+\pi^-$ decays reconstructed in the K^+K^- final state peaks around 1.96 GeV/c^2 and rapidly falls off towards lower masses. The corresponding backgrounds are removed from the samples by choosing the upper

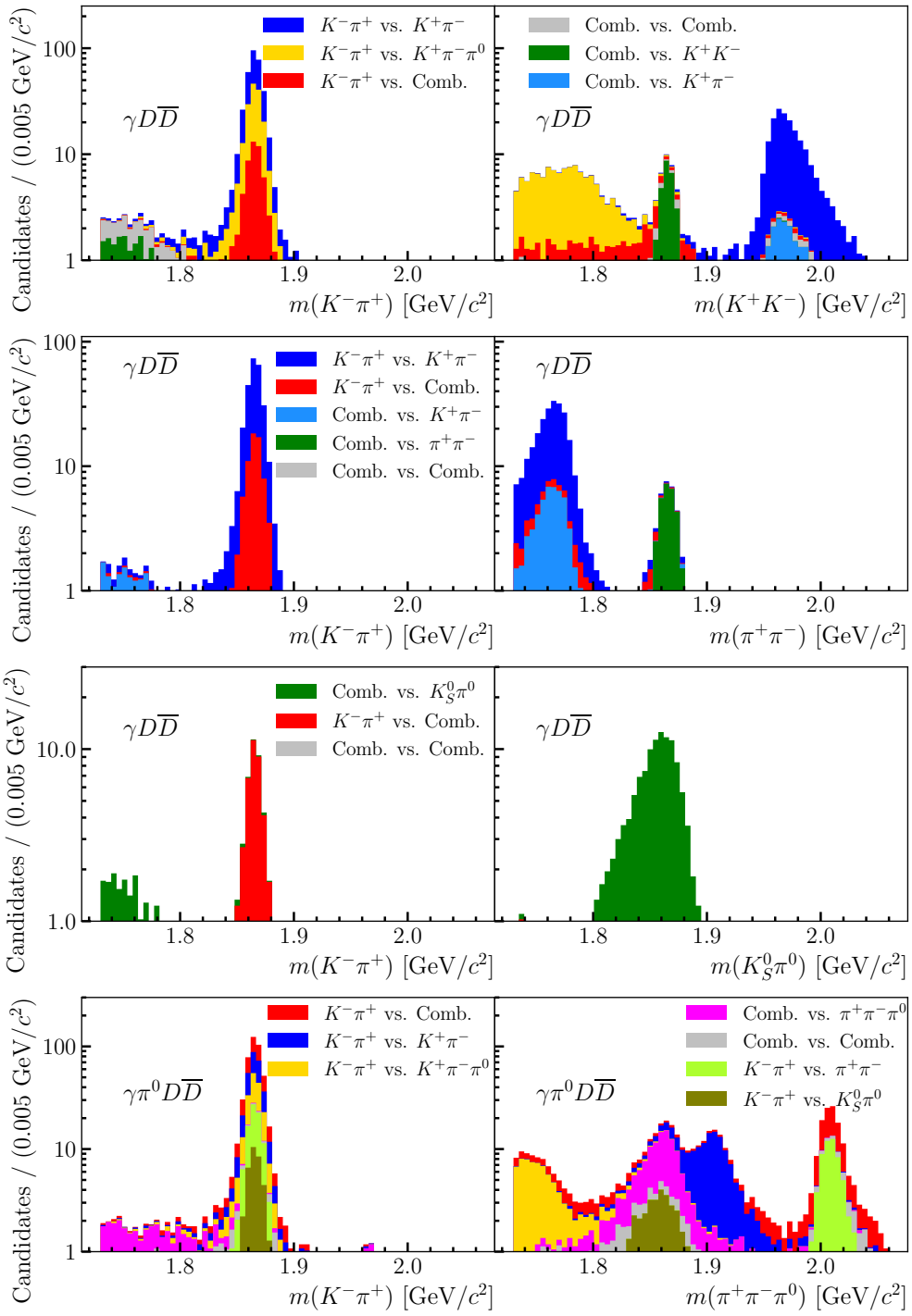

Figure 7.10: Invariant-mass distributions of the backgrounds which originate from $D\overline{D}$ decays in simulation. The left plot in each shows the projections in the $D \to K^-\pi^+$ mass, whilst the right shows the (top) $D \to K^+K^-$, (second from top) $D \to \pi^+\pi^-$, (second from bottom) $D \to K^0_S\pi^0$ and (bottom) $D \to \pi^+\pi^-\pi^0$ mass. In the top three plots the selection requirements are applied to isolate the $D\overline{D}$ pairs produced in the $D^*\overline{D} \to \gamma D\overline{D}$ decay chain. In the bottom plot the criteria for the $D^*\overline{D} \to \pi^0 D\overline{D}$ production mechanism are imposed.

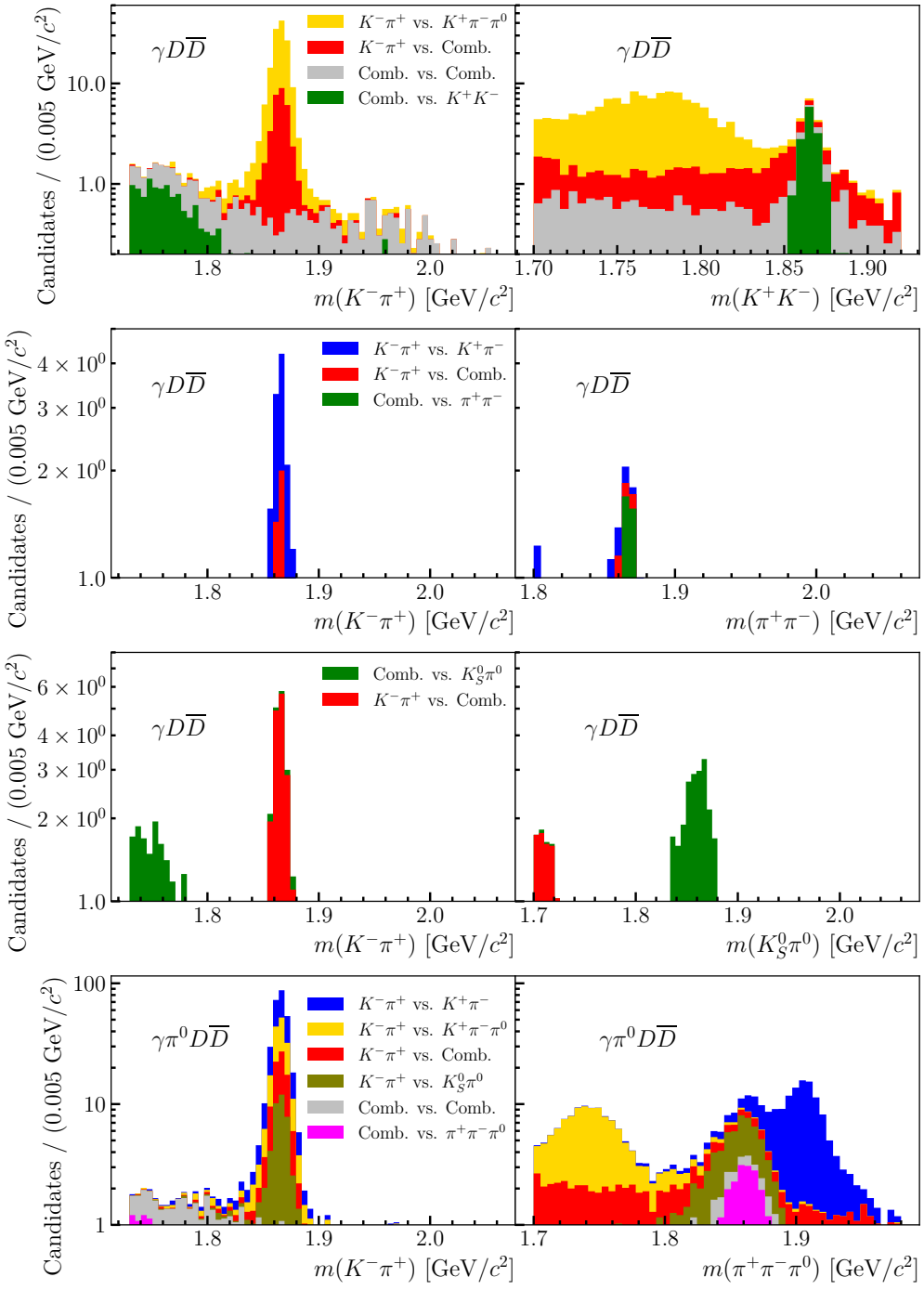

Figure 7.11: Invariant-mass distributions of the backgrounds which are modelled in the fits and originate from $D\overline{D}$ decays in simulation. The left plot in each shows the projections in the $D \to K^-\pi^+$ mass, whilst the right shows the (top) $D \to K^+K^-$, (second from top) $D \to \pi^+\pi^-$, (second from bottom) $D \to K^0_S\pi^0$ and (bottom) $D \to \pi^+\pi^-\pi^0$ mass. In the top three plots the selection requirements are applied to isolate the $D\overline{D}$ pairs produced in the $D^*\overline{D} \to \gamma D\overline{D}$ decay chain. In the bottom plot the criteria for the $D^*\overline{D} \to \pi^0 D\overline{D}$ production mechanism are imposed.

boundary on the reconstructed invariant mass of the $D \to K^+K^-$ candidates to be 1.92 GeV/c^2 in the fits.

The invariant-mass distribution of $D \to K^+\pi^-\pi^0$ decays reconstructed in the K^+K^- final state peaks around 1.77 GeV/c^2. It has a broad spectrum, which is dictated by the momentum of the missing π^0 meson, so it overlaps with the signal region and cannot be easily vetoed. The $D\overline{D} \to K^-\pi^+$ vs. $K^+\pi^-\pi^0$ decays are modelled in the fits, as discussed below, but the predicted yield of the $D\overline{D} \to$ combinatorial vs. $K^+\pi^-\pi^0$ background is less than 3 candidates in each fit and is therefore neglected.

So, there are four backgrounds which are represented in the fits to $D\overline{D} \to K^-\pi^+$ vs. K^-K^+ candidates. In descending order of their predicted yields, they are

- $D\overline{D} \to K^-\pi^+$ vs. $K^+\pi^-\pi^0$,
- $D\overline{D} \to K^-\pi^+$ vs. combinatorial,
- $D\overline{D} \to$ combinatorial vs. combinatorial,
- and $D\overline{D} \to$ combinatorial vs. K^+K^-.

For reference, the top plot in Fig. 7.11 shows the invariant-mass distributions of these backgrounds in the fit range.

In the fits to candidates passing the $D\overline{D}$, $D^*\overline{D} \to \gamma D\overline{D}$ and $D^*\overline{D}^* \to \gamma\gamma/\pi^0\pi^0 D\overline{D}$ requirements, the amount of $D\overline{D} \to K^-\pi^+$ vs. $K^+\pi^-\pi^0$ decays in the samples is expected to be large, and hence the yield is a floating parameter in each. However, in the other fits, the contribution is reduced, so it is fixed relative to the signal yield. The ratio is given by manually correcting the yields in simulation for the effects of the quantum correlations,

$$f(D\overline{D} \to K^-\pi^+ \text{ vs. } K^+\pi^-\pi^0) = \frac{N(K^+\pi^-\pi^0)}{\Sigma_i N^i(K^+K^-)R^i(K^+K^-)}, \tag{7.17}$$

where $N(K^+\pi^-\pi^0)$ is the predicted $D\overline{D} \to K^-\pi^+$ vs. $K^+\pi^-\pi^0$ decay yield in each fit, $N^i(K^+K^-)$ is the true simulated $D\overline{D} \to K^+\pi^-$ vs. K^+K^- decay yield originating from production mechanism, i, and $R^i(K^+K^-)$ is the relative enhancement from

Eq. 7.16. The sum over production mechanisms is necessary to account for the cross-feed. In principle the same sum should apply in the numerator, but the cross-feed and interference in $D\overline{D} \to K^-\pi^+$ vs. $K^+\pi^-\pi^0$ decays are both small effects so it is not necessary.

There are multiple contributions to the uncertainty on each ratio. They are

- the knowledge of the branching fractions which are inputs to the MC,
- differences between the selection efficiencies in data and MC,
- and the assumed value of $\delta_D^{K\pi}$ in the correction factor.

The uncertainty due to the latter is given by the difference in each ratio calculated with $\delta_D^{K\pi} = 170°$ and $\delta_D^{K\pi} = 205°$, which is a 5σ range around the LHCb average [39], and is found to change each ratio by around 1%. The efficiencies in MC are typically accurate to around 1% from internal collaboration studies performed with data. Finally, the relevant branching fractions are $\mathcal{B}(D^0 \to K^+K^-) = (4.08 \pm 0.06) \times 10^{-3}$ and $\mathcal{B}(D^0 \to K^-\pi^+\pi^0) = (14.4 \pm 0.6)\%$ [33]. The latter has a relative error of around 5% and dominates the uncertainty on the ratios, which are $(6.6 \pm 0.3)\%$ and $(10.3 \pm 0.5)\%$ for candidates selected by the $D^*\overline{D} \to \pi^0 D\overline{D}$ and $D^*\overline{D}^* \to \gamma\pi^0 D\overline{D}$ isolation requirements, respectively. In each fit, the ratios are fixed and the errors are propagated as systematic uncertainties in Sec. 7.9.

The three components with a combinatorial background contribution have floating yields in the fits. It is evident from Fig. 7.11 that the expected yield of pure combinatorial background that originates from the decays of $D\overline{D}$ pairs is relatively small. A much larger contribution is seen in data from random combinations of particles produced in the hadronisation of light quarks from the $e^+e^- \to q\bar{q}$ process. Such backgrounds are found to be poorly modelled in simulation. So, in each fit, the pure combinatorial background component is analytically represented by an exponential function in both dimensions with floating slope parameters.

$D\overline{D} \to K^-\pi^+$ vs. $\pi^+\pi^-$

In the fits to the $D\overline{D} \to K^-\pi^+$ vs. $\pi^+\pi^-$ decay candidates, the same two contributions are found in the $D \to K^-\pi^+$ invariant-mass spectrum as mentioned above for the K^+K^- tag. Meanwhile, there are three contributions to the invariant-mass spectrum of the $D \to \pi^+\pi^-$ decay candidates. They are: correctly reconstructed D decays, combinatorial background, and $D \to K^+\pi^-$ decays. In the latter, the kaon is misidentified as a pion, which leads to a distribution that peaks around $1.77\,\text{GeV}/c^2$ and falls sharply towards higher masses.

In total there are five potential backgrounds. Those with a misidentified $D \to K^+\pi^-$ decay are significantly reduced by choosing the lower boundary on the reconstructed invariant mass of the $D \to \pi^+\pi^-$ decay candidates to be $1.8\ \text{GeV}/c^2$ in the fits. With this requirement, the contribution from $D\overline{D} \to$ combinatorial vs. $K^+\pi^-$ decays becomes negligible.

The plot which is second from the top in Fig. 7.11 shows the expected contributions of the remaining backgrounds after the fit range requirements are applied. They are

- $D\overline{D} \to K^-\pi^+$ vs. $K^+\pi^-$,
- $D\overline{D} \to K^-\pi^+$ vs. combinatorial,
- and $D\overline{D} \to$ combinatorial vs. $\pi^+\pi^-$,

and the yield of each is small. Given the first two have similar invariant-mass distributions, they are modelled in the fits by a single component with a floating yield parameter. The background from $D\overline{D} \to$ combinatorial vs. $\pi^+\pi^-$ decays also has a floating yield in each fit.

Finally, the expected contribution from $D\overline{D} \to$ combinatorial vs. combinatorial decays is negligible. However, a component is included in each fit with the same parametrisation as for the equivalent background in the fits to $D\overline{D} \to K^-\pi^+$ vs. K^+K^- decay candidates, which is described above, to represent pure combinatorial background from the $e^+e^- \to q\bar{q}$ process.

$D\overline{D} \to K^-\pi^+$ **vs.** $\pi^+\pi^-\pi^0$

The invariant-mass distribution of candidates reconstructed as the $D \to \pi^+\pi^-\pi^0$ decay contains multiple backgrounds. They are

- correctly reconstructed $D \to \pi^+\pi^-\pi^0$ decays,
- $D \to K^+\pi^-\pi^0$ decays where the K^+ is misidentified as a π^+,
- $D \to K^0_S\pi^0$ decays with $K^0_S \to \pi^+\pi^-$,
- combinatorial background,
- $D \to K^+\pi^-$ decays which are combined with the π^0 from a $D^* \to \pi^0 D$ decay,
- and $D \to \pi^+\pi^-$ decays which are combined with the π^0 from a $D^* \to \pi^0 D$ decay.

As before, there are two contributions to the invariant-mass spectrum of the $D \to K^-\pi^+$ decay candidates. So, there are eleven possible backgrounds. However, some of these are found to be negligible in simulation and those that are not are shown in Fig. 7.10.

The $D\overline{D} \to K^-\pi^+$ vs. $D \to K^+\pi^-\pi^0$, $D\overline{D} \to K^-\pi^+$ vs. combinatorial, $D\overline{D} \to$ combinatorial vs. $\pi^+\pi^-\pi^0$ and $D\overline{D} \to$ combinatorial vs. combinatorial backgrounds are all modelled with floating yield parameters. In the fits to candidates which pass the isolation requirements for the $D\overline{D}$, $D^*\overline{D} \to \gamma D\overline{D}$ and $D^*\overline{D}^* \to \gamma\pi^0 D\overline{D}$ production mechanisms the $D\overline{D} \to$ combinatorial vs. combinatorial component is represented by an exponential function with a floating slope parameter in each dimension. In the other two fits, the exponential does not accurately represent the background in the invariant mass of the $D \to K^-\pi^+$ candidates, and therefore a second order polynomial is used instead.

The backgrounds from the $D \to K^+\pi^-$ and $D \to \pi^+\pi^-$ decays which are combined with the π^0 from a $D^* \to \pi^0 D$ decay are only clearly present in the fits to the $D^*\overline{D} \to \pi^0 D\overline{D}$ and $D^*\overline{D}^* \to \gamma\pi^0 D\overline{D}$ samples. The latter background peaks

at $m_{D^{*0}}$ and is removed by choosing an upper limit of 1.98 GeV/c^2 in the fits. The background from misidentified $D \to K^+\pi^-$ decays combined with the π^0 meson peaks near the signal region. The yield is a floating parameter in the two fits.

Due to the cross-feed only a small amount of the $D\overline{D} \to K^-\pi^+$ vs. $K^+\pi^-$ decays pass the selection criteria imposed to isolate the $D^*\overline{D} \to \gamma D\overline{D}$ and $D^*\overline{D}^* \to \gamma\gamma/\pi^0\pi^0 D\overline{D}$ decay chains. In the corresponding fits the rate of this background is fixed relative to signal. The ratio is calculated similarly to the $D\overline{D} \to K^-\pi^+$ vs. $K^+\pi^-\pi^0$ decay background in Eq. 7.17, and is determined to be (2.74±0.15)% and (4.7±0.2)% in the $D^*\overline{D} \to \gamma D\overline{D}$ and $D^*\overline{D}^* \to \gamma\gamma/\pi^0\pi^0 D\overline{D}$ samples, respectively.

A small number of $D \to K^0_S\pi^0$ decays pass the flight-distance significance requirements on the $\pi^+\pi^-$ pair in the $D \to \pi^+\pi^-\pi^0$ candidates. In the invariant-mass fits this background peaks around m_{D^0} in both dimensions and thus is indistinguishable from signal. It is important to accurately model this background because it is *CP* odd, whereas the $\pi^+\pi^-\pi^0$ decay is mostly *CP* even. One option would be to fix the rate similarly to other backgrounds. However, as mentioned, this is not an ideal solution because the quantum-correlation correction depends on $\delta_D^{K\pi}$. Instead, it is chosen to absorb this contribution into the signal component in each fit and correct the yields later in the analysis using the expected contribution, $R_{K^0_S}$, from simulation, which is around $R_{K^0_S} = 3.2\%$ of the signal. In the fit to determine $r_D^{K\pi}\cos\delta_D^{K\pi}$ discussed in Sec. 7.7 the *CP*-even fraction in the $D \to \pi^+\pi^-\pi^0$ decay, $F_+^{\pi\pi\pi^0}$, is replaced with $F_+^{\pi\pi\pi^0}/(1 + R_{K^0_S})$, which effectively dilutes the *CP*-even content.

$D\overline{D} \to K^-\pi^+$ **vs.** $K^0_S\pi^0$

The stringent requirements placed to reconstruct K^0_S mesons results in a highly pure sample. There are only three background components,

- $D\overline{D} \to K^-\pi^+$ vs. combinatorial,
- $D\overline{D} \to$ combinatorial vs. $K^0_S\pi^0$,
- and $D\overline{D} \to$ combinatorial vs. combinatorial,

Table 7.8: Summary of backgrounds in the fits to the *CP* tags and details of their yield parametrisation.

Background	Production mechanisms	Yield parametrisation	Comment
$D\overline{D} \to K^-\pi^+$ vs. K^+K^-			
$K^-\pi^+$ vs. $K^+\pi^-\pi^0$	$D\overline{D}$ $D^*\overline{D} \to \gamma D\overline{D}$ $D^*\overline{D}^* \to \gamma\gamma/\pi^0\pi^0 D\overline{D}$	Floating yield	–
$K^-\pi^+$ vs. $K^+\pi^-\pi^0$	$D^*\overline{D} \to \pi^0 D\overline{D}$ $D^*\overline{D}^* \to \gamma\pi^0 D\overline{D}$	Fixed relative to signal	$(6.6 \pm 0.3)\%$ $(10.3 \pm 0.5)\%$
$D\overline{D} \to K^-\pi^+$ vs. $\pi^+\pi^-\pi^0$			
$K^-\pi^+$ vs. $K^+\pi^-\pi^0$	All	Floating yield	–
$K^-\pi^+$ vs. $K^+\pi^- + \pi^0_{D^*}$	$D^*\overline{D} \to \pi^0 D\overline{D}$ $D^*\overline{D}^* \to \gamma\pi^0 D\overline{D}$	Floating yield	–
$K^-\pi^+$ vs. $K^+\pi^- + \pi^0_{D^*}$	$D^*\overline{D} \to \gamma D\overline{D}$ $D^*\overline{D}^* \to \gamma\gamma/\pi^0\pi^0 D\overline{D}$	Fixed relative to signal	$(2.74 \pm 0.15)\%$ $(4.7 \pm 0.2)\%$

each of which is modelled in the fits in the same way as for the K^+K^- and $\pi^+\pi^-$ tags.

7.6.1.3 Anti-correlated background

For each final state, a specific type of combinatorial background is present which displays a correlation between the reconstructed invariant masses of the two D-decay candidates. This is most clearly seen in Fig. 7.15, which shows the fit to $D\overline{D} \to K^-\pi^+$ vs. $\pi^+\pi^-$ candidates in the $D^*\overline{D} \to \pi^0 D\overline{D}$ sample.

This background is reconstructed by combining particles produced in the hadronisation of quarks from the $e^+e^- \to q\bar{q}$ process. In these events, no real D mesons are produced. However, the kinematic fits constrain the masses of each D-decay candidate to the PDG value, and therefore the fitted momentum of each D-decay candidate compensates accordingly. Importantly, this introduces a correlation between the average invariant mass of the two D-decay candidates, denoted $\bar{m}_D$, and E_{miss}. For example, suppose the invariant mass of both D-decay candidates in a particular event was around 1.7 GeV/c^2, around 150 MeV/c^2 below the mass of the D^0 meson. To compensate, the kinematically-fitted momentum of

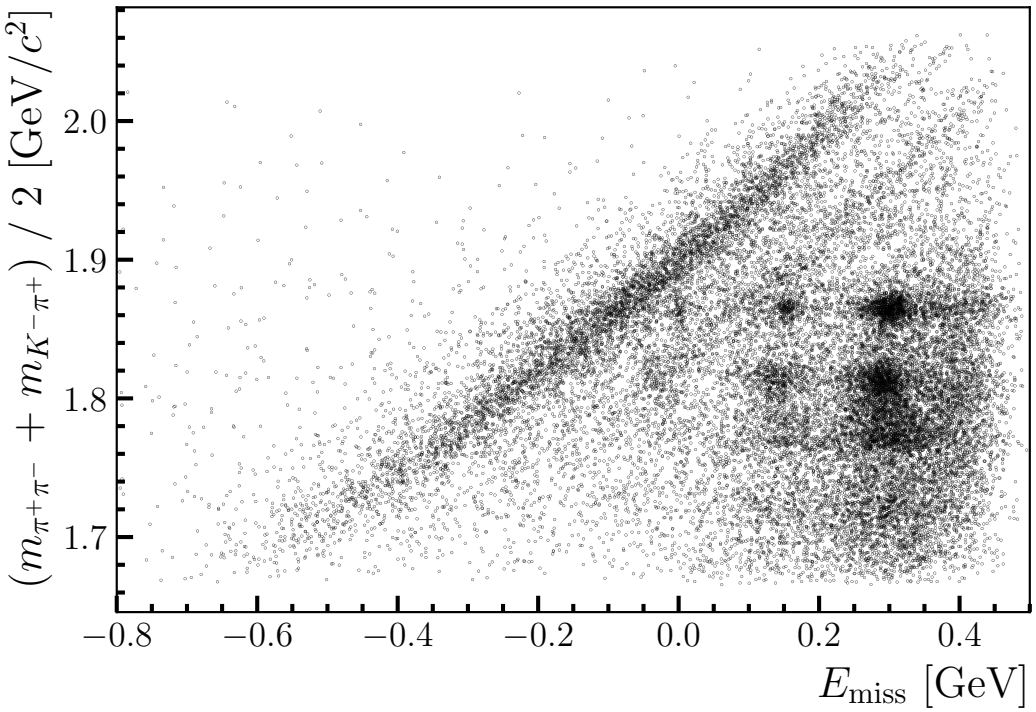

Figure 7.12: Two-dimensional distribution of the missing energy and the average invariant mass of the reconstructed D decays in data for candidates reconstructed in the $D\overline{D} \to K^-\pi^+$ vs. $\pi^+\pi^-$ decay channel. The correlated stripe corresponds to background created by combining random tracks from $e^+e^- \to q\bar{q}$ production.

both candidates will increase, and thus from Eq. 7.3 the E_{miss} will be low. This effect is clearly displayed in Fig. 7.12, which shows a scatter plot of $\bar{m}_D$ and E_{miss} in data for $D\overline{D} \to K^-\pi^+$ vs. $\pi^+\pi^-$ candidates.

When selecting the $D\overline{D}$ pairs in each decay chain a requirement is placed on E_{miss}. Through the correlation, this effectively isolates background candidates with a particular $\bar{m}_D$, which, in the fits, manifests as a component where the reconstructed invariant masses of the two candidates are anti-correlated.

The simulation does not accurately model this background. Therefore, the PDF which represents this component is chosen based on the quality of the fits to data. The PDF used is a Gaussian in the sum of the reconstructed invariant masses of the two D-decay candidates,

$$f(m_{D_1}, m_{D_2}) = \frac{1}{\sigma\sqrt{2\pi}} \exp\left(-\frac{1}{2}\left(\frac{m_{D_1} + m_{D_2} - \mu}{\sigma}\right)^2\right), \tag{7.18}$$

where m_D is the reconstructed invariant mass of a D meson, and μ and σ are floating parameters in the fits. Alternative shapes are used to assign a systematic uncertainty in Sec. 7.9.

As an additional cross-check, the Gaussian PDF is fit to a sample of the anti-correlated background in data, which is isolated by selecting a particular region in $\bar{m}_D$ and $E_{\rm miss}$ in the $D\overline{D} \to K^-\pi^+$ vs. $\pi^+\pi^-$ decay sample. Figure 7.13 displays the good quality fit.

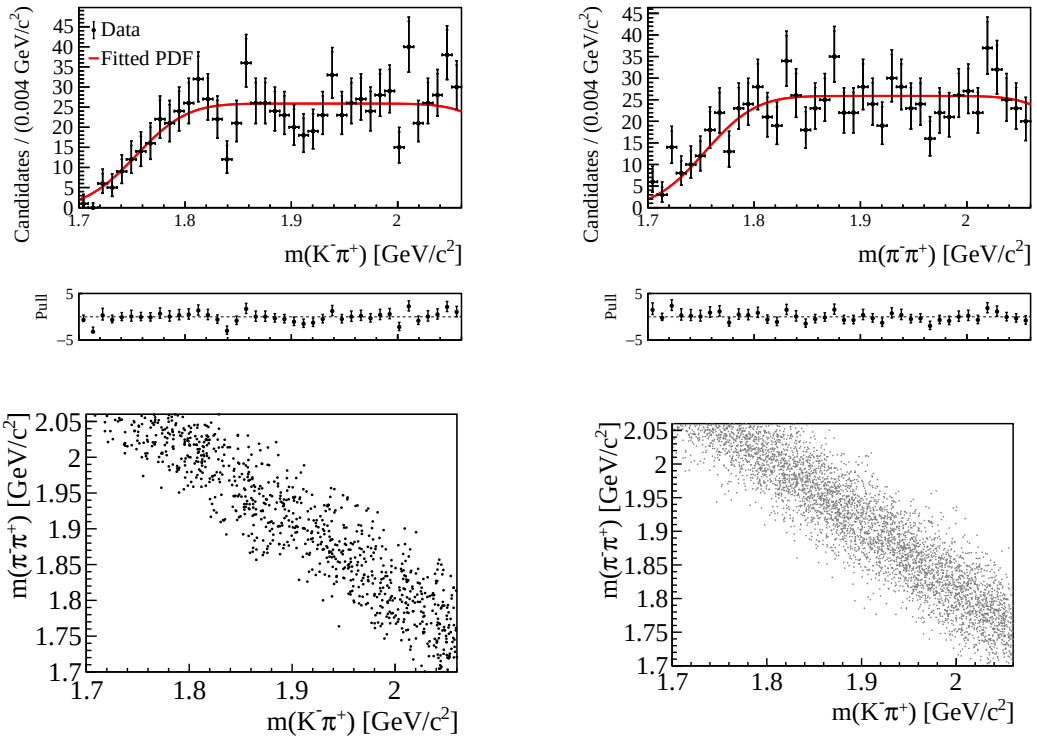

Figure 7.13: Fit to an isolated sample of combinatorial background with anti-correlated D-meson invariant masses in the $D\overline{D} \to K^-\pi^+$ vs. $\pi^+\pi^-$ data sample. The projections of the fit in the reconstructed invariant mass of the (top left) $D \to K^-\pi^+$ and (top right) $D \to \pi^+\pi^-$ decays are shown. The bottom left plot shows a scatter plot of the candidates in data, whilst the bottom right plot shows the same plot of fake candidates generated from the fitted PDF.

7.6.2 Results of the invariant-mass fits

Table 7.9 details the signal yields determined in the fits. Figures 7.14-7.17 display the reconstructed invariant-mass projections for each final state in the $D^*\overline{D} \to \pi^0 D\overline{D}$

and $D^*\overline{D}^* \to \gamma\pi^0 D\overline{D}$ samples, which have the largest signal yields. The pull distributions in the projections suggest the fits are of good quality. They are further judged by examining a two-dimensional scatter plot of the reconstructed invariant masses of both D-decay candidates, where the contribution from each component is clear. For example, in the fit to $D\overline{D} \to K^-\pi^+$ vs. $\pi^+\pi^-\pi^0$ decay candidates which pass the selection requirements to isolate the $D^*\overline{D}^* \to \gamma\pi^0 D\overline{D}$ decay chain shown in Fig. 7.16, the

- signal component can be found at (m_{D^0}, m_{D^0}),
- the $D\overline{D} \to K^-\pi^+$ vs. $K^+\pi^-$ decays can be found around $(m_{D^0}, 1.91\,\text{GeV}/c^2)$,
- the $D\overline{D} \to K^-\pi^+$ vs. $K^+\pi^-\pi^0$ decays can be found around $(m_{D^0}, 1.74\,\text{GeV}/c^2)$,
- the $D\overline{D} \to K^-\pi^+$ vs. combinatorial ($D\overline{D} \to$ combinatorial vs. $\pi^+\pi^-\pi^0$) component corresponds to the vertical (horizontal) stripe,
- and pure combinatorial background with two incorrectly reconstructed D mesons is distributed across the plane.

To ensure that each component is being accurately modelled, the scatter plot of the candidates is compared to that of a pseudo data sample five times larger that is generated from the fitted PDF. An example which highlights the importance of this comparison can be found in Fig. 7.15, which shows the fit $D\overline{D} \to K^-\pi^+$ vs. $\pi^+\pi^-$ decay candidates that pass the $D^*\overline{D} \to \pi^0 D\overline{D}$ isolation requirements. It is clear that the fit is accurately estimating the anti-correlated background component, which is not obvious from the one-dimensional projections.

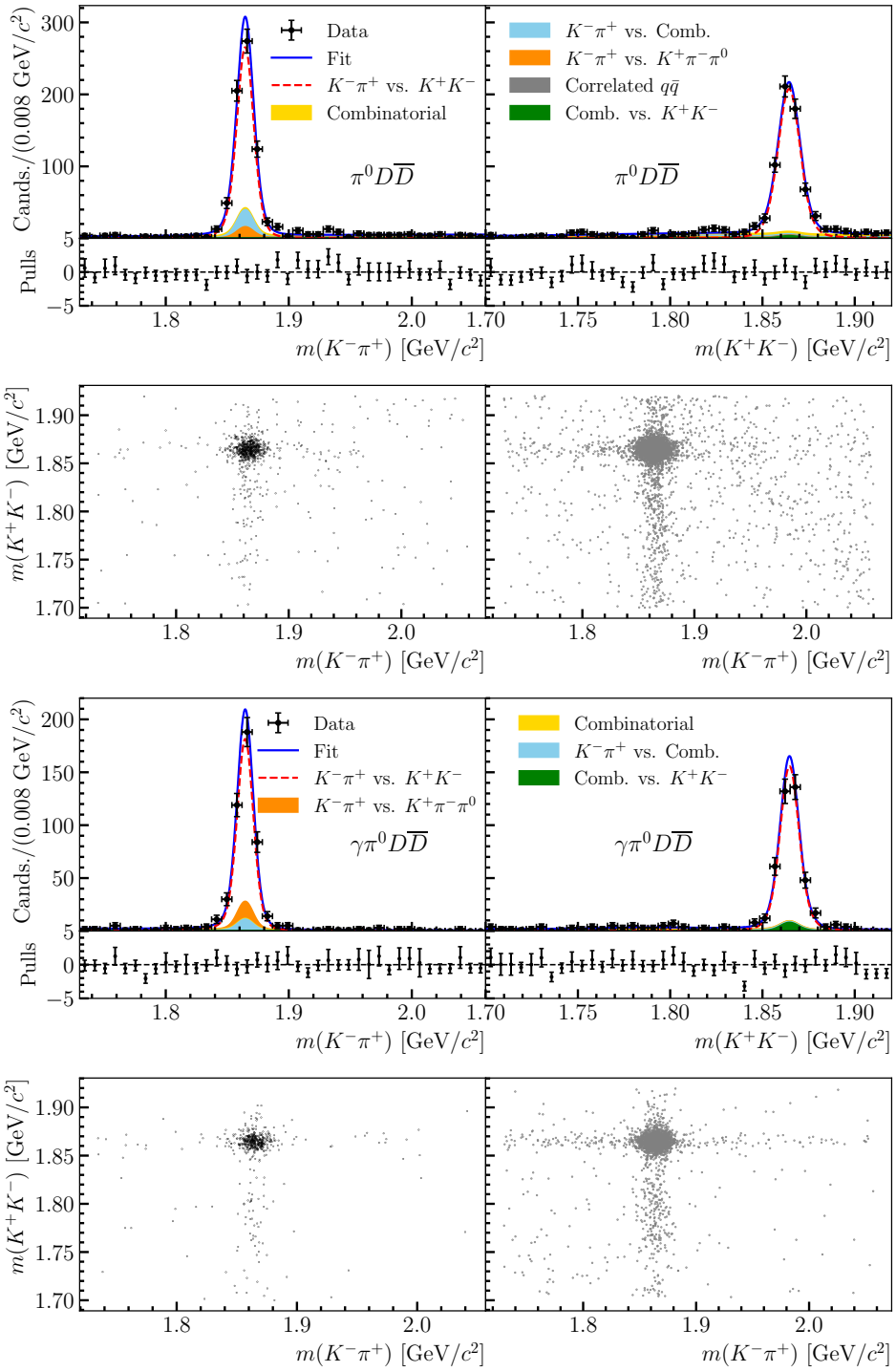

Figure 7.14: The results of the fits to $D\overline{D} \to K^-\pi^+$ vs. K^+K^- candidates which pass the criteria to isolate the (top half) $D^*\overline{D} \to \pi^0 D\overline{D}$ and (bottom half) $D^*\overline{D}^* \to \gamma\pi^0 D\overline{D}$ production mechanisms. In each half, the invariant-mass projections of the (top left) $D \to K^-\pi^+$ and (top right) $D \to K^+K^-$ decay candidates are shown. A scatter plot of the invariant masses of the candidates in (bottom left) data and (bottom right) pseudo data generated from the fitted PDF are displayed.

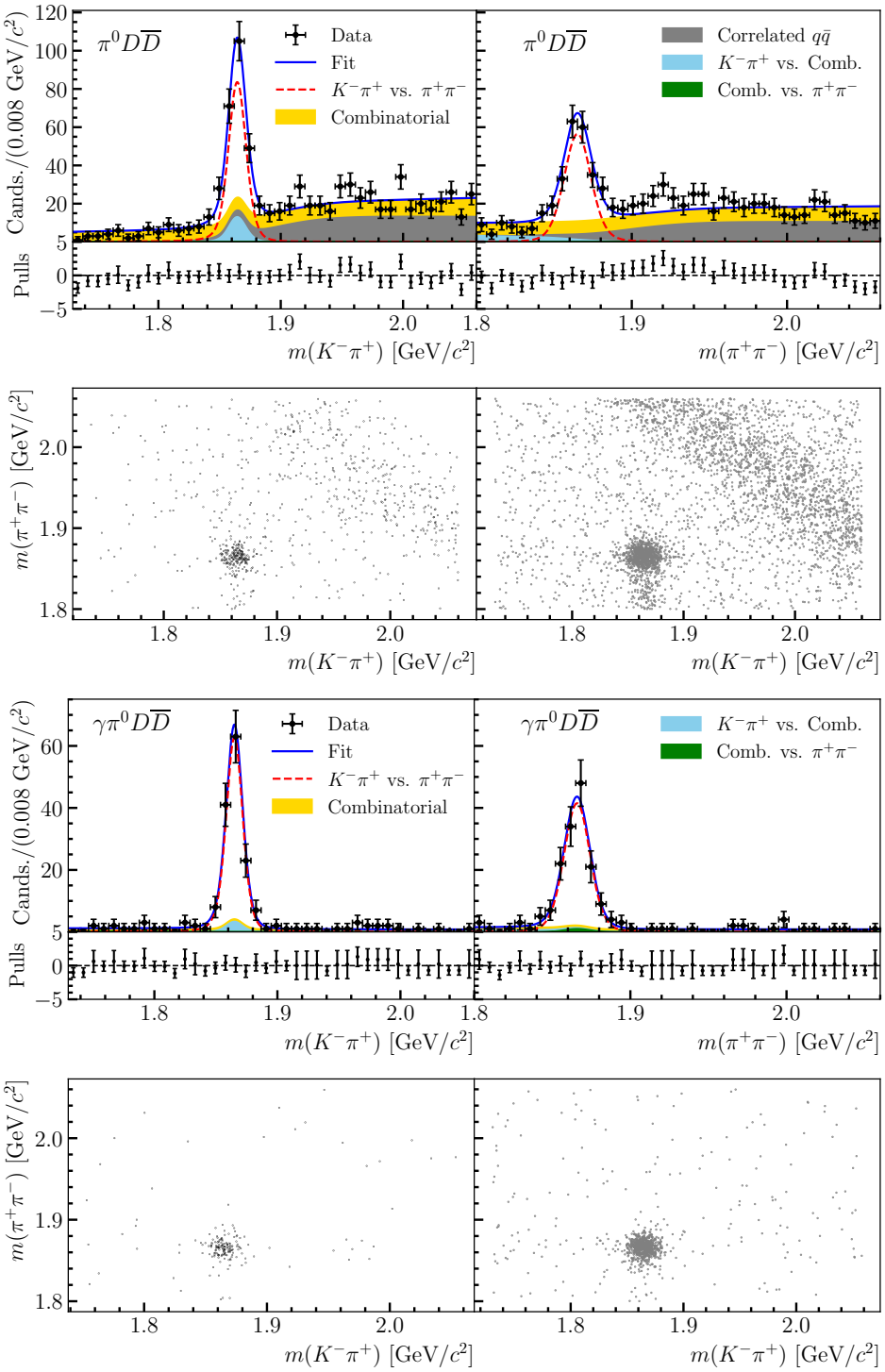

Figure 7.15: The results of the fits to $D\overline{D} \to K^-\pi^+$ vs. $\pi^+\pi^-$ candidates which pass the criteria to isolate the (top half) $D^*\overline{D} \to \pi^0 D\overline{D}$ and (bottom half) $D^*\overline{D}^* \to \gamma\pi^0 D\overline{D}$ production mechanisms. In each half, the invariant-mass projections of the (top left) $D \to K^-\pi^+$ and (top right) $D \to \pi^+\pi^-$ decay candidates are shown. A scatter plot of the invariant masses of the candidates in (bottom left) data and (bottom right) pseudo data generated from the fitted PDF are displayed.

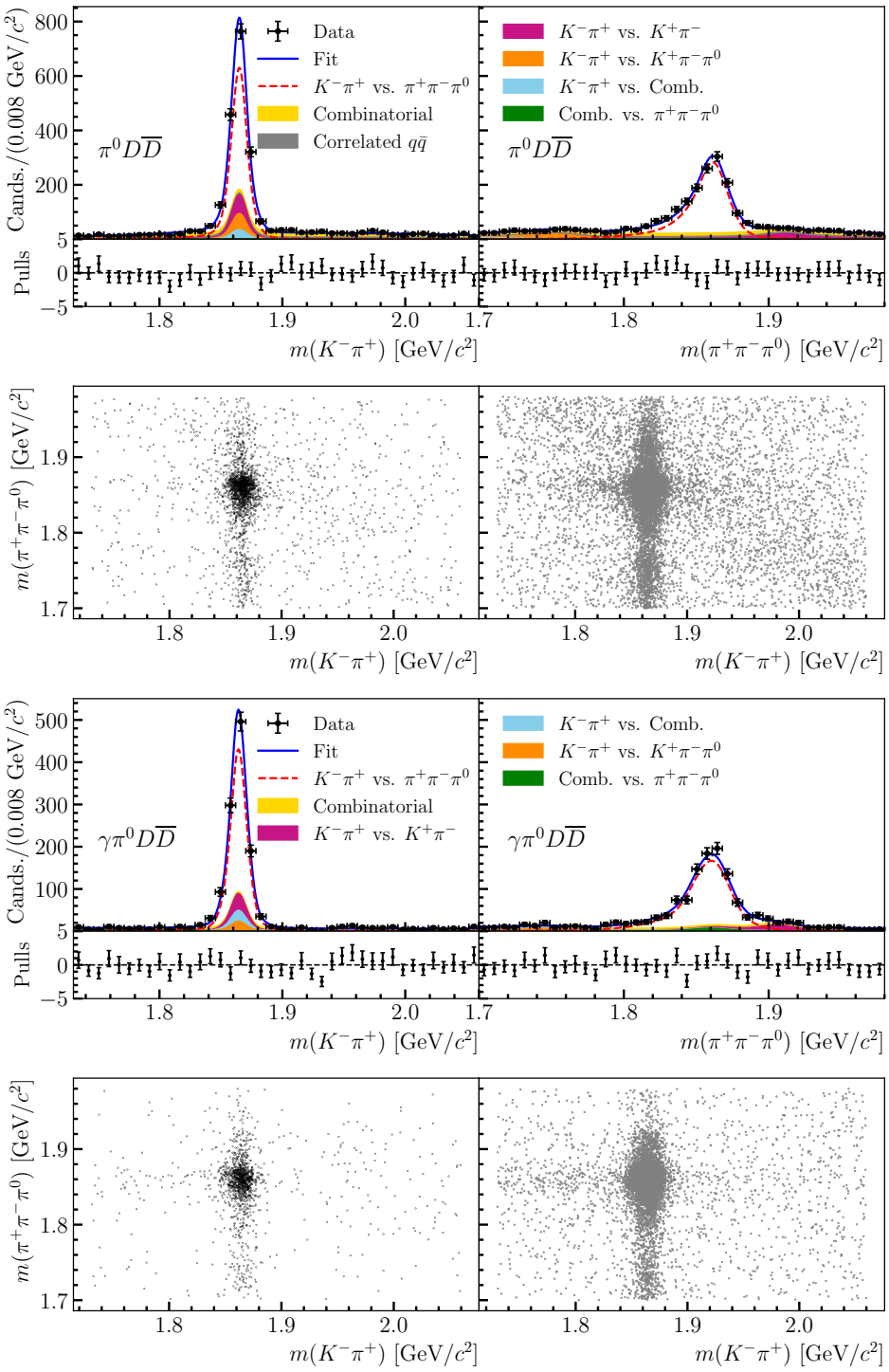

Figure 7.16: The results of the fits to $D\overline{D} \to K^-\pi^+$ vs. $\pi^+\pi^-\pi^0$ candidates which pass the criteria to isolate the (top half) $D^*\overline{D} \to \pi^0 D\overline{D}$ and (bottom half) $D^*\overline{D}^* \to \gamma\pi^0 D\overline{D}$ production mechanisms. In each half, the invariant-mass projections of the (top left) $D \to K^-\pi^+$ and (top right) $D \to \pi^+\pi^-\pi^0$ decay candidates are shown. A scatter plot of the invariant masses of the candidates in (bottom left) data and (bottom right) pseudo data generated from the fitted PDF are displayed.

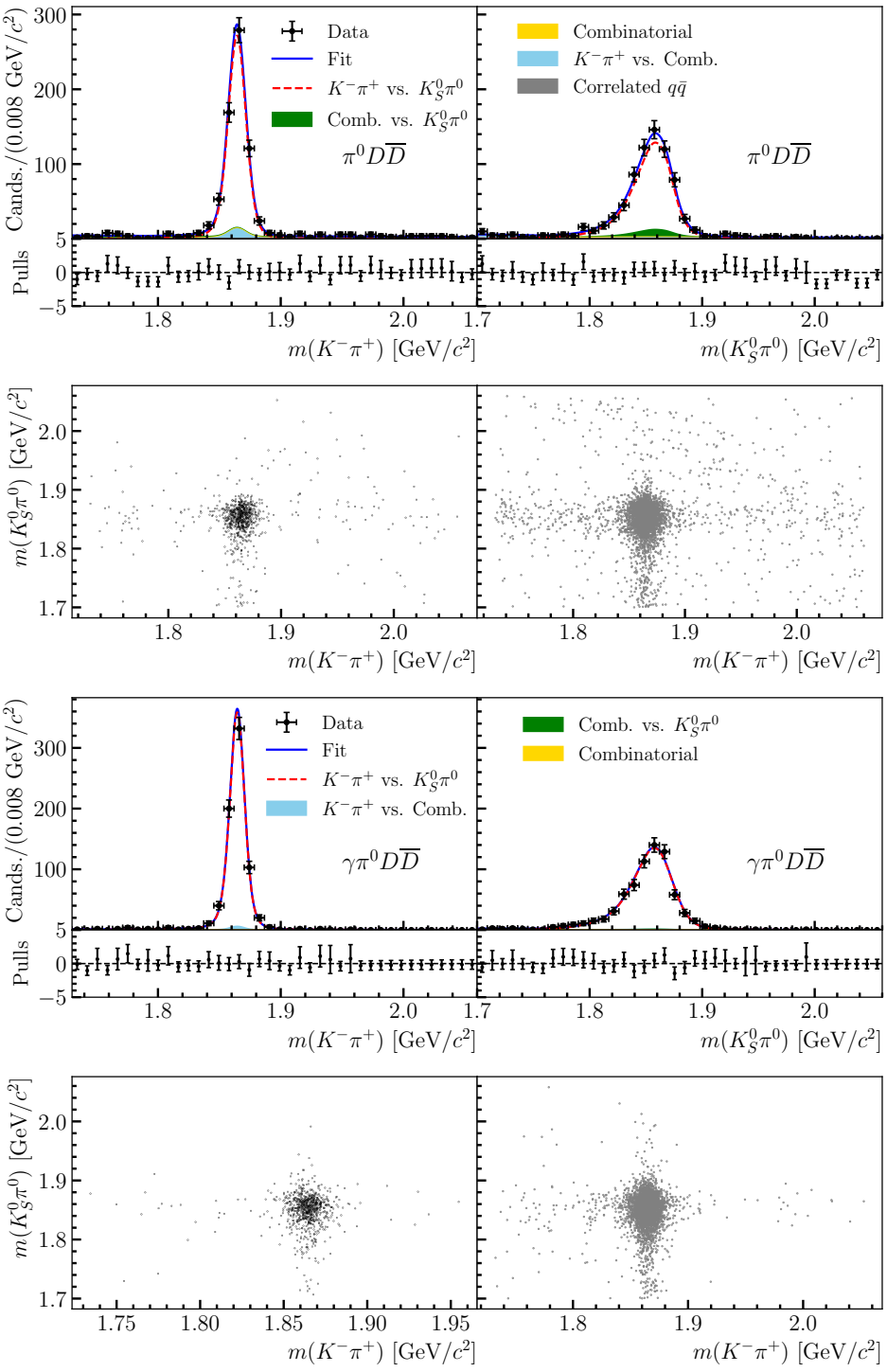

Figure 7.17: The results of the fits to $D\overline{D} \to K^-\pi^+$ vs. $K^0_S\pi^0$ candidates which pass the criteria to isolate the (top half) $D^*\overline{D} \to \pi^0 D\overline{D}$ and (bottom half) $D^*\overline{D}^* \to \gamma\pi^0 D\overline{D}$ production mechanisms. In each half, the invariant-mass projections of the (top left) $D \to K^-\pi^+$ and (top right) $D \to K^0_S\pi^0$ decay candidates are shown. A scatter plot of the invariant masses of the candidates in (bottom left) data and (bottom right) pseudo data generated from the fitted PDF are displayed.

Table 7.9: The signal yields measured for each *CP* tag, after applying the selection requirements to isolate each production mechanism.

CP tag	$D\overline{D}$	$D^*\overline{D} \to \gamma D\overline{D}$	$D^*\overline{D} \to \pi^0 D\overline{D}$	$D^*\overline{D}^* \to \gamma\pi^0 D\overline{D}$	$D^*\overline{D}^* \to \gamma\gamma/\pi^0\pi^0 D\overline{D}$
K^+K^-	157 ± 14	221 ± 17	610 ± 27	398 ± 22	228 ± 17
$\pi^+\pi^-$	79 ± 11	66 ± 10	199 ± 16	139 ± 13	98 ± 10
$\pi^+\pi^-\pi^0$	377 ± 25	578 ± 29	1372 ± 41	935 ± 35	540 ± 26
$K^0_S\pi^0$	158 ± 16	396 ± 21	650 ± 27	721 ± 28	288 ± 18

7.6.3 Correcting for $e^+e^- \to D^{*+}D^{*-}$ background

A background is present from $D^0\overline{D}^0$ decays to the correct final state, where the $D^0\overline{D}^0$ pairs originate from the $e^+e^- \to D^{*+}D^{*-} \to D^0\overline{D}^0\pi^+\pi^-$ process. As discussed in Sec. 7.3, the $D^{*+}D^{*-}$ production is reduced by the requirements placed to isolate the various decay chains, but a small amount remains in the samples. Since the D decay is correctly reconstructed in both dimensions this background is indistinguishable from signal in the invariant-mass fits. Therefore, corrections are applied to the measured signal yields in Tab. 7.9 by subtracting the predicted background yield from simulation, which does not require corrections for quantum correlations because the flavour of the D^0 and $\overline{D}^0$ mesons are specified by the charges on the pions from the $D^{*\pm}$ decays. The corrections are shown in Tab. 7.10, and as expected, they are largest for the $D^*\overline{D}^* \to \gamma\pi^0 D\overline{D}$ and $D^*\overline{D}^* \to \gamma\gamma/\pi^0\pi^0 D\overline{D}$ production mechanisms, but there are also small contributions in the fits to $D\overline{D}$ pairs which pass the $D^*\overline{D} \to \gamma D\overline{D}$ and $D^*\overline{D} \to \pi^0 D\overline{D}$ selection criteria due to cross-feed. The background is largest for the $\pi^+\pi^-\pi^0$ and $K^0_S\pi^0$ tags, which possess higher branching fractions and a worse resolution due to the neutral pion in the final state.

The yields of the backgrounds originating from the $e^+e^- \to D^{*+}D^{*-}$ process in simulation are given by

$$N(f_{CP}, P) = \mathcal{L}\sigma_{D^{*+}D^{*-}}\mathcal{B}^2(D^{*+} \to D^0\pi^+)\mathcal{B}(D^0 \to K^-\pi^+)\mathcal{B}(D^0 \to f_{CP})\epsilon_P, \quad (7.19)$$

where $\mathcal{L}$ is the luminosity, σ is the cross-section and ϵ_P is the selection efficiency for $D^0\overline{D}^0 \to K^-\pi^+$ vs. f_{CP} candidates after applying the criteria to isolate production

Table 7.10: Corrections subtracted from the measured signal yields for each tag and production mechanism to account for $D^0\overline{D}^0$ decays to the correct final state, where the $D^0\overline{D}^0$ pair originates from the $e^+e^- \to D^{*+}D^{*-}$ process. The yields are found using simulation and have a relative error of around 6.5% for the K^+K^-, $\pi^+\pi^-$ and $K^0_S\pi^0$ tags, and around 8% for the $\pi^+\pi^-\pi^0$ tag.

CP tag	$D\overline{D}$	$D^*\overline{D} \to \gamma D\overline{D}$	$D^*\overline{D} \to \pi^0 D\overline{D}$	$D^*\overline{D}^* \to \gamma\pi^0 D\overline{D}$	$D^*\overline{D}^* \to \gamma\gamma/\pi^0\pi^0 D\overline{D}$
K^+K^-	0	0	1.9	2.9	3.4
$\pi^+\pi^-$	0	0	0.8	1.9	0.4
$\pi^+\pi^-\pi^0$	0.4	2.0	4.5	20.1	35.4
$K^0_S\pi^0$	0	0.2	2.3	10.3	17.7

mechanism, P. The uncertainties on the corrections are determined by considering the knowledge of each of these inputs to the MC. The luminosities and efficiencies are known with a relative error of around 1%. This is low in comparison to the knowledge of the $e^+e^- \to D^{*+}D^{*-}$ cross-sections [109], which is around 6%. The relevant branching fractions are shown in Tab. 7.2 which all have a relative error less than 2%, with the exception of the $D^0 \to \pi^+\pi^-\pi^0$ decay where it is around 5%. Combining these sources in quadrature finds a relative error on the yields in Tab. 7.10 of around 8% for the $\pi^+\pi^-\pi^0$ tag and 6.5% for the remainder. The knowledge of these yields is considered as a systematic uncertainty described in Sec. 7.9.2

7.6.4 Invariant-mass fit validation study

A validation study is performed to ensure the signal yields are extracted from the invariant-mass fits without bias and with the appropriate uncertainties. The PDF determined in each fit to data is used to generate 1000 pseudo data samples which are subsequently refit. Figure 7.18 displays the mean bias and the width of the pulls on the signal yields. All uncertainties are found to be correctly estimated and the average biases are less than 3 candidates in each fit. Four of the fits show small biases that deviate from zero by more than 3σ which are shown in Tab. 7.11. Corrections are applied to the signal yields found in data.

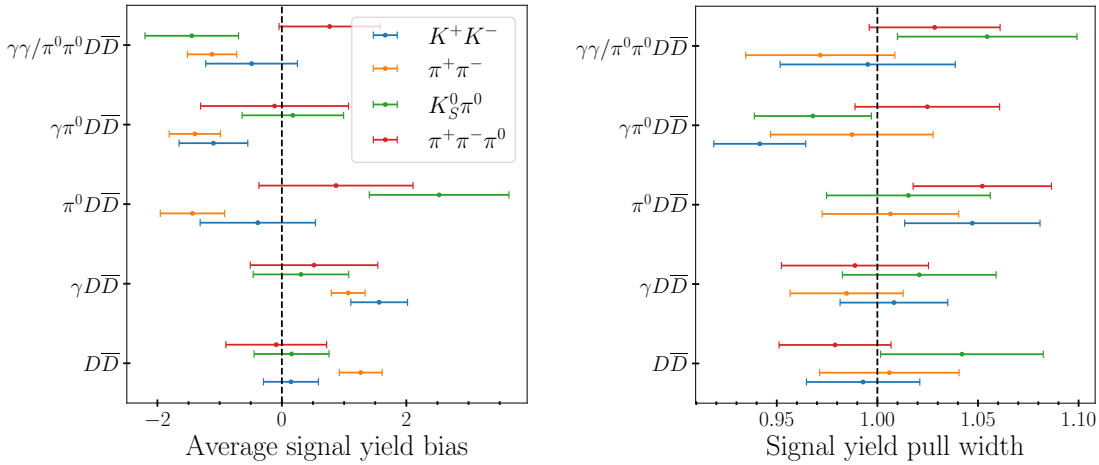

Figure 7.18: The (left) average bias and (right) the width of the pull distributions of the signal yields determined in the invariant-mass fit validation study performed using pseudo data samples.

Table 7.11: Biases on the signal yields which are more than 3σ as determined through studies using pseudo data.

CP tag	Production mechanism	Bias
K^+K^-	$D^*\overline{D} \to \gamma D\overline{D}$	1.6 ± 0.5
$\pi^+\pi^-$	$D\overline{D}$	1.3 ± 0.3
$\pi^+\pi^-$	$D^*\overline{D} \to \gamma D\overline{D}$	1.1 ± 0.3
$\pi^+\pi^-$	$D^*\overline{D}^* \to \gamma\pi^0 D\overline{D}$	-1.4 ± 0.4

7.7 Fit to extract $r_D^{K\pi}\cos\delta_D^{K\pi}$ from the *CP* tags

The parameter $r_D^{K\pi}\cos\delta_D^{K\pi}$ is extracted by comparing the measured yields of the $D\overline{D} \to K^-\pi^+$ vs. f_{CP} decays to predictions given those found in $D\overline{D} \to K^-\pi^+$ vs. $K^+\pi^-$ decays. The latter were determined for the analysis in Sec. 7.4 and are reproduced in Tab. 7.5. To understand the procedure, a scenario is first described where only a single production mechanism exists. A prediction for the $D\overline{D} \to K^-\pi^+$ vs. f_{CP} decay yield is calculated by accounting for differences in the efficiencies, ϵ, and branching fractions, $\mathcal{B}$, between the two channels, such that

$$N^{\text{pred}}_{K\pi,f_{CP}} = 2\frac{\mathcal{B}_{D^0\to K^-\pi^+}\epsilon_{K\pi,f_{CP}}}{\mathcal{B}_{D^0\to f_{CP}}\epsilon_{K\pi,K\pi}} f_C^{\lambda} N^{\text{obs}}_{K\pi,K\pi}, \tag{7.20}$$

where the factor of 2 accounts for charge conjugation. The f_C^λ term is the ratio of Eqs. 7.16 and 7.1, and accounts for the relative enhancement of the decay rate due to the quantum correlations,

$$f_C^\lambda = \frac{1 + (r_D^{K\pi})^2 + 2\lambda C r_D^{K\pi} \cos\delta_D^{K\pi} - \lambda(1+C)y_D}{1 + 2C\left(2(r_D^{K\pi}\cos\delta_D^{K\pi})^2 - (r_D^{K\pi})^2\right)}, \tag{7.21}$$

which depends on the C eigenvalue of the $D\overline{D}$ pair and the CP content of the tag, λ. As a reminder, the parameter $\lambda = 1$ (-1) for CP-even (odd) tags and $2\frac{F_+^{\pi\pi\pi^0}}{1+R_{K^0_S}} - 1$ for the $\pi^+\pi^-\pi^0$ tag.

For multiple production mechanisms, the expression is trivially expanded to a matrix equation, such that

$$\vec{N}^{\rm pred}_{K\pi,f_{CP}} = 2\frac{\mathcal{B}_{D^0\to K^-\pi^+}}{\mathcal{B}_{D^0\to f_{CP}}}\mathbf{A}_{K\pi,f_{CP}}\mathbf{f}_C^\lambda\mathbf{A}^{-1}_{K\pi,K\pi}\vec{N}^{\rm obs}_{K\pi,K\pi}, \tag{7.22}$$

where $\mathbf{A}_{K\pi,X}$ is the efficiency matrix for the $D\overline{D} \to K^-\pi^+$ vs. X final state and $\vec{N}_{K\pi,X}$ is now a vector containing the signal yields after applying the selection requirements to isolate each production mechanism. In this case, $\mathbf{f}_C^\lambda$ is a diagonal matrix with elements given by Eq. 7.21.

It is possible to calculate the predictions without using the $D\overline{D} \to K^-\pi^+$ vs. $K^+\pi^-$ control channel. However, it requires knowledge of the cross-sections of the $e^+e^- \to D\overline{D}$, $e^+e^- \to D^*\overline{D}$ and $e^+e^- \to D^*\overline{D}^*$ processes, and the integrated luminosities of the data samples at each centre-of-mass energy, which would result in large systematic uncertainties. Another benefit of using the control channel is a large cancellation of the systematic uncertainties associated with the differences between the cross-feed efficiencies in data and MC. The efficiency matrices can be roughly factorised into two contributions,

$$\mathbf{A}_{K\pi,X} \simeq \epsilon_{K\pi,X} \times \mathbf{A}^{'}, \tag{7.23}$$

where $\epsilon_{K\pi,X}$ is a constant corresponding to the efficiency of reconstructing the $D\overline{D} \to K^-\pi^+$ vs. X final state, and $\mathbf{A}^{'}$ is the efficiency matrix associated with the cross-feed, which is approximately independent of the final state. Since the predicted

yields are $\propto \mathbf{A}_{K\pi,X}\mathbf{A}^{-1}_{K\pi,K\pi}$, the dependence on the cross-feed efficiencies mostly cancels. This is demonstrated through the product $\mathbf{A}_{K\pi,\pi\pi}\mathbf{A}^{-1}_{K\pi,K\pi}$, which is given by

$$\mathbf{A}_{K\pi,\pi\pi}\mathbf{A}^{-1}_{K\pi,K\pi} = 1.06\begin{pmatrix} 1 & 0 & 0 & 0 & 0 \\ 0.01 & 0.97 & 0 & 0 & 0 \\ 0 & 0.01 & 1 & 0 & 0 \\ 0 & 0 & 0 & 1 & 0.03 \\ 0 & 0 & 0.01 & -0.01 & 1.05 \end{pmatrix} \tag{7.24}$$

and is approximately 1.06 multiplied by the identity matrix.

In principle, one could perform a χ^2 fit which simply compares the fitted and predicted signal yields. However, it would be necessary to include a systematic uncertainty to account for differences between the reconstruction efficiency of the final state ($\epsilon_{K\pi,X}$ in Eq. 7.23) in data and MC. To avoid this, observables are constructed from the yields. Specifically, the ratio of the total measured signal yield originating from C-even and C-odd $D\overline{D}$ pairs is calculated for each CP tag. It is given by

$$R^{\rm obs}_{f_{CP}} = \sum_{\rm E} N_{\rm E} / \sum_{\rm O} N_{\rm O}, \tag{7.25}$$

where $N_{\rm E(O)}$ is the measured signal yield of $D\overline{D} \to K^-\pi^+$ vs. f_{CP} candidates which pass the selection criteria designed to isolate a decay chain which produces C-even (C-odd) $D\overline{D}$ pairs. The ratio also removes any dependence on the D-decay branching fractions, which in some cases are known with an uncertainty of around 5%. The observed ratios are compared to the predictions in a χ^2 fit, where

$$\chi^2 = \sum_{f_{CP}} \left(\frac{R^{\rm obs}_{f_{CP}} - R^{\rm pred}_{f_{CP}}}{\Delta R^{\rm obs}_{f_{CP}}} \right)^2, \tag{7.26}$$

and the sum runs over the CP tags. It is worth highlighting the use of observables calculated from the measured signal yields results in a significantly simplified fit, compared to one that uses efficiency-corrected yields which are all correlated due to the cross-feed.

7.7.1 Closure check

A validation study is performed to ensure that the fit extracts the parameter $r_D^{K\pi}\cos\delta_D^{K\pi}$ without bias and with the appropriate uncertainty. The procedure begins by predicting the signal yields for each final state using,

$$\vec{N}_{K\pi,X} = \mathcal{B}_{D^0\to K^-\pi^+}\mathcal{B}_{\overline{D}^0\to X}\mathbf{A}_{K\pi,X}f_C^X\vec{n}_{D\overline{D}}, \tag{7.27}$$

where $\vec{n}_{D\overline{D}}$ is the total number of $D\overline{D}$ pairs from each production mechanism in simulation and f_C^X is the relative enhancement due to quantum correlations from Eq. 7.16. To calculate f_C^X, the parameters $F_+^{\pi\pi\pi^0} = 0.9406$, $r_D^{K\pi} = 0.05865$, $y_D = 0.636\%$ and $\delta_D^{K\pi} = 190.2^\circ$ are used from Refs. [107, 39]. Then, in each category given by the final state and production mechanism, yields are randomly drawn from a Poisson distribution before the ratios are calculated and the fit is performed to determine $r_D^{K\pi}\cos\delta_D^{K\pi}$. In the fit, the $D\overline{D} \to K^-\pi^+$ vs. $K^+\pi^-$ yields are Gaussian constrained and $(r_D^{K\pi})^2$, $F_+^{\pi\pi\pi^0}$ and y_D are fixed to the values above.

The closure check is initially performed ten thousand times using yields that are multiplied by a factor of 100 to ensure no procedural bias exists. An input value of $r_D^{K\pi}\cos\delta_D^{K\pi} = -0.06$ is used. Figure 7.19 displays the resulting pull distribution for $r_D^{K\pi}\cos\delta_D^{K\pi}$, which has a mean, $\mu = 0.014 \pm 0.009$, and a width, $\sigma = 1.020 \pm 0.009$, that are consistent with expectations. Next, the study is repeated using yields similar to those expected in data, and with a range of $r_D^{K\pi}\cos\delta_D^{K\pi}$ input values. A consistent bias of around 4% of the statistical error is found, as is also shown in Fig. 7.19. Given the bias is smaller than the least significant figure on the uncertainty of $r_D^{K\pi}\cos\delta_D^{K\pi}$ measured in data, a correction is not applied, and instead it is considered as a systematic uncertainty. The widths of the pull distributions are all found to be consistent with one.

7.7.2 Fit results

Having performed the validation study, the fit is repeated using the yields from data, and a value of $r_D^{K\pi}\cos\delta_D^{K\pi} = -0.070 \pm 0.008$ is determined with $\chi^2/\text{n.d.f.} = 2.1/3$.

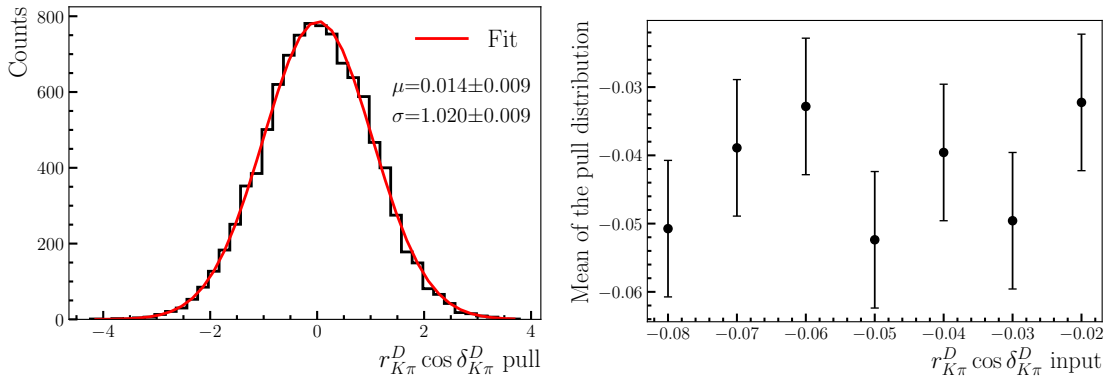

Figure 7.19: Left: distribution of $r_D^{K\pi}\cos\delta_D^{K\pi}$ pulls determined in a validation study using signal yields 100× larger than those in data. The red line corresponds to a fit using a Gaussian. Right: the mean pull on $r_D^{K\pi}\cos\delta_D^{K\pi}$ as a function of the input value used for $r_D^{K\pi}\cos\delta_D^{K\pi}$.

No significant pulls are found on the $D\overline{D} \to K^-\pi^+$ vs. $K^+\pi^-$ decay yields, as the fitted value of each agrees with those in Tab. 7.5 to within 10% of the statistical uncertainties.

Figure 7.20 displays a comparison between the ratios determined in data, which are also detailed in Tab. 7.12, and those found using $r_D^{K\pi}\cos\delta_D^{K\pi}$ from the fit. The ratios are also shown in the scenario without quantum correlations, which are calculated using Eq. 7.22 without the enhancement matrix $\mathbf{f}_C^{\lambda}$. With this, it is clear to see the effects of the quantum correlations. For a *CP*-even tag, the yields originating from *C*-even $D\overline{D}$ pairs would be suppressed by a factor of around 12% relative to the uncorrelated scenario. The inverse is true for decays of *C*-odd $D\overline{D}$ pairs and the rate is suppressed by around 12%. Therefore, neglecting the cross-feed, the expected ratios would be around $(1-0.12)/(1+0.12) \simeq 80\%$ of those in the uncorrelated scenario. The reverse applies to the *CP*-odd $D \to K^0_S\pi^0$ decay and the ratio would be around 127% of the prediction in the case without quantum correlations. These back-of-the-napkin predictions are consistent with the ratios determined in data shown in Tab. 7.12 given that the uncorrelated predictions are around 0.8.

Another interesting observation from Fig. 7.20 is that the uncorrelated predictions are approximately constant across the *CP* tags. This clearly supports the arguments above. It shows that the ratios are independent of the reconstruction

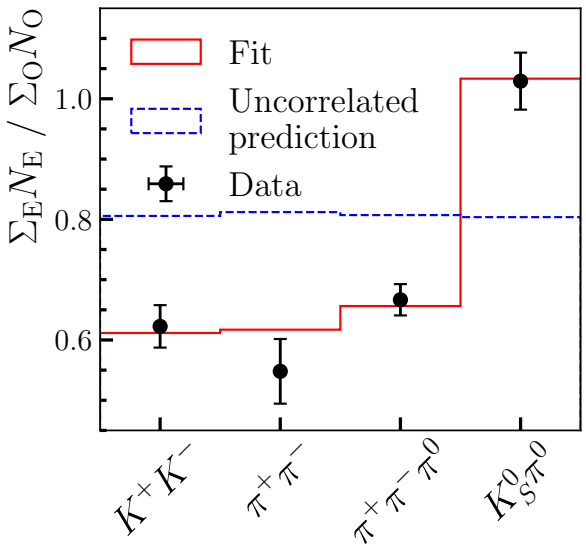

Figure 7.20: The ratio of the sum of signal yields determined after applying the requirements to isolate C-even and C-odd $D\overline{D}$ pairs for each CP tag. The ratios determined (black points) using the yields found in data, (red) using the results of the χ^2 fit and (blue) assuming no quantum correlations are shown.

Table 7.12: Ratios of the total signal yields measured after applying the selection criteria to isolate C-even and odd $D\overline{D}$ pairs.

CP tag	$R^{\rm obs}_{f_{CP}}$
K^+K^-	0.62 ± 0.04
$\pi^+\pi^-$	0.55 ± 0.05
$\pi^+\pi^-\pi^0$	0.67 ± 0.03
$K^0_S\pi^0$	1.03 ± 0.05

efficiency of the final state, so any differences between data and MC will cancel, and that the cross-feed between production mechanisms does not significantly depend on the tag.

7.8 Measurement of $r_D^{K\pi}\cos\delta_D^{K\pi}$ and $r_D^{K\pi}\sin\delta_D^{K\pi}$ using $D \to K^0_S\pi^+\pi^-$ decays

In the previous section, the parameter $r_D^{K\pi}\cos\delta_D^{K\pi}$ is determined in two stages. First, the signal yields are found for each final state and production mechanism

through invariant-mass fits. Then, the yields are used to construct ratio observables which are compared to predictions to evaluate $r_D^{K\pi}\cos\delta_D^{K\pi}$. In the measurement of $r_D^{K\pi}\cos\delta_D^{K\pi}$ and $r_D^{K\pi}\sin\delta_D^{K\pi}$ discussed in this section a different approach is used. The observables are directly determined in the invariant-mass fit by parametrising the signal yields in each of 80 categories, given by the five production mechanisms and the sixteen regions of the *equal-*$\Delta\delta_D$ division of $D \to K^0_S\pi^+\pi^-$ decay phase space, according to their expected distributions after accounting for quantum correlations and efficiencies.

7.8.1 Configuration of the invariant-mass fit

7.8.1.1 Signal

To parameterise the signal yield in each category various efficiency effects are considered:

- the cross-feed between production mechanisms,
- the varying reconstruction efficiency across phase space,
- and the migration of candidates between regions of phase space due to the finite momentum resolution.

Due to the migration and cross-feed, it is possible for decays initially produced in a certain category, $\alpha = (i, A)$, to be reconstructed in any other category, $\beta = (j, B)$. Here, the lowercase (uppercase) Latin letter corresponds to the region of the Dalitz plot (production mechanism) associated with the category. Therefore, in the fit, the signal yield observed in a category, β, is given by

$$N_\beta = \epsilon_{\beta\alpha} n_\alpha, \tag{7.28}$$

where n_α is the true signal yield in category α. The matrix element $\epsilon_{\beta\alpha}$ is the efficiency of reconstructing signal in category β when it is originally produced in category α, which simultaneously accounts for all three efficiency effects outlined above.

Table 7.13: Values of the K_i, c_i and s_i inputs from Ref. [10] used in the measurement of $r_D^{K\pi}\cos\delta_D^{K\pi}$ and $r_D^{K\pi}\sin\delta_D^{K\pi}$ using $D\overline{D} \to K^-\pi^+$ vs. $K^0_S\pi^+\pi^-$ decays.

Region index	K_i	K_{-i}	c_i	s_i
1	0.083 ± 0.002	0.176 ± 0.003	0.699 ± 0.020	-0.091 ± 0.063
2	0.019 ± 0.001	0.087 ± 0.002	0.643 ± 0.036	-0.300 ± 0.110
3	0.021 ± 0.001	0.067 ± 0.002	0.001 ± 0.047	-1.000 ± 0.075
4	0.016 ± 0.001	0.024 ± 0.001	-0.608 ± 0.052	-0.660 ± 0.123
5	0.053 ± 0.002	0.085 ± 0.002	-0.955 ± 0.023	0.032 ± 0.069
6	0.012 ± 0.001	0.058 ± 0.002	-0.578 ± 0.058	0.545 ± 0.122
7	0.012 ± 0.001	0.125 ± 0.003	0.057 ± 0.057	0.854 ± 0.095
8	0.028 ± 0.001	0.134 ± 0.003	0.411 ± 0.036	0.433 ± 0.083

The observables, $r_D^{K\pi}\cos\delta_D^{K\pi}$ and $r_D^{K\pi}\sin\delta_D^{K\pi}$, are included within n_α, which is given by the total number of $D\overline{D} \to K^-\pi^+$ vs. $K^0_S\pi^+\pi^-$ decays that originate from production mechanism, A, multiplied by the fraction that fall in the Dalitz plot region associated with the category, Y_i, such that

$$n_\alpha = Y_i n_A, \tag{7.29}$$

where Y_i is given by Eq. 5.30. In the fit, the observables and the total number of $D\overline{D} \to K^-\pi^+$ vs. $K^0_S\pi^+\pi^-$ decays for each production mechanism are floating parameters, whilst $x_D = (0.398^{+0.050}_{-0.049})\%$, $y_D = (0.636^{+0.020}_{-0.019})\%$ [39] and the K_i, c_i and s_i [10] parameters are fixed. The latter are reproduced in Tab. 7.13 for reference.

Given the full efficiency matrix contains 6400 elements it is not included in the thesis. However, using the simulation, it is found that the migration matrices are consistent across production mechanisms, and furthermore, that the unfolding matrix in a region of the Dalitz plot with index, i, is in good agreement with that in the opposite region $-i$. Therefore, the full efficiency matrix can be factorised into a single 16×16 migration matrix and eight 5×5 unfolding matrices. The former is displayed in Fig. 7.21, and an example of the latter for region with index $|i| = 1$ can be found in Tab. 7.14. The migration is less than 6% between each bin pair, whilst the relative variation in reconstruction efficiency across phase space is at most around 20%.

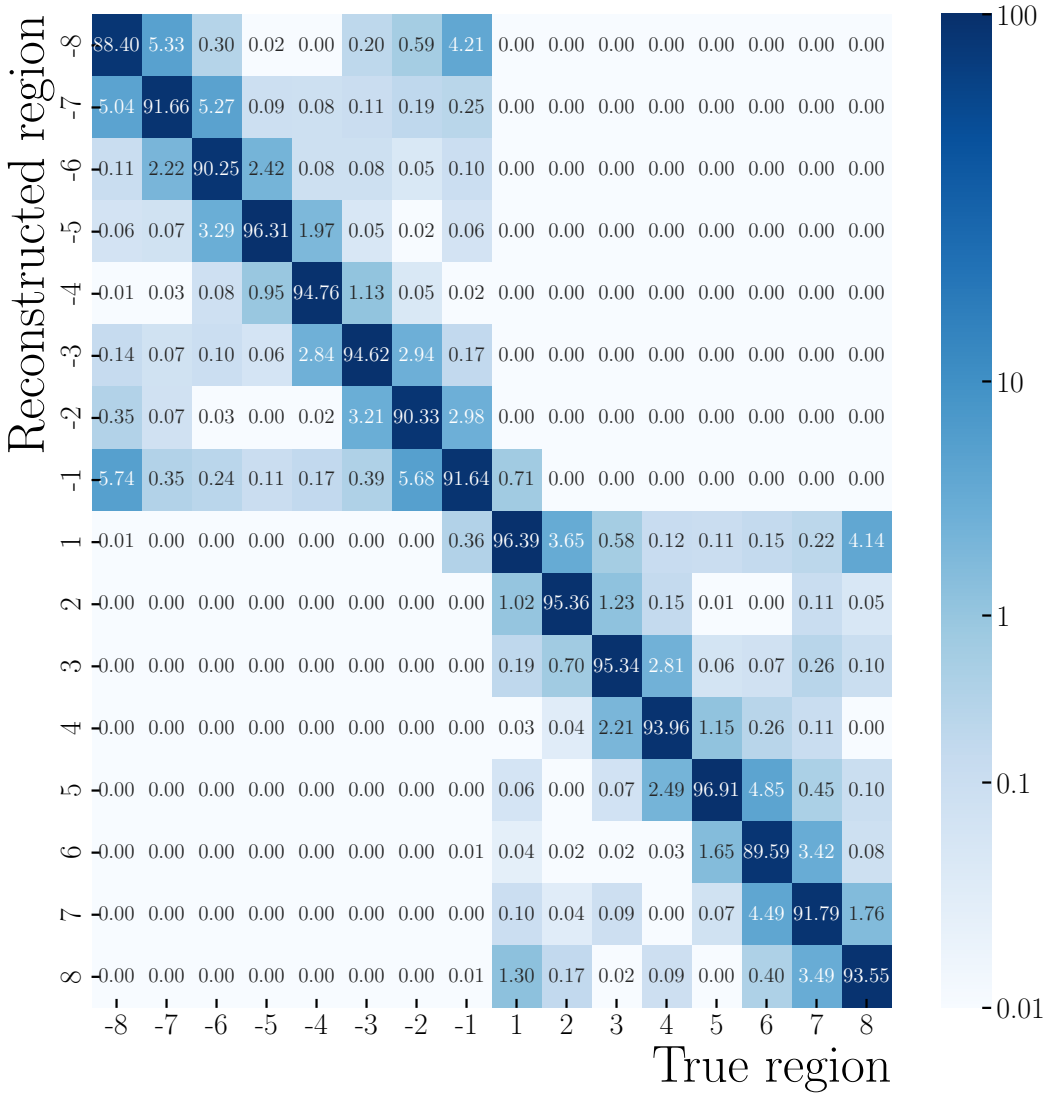

Figure 7.21: Efficiency (in percent) of reconstructing signal candidates in each region of the Dalitz plot, given their true region.

Table 7.14: Efficiency, in percent, of reconstructing the $D\overline{D} \to K^-\pi^+$ vs. $K^0_S\pi^+\pi^-$ final state in Dalitz plot region with index $|i| = 1$ in simulation. An element with row, i, and column, j, gives the efficiency of reconstructing the production mechanism, i, after applying the selection requirements devised to isolate $D\overline{D}$ pairs produced by process, j.

		Identified as				
		$D\overline{D}$	$D^*\overline{D} \to \gamma D\overline{D}$	$D^*\overline{D} \to \pi^0 D\overline{D}$	$D^*\overline{D}^* \to \gamma\pi^0 D\overline{D}$	$D^*\overline{D}^* \to \gamma\gamma/\pi^0\pi^0 D\overline{D}$
True	$D\overline{D}$	20.02	1.73	0.01	0	0.02
	$D^*\overline{D} \to \gamma D\overline{D}$	0.02	15.27	0.96	0.04	0.99
	$D^*\overline{D} \to \pi^0 D\overline{D}$	0	0.32	17.89	0.31	0.20
	$D^*\overline{D}^* \to \gamma\pi^0 D\overline{D}$	0	0.02	0.01	13.75	0.50
	$D^*\overline{D}^* \to \gamma\gamma/\pi^0\pi^0 D\overline{D}$	0	0.01	0	0.33	5.26

In the fit, the signal component is modelled by the KDE of the shape in simulation convolved with a Gaussian which has floating mean and width parameters in both dimensions. A separate Gaussian is used for the different production mechanisms and is shared across the regions of the Dalitz plot.

7.8.1.2 $D\overline{D}$ backgrounds

The flight-distance significance and invariant-mass requirements placed on the K^0_S meson result in a relatively pure sample. Three backgrounds that originate from $D\overline{D}$ decays are modelled in the fit

- $D\overline{D} \to K^-\pi^+$ vs. combinatorial,
- $D\overline{D} \to$ combinatorial vs. $K^0_S\pi^+\pi^-$,
- and $D\overline{D} \to$ combinatorial vs. combinatorial,

each of which has a floating yield parameter in all categories.

The yields of two components where one D meson is correctly reconstructed are expected to be low in each category, so there is limited sensitivity to the combinatorial background shapes. Therefore, they are modelled by an exponential function with a slope parameter that is shared across the Dalitz plot for each production mechanism and D meson. Once again, the pure combinatorial background is larger due to the contribution from $e^+e^- \to q\bar{q}$ production. This component is represented by an exponential function in both dimensions with floating slope parameters in each category.

Two potential backgrounds are investigated in the reconstructed invariant mass of the $D \to K^0_S\pi^+\pi^-$ candidates in simulation. First, a number of $D\overline{D} \to K^-\pi^+$ vs. $K^0_S K^-\pi^+$ decays are found, where the K^- is misidentified as a π^-. These decays have a suppressed branching fraction, low selection efficiency and an invariant-mass distribution that peaks outwith the fit range, leading to a negligible contribution.

Secondly, a background is present from $D\overline{D} \to K^-\pi^+$ vs. $\pi^+\pi^-\pi^+\pi^-$ decays which do not proceed through the intermediate K^0_S meson. This background is significantly suppressed by the selection, and the rate in simulation is around 0.2% of the signal, which is also negligible.

7.8.1.3 Anti-correlated background

The anti-correlated background discussed in Sec. 7.6.1.3 is seen in the categories which isolate the $D\overline{D}$ and $D^*\overline{D} \to \pi^0 D\overline{D}$ production mechanisms. They are represented in the fit by the function described in Eq. 7.18, with separate floating mean and width parameters for the two decay chains, which are shared across the Dalitz plot. The yield is a floating parameter in each relevant category.

7.8.1.4 $e^+e^- \to D^{*+}D^-$ production

In the data samples which isolate the two decay chains originating from the $e^+e^- \to D^*\overline{D}$ process, a background is present from $e^+e^- \to D^{*+}D^-$ production, where $D^{*+} \to [K^-\pi^+]_{D^0}\pi^+$ and $D^- \to K^0_S\pi^-\pi^0$. The π^+ meson from the D^{*+} decay is used to create a $D \to K^0_S\pi^+\pi^-$ decay candidate, and the π^0 meson from the D^- decay is missed. The background is non-negligible despite the mis-reconstruction due to the large branching fraction $\mathcal{B}(D^- \to K^0_S\pi^-\pi^0) = (7.36 \pm 0.20)\%$ [33].

For the background to meet the selection criteria, the π^0 from the D^- decay must have a low momentum, otherwise the event would possess a large missing energy. Therefore, the Dalitz plot coordinate, $m^2(K^0_S\pi^-)$, is relatively large and peaks just below $m^2_{D^0}$. Similarly, since the π^+ meson from the D^{*+} decay is soft, $m^2(K^0_S\pi^+)$ is relatively low and peaks around 0.8 GeV^2/c^4. Therefore, the background only appears in one half of the Dalitz plot, specifically the regions with positive indices, and the corresponding yields from simulation are displayed in Tab. 7.15. The uncertainties are determined similarly to those described in Sec. 7.6.3 and are found to be around 3.7%. In the fit, the yield is fixed in each relevant category and is represented by a KDE of the distribution in MC, which is shown in Fig. 7.22.

Table 7.15: The yield from simulation of the background originating from $e^+e^- \to D^{*+}D^-$ production discussed in the text in each region of phase space and for the $D^*\overline{D} \to \gamma D\overline{D}$ and $D^*\overline{D} \to \pi^0 D\overline{D}$ production mechanisms. The yield in the regions of phase space with negative indices is zero. The relative error on the yields is 3.7%.

Region index	$D^*\overline{D} \to \gamma D\overline{D}$	$D^*\overline{D} \to \pi^0 D\overline{D}$
8	3.2	3.4
7	5.0	7.9
6	4.8	3.2
5	15.6	13.6
4	0	0
3	7.0	6.2
2	4.2	4.4
1	1.0	1.8

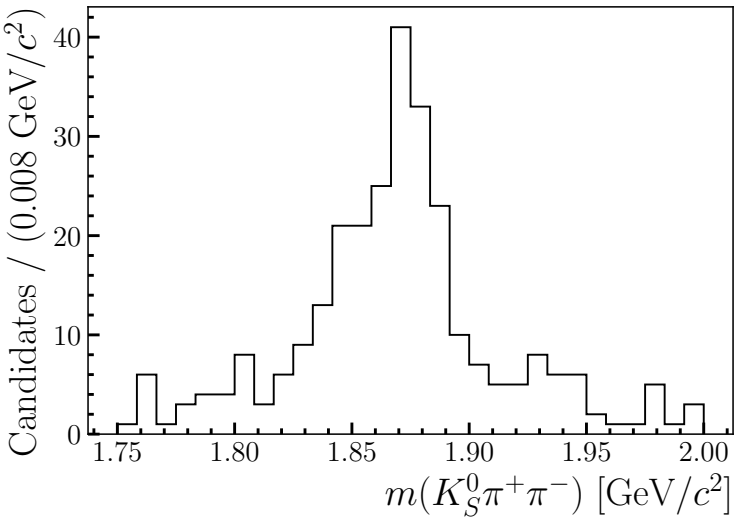

Figure 7.22: Simulated invariant-mass distribution of background candidates reconstructed as $D \to K^0_S\pi^+\pi^-$ decays that originate from the $e^+e^- \to D^{*+}D^-$ process.

7.8.1.5 $e^+e^- \to D^{*+}D^{*-}$ production

Similarly to the *CP* tags, a background is present from $D^0\overline{D}^0$ pairs originating from $e^+e^- \to D^{*+}D^{*-}$ production, which are indistinguishable from signal in the invariant-mass fit. Since the observables are extracted directly from the fit this background must be included as a component. They are represented by the same PDF as signal with fixed yields that are determined in simulation and are shown in Tab. 7.16. The relative uncertainties on the yields are estimated to be around 8.5%. The yields are negligible in the categories which isolate $D\overline{D}$ pairs produced in the $e^+e^- \to D\overline{D}$ and $e^+e^- \to D^*\overline{D}$ processes.

Table 7.16: The yield from simulation of the background from signal decays that originate from the $D^0\overline{D}^0$ pairs produced in the $e^+e^- \to D^{*+}D^{*-}$ process. The relative errors on the yields are 8.5%.

Region index	$D^*\overline{D}^* \to \gamma\pi^0 D\overline{D}$	$D^*\overline{D}^* \to \gamma\gamma/\pi^0\pi^0 D\overline{D}$
-8	1.0	1.3
-7	0.6	0.7
-6	0.7	1.1
-5	2.7	2.4
-4	1.2	0.8
-3	0.5	0.5
-2	0.8	0.7
-1	3.1	3.2
1	3.5	7.0
2	3.6	3.6
3	1.6	3.2
4	0.2	1.1
5	3.4	5.2
6	1.5	2.4
7	3.3	5.4
8	4.8	4.6

7.8.2 Fit validation

A validation study is performed to ensure the fit returns unbiased observables. A fit to the data is performed, and the resulting PDF is used to generate ten thousand pseudo data samples which are subsequently refit. Figure 7.23 shows the pull distributions for the observables which display no evidence of bias. The widths suggest the uncertainties are being overestimated by around 4%, but given this is small no correction is applied.

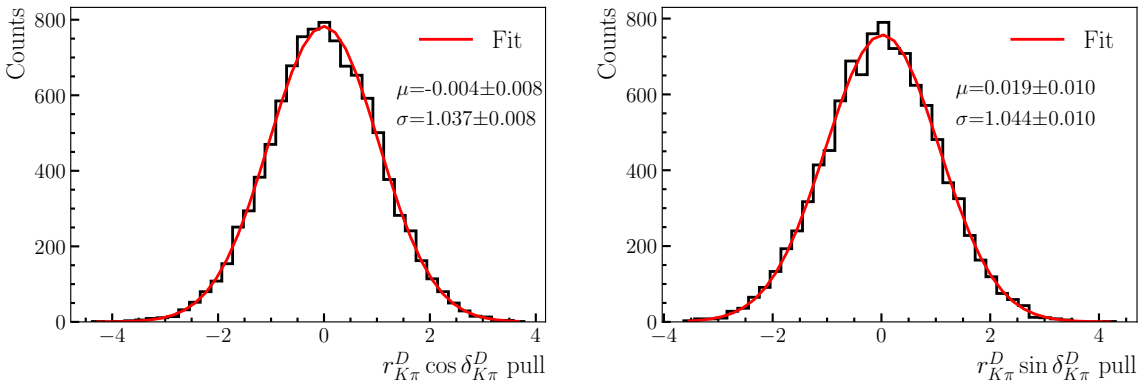

Figure 7.23: Pull distributions for (left) $r_D^{K\pi}\cos\delta_D^{K\pi}$ and (right) $r_D^{K\pi}\sin\delta_D^{K\pi}$ determined using pseudo data samples. The red line shows a fit with a Gaussian function.

7.8.3 Results of the invariant-mass fit

Figures 7.24-7.26 show the fit projections of the invariant mass in the region $i = 1$ for each production mechanism. The fit to data determines the observables to be

$$r_D^{K\pi}\cos\delta_D^{K\pi} = -0.044 \pm 0.014, \qquad (7.30)$$
$$r_D^{K\pi}\sin\delta_D^{K\pi} = -0.022 \pm 0.017,$$

with a statistical correlation coefficient of 3%. The observables are consistent with the values of $r_D^{K\pi}\cos\delta_D^{K\pi} = -0.0562 \pm 0.0081$ and $r_D^{K\pi}\sin\delta_D^{K\pi} = -0.011 \pm 0.012$ found in the measurement performed at the $\psi(3770)$ resonance [13].

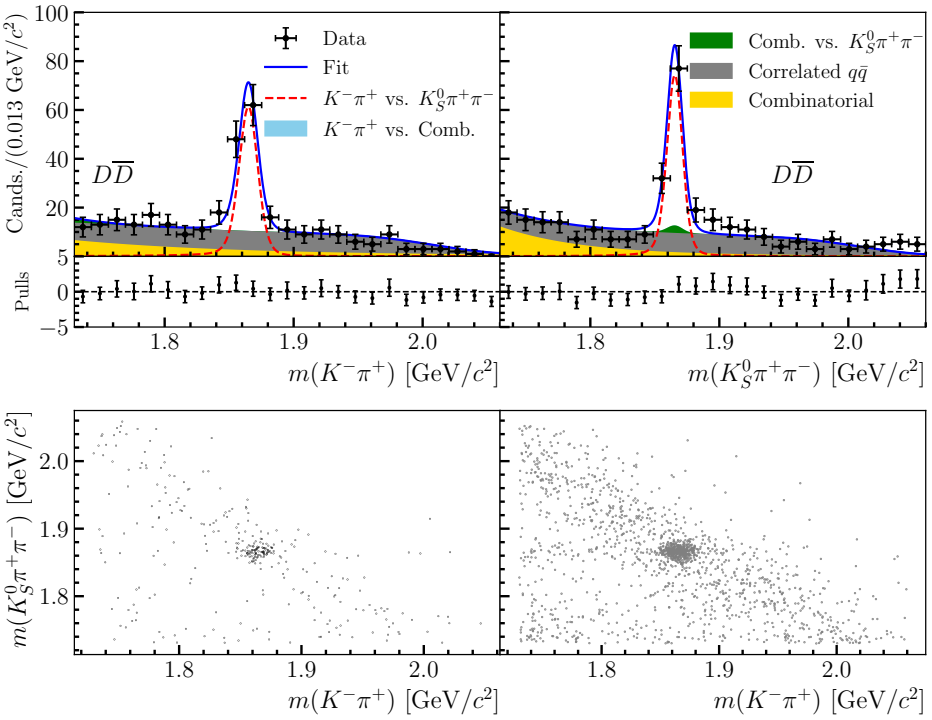

Figure 7.24: The results of the fits to $D\overline{D} \to K^-\pi^+$ vs. $K^0_S\pi^+\pi^-$ candidates in region $i = +1$ which pass the criteria to isolate the $D\overline{D}$ production mechanism. The invariant-mass projections of the (top left) $D \to K^-\pi^+$ and (top right) $D \to K^0_S\pi^+\pi^-$ decay candidates are shown. A scatter plot of the invariant masses of the candidates in (bottom left) data and (bottom right) pseudo data generated from the fitted PDF are displayed.

The fitted integrated yields for each production mechanism are shown in Tab. 7.17. A cross-check can be performed using these yields by examining the ratios,

$$\frac{n(D^*\overline{D} \to \gamma D\overline{D})}{n(D^*\overline{D} \to \pi^0 D\overline{D})} = 0.54 \pm 0.03,$$
$$\frac{n(D^*\overline{D}^* \to \gamma\pi^0 D\overline{D})}{n(D^*\overline{D}^* \to \gamma\gamma/\pi^0\pi^0 D\overline{D})} = 0.89 \pm 0.05,$$

which are in good agreement with the predictions,

$$\frac{n(D^*\overline{D} \to \gamma D\overline{D})}{n(D^*\overline{D} \to \pi^0 D\overline{D})} = \frac{\mathcal{B}(D^{*0} \to \gamma D^0)}{\mathcal{B}(D^{*0} \to \pi^0 D^0)} = 0.55 \pm 0.02,$$
$$\frac{n(D^*\overline{D}^* \to \gamma\pi^0 D\overline{D})}{n(D^*\overline{D}^* \to \gamma\gamma/\pi^0\pi^0 D\overline{D})} = \frac{2\mathcal{B}(D^{*0} \to \gamma D^0)\mathcal{B}(D^{*0} \to \pi^0 D^0)}{\mathcal{B}^2(D^{*0} \to \gamma D^0) + \mathcal{B}^2(D^{*0} \to \pi^0 D^0)} = 0.841 \pm 0.013,$$

where the branching fractions are taken from the PDG.

An alternative fit, where the signal yield is a floating parameter in each category, is performed to ensure that the parametrisations described in Eqs. 7.28 and 7.29

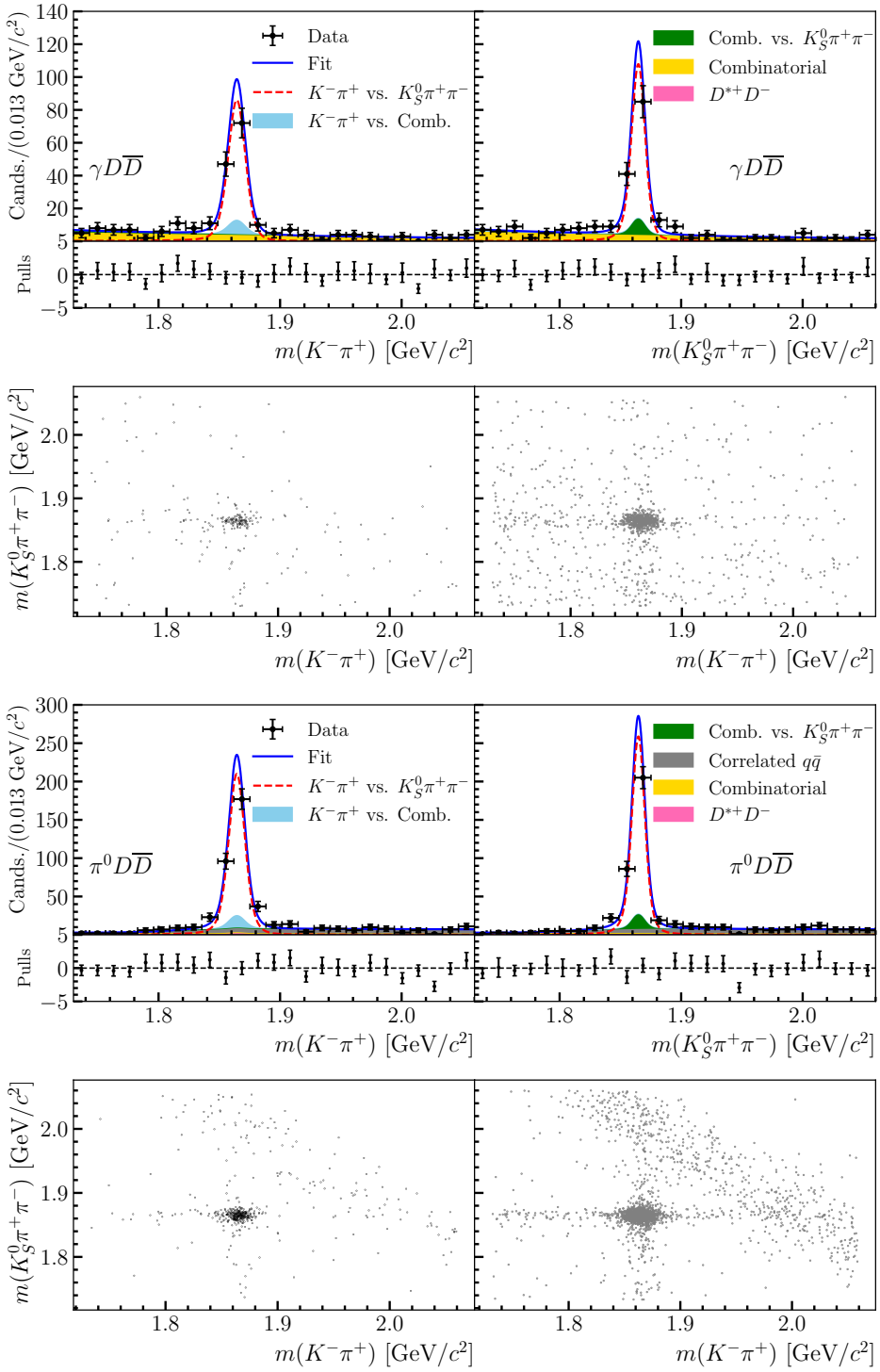

Figure 7.25: The results of the fits to $D\overline{D} \to K^-\pi^+$ vs. $K^0_S\pi^+\pi^-$ candidates in region $i = +1$ which pass the criteria to isolate the (top half) $D^*\overline{D} \to \gamma D\overline{D}$ and (bottom half) $D^*\overline{D} \to \pi^0 D\overline{D}$ production mechanisms. In each half, the invariant-mass projections of the (top left) $D \to K^-\pi^+$ and (top right) $D \to K^0_S\pi^+\pi^-$ decay candidates are shown. A scatter plot of the invariant masses of the candidates in (bottom left) data and (bottom right) pseudo data generated from the fitted PDF are displayed.

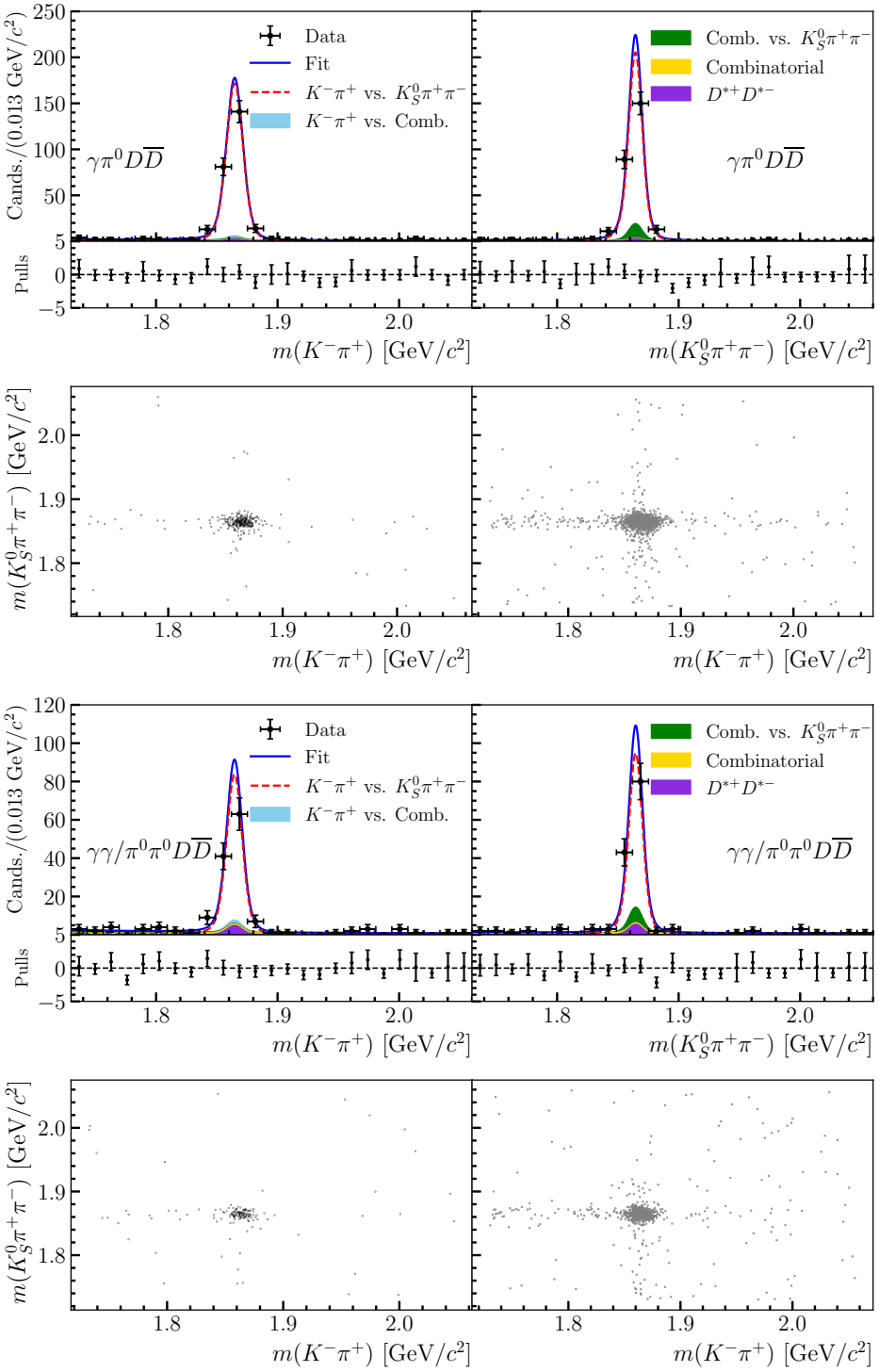

Figure 7.26: The results of the fits to $D\overline{D} \to K^-\pi^+$ vs. $K^0_S\pi^+\pi^-$ candidates in region $i = +1$ which pass the criteria to isolate the (top half) $D^*\overline{D}^* \to \gamma\pi^0 D\overline{D}$ and (bottom half) $D^*\overline{D}^* \to \gamma\gamma/\pi^0\pi^0 D\overline{D}$ production mechanisms. In each half, the invariant-mass projections of the (top left) $D \to K^-\pi^+$ and (top right) $D \to K^0_S\pi^+\pi^-$ decay candidates are shown. A scatter plot of the invariant masses of the candidates in (bottom left) data and (bottom right) pseudo data generated from the fitted PDF are displayed.

Table 7.17: Fitted integrated yields of $D\overline{D} \to K^-\pi^+$ vs. $K^0_S\pi^+\pi^-$ decays.

Production mechanism	Integrated yield
$D\overline{D}$	2411 ± 125
$D^*\overline{D} \to \gamma D\overline{D}$	4752 ± 204
$D^*\overline{D} \to \pi^0 D\overline{D}$	8821 ± 240
$D^*\overline{D}^* \to \gamma\pi^0 D\overline{D}$	9360 ± 284
$D^*\overline{D}^* \to \gamma\gamma/\pi^0\pi^0 D\overline{D}$	10479 ± 528

Table 7.18: Fitted $D\overline{D} \to K^-\pi^+$ vs. $K^0_S\pi^+\pi^-$ decay yields for each region of phase space and production mechanism.

Region	$D\overline{D}$	$D^*\overline{D} \to \gamma D\overline{D}$	$D^*\overline{D} \to \pi^0 D\overline{D}$	$D^*\overline{D}^* \to \gamma\pi^0 D\overline{D}$	$D^*\overline{D}^* \to \gamma\gamma/\pi^0\pi^0 D\overline{D}$
-8	$7.8^{+3.9}_{-3.1}$	$24.1^{+5.7}_{-4.9}$	$57.9^{+8.4}_{-7.7}$	$38.1^{+6.9}_{-6.2}$	$20.3^{+5.1}_{-4.5}$
-7	$3.3^{+3.4}_{-2.4}$	$5.0^{+3.3}_{-2.5}$	$15.8^{+4.6}_{-3.9}$	$16.8^{+4.6}_{-3.9}$	$4.5^{+2.8}_{-2.0}$
-6	$10.1^{+4.0}_{-3.3}$	$11.8^{+4.1}_{-3.4}$	$12.4^{+4.4}_{-3.7}$	$13.0^{+4.1}_{-3.4}$	$13.6^{+4.3}_{-3.6}$
-5	$16.8^{+5.5}_{-4.7}$	$49.1^{+7.7}_{-7.0}$	$72.9^{+9.3}_{-8.6}$	$68.0^{+8.9}_{-8.3}$	$31.4^{+6.3}_{-5.6}$
-4	$5.8^{+3.1}_{-2.4}$	$17.7^{+4.9}_{-4.2}$	$39.1^{+6.7}_{-6.0}$	$27.6^{+5.8}_{-5.1}$	$10.3^{+3.7}_{-3.0}$
-3	$16.8^{+4.9}_{-4.2}$	$11.1^{+4.1}_{-3.3}$	$38.8^{+6.9}_{-6.3}$	$29.4^{+5.9}_{-5.2}$	$13.9^{+4.2}_{-3.5}$
-2	$7.0^{+3.9}_{-3.0}$	$8.3^{+3.5}_{-2.8}$	$30.6^{+6.1}_{-5.4}$	$22.3^{+5.3}_{-4.6}$	$15.8^{+4.5}_{-3.8}$
-1	$51.6^{+8.4}_{-7.6}$	$52.8^{+8.3}_{-7.6}$	$145.7^{+12.8}_{-12.1}$	$99.9^{+10.7}_{-10.0}$	$52.9^{+8.2}_{-7.5}$
+1	$105.8^{+11.5}_{-10.8}$	$118.3^{+12.0}_{-11.3}$	$288.8^{+18.0}_{-17.3}$	$246.0^{+16.5}_{-15.8}$	$110.4^{+11.5}_{-10.8}$
+2	$44.4^{+7.6}_{-6.9}$	$59.8^{+8.7}_{-8.0}$	$155.8^{+13.1}_{-12.4}$	$112.8^{+11.3}_{-10.6}$	$75.2^{+9.4}_{-8.7}$
+3	$41.3^{+7.3}_{-6.6}$	$83.3^{+10.0}_{-9.3}$	$120.3^{+11.8}_{-11.1}$	$102.9^{+10.8}_{-10.1}$	$49.6^{+7.9}_{-7.2}$
+4	$12.9^{+4.4}_{-3.6}$	$21.1^{+5.3}_{-4.6}$	$42.7^{+7.3}_{-6.6}$	$44.5^{+7.2}_{-6.5}$	$11.0^{+3.9}_{-3.2}$
+5	$38.4^{+7.3}_{-6.6}$	$71.8^{+9.7}_{-8.9}$	$138.9^{+12.8}_{-12.1}$	$122.5^{+11.8}_{-11.1}$	$55.0^{+8.5}_{-7.8}$
+6	$26.0^{+6.3}_{-5.6}$	$52.8^{+8.0}_{-7.3}$	$84.3^{+9.9}_{-9.2}$	$88.6^{+9.9}_{-9.3}$	$48.4^{+7.8}_{-7.1}$
+7	$52.8^{+8.1}_{-7.4}$	$90.9^{+10.5}_{-9.8}$	$215.0^{+15.5}_{-14.8}$	$161.3^{+13.5}_{-12.8}$	$86.8^{+10.2}_{-9.5}$
+8	$51.2^{+8.4}_{-7.6}$	$119.1^{+11.7}_{-11.0}$	$208.0^{+15.2}_{-14.5}$	$156.6^{+13.3}_{-12.6}$	$85.1^{+10.0}_{-9.3}$

are representative of the data. Figure 7.27 compares the fitted yields, which are also shown in Tab. 7.18, to those found in the default fit. A good agreement is found between the two determinations which is quantified by $\chi^2/\text{n.d.f.} = 85/73$.

A final alternative fit is performed to display the presence of the quantum correlations in the sample. As displayed in Eq. 5.30 the sign on the interference

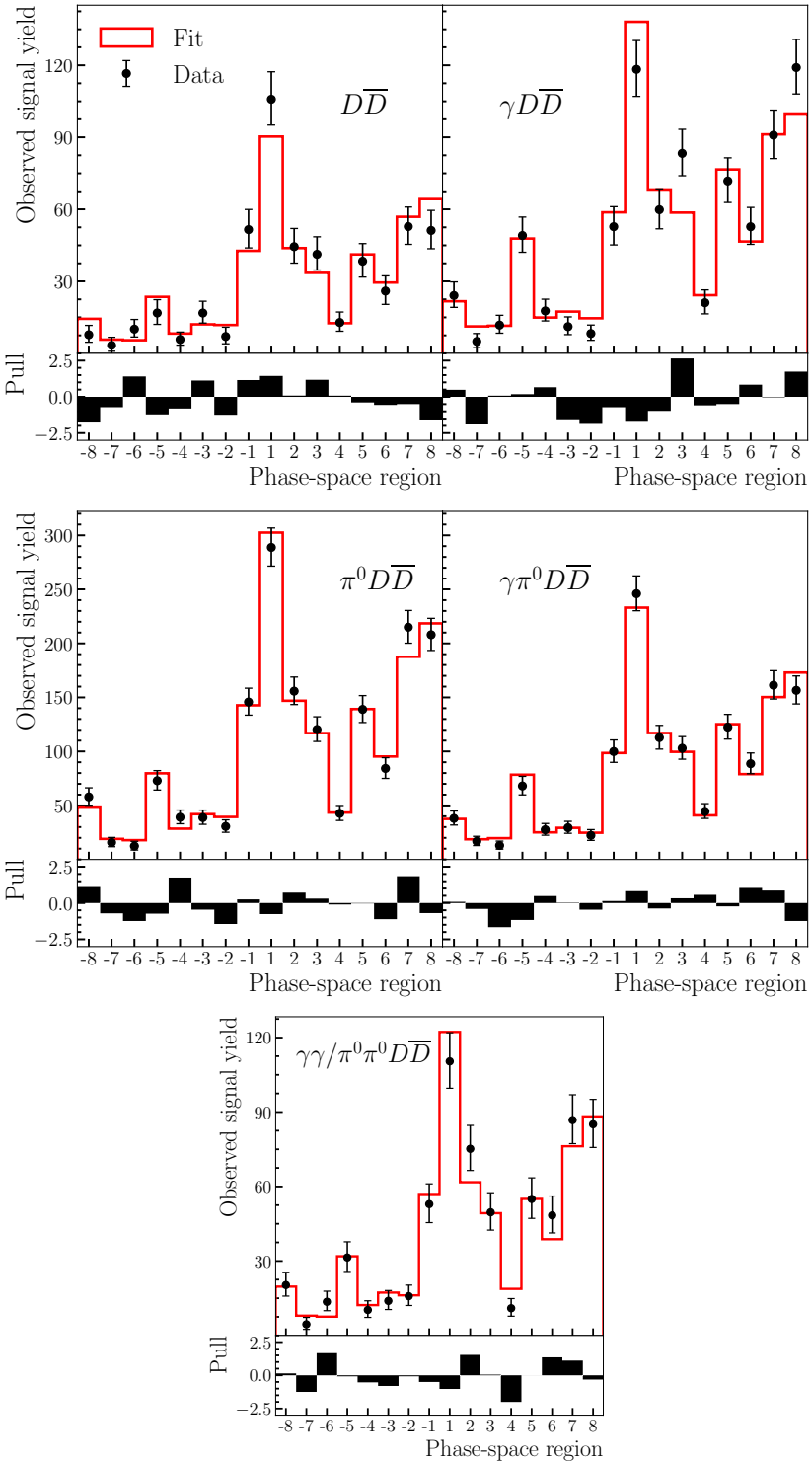

Figure 7.27: Comparison between the signal yields determined in the (red histogram) default fit, where they are parametrised by the observables, and (black points) an alternative fit where the yield is a floating parameter in each category. The plots are divided by the (top left) $D\overline{D}$, (top right) $D^*\overline{D} \to \gamma D\overline{D}$, (centre left) $D^*\overline{D} \to \pi^0 D\overline{D}$, (centre right) $D^*\overline{D}^* \to \gamma\pi^0 D\overline{D}$ and (bottom) $D^*\overline{D}^* \to \gamma\gamma/\pi^0\pi^0 D\overline{D}$ production mechanisms.

term depends on the value of C. Therefore, the fraction of candidates in a particular region of phase space will be different for $D\overline{D}$ pairs in C-even and odd eigenstates. In contrast, it would be the same for all production mechanisms in the scenario where the $D\overline{D}$ pair is not quantum correlated. Therefore, the effects of quantum correlations would be seen in the differences between the Y_i values describing the decay chains with C-even and odd $D\overline{D}$ pairs.

In the alternative fit, the signal yields are described by 32 floating Y_i parameters, 16 each for the production mechanisms with $C = \pm 1$. Figure 7.28 shows that the results of this alternative fit are consistent with the default parametrisation, where the C eigenvalues of each decay chain are assumed, and are in poor agreement with the prediction assuming no quantum correlations.

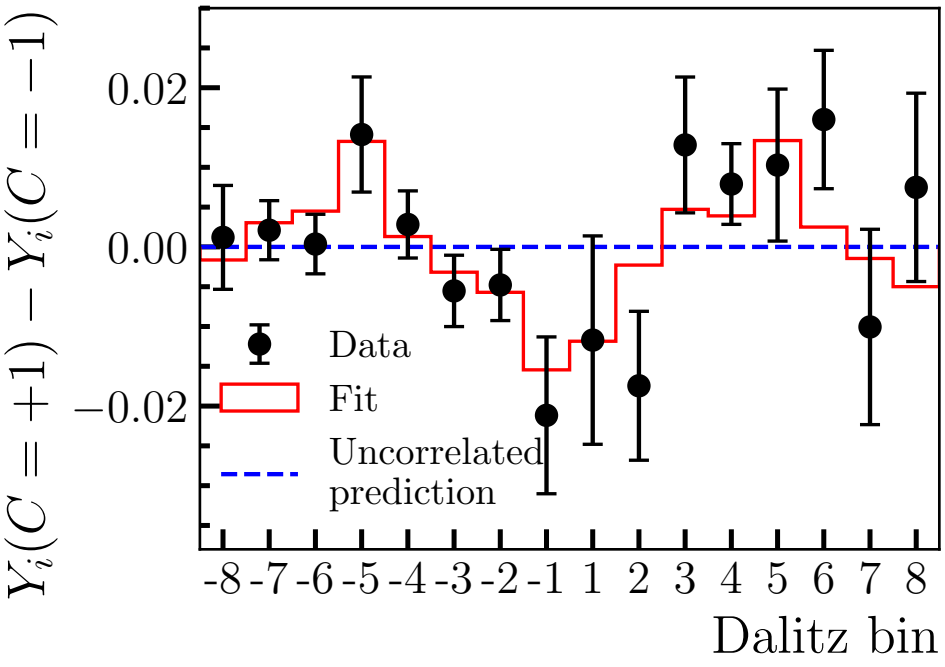

Figure 7.28: Difference between the fraction of $D\overline{D} \to K^-\pi^+$ vs. $K^0_S\pi^+\pi^-$ decays in each Dalitz region in C-even and C-odd production mechanisms. The differences for (solid red line) the default fit, (black points) an alternative fit where the fractional yield is a floating parameter in each category and (dashed blue line) the prediction assuming no quantum correlations are displayed.

7.9 Systematic uncertainties

There are no systematic uncertainties associated with differences between the reconstruction efficiency of the final state in data and MC, or relative normalisations for the signal channels, such as knowledge of luminosities and branching fractions. For the *CP*-eigenstate tags, cancellations occurs due to the use of ratio observables, and effects which are global across the $D \to K^0_S\pi^+\pi^-$ decay phase space are absorbed into the floating normalisation parameters. However, a number of systematic uncertainties are associated with assumptions in the fits, and they are discussed in the remainder of this section.

7.9.1 Invariant-mass fit models

7.9.1.1 Fixed background ratios

Four of the fits to the *CP* tags contain backgrounds with yields which are fixed relative to the signal, as shown in Tab. 7.8. The systematic uncertainty associated with the knowledge of the ratios is evaluated using the signal yields determined in fits to the data where the fixed background rates are varied by $\pm 1\sigma$ (the sources of uncertainty on each ratio are discussed in Sec. 7.6.1.2). They are found to shift by less than a single candidate in each case and thus no systematic uncertainty is assigned.

7.9.1.2 Anti-correlated background shape

As discussed in Sec. 7.6.1.3, the Gaussian shape used to model the anti-correlated backgrounds is chosen because it is found to represent the component well, and provides a good quality fit. A systematic uncertainty associated with this choice is assigned by repeating the relevant fits using alternative PDFs that test different shape characteristics. They are a Crystal Ball function in $m_{D_1} + m_{D_2}$, which examines the tails of the distribution, an asymmetric Gaussian with different left- and right-sided widths, and a Gaussian multiplied by an exponential function,

$$f(m_{D_1}, m_{D_2}) = \exp(-c\frac{m_{D_1}}{m_{D_2}}) \times \exp\left(-\frac{1}{2}\left(\frac{m_{D_1} + m_{D_2} - \mu}{\sigma}\right)^2\right), \qquad (7.31)$$

to allow the density of the background to vary as a function of m_{D_1}, as demonstrated in Fig. 7.29. In each case all parameters describing the functions are floating in the fits.

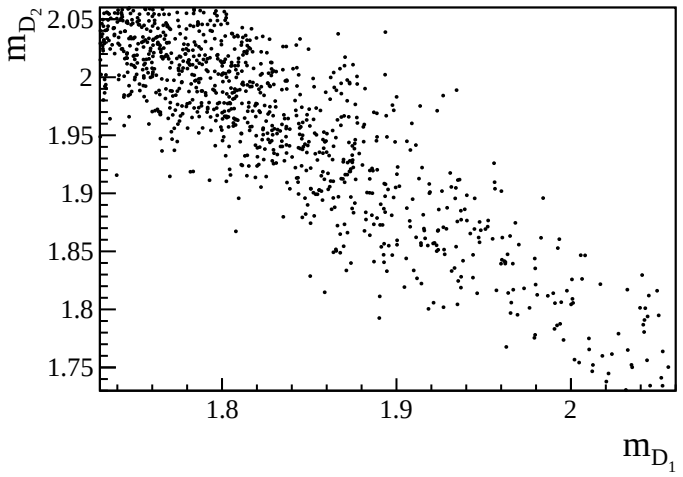

Figure 7.29: Scatter plot of a pseudo data sample generated from the PDF in Eq. 7.31 with $\mu = 1.8$, $\sigma = 0.04$ and $c = 10$.

The shifts in the signal yields for the *CP* tags are typically less than 5% of the statistical uncertainties, with the exception of the fit to the $\pi^+\pi^-$ tag and $D^*\overline{D} \to \pi^0 D\overline{D}$ process, where it is around 15% when using the Crystal Ball function. Independently for each fit containing the anti-correlated background, the alternative signal yield which shows the largest departure from the default value is used as an input in the χ^2 fit to determine the effect on $r_D^{K\pi}\cos\delta_D^{K\pi}$. The systematic uncertainty is given by the quadrature sum of the deviations in $r_D^{K\pi}\cos\delta_D^{K\pi}$, and is found to be 3×10^{-4}, which is small compared to the statistical error.

A similar procedure is used to determine the equivalent systematic uncertainties on the observables measured with the $K^0_S\pi^+\pi^-$ tag. The fit is repeated using each alternative PDF, and the maximum deviations are found to be 6×10^{-4} for $r_D^{K\pi}\cos\delta_D^{K\pi}$ and 1×10^{-4} for $r_D^{K\pi}\sin\delta_D^{K\pi}$, which are taken as the systematic uncertainties.

7.9.1.3 Combinatorial background shape

In the invariant-mass fits, the model used to represent combinatorial background is chosen to be that which provides good pulls in the one-dimensional projections. However, alternative shapes can be used which result in a similar, good-quality fit. Therefore a systematic uncertainty is assigned.

The procedure is similar to the above for the anti-correlated background shape. In each fit an alternative PDF is used. In the cases where the combinatorial background is relatively flat a first order polynomial is used, and when it clearly peaks towards lower invariant masses a second order polynomial is used. In each case the parameters describing the combinatorial background float in the fits. The systematic uncertainty on $r_D^{K\pi}\cos\delta_D^{K\pi}$ determined using the *CP* tags is found to be 7×10^{-4}, whereas it is 3×10^{-4} and 12×10^{-4} for $r_D^{K\pi}\cos\delta_D^{K\pi}$ and $r_D^{K\pi}\sin\delta_D^{K\pi}$ measured using the $K^0_S\pi^+\pi^-$ tag, respectively. This uncertainty is assumed to be 100% correlated between the observables determined using the $K^0_S\pi^+\pi^-$ tag.

7.9.2 Peaking background corrections

Throughout the analysis a number of backgrounds are fixed based on the yields from simulation. Systematic uncertainties are assigned to account for the knowledge of each.

7.9.2.1 $e^+e^- \to D^{*+}D^{(*)-}$ processes

Three backgrounds arise from $e^+e^- \to D^{*+}D^{(*)-}$ production. They are

- $D^0\overline{D}^0$ decays to the correct final state, where the $D^0\overline{D}^0$ originates from $e^+e^- \to D^{*+}D^{*-}$ production,
- $e^+e^- \to [D^0\pi^+]_{D^{*+}}D^-$ where the D^0 and D^- mesons subsequently decay to the $K^-\pi^+$ and $K^0_S\pi^+\pi^0$ final states, respectively, to create $D\overline{D} \to K^-\pi^+$ vs. $K^0_S\pi^+\pi^-$ decay candidates.

The former are subtracted from the signal yields for the *CP* tags, whilst both are fixed in the invariant-mass fit for the $K^0_S\pi^+\pi^-$ tag. Since the background yields are taken directly from simulation they are dependent on the knowledge of the inputs to the MC as discussed in Secs. 7.6.3, 7.8.1.4 and 7.8.1.5. A systematic uncertainty is assigned by repeating the relevant fits with the yields varied by $\pm 1\sigma$, which shifted each observable by a negligible amount, less than 1% of it's statistical uncertainty.

7.9.2.2 $D \to K^0_S\pi^0$ correction

In the fit to extract $r_D^{K\pi}\cos\delta_D^{K\pi}$ from the *CP*-tag yields, a correction is applied to account for $D\overline{D} \to K^-\pi^+$ vs. $K^0_S\pi^0$ decays which are reconstructed as $D\overline{D} \to K^-\pi^+$ vs. $\pi^+\pi^-\pi^0$ candidates. The ratio is found to be $R_{K^0_S} = 3.2\%$ in simulation. However, potential disagreement between the flight-distance significance of the $\pi^+\pi^-$ pair in data and MC can alter the correction.

A systematic uncertainty is assigned by subtracting the measured yields of the $D\overline{D} \to K^-\pi^+$ vs. $K^0_S\pi^0$ decay background found in data. They are determined through a two-dimensional fit to the invariant mass of the $D \to K^-\pi^+$ decay candidate and that of the $\pi^+\pi^-$ pair from the $D \to \pi^+\pi^-\pi^0$ decay candidate. The $D\overline{D} \to K^-\pi^+$ vs. $K^0_S\pi^0$ decays will peak in both dimensions at the D^0 and K^0_S-meson masses, respectively.

For each production mechanism, a fit is performed to candidates in the region $m_{K\pi} \in [1.81, 1.91]\,\text{GeV}/c^2$ and $m_{\pi^+\pi^-} \in [0.35, 0.6]\,\text{GeV}/c^2$. To further reduce background contributions, only candidates where the invariant mass of the $D \to \pi^+\pi^-\pi^0$ decay satisfies $m(\pi^+\pi^-\pi^0) \in [1.8, 1.92]\,\text{GeV}/c^2$ are used. Each fit contains 5 components:

- $D\overline{D} \to K^-\pi^+$ vs. $K^0_S\pi^0$,
- $D\overline{D} \to K^-\pi^+$ vs. $\pi^+\pi^-\pi^0$,
- $D\overline{D} \to K^-\pi^+$ vs. combinatorial,
- $D\overline{D} \to$ combinatorial vs. $\pi^+\pi^-\pi^0$,

- and $D\overline{D} \to$ combinatorial vs. combinatorial,

each of which has a floating yield parameter. A $D\overline{D} \to$ combinatorial vs. $K^0_S\pi^0$ component is not included because the predicted yield from MC is negligible. The $D \to K^-\pi^+$, $D \to K^0_S\pi^0$ and $D \to \pi^+\pi^-\pi^0$ contributions are represented by KDEs of the distributions in MC convolved with a Gaussian which has floating mean and width parameters. The combinatorial background components are modelled by exponential functions with floating slope parameters.

Figure 7.30 displays an example fit to candidates which pass the selection requirements designed to isolate the $D^*\overline{D} \to \pi^0 D\overline{D}$ decay chain. The yield of the pure combinatorial background is determined to be zero and is not plotted. The $D\overline{D} \to K^-\pi^+$ vs. $K^0_S\pi^0$ decay yields, and the ratios relative to those measured for the $D\overline{D} \to K^-\pi^+$ vs. $\pi^+\pi^-\pi^0$ decays, are given in Tab. 7.19. The ratios presented are in good agreement with each other, and with the MC prediction.

The systematic uncertainty is evaluated by repeating the fit to extract $r_D^{K\pi}\cos\delta_D^{K\pi}$ with the measured $D\overline{D} \to K^-\pi^+$ vs. $K^0_S\pi^0$ decay yields subtracted from those of the $D\overline{D} \to K^-\pi^+$ vs. $\pi^+\pi^-\pi^0$ decay. The fit is repeated one thousand times with the corrections smeared around their errors. The mean of the distribution of $r_D^{K\pi}\cos\delta_D^{K\pi}$ values is shifted by 9×10^{-4} compared to the default value, which is assigned as the systematic uncertainty.

Table 7.19: Fitted yield of the $D\overline{D} \to K^-\pi^+$ vs. $K^0_S\pi^0$ decay background found in the $D\overline{D} \to K^-\pi^+$ vs. $\pi^+\pi^-\pi^0$ decay data samples for each production process. The default ratio used is 3.2% from MC predictions.

Production mechanism	Yield	Ratio w.r.t. signal (%)
$D\overline{D}$	15.9 ± 6.6	4.2 ± 1.8
$D^*\overline{D} \to \gamma D\overline{D}$	32.3 ± 7.6	5.6 ± 1.3
$D^*\overline{D} \to \pi^0 D\overline{D}$	44.1 ± 8.9	3.2 ± 0.7
$D^*\overline{D}^* \to \gamma\pi^0 D\overline{D}$	33.6 ± 8.5	3.6 ± 0.9
$D^*\overline{D}^* \to \gamma\gamma/\pi^0\pi^0 D\overline{D}$	16.3 ± 6.7	3.1 ± 1.3
Average	–	3.7 ± 0.4

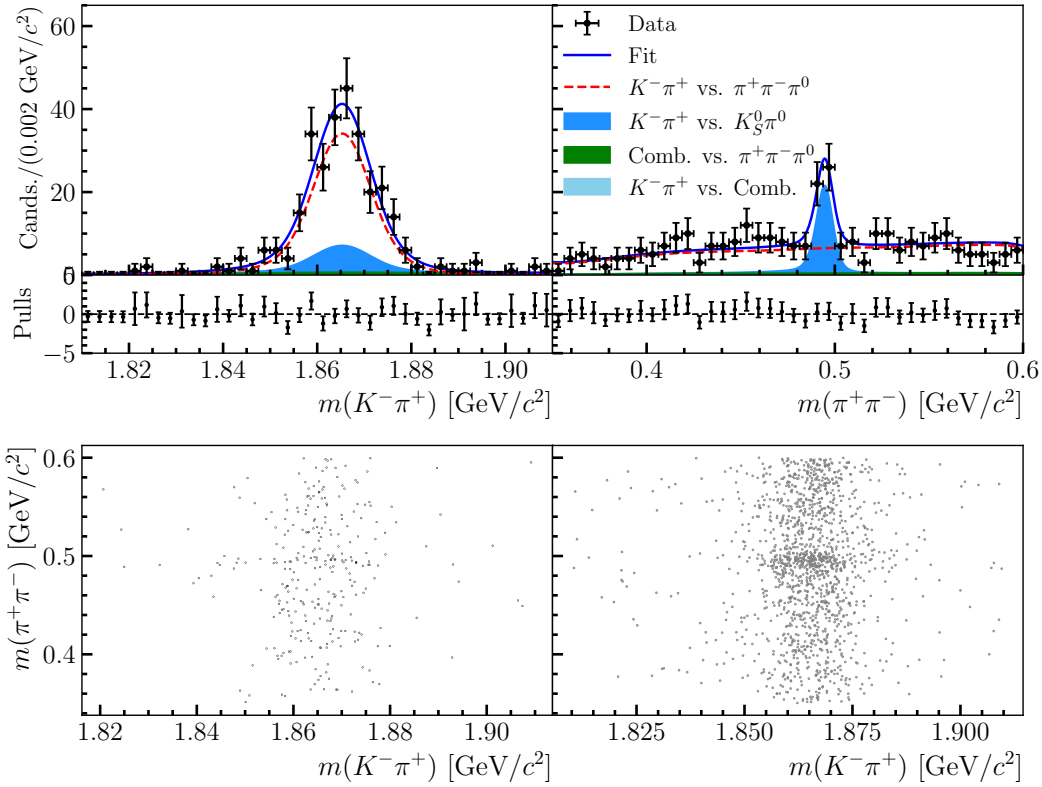

Figure 7.30: Fits to $D\overline{D} \to K^-\pi^+$ vs. $\pi^+\pi^-\pi^0$ decay candidates to determine the $D\overline{D} \to K^-\pi^+$ vs. $K^0_S\pi^0$ decay background yield in the sample which isolates the $D^*\overline{D} \to \pi^0 D\overline{D}$ production mechanism. The invariant-mass projections of the (top left) $D \to K^-\pi^+$ candidates and the (top right) $\pi^+\pi^-$ pair from the $D \to \pi^+\pi^-\pi^0$ candidates are shown. A scatter plot of the invariant masses of the candidates in (bottom left) data and (bottom right) pseudo data generated from the fitted PDF are displayed.

7.9.3 Isolation selection efficiencies

The cross-feed between production mechanisms is caused by two effects, ISR and the detector resolution. As highlighted above, the observables are not particularly sensitive to the selection efficiency differences between data and MC. However, in the case of the *CP* tags, resolution differences between the final states can mean the systematic cancellations due to the aforementioned effects are not exact. Furthermore, for the $K^0_S\pi^+\pi^-$ tag, it is possible that the discrepancy between the detector resolution in data and MC could differ across phase space. Therefore, a study is performed to estimate any residual systematic uncertainty.

Table 7.20: Efficiency, in percent, of reconstructing the $D\overline{D} \to K^-\pi^+$ vs. $K^+\pi^-$ final state in simulation where the fraction of ISR is reduced by 20%. An element with row, i, and column, j, gives the efficiency of reconstructing the production mechanism, i, after applying the selection requirements devised to isolate $D\overline{D}$ pairs produced by process, j.

		Identified as				
		$D\overline{D}$	$D^*\overline{D} \to \gamma D\overline{D}$	$D^*\overline{D} \to \pi^0 D\overline{D}$	$D^*\overline{D}^* \to \gamma\pi^0 D\overline{D}$	$D^*\overline{D}^* \to \gamma\gamma/\pi^0\pi^0 D\overline{D}$
True	$D\overline{D}$	31.48	3.18	0	0	0.02
	$D^*\overline{D} \to \gamma D\overline{D}$	0	27.80	1.40	0	0
	$D^*\overline{D} \to \pi^0 D\overline{D}$	0	0.4	32.71	0.44	0
	$D^*\overline{D}^* \to \gamma\pi^0 D\overline{D}$	0	0	0	25.78	0.50
	$D^*\overline{D}^* \to \gamma\gamma/\pi^0\pi^0 D\overline{D}$	0	0	0	0.72	9.73

7.9.3.1 Mis-modelling the rate of ISR

When an ISR event occurs the effective centre-of-mass energy of the e^+e^- pair is reduced. Accurately modelling the ISR rate in simulation requires precise knowledge of the $e^+e^- \to D\overline{D}$, $D^*\overline{D}$ and $D^*\overline{D}^*$ cross-sections at the lower energies. The typical energy of the radiated photon in simulation is between zero and 100 MeV, and the average centre-of-mass energy used to collect the data is around 4180 MeV. The cross-sections reported in Ref. [119] at the corresponding centre-of-mass energies are known with a typical relative error of around 10%, but around 20% in the least-precise cases. Therefore, the systematic uncertainty is evaluated by repeating the fits using alternative efficiency matrices where the ISR fraction in simulation is reweighted by $\pm 20\%$ for each final state. Table 7.20 displays the efficiency matrix in the -20% scenario for the $D\overline{D} \to K^-\pi^+$ vs. $K^+\pi^-$ decay, where, in comparison to Tab. 7.6, the amount of cross-feed is reduced and the rate of correctly identifying the production mechanism is increased. With these reweighted efficiencies, $r_D^{K\pi}\cos\delta_D^{K\pi}$ determined using the *CP* ($K^0_S\pi^+\pi^-$) tags deviated by 8×10^{-4} (6×10^{-4}), whilst the effect on $r_D^{K\pi}\sin\delta_D^{K\pi}$ is negligible. This uncertainty is fully correlated between all observables.

7.9.3.2 Detector resolution

To estimate the systematic uncertainty associated with mis-modelling the detector resolution, the observables are determined using alternative efficiency matrices

which are calculated after smearing the simulated distributions of the selection variables with a Gaussian. It is challenging to estimate appropriate values for the mean and width of that Gaussian. For example, this could be achieved by fitting the selection variables using templates from simulation. However, there are backgrounds present from $e^+e^- \to q\bar{q}$ production which are not accurately modelled, and hence their distributions are unknown. Accounting for the quantum correlations in data would also pose a challenge. Given that the systematic uncertainty is expected to be small, performing such a complicated study is unnecessary.

Instead, a simpler solution is employed. Conservative estimates for the parameters are found by smearing the ΔM_{D^*} and M_{rec,D^*} distributions in simulated $D\overline{D} \to K^-\pi^+$ vs. $K^+\pi^-$ decay candidates until the agreement with data is visibly very poor. These variables are chosen to estimate the smearing parameters for two reasons. First, they display the worst discrimination so necessarily tight requirements are placed on them, and thus they are the most sensitive to the resolution mis-modelling. And secondly, the contribution from $e^+e^- \to q\bar{q}$ backgrounds is low in comparison to the other variables, which allows for a more accurate comparison between data and MC. Figure 7.31 displays $D\overline{D} \to K^-\pi^+$ vs. $K^+\pi^-$ candidates in data and simulation that has been smeared with a Gaussian with $\mu = -0.5\,\mathrm{MeV}/c^2$ and $\sigma = 4.5\,\mathrm{MeV}/c^2$. A clear and significant disagreement is seen in the signal region, highlighting that the values used are conservative. Table 7.21 shows the differences between the default and smeared efficiencies for the $D\overline{D} \to K^-\pi^+$ vs. $K^+\pi^-$ decay channel which are all $\lesssim 0.3\%$.

When all final states are smeared equally the deviation in the observable $r_D^{K\pi}\cos\delta_D^{K\pi}$ determined with the *CP* tags is found to negligible. A further study is performed to probe the effect of resolution mis-modelling that differs by final state, where the smeared efficiencies are only used for the decays with a π^0 meson, which shifted $r_D^{K\pi}\cos\delta_D^{K\pi}$ by around 2% of the statistical error.

A systematic uncertainty is considered for the $K^0_S\pi^+\pi^-$ tag by repeating the fit 100 times, with selection efficiencies describing each pair of regions i and $-i$ smeared by a Gaussian with a random mean (width) between -0.5 (0) MeV/c^2

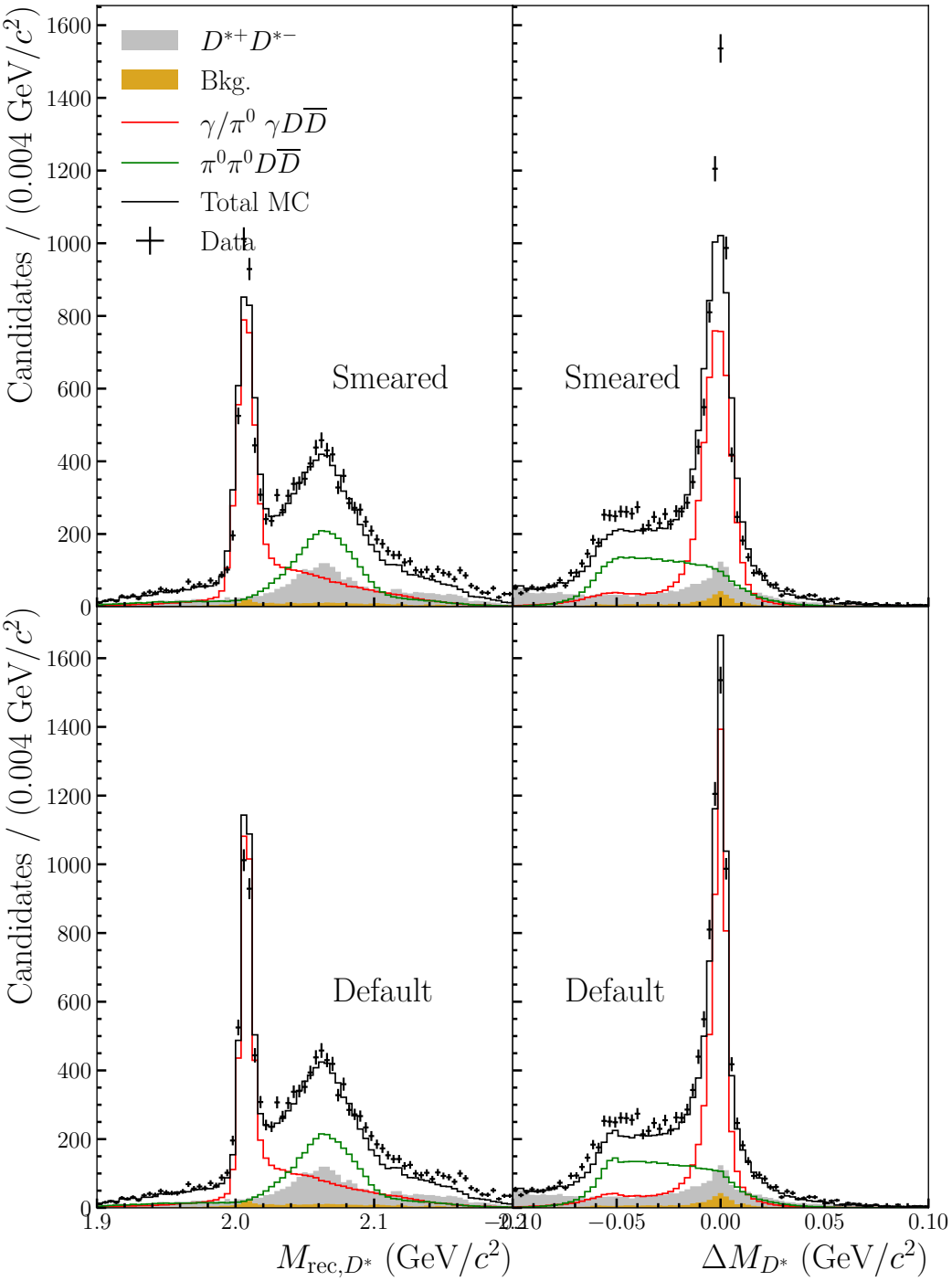

Figure 7.31: Comparison between the (left) M_{rec,D^*} and (right) ΔM_{D^*} for $D\overline{D} \to K^-\pi^+$ vs. $K^+\pi^-$ decays in data and simulation. The plots show that (top half) smearing the distributions in MC results in a clear disagreement from data in the signal regions (around the red histograms) that is not seen in the default MC (bottom half).

Table 7.21: Difference in default and smeared efficiencies, in percent, of reconstructing the $D\overline{D} \to K^-\pi^+$ vs. $K^+\pi^-$ final state in simulation. An element with row, i, and column, j, gives the efficiency of reconstructing the production mechanism, i, after applying the selection requirements devised to isolate $D\overline{D}$ pairs produced by process, j.

		Identified as				
		$D\overline{D}$	$D^*\overline{D} \to \gamma D\overline{D}$	$D^*\overline{D} \to \pi^0 D\overline{D}$	$D^*\overline{D}^* \to \gamma\pi^0 D\overline{D}$	$D^*\overline{D}^* \to \gamma\gamma/\pi^0\pi^0 D\overline{D}$
True	$D\overline{D}$	0.03	-0.02	0	0	0
	$D^*\overline{D} \to \gamma D\overline{D}$	0	-0.11	0.01	0	-0.02
	$D^*\overline{D} \to \pi^0 D\overline{D}$	0	0.02	-0.03	0	-0.01
	$D^*\overline{D}^* \to \gamma\pi^0 D\overline{D}$	0	0	0	-0.31	-0.02
	$D^*\overline{D}^* \to \gamma\gamma/\pi^0\pi^0 D\overline{D}$	0	0	0	-0.01	-0.12

and 0.5 (3.5) MeV/c^2, which probes the effect of the varying resolution across phase space. The largest shift in $r_D^{K\pi}\cos\delta_D^{K\pi}$ is found to be 7×10^{-4}, whilst the effect on $r_D^{K\pi}\sin\delta_D^{K\pi}$ is negligible.

7.9.4 Fixed inputs

Systematic uncertainties are included to account for the limited knowledge of various parameters which are fixed in the fits to determine the observables.

7.9.4.1 K_i inputs

In the fit to the $D\overline{D} \to K^-\pi^+$ vs. $K^0_S\pi^+\pi^-$ decays the K_i parameters are fixed to the values in Tab. 7.13. The corresponding systematic uncertainty is evaluated by refitting the data one thousand times using alternative K_i values which are generated according to their uncertainties. The widths of the distributions of the measured observables are 11×10^{-4} and 10×10^{-4} for $r_D^{K\pi}\cos\delta_D^{K\pi}$ and $r_D^{K\pi}\sin\delta_D^{K\pi}$, respectively. The correlation between the observables due to this systematic uncertainty is only 3%.

The previous BESIII measurement of $\delta_D^{K\pi}$ performed at the $\psi(3770)$ resonance [13] determined the parameters $r_D^{K\pi}\cos\delta_D^{K\pi}$ and $r_D^{K\pi}\sin\delta_D^{K\pi}$ by simultaneously fitting candidates in regions of $D \to K^0_S\pi^+\pi^-$ and $D \to K^0_L\pi^+\pi^-$ decay phase space. The equivalent systematic uncertainties in Ref. [13] were found to be much larger

than those reported above, around 50×10^{-4} and 70×10^{-4} for $r_D^{K\pi} \cos\delta_D^{K\pi}$ and $r_D^{K\pi} \sin\delta_D^{K\pi}$, respectively, and was the dominant systematic in the analysis.

Additional studies are performed to understand the reduction using a simplified fit which considers only the signal yields, rather than a full invariant-mass fit. The procedure is to calculate and refit predictions for the signal yields in each category assuming the central values for the K_i, c_i, s_i [10], $\delta_D^{K\pi}$ and $r_D^{K\pi}$ [39] parameters, and the integrated yields in Tab. 7.17. As a cross-check, the fit is performed one thousand times using the smeared K_i inputs, which found distributions of $r_D^{K\pi} \cos\delta_D^{K\pi}$ and $r_D^{K\pi} \sin\delta_D^{K\pi}$ with a similar width to those reported above for this measurement. The procedure is repeated twice more, assuming that all of the production mechanisms produced $D\overline{D}$ pairs in C-even and C-odd eigenstates, and both found similar widths to those in Ref. [13]. Furthermore, the observables in the two mock scenarios are found to be greater than 97% anti-correlated. Therefore, the reduction is caused by simultaneously using C-even and C-odd $D\overline{D}$ pairs.

The effect can be explained as follows. The non-interference terms in Eq. 5.30 are the same for $D\overline{D}$ pairs which are in C-even and C-odd eigenstates, so varying the K_i parameters will have the same effect on these terms in both cases. The best fit will have roughly the same fractional yields as in the default fit, since this maximises the likelihood, and therefore the interference terms will act to compensate this shift. But the interference is proportional to C. So, the categories where $C = 1$ will force the observables to shift in the opposite direction from those with $C = -1$, hence the partial cancellation, which is not exact because there are a different number of C-even and C-odd $D\overline{D}$ pairs.

7.9.4.2 c_i and s_i inputs

The systematic uncertainty due to the limited knowledge of the c_i and s_i parameters is found by repeating the fit to data one thousand times using alternative inputs which are smeared according to their statistical errors and correlations [10]. The standard deviation on the distribution of observables is 8×10^{-4} for $r_D^{K\pi} \cos\delta_D^{K\pi}$ and 27×10^{-4} for $r_D^{K\pi} \sin\delta_D^{K\pi}$, which are assigned as the systematic uncertainties

with a correlation coefficient of 8%. These values are consistent with those reported in Ref. [13].

7.9.4.3 Other inputs

The systematic uncertainties associated with the remaining fixed inputs, $(r_D^{K\pi})^2$, x_D, y_D and $F_+^{\pi\pi\pi^0}$, are expected to be small because they are measured to a high precision, or impact the observables at second order. They are estimated by repeating the relevant fits using inputs which are shifted up and down by one standard deviation from the central value. In each case the systematic uncertainty is found to be negligible.

7.9.5 Summary

A summary of the systematic uncertainties is displayed in Table 7.22. The total systematic uncertainty on $r_D^{K\pi}\cos\delta_D^{K\pi}$ from the *CP* tags is approximately 19% of the statistical uncertainty, whilst it is around 13% and 18% for $r_D^{K\pi}\cos\delta_D^{K\pi}$ and $r_D^{K\pi}\sin\delta_D^{K\pi}$ measured using the $D \to K^0_S\pi^+\pi^-$ decay, respectively. Table 7.23 displays the correlation matrix due to the systematic errors.

7.10 Fit to extract $\delta_D^{K\pi}$

The strong-phase difference $\delta_D^{K\pi}$ is determined by combining the three observables, which are summarised in Tab. 7.24, in a χ^2 fit where $r_D^{K\pi}$ is fixed to $r_D^{K\pi} = (0.05865^{+0.00015}_{-0.00014})$ [39]. The likelihood is given by

$$\chi^2 \propto (\vec{A}_{\rm obs} - \vec{A}(\vec{\alpha})_{\rm pred})^T V^{-1} (\vec{A}_{\rm obs} - \vec{A}(\vec{\alpha})_{\rm pred}), \tag{7.32}$$

where

$$\vec{A}_{\rm obs} = \{(r_D^{K\pi}\cos\delta_D^{K\pi})^\dagger, (r_D^{K\pi}\cos\delta_D^{K\pi})^\ddagger, (r_D^{K\pi}\sin\delta_D^{K\pi})^\ddagger\}, \tag{7.33}$$

$$\vec{\alpha} = \{r_D^{K\pi}, \delta_D^{K\pi}\}, \tag{7.34}$$

Table 7.22: Summary of the systematic uncertainties, in units of $\times 10^{-4}$, on the observables, $r_D^{K\pi}\cos\delta_D^{K\pi}$ and $r_D^{K\pi}\sin\delta_D^{K\pi}$, determined using D decays to the *CP* eigenstates and $K^0_S\pi^+\pi^-$. Entries denoted with '–' are negligible or do not apply to the relevant observable.

Systematic	$r_D^{K\pi}\cos\delta_D^{K\pi}$ $D\to f_{CP}$	$r_D^{K\pi}\cos\delta_D^{K\pi}$ $D\to K^0_S\pi^+\pi^-$	$r_D^{K\pi}\sin\delta_D^{K\pi}$ $D\to K^0_S\pi^+\pi^-$
c_i, s_i	–	8	27
K_i	–	11	10
ISR	8	6	–
$D\to K^0_S\pi^0$ bkg	9	–	–
Comb. bkg	7	3	12
Anti-corr. bkg	3	6	1
MC resolution	–	7	–
Bias	4	–	–
Total	15	18	31
Statistical	80	140	170

Table 7.23: The correlations between the systematic uncertainties on the observables. The observable $r_D^{K\pi}\cos\delta_D^{K\pi}$ with the † (‡) symbol is determined using the *CP* ($K^0_S\pi^+\pi^-$) tags.

	$(r_D^{K\pi}\cos\delta_D^{K\pi})^\dagger$	$(r_D^{K\pi}\cos\delta_D^{K\pi})^\ddagger$	$r_D^{K\pi}\sin\delta_D^{K\pi}$
$(r_D^{K\pi}\cos\delta_D^{K\pi})^\dagger$	1	0.18	0
$(r_D^{K\pi}\cos\delta_D^{K\pi})^\ddagger$		1	0.19
$r_D^{K\pi}\sin\delta_D^{K\pi}$			1

and V is the total covariance matrix which accounts for the statistical and systematic uncertainties and their correlations. In the above equations, the † (‡) symbol denotes an observable found using the *CP* tags ($K^0_S\pi^+\pi^-$ tag). The fit determines

$$\delta_D^{K\pi} = \left(192.8^{+11.0+1.9}_{-12.4-2.4}\right)^\circ, \tag{7.35}$$

where the first uncertainty is statistical and the second is systematic. Varying $r_D^{K\pi}$ within its uncertainty has a negligible impact on $\delta_D^{K\pi}$. The value presented

is in excellent agreement with those measured by the BESIII collaboration at the $\psi(3770)$ resonance, $\delta_D^{K\pi} = \left(187.6^{+8.9_{\text{stat.}}+5.4_{\text{syst.}}}_{-9.7_{\text{stat.}}-6.4_{\text{syst.}}}\right)^\circ$ [13], and by the LHCb experiment, $\delta_D^{K\pi} = \left(191.6^{+2.5}_{-2.4}\right)^\circ$ [15].

Table 7.24: Values of the measured observables. The first uncertainty is statistical and the second is systematic.

Source	Observable	Value
$D \to f_{CP}$	$r_D^{K\pi}\cos\delta_D^{K\pi}$	$-0.070 \pm 0.008 \pm 0.0015$
$D \to K^0_S\pi^+\pi^-$	$r_D^{K\pi}\cos\delta_D^{K\pi}$	$-0.044 \pm 0.014 \pm 0.0018$
$D \to K^0_S\pi^+\pi^-$	$r_D^{K\pi}\sin\delta_D^{K\pi}$	$-0.022 \pm 0.017 \pm 0.0031$

7.11 Combined value of $\delta_D^{K\pi}$ from BESIII measurements

A combination of the results presented here and in Ref. [13] is performed to find the average value of $\delta_D^{K\pi}$ measured with quantum-correlated $D\overline{D}$ pairs. Before the results of the combination a discussion comparing the two measurements is presented.

From Eq. 7.16, it can be shown the rate of $D\overline{D} \to K^-\pi^+$ vs. f_{CP} decays is suppressed relative to the scenario where the D and $\overline{D}$ mesons decay independently when $C = -1$ and f_{CP} is CP odd, and it is enhanced when f_{CP} is CP even. Therefore, the ratio

$$\rho_{CP}^{\alpha} = \frac{\Gamma(D\overline{D} \to K^-\pi^+ \text{ vs. } f_{CP})}{\mathcal{B}_{D^0\to K^-\pi^+}\mathcal{B}_{D^0\to f_{CP}}}, \tag{7.36}$$

where $\alpha = +\ (-)$ when the tag is CP even (odd), is sensitive to $r_D^{K\pi}\cos\delta_D^{K\pi}$. In the measurement performed at the $\psi(3770)$ resonance, the observable which is constructed to extract $r_D^{K\pi}\cos\delta_D^{K\pi}$ is an asymmetry between the efficiency-corrected yields of CP-even and odd tags,

$$\mathcal{A}_{K\pi} = \frac{\rho_{CP}^{+} - \rho_{CP}^{-}}{\rho_{CP}^{+} + \rho_{CP}^{-}} = \frac{-2r_D^{K\pi}\cos\delta_D^{K\pi} + y_D}{1 + (r_D^{K\pi})^2}. \tag{7.37}$$

A separate asymmetry, $\mathcal{A}_{K\pi}^{\pi\pi\pi^0}$, is defined for the $D \to \pi^+\pi^-\pi^0$ decay to account for the small CP-odd content.

Clearly, the branching fraction of the $D^0 \to K^-\pi^+$ decay cancels in this observable. However, that of the tag, $\mathcal{B}_{D^0\to f_{CP}}$, must be considered, and in some cases it is known with a limited precision. Therefore, it is replaced with the efficiency-corrected yield of $D \to f_{CP}$ decays, where the other D meson is not reconstructed. This has the added benefit of cancelling systematic uncertainties associated with the reconstruction efficiency of the tag decay. The asymmetries are found to be,

$$\mathcal{A}_{K\pi} = 0.132 \pm 0.011 \pm 0.007, \tag{7.38}$$

$$\mathcal{A}_{K\pi}^{\pi\pi\pi^0} = 0.130 \pm 0.012 \pm 0.008, \tag{7.39}$$

where the first uncertainty is statistical and the second is systematic. The latter is around 64% of the statistical error, with large contributions coming from the limited knowledge of the normalisations and the efficiencies from MC, which do not exactly cancel for the $D \to K^-\pi^+$ decay. In the measurement presented in this thesis, both of these sources naturally cancel in the ratio observables, which are a particular benefit of simultaneously analysing C-even and odd $D\overline{D}$ pairs, and the systematic uncertainty is only around 18% of the statistical.

In the two analyses the observed yields of the $D\overline{D} \to K^-\pi^+$ vs. K^+K^-, $\pi^+\pi^-$, $\pi^+\pi^-\pi^0$ and $K^0_S\pi^0$ decays are similar. However, the dataset used in Ref. [13] corresponds to an integrated luminosity of around $3\,\text{fb}^{-1}$, compared to around $7\,\text{fb}^{-1}$ in the measurement presented here. Thus, the achievable statistical precision is better at $\psi(3770)$. Furthermore, Ref. [13] gains additional precision by using tags with a K^0_L meson, which typically decay outside the BESIII detector due to their long lifetime, and are therefore inferred through the missing momentum. This technique is not possible in the measurement presented in this thesis because distinguishing between the production mechanisms requires fully reconstructing both D decays.

In Ref. [13], the observables, $r_D^{K\pi}\cos\delta_D^{K\pi}$ and $r_D^{K\pi}\sin\delta_D^{K\pi}$, are measured through the distribution of $D\overline{D} \to K^-\pi^+$ vs. $K^0_{S,L}\pi^+\pi^-$ decays across the phase space of

the tag, similarly to Sec. 7.8. They are determined to be

$$r_D^{K\pi} \cos\delta_D^{K\pi} = -0.0562 \pm 0.0081 \pm 0.0050 \pm 0.0010, \tag{7.40}$$

$$r_D^{K\pi} \sin\delta_D^{K\pi} = -0.011 \pm 0.012 \pm 0.007 \pm 0.003, \tag{7.41}$$

where the first uncertainty is statistical, the second is the systematic uncertainty from the knowledge of the $K_i^{(\prime)}$ inputs, and the third corresponds to the knowledge of the $c_i^{(\prime)}$ and $s_i^{(\prime)}$ parameters. Here, the $\prime$ denotes the equivalent input for the $D \to K^0_{\rm L}\pi^+\pi^-$ decay [10]. The total systematic uncertainties are around 60% of the statistical errors, compared to around 15% for the observables measured in this thesis. The simultaneous use of C-even and odd $D\overline{D}$ pairs is responsible for the reduction, which results in a partial cancellation of the K_i systematic uncertainty as discussed in Sec. 7.9.4.1.

The combined value of $\delta_D^{K\pi}$ is determined through a χ^2 fit to the three observables from this analysis (displayed in Tab. 7.24), and the four observables from Ref. [13] shown in Eqs. 7.38-7.41. The common systematic uncertainties are considered and the correlation matrix is shown in Table 7.25. In the fit, the values of $r_D^{K\pi}$, y_D and $F_+^{\pi\pi\pi^0}$ are fixed to the values in Refs. [39, 107], which yields $\delta_D^{K\pi} = (189.2^{+6.9+3.4}_{-7.4-3.8})^\circ$, where the first uncertainty is statistical and the second is systematic.

Table 7.25: The correlations between the systematic uncertainties on the observables in this measurement (denoted by an asterisk) and Ref. [13]. The observables with the † (‡) symbol is determined using the *CP*-eigenstate ($K^0_{\rm S}\pi^+\pi^-$) tags.

	$(r_D^{K\pi}\cos\delta_D^{K\pi})^{*\dagger}$	$(r_D^{K\pi}\cos\delta_D^{K\pi})^{*\ddagger}$	$(r_D^{K\pi}\sin\delta_D^{K\pi})^{*\ddagger}$	$\mathcal{A}_{K\pi}$	$\mathcal{A}_{K\pi}^{\pi\pi\pi^0}$	$r_D^{K\pi}\cos\delta_D^{K\pi}$	$r_D^{K\pi}\sin\delta_D^{K\pi}$
$(r_D^{K\pi}\cos\delta_D^{K\pi})^{*\dagger}$	1	0.18	0	0	0	0	0
$(r_D^{K\pi}\cos\delta_D^{K\pi})^{*\ddagger}$		1	0.19	0	0	0.09	0
$(r_D^{K\pi}\sin\delta_D^{K\pi})^{*\ddagger}$			1	0	0	0	0.34
$\mathcal{A}_{K\pi}$				1	0.16	0	0
$\mathcal{A}_{K\pi}^{\pi\pi\pi^0}$					1	0	0
$r_D^{K\pi}\cos\delta_D^{K\pi}$						1	0
$r_D^{K\pi}\sin\delta_D^{K\pi}$							1

7.12 Summary

The strong-phase difference between $D^0 \to K^-\pi^+$ and $\overline{D}^0 \to K^-\pi^+$ decays, $\delta_D^{K\pi}$, is measured to be $\delta_D^{K\pi} = \left(192.8^{+11.0+1.9}_{-12.4-2.4}\right)^\circ$, where the first uncertainty is statistical and the second is systematic. A novel approach is used in this chapter which exploits quantum-correlated $D\overline{D}$ pairs in C-even and odd eigenstates produced at energies above the $\psi(3770)$ resonance for the first time. A combination is performed with the previous BESIII analysis [13] which determines $\delta_D^{K\pi} = (189.2^{+6.9+3.4}_{-7.4-3.8})^\circ$. The value is in good agreement with that found by the LHCb experiment in a fit to the results of studies of charm mixing and b decays[2], $\delta_D^{K\pi} = (191.6^{+2.5}_{-2.4})^\circ$ [15].

[2]It should be noted that the BESIII measurement in Ref. [13] is included in the combination described in Ref. [15].

8

Summary and outlook

The most precise determinations of the CKM angle γ are performed using $B^{\pm} \to DK^{\pm}$ decays due to the large branching fractions [88, 12]. However, other channels are useful for consistency checks and to increase precision. In 2022, the LHCb collaboration combined the results of their γ measurements, which found a $\sim 2\sigma$ discrepancy between the values determined using B^0 and $B^{\pm}$ decays [39]. Therefore, an improved measurement of γ using B^0 decays is of particular interest, and is the subject of Chap. 4. In B^0 decays that are sensitive to γ, the ratio of amplitudes between the suppressed and favoured paths to the final state is around three times larger than it is in $B^{\pm}$ decays, and thus impressive precision is achieved due to the increased interference despite the lower branching fractions.

In Chapter 4, the CKM angle γ is measured using $B^0 \to DK^*(892)^0$ decays, where the D mesons decay to the $K^0_S\pi^+\pi^-$ and $K^0_S K^+ K^-$ final states, using around $9\,\text{fb}^{-1}$ data collected by the LHCb experiment. The method exploits CP violation in interference between $B^0 \to D^0 K^{*0}$ and $B^0 \to \overline{D}^0 K^{*0}$ decays across the kinematic phase space of the D decay. In order to study the CP violation, the flavour of the B^0 meson at decay must be known, and it is unambiguously provided by the charge of the kaon from the $K^{*0} \to K^+\pi^-$ decay. The CKM angle γ, and the strong-phase

difference, δ_s and amplitude ratio, r_s, of the B^0 decays are found to be

$$\gamma = \left(49^{+22}_{-19}\right)^\circ,$$
$$r_s = 0.271^{+0.065}_{-0.066},$$
$$\delta_s = \left(236^{+19}_{-21}\right)^\circ,$$

where the uncertainties combine statistical and systematic sources. The above parameters are consistent with the previous determination [89] and the LHCb average [39].

In 2024, the LHCb collaboration published another measurement of the CKM angle γ using $B^0 \to DK^{*0}$ decays with different D-decay final states [96]. The LHCb combination was repeated [15], and determined $\gamma = \left(64.6^{+6.5}_{-7.5}\right)^\circ$ from the B^0 decays. This value is in excellent agreement with that found in $B^\pm$ decays, $\gamma = \left(63.4^{+3.2}_{-3.3}\right)^\circ$, diminishing the significance of the aforementioned discrepancy. Furthermore, alongside other measurements [134, 135, 136], the studies of $B^0 \to DK^{*0}$ decays contribute to the 0.8° precision improvement on the average value of γ compared to the previous determination [39].

The LHCb average of direct γ measurements is $\gamma = (64.6 \pm 2.8)^\circ$ [15], which currently agrees with the indirect determinations found by constraining the sides and other angles of the Unitarity Triangle, $\gamma = \left(66.29^{+0.72}_{-1.86}\right)^\circ$ [8]. At present, the precision is clearly not sufficient to resolve non-unitarity of the CKM matrix. However, all is not lost. The LHCb experiment has recently completed an upgrade [16] which allows the detector to operate at a higher instantaneous luminosity, and in a single year it has collected a dataset which is a similar size to the run 1 and run 2 samples combined.

Analysis of the dataset collected by the upgraded LHCb detector will significantly improve the precision on γ. One of the leading channels uses $B^\pm \to DK^\pm$ decays with the $D \to K^-\pi^+$ final state [12]. However, at present, this channel's contribution to the precision on γ is limited by the knowledge of the strong-phase difference between $D^0 \to K^-\pi^+$ and $\overline{D}^0 \to K^-\pi^+$ decays, $\delta_D^{K\pi}$. The parameter $\delta_D^{K\pi}$ is known to around 10° in BESIII measurements using quantum-correlated $D\overline{D}$ pairs that are produced at the charm threshold of the $\psi(3770)$ resonance [13].

Chapter 7 presents a determination of $\delta_D^{K\pi}$ using a different BESIII dataset, which is collected in e^+e^- collisions at centre-of-mass energies between 4.13 and 4.23 GeV, and has an integrated luminosity of $7.13\,\text{fb}^{-1}$. The analysis represents the first direct measurement of a hadronic charm parameter to use data collected above the $\psi(3770)$ resonance. At these energies, the quantum-correlated $D\overline{D}$ pairs are produced through the $e^+e^- \to D\overline{D}$, $D^*\overline{D}$ and $D^*\overline{D}^*$ processes, where each D^* meson decays into a D meson and a photon or π^0. Therefore, the $D\overline{D}$ pair can be in even and odd eigenstates of the charge-conjugation operator, C, whereas only the latter are available at $\psi(3770)$.

The C-even $D\overline{D}$ pairs, which are observed and used for the first time in Chap. 7, have prospects beyond hadronic charm inputs. They can be applied to measure the charm-mixing parameters, x_D and y_D, which affect decay rates at first order compared to a second-order dependence in the C-odd scenario [90]. Studies inspired by the technique of the analysis described in Chap. 7 find that a dataset with an integrated luminosity of around $2\,\text{ab}^{-1}$, which is well within the capabilities of future proposed colliders [103], is sufficient to observe the charm-mixing parameters [137]. Of course, this has already been accomplished by LHCb using time-dependent methods [138], but a measurement using C-even $D\overline{D}$ pairs would be time-integrated and thus is an important consistency check.

In Chap. 7, the strong-phase difference $\delta_D^{K\pi}$ is found using interference in $D\overline{D} \to K^-\pi^+$ vs. X decays, where $X \in \{K^+K^-, \pi^+\pi^-, K^0_S\pi^0, \pi^+\pi^-\pi^0, K^0_S\pi^+\pi^-\}$. It is determined to be

$$\delta_D^{K\pi} = \left(192.8^{+11.0_{\text{stat.}}+1.9_{\text{syst.}}}_{-12.4_{\text{stat.}}-2.4_{\text{syst.}}}\right)^\circ, \tag{8.1}$$

which agrees and is competitive with the previous result from BESIII using around $3\,\text{fb}^{-1}$ data collected at $\psi(3770)$, $\delta_D^{K\pi} = \left(187.6^{+8.9_{\text{stat.}}+5.4_{\text{syst.}}}_{-9.7_{\text{stat.}}-6.4_{\text{syst.}}}\right)^\circ$ [13]. Novel experimental observables that combine C-even and C-odd $D\overline{D}$ pairs are constructed, which leads to significantly reduced systematic uncertainties compared to the measurement performed at $\psi(3770)$. The combination of BESIII measurements is $\delta_D^{K\pi} = (189.2^{+6.9_{\text{stat.}}+3.4_{\text{syst.}}}_{-7.4_{\text{stat.}}-3.8_{\text{syst.}}})^\circ$ which is consistent with the current LHCb average,

$\delta_D^{K\pi} = \left(191.6^{+2.5}_{-2.4}\right)^\circ$ [15], where the precision is driven by indirect determinations using $b-$decays [12].

Looking further ahead, the LHCb collaboration has ambitious data-taking plans, and by the end of the LHC it expects to boast a sample corresponding to an integrated luminosity of $300\,\text{fb}^{-1}$ [139]. With these data it will be possible to constrain the CKM angle γ to around 0.35° [140], which could be enough to find New Physics. The knowledge of the hadronic charm inputs requires significant improvement if it is not to limit the precision on γ. Such measurements can be performed at future e^+e^- colliders, for example the Super τ-Charm Factory (STCF) [103]. Although STCF plans to operate at the $\psi(3770)$ resonance, the majority of the data will be collected at other centre-of-mass energies between $2-7$ GeV, where a variety of interesting physics can be explored. Therefore, in addition to improving the current precision on $\delta_D^{K\pi}$, paving the way for determinations of hadronic charm parameters at high energies and enabling studies of charm mixing through the first observation of C-even $D\overline{D}$ pairs, the measurement described in Chap. 7 also boosts centre-of-mass energy proposals at future colliders by creating further physics use cases for the higher energy data.

Appendices

A

Strong-phase difference uncertainty correlation matrix

As discussed in Sec. 4.6.1, common strong-phase inputs are used when estimating the systematic uncertainty due to their limited precision in the measurement of γ described in Chap. 4 and in Ref. [88]. For use in future combinations of results the correlation matrix is necessary, and it is shown in Tab. A.1. The parameters $x_\xi^{D\pi}$ and $y_\xi^{D\pi}$ are the observables which parameterise the $B^\pm \to D\pi^\pm$ decay yields in the fit in Ref. [88]. They are defined as

$$\begin{aligned} x_\xi^{D\pi} &= Re[\xi_{D\pi}], \\ y_\xi^{D\pi} &= Im[\xi_{D\pi}], \end{aligned} \tag{A.1}$$

where

$$\xi_{D\pi} = \frac{r_B^{D\pi}}{r_B^{DK}} \exp\left[i(\delta_B^{D\pi} - \delta_B^{DK})\right]. \tag{A.2}$$

This definition still produces the necessary *CP*-violation observables,

$$\begin{aligned} x_\pm^{D\pi} &= x_\xi^{D\pi} x_\pm^{DK} - y_\xi^{D\pi} y_\pm^{DK}, \\ y_\pm^{D\pi} &= x_\xi^{D\pi} y_\pm^{DK} + y_\xi^{D\pi} x_\pm^{DK}, \end{aligned} \tag{A.3}$$

and they are chosen because they improve the fit stability compared to using $x_\pm^{D\pi}$ and $y_\pm^{D\pi}$ directly.

Table A.1: Correlation coefficients (in percent) between the *CP*-violation observables in this measurement and Ref. [88] for the systematic uncertainty associated with fixing the D-decay strong-phase inputs.

	$x_+^{DK^{*0}}$	$x_-^{DK^{*0}}$	$y_+^{DK^{*0}}$	$y_-^{DK^{*0}}$	x_-^{DK}	x_+^{DK}	y_-^{DK}	y_+^{DK}	$y_\xi^{D\pi}$	$x_\xi^{D\pi}$
$x_+^{DK^{*0}}$	100	-14	34	-9	-29	-6	-11	-6	30	-16
$x_-^{DK^{*0}}$		100	-4	17	-31	48	22	-49	12	4
$y_+^{DK^{*0}}$			100	-4	35	3	12	27	32	29
$y_-^{DK^{*0}}$				100	13	-15	22	-1	36	21
x_-^{DK}					100	-49	-5	32	14	19
x_+^{DK}						100	6	6	-14	0
y_-^{DK}							100	-24	-12	-12
y_+^{DK}								100	-20	12
$x_\xi^{D\pi}$									100	64
$y_\xi^{D\pi}$										100

References

1. Christenson, J. H., Cronin, J. W., Fitch, V. L. & Turlay, R. Evidence for the 2π decay of the K_2^0 meson. *Phys. Rev. Lett.* **13,** 138–140 (1964).
2. Abe, K. *et al.* Observation of large CP violation in the neutral B meson system. *Phys. Rev. Lett.* **87,** 091802. arXiv: `hep-ex/0107061` (2001).
3. Aubert, B. *et al.* Observation of CP violation in the B^0 meson system. *Phys. Rev. Lett.* **87,** 091801. arXiv: `hep-ex/0107013` (2001).
4. Aaij, R. *et al.* Observation of CP violation in charm decays. *Phys. Rev. Lett.* **122,** 211803. arXiv: `1903.08726 [hep-ex]` (2019).
5. Aaij, R. *et al.* Observation of charge-parity symmetry breaking in baryon decays. arXiv: `2503.16954 [hep-ex]` (Mar. 2025).
6. Kobayashi, M. & Maskawa, T. CP Violation in the renormalizable theory of weak interaction. *Prog. Theor. Phys.* **49,** 652–657 (1973).
7. Cabibbo, N. Unitary symmetry and leptonic decays. *Phys. Rev. Lett.* **10,** 531–533 (1963).
8. Charles, J. *et al.* CP violation and the CKM matrix: Assessing the impact of the asymmetric B factories. *Eur. Phys. J. C* **41.** Updated results and plots available at: http://ckmfitter.in2p3.fr, 1–131. arXiv: `hep-ph/0406184` (2005).
9. Ablikim, M. *et al.* Determination of strong-phase parameters in $D \to K^0_{S,L}\pi^+\pi^-$. *Phys. Rev. Lett.* **124,** 241802. arXiv: `2002.12791 [hep-ex]` (2020).
10. Ablikim, M. *et al.* Model-independent determination of the relative strong-phase difference between D^0 and $\bar{D}^0 \to K^0_{S,L}\pi^+\pi^-$ and its impact on the measurement of the CKM angle γ/ϕ_3. *Phys. Rev. D* **101,** 112002. arXiv: `2003.00091 [hep-ex]` (2020).
11. Ablikim, M. *et al.* Improved model-independent determination of the strong-phase difference between D^0 and $\bar{D}^0 \to K^0_{\mathrm{S,L}}K^+K^-$ decays. *Phys. Rev. D* **102,** 052008. arXiv: `2007.07959 [hep-ex]` (2020).
12. Aaij, R. *et al.* Measurement of CP observables in $B^\pm \to D^{(*)}K^\pm$ and $B^\pm \to D^{(*)}\pi^\pm$ decays using two-body D final states. *JHEP* **04,** 081. arXiv: `2012.09903 [hep-ex]` (2021).
13. Ablikim, M. *et al.* Improved measurement of the strong-phase difference $\delta_D^{K\pi}$ in quantum-correlated $D\bar{D}$ decays. *Eur. Phys. J. C* **82,** 1009. arXiv: `2208.09402 [hep-ex]` (2022).
14. Asner, D. M. *et al.* Updated measurement of the strong phase in $D^0 \to K^+\pi^-$ decay using quantum correlations in $e^+e^- \to D^0\bar{D}^0$ at CLEO. *Phys. Rev. D* **86,** 112001. arXiv: `1210.0939 [hep-ex]` (2012).

15. LHCb collaboration. Simultaneous determination of the CKM angle γ and parameters related to mixing and *CP* violation in the charm sector, *LHCb-CONF-2024-004* (2024).

16. Aaij, R. *et al.* The LHCb Upgrade I. *JINST* **19,** P05065. arXiv: 2305.10515 [hep-ex] (2024).

17. Aad, G. *et al.* Observation of a new particle in the search for the Standard Model Higgs boson with the ATLAS detector at the LHC. *Phys. Lett. B* **716,** 1–29. arXiv: 1207.7214 [hep-ex] (2012).

18. Chatrchyan, S. *et al.* Observation of a new boson at a mass of 125 GeV with the CMS experiment at the LHC. *Phys. Lett. B* **716,** 30–61. arXiv: 1207.7235 [hep-ex] (2012).

19. Symmetry Magazine. *The Standard Model* https://www.symmetrymagazine.org/standard-model/ [Accessed: 02/04/25].

20. Thomson, M. *Modern particle physics* (Cambridge University Press, New York, Oct. 2013).

21. Glashow, S. L. The renormalizability of vector meson interactions. *Nucl. Phys.* **10,** 107–117 (1959).

22. Salam, A. Weak and electromagnetic interactions. *Conf. Proc. C* **680519,** 367–377 (1968).

23. Weinberg, S. A Model of Leptons. *Phys. Rev. Lett.* **19,** 1264–1266 (1967).

24. Arnison, G. *et al.* Experimental observation of isolated large transverse energy electrons with associated missing energy at $\sqrt{s} = 540$ GeV. *Phys. Lett. B* **122,** 103–116 (1983).

25. Arnison, G. *et al.* Experimental observation of lepton pairs of invariant mass around 95 GeV/c^2 at the CERN SPS collider. *Phys. Lett. B* **126,** 398–410 (1983).

26. Englert, F. & Brout, R. Broken symmetry and the mass of gauge vector mesons. *Phys. Rev. Lett.* **13,** 321–323 (1964).

27. Higgs, P. W. Broken symmetries and the masses of gauge bosons. *Phys. Rev. Lett.* **13,** 508–509 (1964).

28. Lee, T. D. & Yang, C.-N. Question of parity conservation in weak interactions. *Phys. Rev.* **104,** 254–258 (1956).

29. Wu, C. S., Ambler, E., Hayward, R. W., Hoppes, D. D. & Hudson, R. P. Experimental test of parity conservation in β decay. *Phys. Rev.* **105,** 1413–1414 (1957).

30. Sakharov, A. D. Violation of CP invariance, C asymmetry, and baryon asymmetry of the universe. *Pisma Zh. Eksp. Teor. Fiz.* **5,** 32–35 (1967).

31. Chau, L. L. & Keung, W. Y. Comments on the parametrization of the Kobayashi-Maskawa matrix. *Phys. Rev. Lett.* **53,** 1802 (1984).

32. Wolfenstein, L. Parametrization of the Kobayashi-Maskawa matrix. *Phys. Rev. Lett.* **51,** 1945 (1983).

33. Navas, S. *et al.* Review of particle physics. *Phys. Rev. D* **110,** 030001 (2024).

34. Brod, J. & Zupan, J. The ultimate theoretical error on γ from $B \to DK$ decays. *JHEP* **01,** 051. arXiv: 1308.5663 [hep-ph] (2014).

35. Bona, M. *et al.* New UTfit analysis of the Unitarity Triangle in the Cabibbo-Kobayashi-Maskawa scheme. *Rend. Lincei Sci. Fis. Nat.* **34,** 37–57. arXiv: 2212.03894 [hep-ph] (2023).

36. Banerjee, S. *et al.* Averages of b-hadron, c-hadron, and τ-lepton properties as of 2023. See https://hflav.web.cern.ch for updates. arXiv: 2411.18639 [hep-ex] (Nov. 2024).

37. Lenz, A. & Wilkinson, G. Mixing and CP violation in the charm system. *Ann. Rev. Nucl. Part. Sci.* **71,** 59–85. arXiv: 2011.04443 [hep-ph] (2021).

38. Dunietz, I. *CP* violation with self-tagging B_d modes. *Phys. Lett. B* **270,** 75–80 (1991).

39. LHCb collaboration. Simultaneous determination of the CKM angle γ and parameters related to mixing and *CP* violation in the charm sector, *LHCb-CONF-2022-003* (2022).

40. Aaij, R. *et al.* Constraints on the unitarity triangle angle γ from Dalitz plot analysis of $B^0 \to DK^+\pi^-$ decays. *Phys. Rev. D* **93.** [Erratum: Phys.Rev.D 94, 079902 (2016)], 112018. arXiv: 1602.03455 [hep-ex] (2016).

41. Gronau, M. & London, D. How to determine all the angles of the unitarity triangle from $B^0_d \to DK_s$ and $B^0_s \to D\phi$. *Phys. Lett. B* **253,** 483–488 (1991).

42. Gronau, M. & Wyler, D. On determining a weak phase from *CP* asymmetries in charged B decays. *Phys. Lett. B* **265,** 172–176 (1991).

43. Atwood, D., Dunietz, I. & Soni, A. Enhanced *CP* violation with $B \to KD^0(\overline{D}^0)$ modes and extraction of the CKM angle gamma. *Phys. Rev. Lett.* **78,** 3257–3260. arXiv: hep-ph/9612433 (1997).

44. Bondar, A. Proceedings of BINP special analysis meeting on Dalitz analysis, 24-26 Sep. 2022, unpublished.

45. Bondar, A. & Poluektov, A. Feasibility study of model-independent approach to ϕ_3 measurement using Dalitz plot analysis. *Eur. Phys. J. C* **47,** 347–353. arXiv: hep-ph/0510246 (2006).

46. Bondar, A. & Poluektov, A. The use of quantum-correlated D^0 decays for ϕ_3 measurement. *Eur. Phys. J. C* **55,** 51–56. arXiv: 0801.0840 [hep-ex] (2008).

47. Giri, A., Grossman, Y., Soffer, A. & Zupan, J. Determining γ using $B^\pm \to DK^\pm$ with multibody D decays. *Phys. Rev. D* **68,** 054018. arXiv: hep-ph/0303187 (2003).

48. Aaij, R. *et al.* Measurement of CP violation and constraints on the CKM angle γ in $B^\pm \to DK^\pm$ with $D \to K^0_S\pi^+\pi^-$ decays. *Nucl. Phys. B* **888,** 169–193. arXiv: 1407.6211 [hep-ex] (2014).

49. Libby, J. *et al.* Model-independent determination of the strong-phase difference between D^0 and $\bar{D}^0 \to K^0_{S,L}h^+h^-$ ($h = \pi, K$) and its impact on the measurement of the CKM angle γ/ϕ_3. *Phys. Rev. D* **82,** 112006. arXiv: 1010.2817 [hep-ex] (2010).

50. Aubert, B. *et al.* Improved measurement of the CKM angle γ in $B^{\mp} \to D^{(*)}K^{(*\mp)}$ decays with a Dalitz plot analysis of D decays to $K^0_S\pi^+\pi^-$ and $K^0_S K^+K^-$. *Phys. Rev. D* **78,** 034023. arXiv: `0804.2089 [hep-ex]` (2008).
51. Evans, L. & Bryant, P. LHC Machine. *JINST* **3,** S08001 (2008).
52. Amaldi, U. & La Rana, A. *Particle accelerators: From big bang physics to hadron therapy* (Springer, Cham, 2015).
53. LHCb collaboration. LHCb Letter of Intent, *CERN-LHCb-95-001* (1995).
54. Alves Jr., A. A. *et al.* The LHCb detector at the LHC. *JINST* **3,** S08005 (2008).
55. LHCb collaboration. LHCb VELO (VErtex LOcator): Technical Design Report, *CERN-LHCC-2001-011* (2001).
56. LHCb collaboration. LHCb inner tracker: Technical Design Report, *CERN-LHCC-2002-029* (2002).
57. LHCb collaboration. LHCb outer tracker: Technical Design Report, *CERN-LHCC-2001-024* (2001).
58. LHCb collaboration. LHCb magnet: Technical Design Report, *CERN-LHCC-2000-007* (2000).
59. LHCb collaboration. LHCb RICH: Technical Design Report, *CERN-LHCC-2000-037* (2000).
60. LHCb collaboration. LHCb muon system: Technical Design Report, *CERN-LHCC-2001-010* (2001).
61. LHCb collaboration. LHCb calorimeters: Technical Design Report, *CERN-LHCC-2000-036* (2000).
62. LHCb collaboration. LHCb trigger system: Technical Design Report, *CERN-LHCC-2003-031* (2003).
63. Wenninger, J. & Gorzawski, A. *Implementation of luminosity leveling by betatron function adjustment at the LHC interaction points* in *5th International Particle Accelerator Conference* (July 2014), TUPRO022.
64. Dijkstra, H. B. CP violation prospects at the LHC. *Braz. J. Phys.* **34,** 1295–1306 (2004).
65. Aaij, R. *et al.* Performance of the LHCb Vertex Locator. *JINST* **9,** P09007. arXiv: `1405.7808 [physics.ins-det]` (2014).
66. Cowan, G. A. Performance of the LHCb silicon tracker. *Nucl. Instrum. Meth. A* **699,** 156–159 (2013).
67. Arink, R. *et al.* Performance of the LHCb Outer Tracker. *JINST* **9,** P01002. arXiv: `1311.3893 [physics.ins-det]` (2014).
68. Aaij, R. *et al.* LHCb detector performance. *Int. J. Mod. Phys. A* **30,** 1530022. arXiv: `1412.6352 [hep-ex]` (2015).
69. Aaij, R. *et al.* Design and performance of the LHCb trigger and full real-time reconstruction in Run 2 of the LHC. *JINST* **14,** P04013. arXiv: `1812.10790 [hep-ex]` (2019).

70. Callot, O. & Hansmann-Menzemer, S. The forward tracking: algorithm and performance studies, *CERN-LHCb-2007-015* (2007).

71. Needham, M. & Van Tilburg, J. Performance of the track matching, *CERN-LHCb-2007-020* (2007).

72. Aaij, R. *et al.* Measurement of the track reconstruction efficiency at LHCb. *JINST* **10,** P02007. arXiv: 1408.1251 [hep-ex] (2015).

73. Papanestis, A. & D'Ambrosio, C. Performance of the LHCb RICH detectors during the LHC Run II. *Nucl. Instrum. Meth. A* **876,** 221–224. arXiv: 1703.08152 [physics.ins-det] (2017).

74. Forty, R. W. & Schneider, O. RICH pattern recognition, *CERN-LHCb-98-040* (1998).

75. Marin Benito, C. PID strategy and performance at LHCb in Run 2. *PoS* **ICHEP2018,** 687 (2019).

76. Abellán Beteta, C. *et al.* Calibration and performance of the LHCb calorimeters in Run 1 and 2 at the LHC. arXiv: 2008.11556 [physics.ins-det] (Aug. 2020).

77. Archilli, F. *et al.* Performance of the muon identification at LHCb. *JINST* **8,** P10020. arXiv: 1306.0249 [physics.ins-det] (2013).

78. Alves Jr., A. A. *et al.* Performance of the LHCb muon system. *JINST* **8,** P02022. arXiv: 1211.1346 [physics.ins-det] (2013).

79. LHCb collaboration. *Trigger Schemes* http://lhcb.web.cern.ch/lhcb/speakersbureau/html/TriggerScheme.html [Accessed: 15/03/25].

80. Sjöstrand, T., Mrenna, S. & Skands, P. A brief introduction to PYTHIA 8.1. *Comput. Phys. Commun.* **178,** 852–867. arXiv: 0710.3820 [hep-ph] (2008).

81. Sjöstrand, T., Mrenna, S. & Skands, P. PYTHIA 6.4 physics and manual. *JHEP* **05,** 026. arXiv: hep-ph/0603175 [hep-ph] (2006).

82. Belyaev, I. *et al.* Handling of the generation of primary events in Gauss, the LHCb simulation framework. *J. Phys. Conf. Ser.* **331,** 032047 (2011).

83. Lange, D. J. The EvtGen particle decay simulation package. *Nucl. Instrum. Meth.* **A462,** 152–155 (2001).

84. Davidson, N., Przedzinski, T. & Was, Z. PHOTOS interface in C++: Technical and physics documentation. *Comp. Phys. Comm.* **199,** 86. arXiv: 1011.0937 [hep-ph] (2016).

85. Allison, J., Amako, K., Apostolakis, J., Araujo, H., Dubois, P., *et al.* Geant4 developments and applications. *IEEE Trans.Nucl.Sci.* **53,** 270 (2006).

86. Agostinelli, S. *et al.* Geant4: A simulation toolkit. *Nucl. Instrum. Meth.* **A506,** 250 (2003).

87. Clemencic, M. *et al.* The LHCb simulation application, Gauss: Design, evolution and experience. *J. Phys. Conf. Ser.* **331,** 032023 (2011).

88. Aaij, R. *et al.* Measurement of the CKM angle γ in $B^{\pm} \to DK^{\pm}$ and $B^{\pm} \to D\pi^{\pm}$ decays with $D \to K^0_S h^+ h^-$. *JHEP* **02,** 169. arXiv: 2010.08483 [hep-ex] (2021).

89. Aaij, R. *et al.* Model-independent measurement of the CKM angle γ using $B^0 \to DK^{*0}$ decays with $D \to K^0_S\pi^+\pi^-$ and $K^0_SK^+K^-$. *JHEP* **06,** 131. arXiv: 1604.01525 [hep-ex] (2016).

90. Bondar, A., Poluektov, A. & Vorobiev, V. Charm mixing in the model-independent analysis of correlated $D^0\overline{D}^0$ decays. *Phys. Rev. D* **82,** 034033. arXiv: 1004.2350 [hep-ph] (2010).

91. Rama, M. Effect of D-$\overline{D}$ mixing in the extraction of gamma with $B^- \to D^0K^-$ and $B^- \to D^0\pi^-$ decays. *Phys. Rev. D* **89,** 014021. arXiv: 1307.4384 [hep-ex] (2014).

92. Workman, R. L. *et al.* Review of particle physics. *Prog. Theor. Exp. Phys.* **2022,** 083C01 (2022).

93. Hulsbergen, W. D. Decay chain fitting with a Kalman filter. *Nucl. Instrum. Meth. A* **552,** 566–575. arXiv: physics/0503191 (2005).

94. Breiman, L., Friedman, J., Stone, C. & Olshen, R. *Classification and Regression Trees* https://books.google.co.uk/books?id=JwQx-WOmSyQC (Taylor & Francis, 1984).

95. NIST. *Chi-square two sample test* https://www.itl.nist.gov/div898/software/dataplot/refman1/auxillar/chi2samp.htm [Accessed: 11/07/25].

96. Aaij, R. *et al.* Study of CP violation in $B^0 \to DK^*(892)^0$ decays with $D \to K\pi(\pi\pi)$, $\pi\pi(\pi\pi)$, and KK final states. *JHEP* **05,** 025. arXiv: 2401.17934 [hep-ex] (2024).

97. Skwarnicki, T. *A study of the radiative CASCADE transitions between the Upsilon-Prime and Upsilon resonances* PhD thesis (Cracow, INP, 1986).

98. Aaij, R. *et al.* Measurement of the fragmentation fraction ratio f_s/f_d and its dependence on B meson kinematics. *JHEP* **04,** 001. arXiv: 1301.5286 [hep-ex] (2013).

99. Aaij, R. *et al.* Precise measurement of the f_s/f_d ratio of fragmentation fractions and of B^0_s decay branching fractions. *Phys. Rev. D* **104,** 032005. arXiv: 2103.06810 [hep-ex] (2021).

100. Aaij, R. *et al.* Simultaneous determination of CKM angle γ and charm mixing parameters. *JHEP* **12,** 141. arXiv: 2110.02350 [hep-ex] (2021).

101. Adachi, I. *et al.* Measurement of $\cos 2\beta$ in $B^0 \to D^{(*)}h^0$ with $D \to K^0_S\pi^+\pi^-$ decays by a combined time-dependent Dalitz plot analysis of BaBar and Belle data. *Phys. Rev. D* **98,** 112012. arXiv: 1804.06153 [hep-ex] (2018).

102. Aaij, R. *et al.* Measurement of CP observables in the process $B^0 \to DK^{*0}$ with two- and four-body D decays. *JHEP* **08,** 041. arXiv: 1906.08297 [hep-ex] (2019).

103. Achasov, M. *et al.* STCF conceptual design report (Volume 1): Physics & detector. *Front. Phys. (Beijing)* **19,** 14701. arXiv: 2303.15790 [hep-ex] (2024).

104. Ablikim, M. *et al.* First observation of quantum correlations in $e^+e^- \to XD\bar{D}$ and C-even constrained $D\bar{D}$ pairs. arXiv: 2506.07906 [hep-ex] (June 2025).

105. Glashow, S. L., Iliopoulos, J. & Maiani, L. Weak interactions with lepton-hadron symmetry. *Phys. Rev. D* **2,** 1285–1292 (1970).

106. Xing, Z.-z. D^0–$\overline{D}^0$ mixing and *CP* violation in neutral D meson decays. *Phys. Rev. D* **55,** 196–218. arXiv: hep-ph/9606422 (1997).

107. Ablikim, M. *et al.* Measurements of the CP-even fractions of $D^0 \to \pi^+\pi^-\pi^0$ and $D^0 \to K^+K^-\pi^0$ at BESIII. *Phys. Rev. D* **111,** 012007. arXiv: 2409.07197 [hep-ex] (2025).

108. Ablikim, M. *et al.* Design and construction of the BESIII detector. *Nucl. Instrum. Meth. A* **614,** 345–399. arXiv: 0911.4960 [physics.ins-det] (2010).

109. Ablikim, M. *et al.* Cross section measurements of the $e^+e^- \to D^{*+}D^{*-}$ and $e^+e^- \to D^{*+}D^-$ processes at center-of-mass energies from 4.085 to 4.600 GeV. *JHEP* **05,** 155. arXiv: 2112.06477 [hep-ex] (2022).

110. Bai, J. Z. *et al.* The BES upgrade. *Nucl. Instrum. Meth. A* **458,** 627–637 (2001).

111. Ablikim, M. *et al.* Precision measurement of the mass of the τ lepton. *Phys. Rev. D* **90,** 012001. arXiv: 1405.1076 [hep-ex] (2014).

112. Ablikim, M. *et al.* Analysis of $D^+ \to \bar{K}^0 e^+\nu_e$ and $D^+ \to \pi^0 e^+\nu_e$ semileptonic decays. *Phys. Rev. D* **96,** 012002. arXiv: 1703.09084 [hep-ex] (2017).

113. Ablikim, M. *et al.* Study of the $D^0 \to K^-\mu^+\nu_\mu$ dynamics and test of lepton flavor universality with $D^0 \to K^-\ell^+\nu_\ell$ decays. *Phys. Rev. Lett.* **122,** 011804. arXiv: 1810.03127 [hep-ex] (2019).

114. Ablikim, M. *et al.* Confirmation of the $X(1835)$ and observation of the resonances $X(2120)$ and $X(2370)$ in $J/\psi \to \gamma\pi^+\pi^-\eta'$. *Phys. Rev. Lett.* **106,** 072002. arXiv: 1012.3510 [hep-ex] (2011).

115. Zhang, C.-A. *Performance of the BEPC and progress of the BEPCII* in *32nd International Conference on High Energy Physics* (Aug. 2004), 993–997.

116. Yuan, C.-Z. & Olsen, S. L. The BESIII physics programme. *Nature Rev. Phys.* **1,** 480–494. arXiv: 2001.01164 [hep-ex] (2019).

117. CERN Courier. *BESIII passes milestone at the charm threshold* https://cerncourier.com/a/besiii-passes-milestone-at-the-charm-threshold/ [Accessed: 11/04/25].

118. Yu, C. *et al. BEPCII Performance and Beam Dynamics Studies on Luminosity* in *7th International Particle Accelerator Conference* (2016), TUYA01.

119. Cronin-Hennessy, D. *et al.* Measurement of charm production cross sections in e^+e^- annihilation at energies between 3.97 and 4.26-GeV. *Phys. Rev. D* **80,** 072001. arXiv: 0801.3418 [hep-ex] (2009).

120. Huang, K.-X. *et al.* Method for detector description transformation to Unity and application in BESIII. *Nucl. Sci. Tech.* **33,** 142. arXiv: 2206.10117 [physics.ins-det] (2022).

121. Küßner, M. *Coupled channel partial wave analysis of two-photon reactions at BESIII* PhD thesis (Ruhr U., Bochum, 2022).

122. Liu, J. B. *et al.* A beam test of a prototype of the BESIII drift chamber in magnetic field. *Nucl. Instrum. Meth. A* **557,** 436–444 (2006).

123. Gang, Q. *et al.* Particle identification using artificial neural networks at BESIII. *Chinese Physics C* **32,** 1. https://dx.doi.org/10.1088/1674-1137/32/1/001 (Jan. 2008).

124. Cao, P. *et al.* Design and construction of the new BESIII endcap Time-of-Flight system with MRPC Technology. *Nucl. Instrum. Meth. A* **953,** 163053 (2020).

125. He, M. Simulation and reconstruction of the BESIII EMC. *J. Phys. Conf. Ser.* **293,** 012025 (2011).

126. Bai, J. Z. *et al.* The BES detector. *Nucl. Instrum. Meth. A* **344,** 319–334 (1994).

127. Ablikim, M. *et al.* Study of BESIII trigger efficiencies with the 2018 J/ψ data. *Chin. Phys. C* **45,** 023002. arXiv: 2009.11566 [hep-ex] (2021).

128. Cheng-Dong, F. *et al.* Study of the online event filtering algorithm for BESIII. *Chinese Physics C* **32,** 329. https://dx.doi.org/10.1088/1674-1137/32/5/001 (May 2008).

129. Jadach, S., Ward, B. F. L. & Was, Z. Coherent exclusive exponentiation for precision Monte Carlo calculations. *Phys. Rev. D* **63,** 113009. arXiv: hep-ph/0006359 (2001).

130. Jadach, S., Ward, B. F. L. & Was, Z. The precision Monte Carlo event generator K K for two fermion final states in e^+e^- collisions. *Comput. Phys. Commun.* **130,** 260–325. arXiv: hep-ph/9912214 (2000).

131. Ping, R.-G. Event generators at BESIII. *Chin. Phys. C* **32,** 599 (2008).

132. Chen, J. C., Huang, G. S., Qi, X. R., Zhang, D. H. & Zhu, Y. S. Event generator for J/ψ and $\psi(2S)$ decay. *Phys. Rev. D* **62,** 034003 (2000).

133. Yang, R.-L., Ping, R.-G. & Chen, H. Tuning and validation of the Lundcharm model with J/ψ decays. *Chin. Phys. Lett.* **31,** 061301 (2014).

134. Aaij, R. *et al.* A model-independent measurement of the CKM angle γ in partially reconstructed $B^\pm \to D^* h^\pm$ decays with $D \to K^0_S h^+ h^-$ ($h = \pi, K$). *JHEP* **02,** 118. arXiv: 2311.10434 [hep-ex] (2024).

135. Aaij, R. *et al.* Measurement of the CKM angle γ using the $B^\pm \to D^* h^\pm$ channels. *JHEP* **12,** 013. arXiv: 2310.04277 [hep-ex] (2023).

136. Aaij, R. *et al.* Measurement of the CKM angle γ in $B^\pm \to DK^*(892)^\pm$ decays. *JHEP* **02,** 113. arXiv: 2410.21115 [hep-ex] (2025).

137. Gilman, A. Private communication, publication in preparation. Apr. 22, 2025.

138. Aaij, R. *et al.* Observation of the mass difference between neutral charm-meson eigenstates. *Phys. Rev. Lett.* **127,** 111801. arXiv: 2106.03744 [hep-ex] (2021).

139. Physics case for an LHCb Upgrade II: Opportunities in flavour physics, and beyond, in the HL-LHC era (2018).

140. LHCb collaboration. Future physics potential of LHCb, *LHCb-PUB-2022-012* (2022).